UNIVERSIDADE FEDERAL DO RIO GRANDE DO SUL

INSTITUTO DE PESQUISAS HIDRÁULICAS

PROGRAMA DE PÓS-GRADUAÇÃO EM RECURSOS HÍDRICOS E SANEAMENTO AMBIENTAL

JOÃO PEDRO TAUSCHECK ZIELINSKI

AVALIAÇÃO HIDROGEOQUÍMICA DA INTERAÇÃO CO_2-ÁGUA SUBTERRÂNEA-MINERAL EM AQUÍFERO RASO: IMPLICAÇÕES PARA O MONITORAMENTO AMBIENTAL EM PROJETOS DE ARMAZENAMENTO GEOLÓGICO DE CARBONO (CCS)

Porto Alegre

2024

JOÃO PEDRO TAUSCHECK ZIELINSKI

AVALIAÇÃO HIDROGEOQUÍMICA DA INTERAÇÃO CO_2-ÁGUA SUBTERRÂNEA-MINERAL EM AQUÍFERO RASO: IMPLICAÇÕES PARA O MONITORAMENTO AMBIENTAL EM PROJETOS DE ARMAZENAMENTO GEOLÓGICO DE CARBONO (CCS)

Tese de Doutorado apresentada ao Programa de Pós-graduação em Recursos Hídricos e Saneamento Ambiental do Instituto de Pesquisas Hidráulicas da Universidade Federal do Rio Grande do Sul, como parte dos requisitos para a obtenção do título de Doutor em Recursos Hídricos e Saneamento Ambiental.

Orientador: Prof. Dr. Pedro A. R. Reginato (UFRGS)

Coorientadora: Dra. Clarissa Lovato Melo (IPR/PUCRS)

Porto Alegre

2024

CIP - Catalogação na Publicação

Tauscheck Zielinski, João Pedro
Avaliação hidrogeoquímica da interação CO2-água subterrânea-mineral em aquífero raso: implicações para o monitoramento ambiental em projetos de armazenamento geológico de carbono (CCS) / João Pedro Tauscheck Zielinski. -- 2024.
216 f.
Orientador: Pedro Antonio Roehe Reginato.

Coorientadora: Clarissa Lovato Melo.

Tese (Doutorado) -- Universidade Federal do Rio Grande do Sul, Instituto de Pesquisas Hidráulicas, Programa de Pós-Graduação em Recursos Hídricos e Saneamento Ambiental, Porto Alegre, BR-RS, 2024.

1. hidrogeoquímica. 2. CO2. 3. CCS. 4. monitoramento ambiental. 5. hidrogeologia. I. Roehe Reginato, Pedro Antonio, orient. II. Lovato Melo, Clarissa, coorient. III. Título.

Elaborada pelo Sistema de Geração Automática de Ficha Catalográfica da UFRGS com os dados fornecidos pelo(a) autor(a).

JOÃO PEDRO TAUSCHECK ZIELINSKI

AVALIAÇÃO HIDROGEOQUÍMICA DA INTERAÇÃO CO_2-ÁGUA SUBTERRÂNEA-MINERAL EM AQUÍFERO RASO: IMPLICAÇÕES PARA O MONITORAMENTO AMBIENTAL EM PROJETOS DE ARMAZENAMENTO GEOLÓGICO DE CARBONO (CCS)

Tese de Doutorado apresentada ao Programa de Pós-graduação em Recursos Hídricos e Saneamento Ambiental do Instituto de Pesquisas Hidráulicas da Universidade Federal do Rio Grande do Sul, como parte dos requisitos para a obtenção do título de Doutor em Recursos Hídricos e Saneamento Ambiental.

Aprovado em: Porto Alegre, 4 de outubro de 2024.

_____

Prof. Dr. Pedro A. R. Reginato (UFRGS)
Orientador

_____

Dra. Clarissa Lovato Melo (IPR/PUCRS)

Coorientadora

_____

Prof. Dr. Tiago de Vargas - PPGGEO/UFRGS

Examinador

_____

Dra. Fátima Ferreira do Rosário – CENPES/Petrobras

Examinadora

_____

Prof. Dr. Rafael Manica – IPH/UFRGS

Examinador

AGRADECIMENTOS

Um doutorado não se faz sozinho, e diria que o apoio emocional é tão, senão mais importante, quanto o esforço técnico para concretizá-lo. Tive a felicidade de contar com familiares, amigos e colegas que sempre me apoiaram e trouxeram paz durante esse período. Minha esposa Monique e minha filha Ayla são mais do que importantes; elas são a base que sustenta quem sou. Sem elas, não teria onde me apoiar. Meus pais e sogros, ao longo de todos esses anos, sempre estiveram ao meu lado e fizeram de tudo para que eu continuasse nessa trajetória, mesmo que isso significasse a abdicação do meu tempo com eles. Da mesma forma, meus familiares mais próximos sempre enviaram mensagens de apoio que me fortaleceram ao longo dessa caminhada.

No âmbito técnico, é impossível iniciar qualquer agradecimento sem antes mencionar o papel extraordinário do professor Reginato como orientador. Seu compromisso, dedicação e disponibilidade para me auxiliar nessa importante etapa merecem ser reconhecidos e elogiados. Em toda minha trajetória acadêmica, que começou em 2008 e teve muitos altos e baixos, conheci pouquíssimos professores que honram plenamente o título de "professor orientador". O professor Reginato é, sem dúvida, alguém que vive e transparece essa missão de forma exemplar. Obrigado, professor!

Além disso, sou profundamente grato à equipe do Instituto do Petróleo e dos Recursos Naturais (IPR) da PUCRS, especialmente à minha coorientadora Clarissa Lovato Melo e ao Felipe Dalla Vecchia, que desde o início da minha trajetória na instituição acreditaram na minha capacidade e dedicação técnica. Se eu tentasse nomear todos que interagiram comigo nos últimos quatro anos e meio, certamente correria o risco de esquecer alguém. Mesmo que a contribuição de algumas pessoas tenha sido momentânea, todas desempenharam um papel fundamental no meu desenvolvimento e na realização deste trabalho. Minha gratidão vai a todos que me apoiaram ao longo desses anos.

No aspecto financeiro, agradeço às seguintes instituições pelo suporte: a) à Coordenação de Aperfeiçoamento de Pessoal de Nível Superior (CAPES), por meio do Programa de Excelência Acadêmica (PROEX), pela alocação de parte dos recursos para o financiamento de análises químicas; b) à Petrobras S.A., que possibilitou parte do desenvolvimento desta pesquisa através de investimentos nos

projetos CO_2Move I e II; e c) à Financiadora de Estudos e Projetos (FINEP), cujo apoio foi essencial para a realização do experimento de injeção controlada de CO_2, viabilizado pelo projeto ECO_2A. Por último, mas não menos importante, agradeço aos professores e colegas do Programa de Pós-Graduação em Recursos Hídricos e Saneamento Ambiental (PPGRHSA) do Instituto de Pesquisas Hidráulicas (IPH).

Finalmente, gostaria de compartilhar o sentimento de fazer pesquisa científica no Brasil. É impressionante como, apesar da alternância de governos sem um plano sólido de Estado para a ciência, das campanhas de descredibilização da educação superior propagadas por políticos de extrema-direita mal-intencionados, da falta de investimentos contínuos e proporcionais à significância econômica do Brasil, e da necessidade de currículos de pós-graduação atualizados e bem estruturados, ainda conseguimos produzir ciência de qualidade, mesmo diante de enormes adversidades. Imagine onde poderíamos estar se ao menos um ou dois desses fatores fossem mais favoráveis.

Além disso, a cultura do doutorado no Brasil precisa evoluir. Não podemos continuar formando doutores(as) exclusivamente para as universidades; o cenário já mudou há muitos anos, e estamos inquestionavelmente atrasados. Para alguns, fazer doutorado tornou-se mais um fardo do que uma realização pessoal e profissional, o que está completamente errado. Espero, sinceramente, que esse quadro melhore num futuro próximo.

“The final chapter is ours to write. We know what we need to do. What happens next is up to us.”

(Sir David Attenborough)

RESUMO

O aumento contínuo da concentração de CO_2 atmosférico, decorrente das atividades humanas, está causando graves consequências climáticas. Nesse contexto, tecnologias como a Captura e Armazenamento Geológico de Carbono (CCS) são essenciais para reduzir as emissões. No entanto, essa técnica, que envolve a injeção de CO_2 em reservatórios geológicos, levanta preocupações quanto ao potencial vazamento do gás em direção à superfície, o que poderia comprometer a qualidade da água subterrânea acima desses reservatórios. Embora o CO_2 não seja intrinsecamente um contaminante, sua concentração excessiva pode desencadear reações com a mineralogia do aquífero, alterando a qualidade da água, tornando crucial a avaliação das possíveis consequências dessa interação. Este estudo objetiva avaliar a interação CO_2-água subterrânea-mineral em um aquífero poroso raso de mineralogia aluminossilicática, identificando alterações hidrogeoquímicas e determinando parâmetros indicativos desse processo. Para isso, foi realizada uma caracterização hidrogeológica e geofísica no campo experimental do TECNOPUC-Viamão (RS), além do monitoramento da variabilidade hidroquímica e da assinatura isotópica de carbono (δ^{13}C-DIC) ao longo de três anos. A água subterrânea foi coletada em poços de monitoramento multiníveis em diferentes unidades hidroestratigráficas. Em seguida, um experimento de vazamento controlado de CO_2 foi conduzido com monitoramento frequente da interação por meio de análises físico-químicas e químicas de elementos maiores, menores e traços. Apesar do impacto de eventos de precipitação em alguns parâmetros, observou-se uma alta correlação ($\rho > 0,70$) e um padrão linear cronológico de evolução entre a pressão parcial de CO_2 (PCO_2) e variáveis como Condutividade Elétrica (CE), pH, ORP, Alcalinidade Total (AT), Ca, Mg, K, Na, Si, Ba, Sr, Fe, Mn, PO_4^{3-} e HCO_3^-, com alguns parâmetros destacando-se como indicadores mais eficazes do impacto de vazamentos de CO_2. Alguns elementos, como Fe e Mn exigem atenção, pois excederam limites legais. Esses resultados indicam que, com monitoramento adequado e um background sazonal bem estabelecido, é possível diagnosticar e avaliar eficazmente os impactos de vazamentos não intencionais de CO_2 em projetos de CCS.

PALAVRAS-CHAVE: vazamento de CO_2, hidrogeoquímica, monitoramento ambiental, CCS

ABSTRACT

The continuous increase in atmospheric CO_2 concentration, driven by human activities, is causing severe climatic consequences. In this context, technologies such as Carbon Capture and Storage (CCS) are essential for reducing emissions. However, this technique, which involves the injection of CO_2 into geological reservoirs, raises concerns about the potential for gas leakage towards the surface, which could compromise the quality of groundwater above these reservoirs. Although CO_2 is not inherently a contaminant, its excessive concentration can trigger reactions with the aquifer mineralogy, altering the water natural quality, making it crucial to assess the potential consequences of this interaction. This study aims to evaluate the CO_2-groundwater-mineral interaction in a shallow, aluminosilicate-rich porous aquifer at the TECNOPUC-Viamão experimental site in Southern Brazil, identifying hydrogeochemical alterations and determining key indicators of this process. To achieve this, a hydrogeological and geophysical characterization was conducted, along with monitoring hydrochemical variability and the carbon isotopic signature ($\delta^{13}C$-DIC) over three years. Groundwater samples were collected from multilevel monitoring wells across different hydrostratigraphic units. Subsequently, a controlled CO_2 leakage experiment was conducted, with frequent monitoring of the interaction through physicochemical and chemical analyses of major, minor, and trace elements. Despite the impact of precipitation events on some parameters, a high correlation ($\rho > 0.70$) and a chronological linear evolution pattern were observed between the partial pressure of CO_2 (PCO_2) and variables such as Electrical Conductivity (EC), pH, ORP, Total Alkalinity (TA), Ca, Mg, K, Na, Si, Ba, Sr, Fe, Mn, PO_4^{3-}, and HCO_3^-, with some parameters standing out as more effective indicators of CO_2 leakage impacts. Certain elements, such as Fe and Mn, require attention, as they exceeded legal limits. These results indicate that, with adequate monitoring and a well-established seasonal background, it is possible to effectively diagnose and assess the impacts of unintentional CO_2 leaks in CCS projects.

KEYWORDS: CO_2 leakage, hydrogeochemistry, environmental monitoring, CCS

LISTA DE SIGLAS E ABREVIATURAS

CCS - *Carbon Capture and Storage*

GEE – Gases de Efeito Estufa

Gt_{GEE} – Bilhões de toneladas de Gases de Efeito Estufa

CO_2e – CO_2 equivalente

SEEG-OC - Sistema de Estimativas de Emissões e Remoções de Gases de Efeito Estufa do Observatório do Clima

IPCC - Painel Intragovernamental sobre Mudanças Climáticas

NDCs - Contribuições Nacionalmente Determinadas

CDR - *Carbon Dioxide Removal*

CCS-EOR – *Carbon Capture and Storage – Enhanced Oil Recovery*

O&G – Óleo e Gás

COT – Carbono Orgânico Total

MMV – Monitoramento, Medição e Verificação

IEA – *International Energy Agency*

EPA - *Environmental Protection Agency*

TECNOPUC - Parque Científico e Tecnológico da PUCRS

ECGP - Embasamento Cristalino Granítico-Gnáissico Pré-Cambriano

NE - Nível Estático

DPT - *Direct Push Technology*

CE – Condutividade Elétrica, µS/cm

OD – Oxigênio Dissolvido, mg/L

ORP – Potencial de Oxirredução, mV

DIC - Carbono Inorgânico Dissolvido

$\delta^{13}C_{\text{-DIC}}$ – Razão isotópica $^{13}C/^{12}C$ do DIC

$\delta^{13}C_{\text{-}CO_2}$ - Razão isotópica $^{13}C/^{12}C$ do CO_2 (g)

PCO_2 - Pressão parcial do CO_2

MDT - Modelo Digital do Terreno

SPT - *Standard Penetration Test*

PHREEQC – software de modelagem geoquímica

VPDB - *Vienna Pee Dee Belemnite*

LISTA DE FIGURAS

Figura 1. 1. Infográfico sobre as emissões de gases do efeito estufa no Brasil. Fonte: Modificada de SEEG-OC (2024). 21
Figura 1. 2. Cenários modelados de emissões de GEE considerando as metas necessárias e as políticas implementadas. Fonte: IPCC (2022). 22
Figura 1. 3. Exemplo de uma configuração possível de projeto de CCS. Fonte: Geospatial Research Ltd. 23
Figura 1. 4. Alternativas de reservatórios geológicos para armazenamento de CO_2. Fonte: Traduzido de IPCC (2005). 24
Figura 1. 5. Mecanismos de aprisionamento geológico de CO_2. Modificado de (Ketzer et al., 2016). 26
Figura 1. 6. Principais rotas de escape de CO_2 do reservatório geológico: A) vazamento por meio da rocha selante; B) vazamento via falha existente; e C) vazamento através de poço abandonado ou mal cimentado (completado). Modificado de Bouc et al. (2009)..... 28
Figura 1. 7. Técnicas de MMV onshore e offshore aplicados em diferentes compartimentos geológicos. Fonte: Global Status of CCS 2019. 30
Figura 1. 8. Diagrama esquemático da distribuição da pluma de CO_2 (e da salmoura), posicionamento espacial dos poços e comportamento dinâmico em diferentes aquíferos (livre e confinado). Modificado de Jones et al. (2015). 32
Figura 2. 1. Resultados reportados de $\delta^{13}C_{\text{-DIC}}$ de (a) Schulz et al. (2012), onde os círculos representam a assinatura isotópica e os quadrados o pH para diferentes poços (de 1C-3 a 1G-3); (b) Yang et al. (2013), cujos pontos simbolizam os valores medidos de isótopos de $^{13}C/^{12}C$ e a linha o modelo calculado; (c) Newell et al. (2014), que demonstra os valores isotópicos para os poços BG-1 a MW-4; e (d) Do et al. (2022), exemplificado pela alteração isotópica do $\delta^{13}C_{\text{-DIC}}$ em relação ao background $\Delta\delta^{13}C_{\text{-DIC}}$ para o poço SMW-1 (mais próximo e correspondentes à direção de fluxo)..... 37
Figura 3. 1 Fluxograma de desenvolvimento dos trabalhos, métodos aplicados e relação entre as etapas, bem como os resultados de cada uma das etapas (artigos produzidos)..... 41
Figure 4. 1. Representative illustration of CO_2 reaching near surface zones through possible leakage routes and its interaction with groundwater and aquifer minerals..... 45
Figure 4. 2. Total mass (a) and average rate (b) of CO_2 (kg) release in each experiment, either as gaseous phase or CO_2-saturated groundwater. 59
Figure 4. 3. Average CO_2 leakage rate normalized by average hydraulic conductivity of each experimental study grouped by aquifer type..... 60
Figure 4. 4. *Length of injection and monitoring phases of analyzed experimental sites.* 61

Figure 4. 5. Observed physicochemical changes for pH (a), EC (b) and alkalinity (c) from background to post-injection considering both injection length (days) and average leaked normalized by average hydraulic conductivity (kg of CO_2/m). Bar colors represent injection length and numbers inside the bars symbolize kg of CO_2/m. 64
Figure 4. 6. Observed relative physicochemical changes for pH (a), EC (b) and alkalinity (c) from background to injection considering both injection depth (m bsl) and average leaked normalized by average hydraulic conductivity (kg of CO_2/m) in each aquifer type. 66
Figure 4. 7. Example of three elements with a pulse-like behavior from background to post-injection in different studies: a) Ca (mg/L); b) Zn (µg/L); and c) Si (mg/L). Bar colors represent injection length (days) and numbers inside the bars symbolize kg of CO_2/m. 68
Figure 4. 8. Concentration variation of two chemical species with an unaffected or negligible change behavior from background to post-injection in different studies: a) Cl^- (mg/L); and b) K (mg/L). Bar colors represent injection length (days) and numbers inside the bars symbolize kg of CO_2/m. 69
Figure 4. 9. Concentration variation of four elements with an irregular behavior from background to post-injection in different studies: a) Na (mg/L); b) Mn (mg/L); c) Al (µg/L); and d) Pb (µg/L). Bar colors represent injection length (days) and numbers inside the bars symbolize kg of CO_2/m. 70
Figure 4. 10. Hydrogeochemical mechanisms related to induced higher pCO_2 as a result of CO_2 release in the aquifer. Modified from Cahill (2013). 72
Figure 5. 1. Location map of the experimental small-scale CO_2 release site: a) location in relation to Brazil; b) situation in relation to capital of Rio Grande do Sul (RS) state, which is the municipality of Porto Alegre; c) detailed vision of the study site. 92
Figure 5. 2. Topographic map of the site with location of water level monitoring wells and sampling wells along with the general groundwater flow direction (towards NE). 94
Figure 5. 3. Fence diagram illustrating the lateral and vertical distribution of described hydrostratigraphic units. 101
Figure 5. 4. Diagram depicting the 2D geoelectric cross-sectional profiles acquired, along with the interpretation of hydrostratigraphic units. 103
Figure 5. 5. Variation of hydraulic head (m) of multilevel monitoring wells from April 2019 to February 2022 with total precipitation data (mm). Green arrows indicate the HU St, while the dark arrow indicates the HU Aa. 105
Figure 5. 6. Representative boxplot of the seasonal variation of the physicochemical parameters measured in the field, individually grouped by sampled well. 107
Figure 5. 7. Boxplot showing the overall variation of cations and anions (major elements) per well. 108

Figure 5. 8. Boxplot showing the overall variation of minor elements and traces per well.111
Figure 5. 9. Global variation of δ^{13}C-DIC background of all sampled wells. 115
Figure 5. 10. Chadha's diagram showing the distribution of samples and its hydrochemical facies in the studied area. 116
Figure 5. 11. Seasonal variation of physicochemical parameters of the sampled wells across the representative climatic seasons of each campaign. 119
Figure 5. 12. Scatter plot illustrating the relationship between major ions (cations and anions) and minor ions & trace elements concentrations with temperature across different climatic seasons according to each hydrostratigraphic unit. Dashed black squares symbolize a set of samples that show a relative increase in concentration (even if slightly) in the warmer seasons compared to winter (dashed green circles). Note that some wells have been highlighted to emphasize well-by-well increases that might not be clear at first.....121
Figure 5. 13. Miller-Tans plot demonstrating the relationship between δ^{13}C-DIC x DIC as a function of DIC concentration in the samples. 123
Figure 5. 14. Individual control chart of some hydrochemical parameters showing natural seasonal variation observed in wells M1 and M2 (St unit) and M3 and M4 (Aa unit). Center line (solid black) indicate the mean value. Solid red lines represent both the Upper Control Limit (UCL) and Lower Control Limit (LCL). Dashed yellow line indicate maximum alteration values either at 22 or 26m-distance wells described in Do et al. (2022). 127
Figure 6.1. Location map of the small-scale TECNOPUC-Viamão experimental CO_2 release site and the installed infrastructure. Multilevel sampling wells are shown in blue, with gray dashed line symbolizing the linear distance between the injection well (IW1) and each sampling well. Groundwater general trend flow is towards the northeast (NE). Letters A and B (in red) illustrates the transect between M1 and M2, detailed in Figure 6.2.....134
Figure 6.2. Hydrostratigraphic units and constructive characteristics of the monitoring wells (M1 and M2) and injection well (IW1). 136
Figure 6.3. Simplified schematic sketch of the CO_2 injection system and its associated components from the cylinder to the injection well. 137
Figure 6.4. Evolution of physicochemical parameters across different phases: background, CO_2 injection, and post-injection (immediate and long-term). The gray shaded area represents the CO_2 injection phase. Vertical dotted lines indicate the increase in CO_2 injection rate on January 29 (10 kg/day) and February 15 (12.5 kg/day). 141
Figure 6.5. Evolution of total alkalinity (measured in mg/L as CaCO3) and partial pressure of CO_2 (in atm) across the background, CO_2 injection, and post-injection (immediate and long-term) phases. The gray shaded area indicates the CO_2 injection phase. Vertical dotted lines

indicate the increase in CO_2 injection rate on January 29 (10 kg/day) and February 15 (12.5 kg/day).....143
Figure 6.6. Time series of dissolved cation concentration trends for the sampled wells throughout the experimental period. The gray shaded area denotes the CO_2 injection phase. Vertical dotted lines mark the increases in CO_2 injection rate on January 29 (to 10 kg/day) and February 15 (to 12.5 kg/day).....145
Figure 6.7. Time series of dissolved anions concentration trends for the sampled wells throughout the experimental period. The gray shaded area denotes the CO_2 injection phase. Vertical dotted lines mark the increases in CO_2 injection rate on January 29 (to 10 kg/day) and February 15 (to 12.5 kg/day).....147
Figure 6.8. Observed trends and patterns in the saturation indices (SI) of secondary minerals, oxyhydroxide phases, and primary minerals observed during the CO_2 injection experiment in wells M1A (A) and M1B (B).....148
Figure 6.9. PCA analysis of all groundwater samples collected during background, CO_2 injection and post-injection: A) segmented groups base on scores of water samples by PC1 and PC2; and B) loadings of evaluated variables and their respective eigenvectors. 150
Figure 6.10. Evolutionary pathway of ion and trace element concentrations during background conditions, low CO_2 injection rates, increasing injection rates, peak levels, and subsequent return to background levels during both immediate and long-term post-injection phases. 154
Figure 6.11. Bivariate geochemical plots: (A) and (B) depict Gaillardet's sodium-normalized HCO_3^- and Mg versus Ca/Na relationship; (C) and (D) show Total Cations (TC) versus Ca + Mg and Na + K (in meq/L); and (E) and (F) evaluate ion exchange processes with Ca + Mg versus HCO_3^- + SO_4^{2-} (in meq/L) and (Ca + Mg) – (HCO_3^- + SO_4^{2-}) versus Na - Cl (in meq/L), respectively.....155

LISTA DE TABELAS

Table 4. 1. List of keywords used to find peer-reviewed research papers dealing with shallow release of CO_2 and groundwater monitoring. 47
Table 4. 2. Summary of selected studies, injection types and depth of releasing CO_2 and water table..... 49
Table 4. 3. Summary of mineral composition of each experimental investigation site. 55
Table 4. 4. Hydraulic conductivity measured at each site and its classified aquifer type based on mineralogy and flow characteristics..... 56
Table 4. 5. Apparent relative change of element concentration in groundwater from background to CO_2 injection in each field experiment, as reported in the original papers... 76
Table 4. 6. Summary of observed chemical species concentration patterns in groundwater and probable geochemical mechanisms responsible for their alteration in each analyzed study. 82
Table 5. 1. Sampling campaigns carried out for seasonal monitoring of the hydrochemical characteristic of groundwater..... 97
Table 5. 2. Classified hydrostratigraphic units and properties used to segment the geological profile of the studied area. 100
Table 5. 3. Summary of the amplitude and median values of physicochemical parameters, categorized into shallow and deeper wells. 107
Table 5. 4. Statistical summary of the mineral saturation index (SI) for the representative wells M1B, M2B, M3B, and M4C. 113
Table 5. 5. DIC concentration (ppm C) and δ^{13}C-DIC (‰) isotopic signatures of samples evaluated. 123
Table 6.1. Installed water sampling wells and their corresponding screened intervals. Sampling depth indicates the distance from the surface to the point of water extraction, where samples were collected during each sampling campaign..... 135
Table 6.2. Sampling campaigns conducted during background (BG), injection, and post-injection (PI) periods, indicating the number of wells sampled and the relative timing of each campaign with respect to the start date of CO_2 injection. 138
Table 6.3. Pearson's Correlation Coefficient for PCO_2 and the corresponding variables, according to the degree of CO_2 impact: a) M1A and M1B are highly impacted wells; b) M2B is moderately impacted; and c) M3B and M4B are considered unimpacted wells. 152
Table 6.4. Parameter variations (%) of each evaluated variable consistently exhibiting either positive or negative correlation to PCO_2 (wells M1A, M1B and M2B), referenced to the UCL or LCL of the natural background level monitored for at least 3 years prior to the execution of the CO_2 injection experiment. 159

SUMÁRIO

CAPÍTULO 1: Introdução 19
1.1. Organização da tese 19
1.2. Crise climática e a tecnologia CCS.....20
1.3. Técnicas de MMV para CO_2 29
1.4. Diretrizes ambientais de CCS e justificativa da tese.....32
1.5. Objetivos da tese.....34
CAPÍTULO 2: Breve fundamentação teórica do tema 36
2.1. Processos hidrogeoquímicos relacionados 36
2.2. Isótopos do carbono inorgânico dissolvido (δ^{13}C-DIC) 37
CAPÍTULO 3: Materiais e métodos aplicados 40
CAPÍTULO 4: CO_2-shallow groundwater interaction and related hydrogeochemical mechanisms: A review on reduced-scale CO_2 release field experiments 42
4.1. Introduction 43
4.1.1. Simulating CO_2 leakage at reduced scale experiments.....44
4.2. Methods and premises followed.....47
4.3. Results on selected studies 48
4.3.1. Mineral composition (V1) 50
4.3.2. Hydraulic aquifer parameters (V2) 56
4.3.3. Total mass and rate of leaked CO_2 (V3).....58
4.3.4. Length of injection experiment (V4).....60
4.3.5. Hydrogeochemical characteristics (V5).....62
4.4. Hydrogeochemical mechanisms 71
4.4.1. Ion exchange.....72
4.4.2. Sorption and desorption 74
4.4.3. Silicate and carbonate dissolution.....78
4.4.4. Mechanisms regulating Cl^-, SO_4^{2-} and NO_3^- 81
4.5. Conclusions.....85
CAPÍTULO 5: Hydrogeological assessment and seasonal hydrogeochemical monitoring of the TECNOPUC-Viamão CO_2 controlled-release experimental site, Rio Grande do Sul state, Southern Brazil 88
5.1. Introduction 89
5.1.1. Study area 91

5.2. Materials and methods 94
5.2.1. Topographic survey 94
5.2.2. Geological characterization (texture and mineralogy) 95
5.2.3. Geoelectric survey (DC resistivity) 95
5.2.4. Water table monitoring 96
5.2.5. Permeability tests and slug tests 96
5.2.6. Hidrochemistry characterization (sampling campaings and analysis) 97
5.3. Results 99
5.3.1. Lithology, mineral composition and hydrostratigraphic units 99
5.3.2. Geoelectric model of the study area 102
5.3.3. Hydraulic aquifer parameters and water level fluctuation 104
5.3.4. Hydrogeochemical and $\delta^{13}C$-DIC characteristics 106
5.4. Discussion 115
5.4.1. Hydrochemical type of groundwaters 115
5.4.2. Seasonal variation of physicochemical parameters 117
5.4.3. Seasonal influence on groundwater geochemistry and mineral saturation indices 120
5.4.4. Carbon isotopes ($\delta^{13}C_{-DIC}$) and CO_2 sources 122
5.4.5. The importance of seasonal background monitoring 124
5.5. Conclusions 128
CAPÍTULO 6: Hydrogeochemical changes in a silicate-dominated aquifer during a controlled CO_2 release: insights for monitoring unintended CO_2 leakage at CCS sites 130
6.1. Introduction 131
6.2. Materials and methods 133
6.2.1. Design and execution of the controlled-release CO_2 experiment 136
6.2.2. Sampling procedure and chemical analysis 138
6.3. Results 140
6.3.1. Temporal evolution of physicochemical parameters 140
6.3.2. Alkalinity and PCO_2 behavior 142
6.3.3. Dissolved ions time series trend 144
6.3.4. Mineral Saturation Indexes 147
6.4. Discussion 149
6.4.1. PCA analysis and CO_2-impacted groups 149

6.4.2. Correlation analysis and PCO_2 vs. dissolved ions evolution path ...150
6.4.3. Bivariate plots and geochemical process ...155
6.4.4. Influence of precipitation events ...157
6.4.5. Parameters variation and sensitiveness to CO_2 leakage ...158
6.4.6. Environmental risks to groundwater quality ...162
6.5. Conclusions ...163
CAPÍTULO 7: Conclusões finais ...166
7.1. Mecanismos geoquímicos vinculados ao processo interativo CO_2-água-mineral ...166
7.2. Avaliação hidrogeológica e hidrogeoquímica sazonal do *site* experimental 167
7.3. Alterações hidrogeoquímicas em aquífero dominado por silicatos durante liberação controlada de CO_2 ...169
7.4. Considerações finais e perspectivas futuras ...170
Referências bibliográficas ...171
ANEXO A ...196
ANEXO B ...205

CAPÍTULO 1: Introdução

1.1. Organização da tese

Esta tese é composta por sete capítulos. O primeiro capítulo introduz o contexto atual da crise climática global, os conceitos técnicos da tecnologia de Captura e Armazenamento Geológico de CO_2 (CCS) e fornece uma visão geral das técnicas de Monitoramento, Medição e Verificação (MMV) de CO_2, com ênfase no monitoramento hidroquímico de vazamentos não intencionais e sua relação com as diretrizes ambientais para a contenção de CO_2 em reservatórios geológicos O segundo capítulo oferece uma fundamentação teórica concisa sobre os processos hidrogeoquímicos relacionados à interação CO_2-água subterrânea-mineral em aquíferos rasos, além de discutir a aplicabilidade do uso de isótopos estáveis de carbono ($^{13}C/^{12}C$) no estudo do carbono inorgânico dissolvido na água subterrânea.

O terceiro capítulo detalha os materiais e métodos utilizados, descrevendo as etapas envolvidas e o fluxo de trabalho que levou à produção dos artigos. No quarto capítulo, estruturado na forma de um artigo de revisão já publicado, é apresentado uma discussão abrangente de estudos voltados para a compreensão da resposta da água subterrânea à presença de concentrações elevadas de CO_2 e os mecanismos geoquímicos responsáveis pela liberação de elementos.

O quinto capítulo, consolidado num artigo de estudo de caso, também já publicado, foca na caracterização geológica, hidrogeológica e geoelétrica do campo experimental de vazamento controlado de CO_2 do TECNOPUC-Viamão, além de apresentar os resultados de um monitoramento hidrogeoquímico sazonal realizado em diferentes estações ao longo de mais de três anos prévio ao experimento de liberação controlada de CO_2.

O sexto capítulo discute os resultados do experimento de injeção controlada de CO_2 realizado durante mais de sessenta dias, sob diferentes taxas e a influência de eventos de precipitação, com foco na interação CO_2-água subterrânea-mineral e sua importância para o monitoramento ambiental de vazamentos não intencionais em projetos de CCS. Finalmente, o sétimo capítulo conclui o trabalho com as considerações finais e observações gerais da tese.

1.2. Crise climática e a tecnologia CCS

As emissões antropogênicas totais de Gases de Efeito Estufa (GEE) tem aumentado cumulativamente desde 1850, período coincidente com a denominada Revolução Industrial. Enquanto naquele período a concentração de CO_2 atmosférico era estimada entre 270 e 285 ppm (RITCHIE, ROSER e ROSADO, 2020), os níveis atuais ultrapassam 400 ppm, tendo o ano de 2023 encerrado com a concentração global calculada em 421,08 ppm (STATISTA, 2024). Esse avanço representa um aumento de aproximadamente 50% em pouco mais de 170 anos, fazendo com que o patamar atingido seja considerado o maior em pelo menos 3 milhões de anos, quando a Terra estava no período Plioceno (JONES, 2017; NUGENT, 2019). Nesse contexto, embora as atividades antropogênicas contribuam com um fluxo anual de 5 a 6 Gt de CO_2 por ano para a atmosfera por conta da queima de combustíveis fósseis — representando menos de 10% do fluxo total (HANNAH, 2011) —, quase todo esse CO_2 emitido é adicional, ou seja, não é naturalmente compensado pelo ciclo do carbono. Dessa forma, há um consenso na comunidade científica global de que a principal fatia contributiva do aumento na concentração atmosférica de CO_2 é a interferência humana.

Isso se deve ao fato de que coletivamente, como seres humanos, emitimos anualmente bilhões de toneladas de GEE (Gt_{GEE}) na atmosfera. Para se ter uma ideia, passamos de emitir 32,65 Gt_{GEE} em 1990 para emitir quase 50 Gt_{GEE} nos dias atuais, um aumento de 56% nos últimos 30 anos (RITCHIE, ROSER e ROSADO, 2020). Desse total de GEE emitidos, aproximadamente 70% correspondem ao CO_2, volumetricamente o mais significativo de todos os gases e o mais relevante causador das mudanças climáticas enfrentadas pela humanidade. Nesse contexto, o Brasil contribuiu, em média, com emissões acima de 2 $GtCO_2e$ por ano desde 1990, sendo que no ano de 2022 o total de emissões brutas foi de 2,32 $GtCO_2e$ (Figura 1.1), o sétimo maior emissor global de GEE.

Figura 1. 1. *Infográfico sobre as emissões de gases do efeito estufa no Brasil. Fonte: Modificada de SEEG-OC (2024).*

As consequências dos elevados níveis de GEE atmosférico já têm sido sentidas ao redor do globo e eventos climáticos extremos são cada vez mais frequentes (EUROPEAN ACADEMIES' SCIENCE ADVISORY COUNCIL, 2018; YALE ENVIRONMENT360, 2020; CHADE, 2021; CARBONBRIEF, 2022; CARMEN ANG, 2022;). Para que implicações mais drásticas sejam evitadas, no entanto, inúmeros esforços globais são esperados. Nesse sentido, o mais importante pacto climático global já assinado na história, o Acordo de Paris de 2014, descreve que a humanidade deve reduzir as emissões de GEE para:

> "(a) Assegurar que o aumento da temperatura média global fique abaixo de 2 °C acima dos níveis pré-industriais e prosseguir os esforços para limitar o aumento da temperatura a até 1,5 °C acima dos níveis pré-industriais, reconhecendo que isto vai reduzir significativamente os riscos e impactos das alterações climáticas;
> (b) Aumentar a capacidade de adaptação aos impactos adversos das alterações climáticas e promover a resiliência do clima e o baixo desenvolvimento de emissões de gases do efeito estufa, de maneira que não ameace a produção de alimentos;
> (c) Criar fluxo financeiros consistentes na direção de promover baixas emissões de gases de efeito estufa e o desenvolvimento resistente ao clima."

Porém, projeções globais recentes feitas pelo Painel Intragovernamental sobre Mudanças Climáticas (IPCC, 2022) demonstram que as políticas divulgadas pelos países para ajudar a combater as mudanças climáticas, conhecidas oficialmente como

Contribuições Nacionalmente Determinadas (NDCs), são insuficientes e que a temperatura média global muito provavelmente ultrapassará os 1,5 °C até o final do século e que, se assim continuarem os padrões de emissões e comprometimentos de redução nacionais dos países, após 2030 será muito difícil limitar o aumento em 2 °C até 2100, descumprindo as metas assinadas no Acordo de Paris (Figura 1.2)

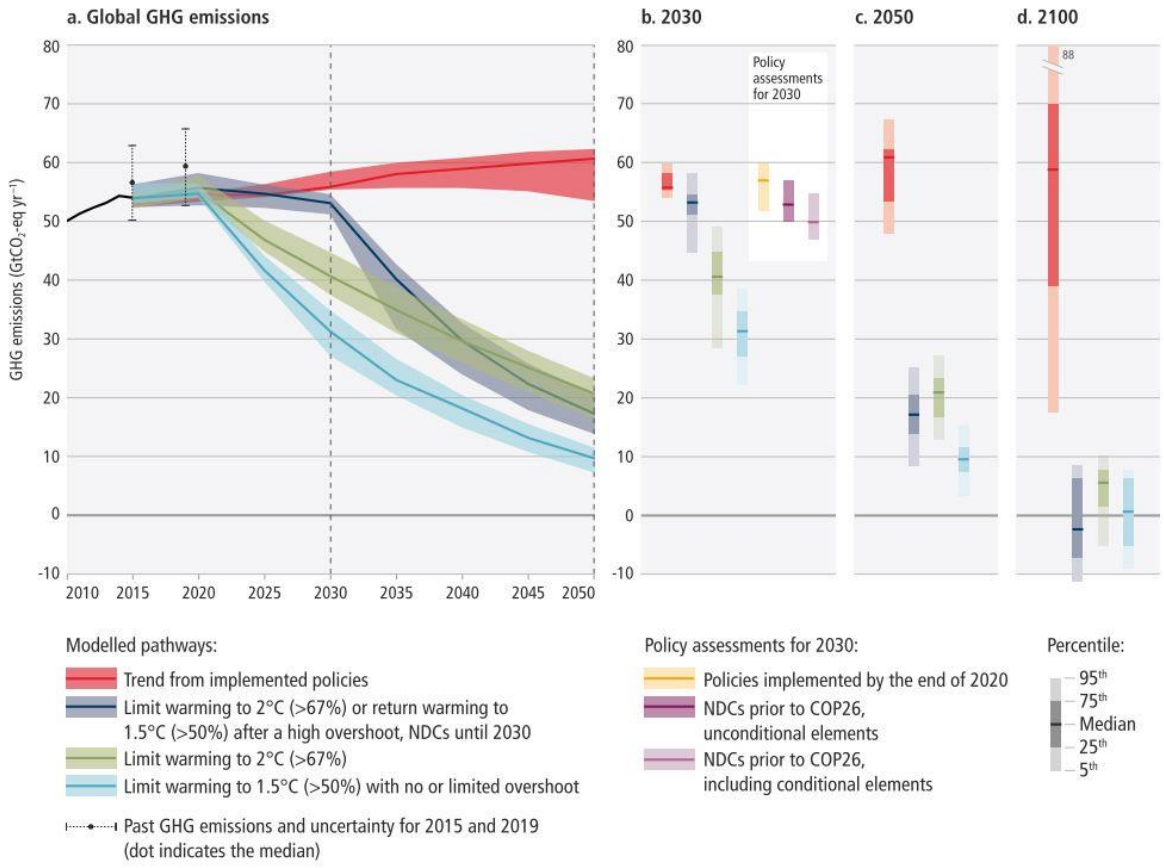

Figura 1. 2. *Cenários modelados de emissões de GEE considerando as metas necessárias e as políticas implementadas. Fonte: IPCC (2022).*

É por essa e por inúmeras outras razões que cada vez mais especialistas, políticos ativistas, mídia especializada, ambientalistas, pesquisadores e cidadãos engajados categorizam esse fenômeno como uma “crise climática” (UN, 2019). Por isso, a implementação de um portfólio de soluções naturais e tecnológicas que reduzam e mitiguem as emissões, aliadas às abordagens que removam os GEE da atmosfera (conhecidas como tecnologias CDR, *Carbon Dioxide Removal*) deixaram de ser meros conceitos elaborados e hoje assumem um papel imprescindível (IEA, 2020).

Dentro desse rol de tecnologias de abatimento está a Captura e Armazenamento Geológico de CO_2 (CCS, em inglês), uma técnica aplicada desde a década de 1970 nos EUA (CRABTREE, 2016) - mas que se tornou mais conhecida globalmente no

início dos anos 2000 -, que consiste na captura do CO_2 produzido de fontes estacionárias e injeção em reservatórios geológicos específicos, garantindo o armazenamento seguro por milhares ou milhões de anos, evitando que a concentração de CO_2 na atmosfera seja incrementada (AJAYI & BERA, 2019; IPCC, 2005; KETZER; IGLESIAS e EINLOFT, 2012; MARTIN-ROBERTS et al., 2021). Esta abordagem está fundamentada na lógica inversa das emissões atmosféricas, onde o CO_2 que seria lançado pelos sistemas de exaustão industrial (chaminés das fábricas) é, alternativamente, capturado, separados dos outros gases que compõem a corrente gasosa, comprimido, transportado e encaminhado à um poço para injeção subterrânea e endereçado ao reservatório de armazenamento selecionado (Figura 1.3).

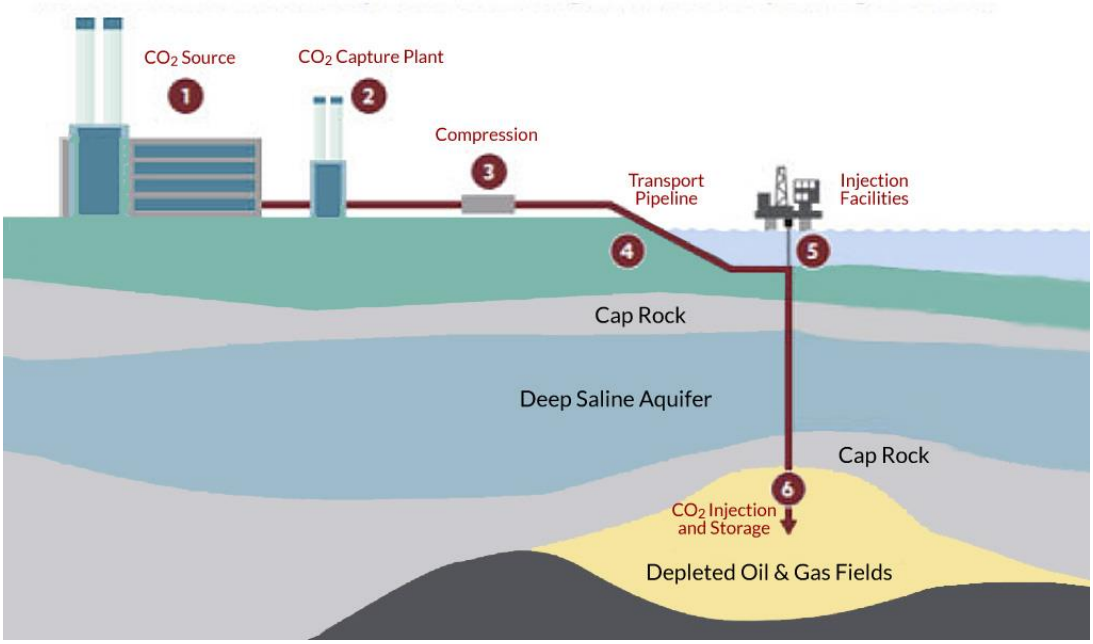

Figura 1. 3. *Exemplo de uma configuração possível de projeto de CCS. Fonte: Geospatial Research Ltd.*

Embora inicialmente aplicada para recuperação avançada de petróleo (CCS-EOR), onde o CO_2 era injetado nos reservatórios petrolíferos para aumento da produção de óleo e gás (MARTIN-ROBERTS et al., 2021), a aplicabilidade da técnica foi ganhando terreno ao longos dos anos e novos locais de armazenamento dedicados – aqueles destinados exclusivamente para estocagem permanente do gás - foram se tornando operacionais, especialmente no hemisfério norte em projetos como Sleipner e SnØvit (Noruega), In Salah (Argélia), Quest (Canadá) e Illinois Industrial (EUA) (GLOBAL CCS INSTITUTE, 2018, 2020, 2021).

Nesse contexto, do ponto de vista geológico, as opções de reservatórios alvos podem ser classificados em: 1) Reservatórios de O&G depletados – formações que foram utilizadas para extração comercial de óleo e/ou gás, mas que se encontram esgotados ou com reservas não recuperáveis; 2) Reservatórios de O&G ativos (CCS-EOR) – formações que estão sendo explotadas para recuperação comercial de óleo e gás sob técnicas de recuperação terciária (avançada); 3) Aquíferos salinos profundos (não potáveis) – unidades aquíferas preenchidas por água salina (salmoura) e não usuais para dessedentação humana ou animal; 4) Camadas de carvão não mineradas – unidades litológicas formadas por carvão e rochas associadas situadas em profundidades e que não foram explotadas comercialmente; 5) Evaporitos (sal) – formação constituída por rochas de natureza evaporítica (ex. halita) e cujo reservatório é formado por cavernas construídas artificialmente pela injeção de solução que promova a criação de espaço para armazenamento de CO_2; e 6) Rochas vulcânicas básicas (*i.e.*, basaltos) - unidades litológicas cuja composição geoquímica propicia a ocorrência de elementos químicos reativos (fundamentalmente Ca, Mg e Fe) e cuja reação com CO_2 permite o sequestro do carbono na forma mineral (Figura 1.4).

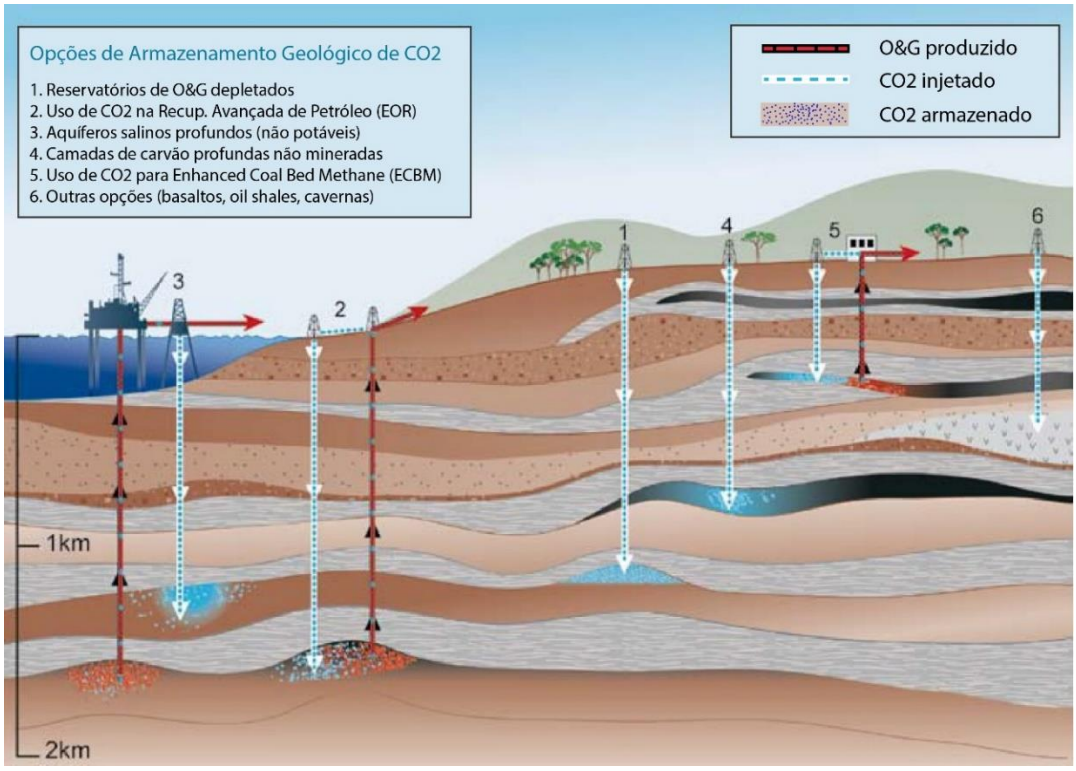

Figura 1. 4*. Alternativas de reservatórios geológicos para armazenamento de CO_2.*
Fonte: Traduzido de IPCC (2005).

Considerando os regimes de pressão e temperatura em que os reservatórios geológicos normalmente se encontram e as propriedades físico-químicas do CO_2, esse composto é tradicionalmente injetado para armazenamento em estado supercrítico (acima de 31 ºC e 74 bar), visto que nessas condições o CO_2 adquire uma densidade similar à um líquido (500 a 800 kg/m^3) e ocupa um menor volume poroso. Isso garante um melhor aproveitamento da capacidade de armazenamento do reservatório, uma vez que abaixo da profundidade crítica (aprox. 800 m, considerando um regime geotérmico de 25 ºC/km e pressão hidrostática), o CO_2 ocupa entre 2,7 % e 3,8 % do volume que ocuparia em superfície (sob estado gasoso), diminuindo, portanto, em mais de 96 % seu volume em profundidade (IPCC, 2005; KETZER; IGLESIAS e EINLOFT, 2012; KETZER et al., 2016). Entretanto, para o armazenamento do CO_2 na forma mineral, como feito pelo projeto Carbfix (SNÆBJÖRNSDÓTTIR et al., 2020), a injeção também pode ser feita na forma de solução carbonatada (água + CO_2 dissolvido), eliminando a etapa de solubilização do CO_2 que ocorre naturalmente no próprio reservatório em etapa futura do processo.

Logo, nota-se que para que o CO_2 fique contido nos reservatórios nessas circunstâncias, uma combinação de fatores físicos e geoquímicos fornecem as condições básicas de trapeamento. Assim, existem cinco mecanismos que favorecem o aprisionamento, condicionando a efetividade e a seguridade do armazenamento geológico (IPCC, 2005; KETZER et al., 2016). O primeiro, e mais importante mecanismo de “curto” prazo, é o *trapeamento físico*, que é regulado pela ocorrência estratigráfica de camadas de baixa permeabilidade, as quais agem como um selo para contenção do CO_2 em subsuperfície, barrando a mobilização ascendente do gás em direção à superfície. Esse efeito de contenção também pode ser exercido pela existência de feições tectônicas (falhas, fraturas ou dobras) que formam estruturas geológicas fechadas (pouco permeáveis ao CO_2) que permitem a imobilização do CO_2 em fase livre no topo do reservatório alvo (Figura 1.5A).

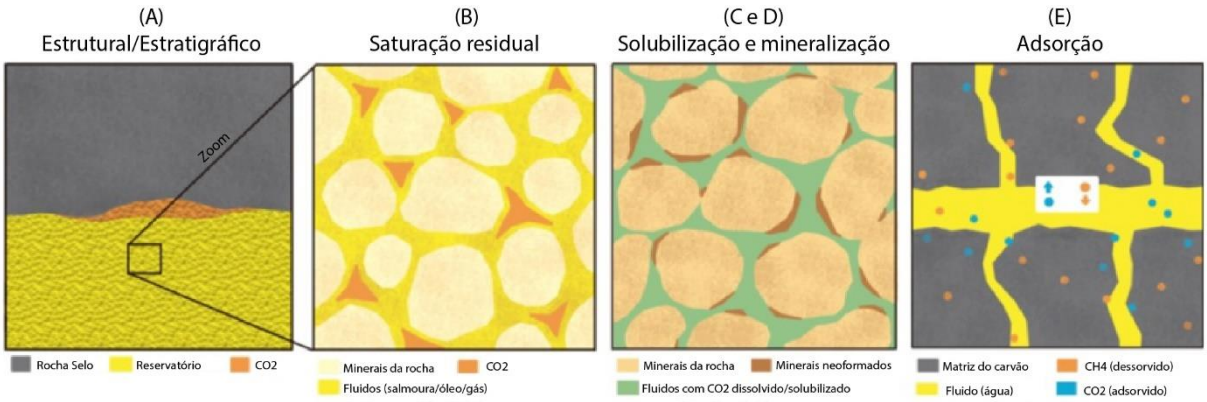

Figura 1. 5*. Mecanismos de aprisionamento geológico de CO_2. Modificado de* (Ketzer et al., 2016).

O segundo mecanismo corresponde ao *trapeamento residual*, que acontece quando o CO_2, menos denso que a água de formação (salmoura ou água subterrânea doce), se desloca no sentido vertical e ascendente pelo efeito de empuxo (flutuabilidade). Nesse movimento, a pluma de CO_2 perde continuidade em virtude da heterogeneidade do espaço poroso da rocha (tortuosidade) e moléculas de CO_2 são desprendidas do corpo principal, ficando aprisionadas nos poros da rocha - envoltas pelo fluido da formação - e imobilizadas de forma permanente, formando uma fase saturada residual (Figura 1.5B).

O terceiro e quarto mecanismo são coletivamente conhecidos como *trapeamento geoquímico***,** pois estão relacionados com fenômenos de interação química entre a mineralogia da rocha e a água de formação. Por esse motivo, são importantes a longo prazo, pois dependem da velocidade das reações químicas e os fatores que as influenciam. Nesse contexto, o processo inicial corresponde à solubilização do CO_2, isto é, a transformação do gás carbônico em espécies iônicas que ficam dissolvidas na água (Figura 1.5C), processo que pode ser simplificado conforme reação abaixo:

$$CO_2(g) + H_2O \underset{ác.carbônico}{\longleftrightarrow} H_2CO_3 \underset{bicarbonato}{\longleftrightarrow} HCO_3^- + H^+ \underset{carbonato}{\longleftrightarrow} CO_3^{2-} + 2H^+$$

Com o avanço do tempo, o CO_2 dissolvido na água de formação passa a interagir com os minerais da rocha reservatório, principalmente com silicatos que contenham Na^+, K^+, Ca^{2+}, Mg^{2+} e Fe^{2+}, além de carbonatos com cátions de Mg e Fe, liberando ânions bicarbonato e carbonato em condições ácidas a levemente ácidas, principalmente na região adjacente do poço injetor. Entretanto, com o avanço da

pluma de CO_2 e espécies carbônicas dissolvidas, além do transporte dos íons divalentes, esses elementos passam a se ligar em condições mais alcalinas (pH mais elevados), formando minerais carbonáticos que aprisionam o CO_2 injetado na forma mineral, a mais estável condição possível de armazenamento geológico (Figura 1.5D).

O quinto mecanismo corresponde ao *trapeamento por adsorção* do CO_2 em substituição ao CH_4 (metano), processo que acontece em carvões ou rochas de baixa permeabilidade com elevados teores de Carbono Orgânicos Total (COT). Nesse contexto, o CO_2 compete seletivamente por sítios de adsorção na matriz do carvão ou nos microporos e fraturas da rocha, causando a dessorção (expulsão) do CH_4 (Figura 1.5E), ficando retido em seu lugar e, consequentemente, produzindo metano em decorrência da interação (TAMBARIA; SUGAI e NGUELE, 2022).

Embora esses mecanismos, em teoria, garantam a contenção do CO_2 em subsuperfície, falhas na etapa de caracterização e modelagem geológica do reservatório, construção dos poços de injeção ou monitoramento e condições operacionais imprevistas (ex., sobrepressão do reservatório e reativação de falhas/fraturas) podem condicionar o vazamento do CO_2 ou salmoura do reservatório, mesmo que de forma parcial. Dessa forma, é preciso conhecer em detalhe as características do projeto de armazenamento e realizar uma boa análise de riscos para compreender as possíveis rotas de fuga.

Depois de anos de aplicação da técnica, já há um consenso global entre operadores e pesquisadores de que entre todos os possíveis caminhos pelos quais o CO_2 poderá escapar, três se destacam como os de maior probabilidade, representando pontos frágeis dentro do projeto e que merecem atenção (Figura 1.6):

A. Vazamento devido a ineficiência de aprisionamento da rocha selo imediatamente sobreposta ao reservatório de injeção;
B. Vazamento via uma falha existente (ou até mesmo reativada pela operação de injeção do CO_2); e
C. Vazamento através de um poço abandonado (ou poço ativo mal completado)

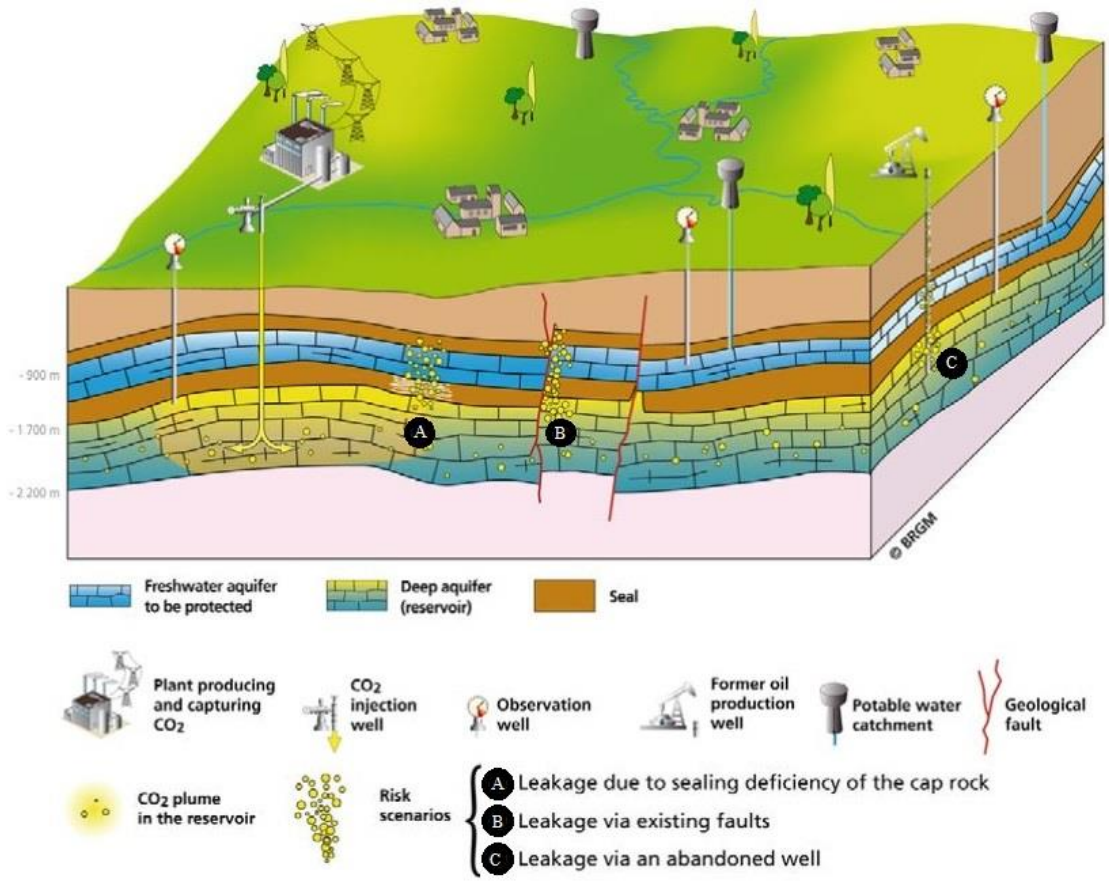

Figura 1. 6. *Principais rotas de escape de CO_2 do reservatório geológico: A) vazamento por meio da rocha selante; B) vazamento via falha existente; e C) vazamento através de poço abandonado ou mal cimentado (completado). Modificado de* Bouc et al. (2009).

Por isso, diversas técnicas de Monitoramento, Medição e Verificação (MMV) devem ser empregadas em diferentes etapas do projeto e em distintos compartimentos ambientais – da subsuperfície até a superfície - para a garantia da conformidade da estocagem e correspondência com a simulação computacional do comportamento esperado da pluma de CO_2 (DEAN et al., 2020; JENKINS; CHADWICK; HOVORKA, 2015a; TIWARI et al., 2021). Além disso, os métodos aplicados devem ser capazes de comprovar a contenção do CO_2 ou, em caso adverso, traçar a trajetória de saída do reservatório, identificar a rota de fuga e acompanhar os possíveis impactos ambientais que a fração vazada pode ocasionar nas camadas sobrejacentes ao reservatório alvo, incluindo aquíferos com água potável usados para consumo humano e zonas vadosa/insaturada utilizada como suporte às atividades agrícolas nos locais próximos aos sites de armazenamento de CO_2.

1.3. Técnicas de MMV para CO_2

Para que um projeto de CCS possa seguir seu curso sem enfrentar problemas de aceitabilidade pública e efetivamente proporcionar uma redução de emissões atmosféricas de CO_2, há fatores operacionais, regulatórios e parâmetros técnicos que precisam ser atendidos. Nesse sentido, as técnicas de MMV empregadas são resultado de uma herança decorrente das indústrias de O&G e das atividades de exploração de águas subterrâneas. Logo, existem diversos equipamentos e métodos, cada qual com seu ambiente de aplicação, compartimento geológico/ambiental a ser instalado e objetivo principal da análise.

Assim, técnicas de MMV de *alcance profundo* (> 500 m) estão normalmente relacionados com a verificação da contenção do CO_2 no reservatório de armazenamento e/ou adjacências, sendo fundamentais do ponto de vista operacional. Para este ambiente são empregas as técnicas geofísicas que podem ser aplicadas independentemente se o *site* de injeção for localizado *onshore* ou *offshore*, pois são relacionadas a poços, como perfilagem geofísica, medições da pressão e temperatura no poço, métodos eletromagnéticos (*EM*), tomografia de resistividade elétrica (*ERT*) e sísmica em poços (*cross-hole*), perfilagem sísmica vertical (*VSP*), gravimetria de poço e microssísmica. Além disso, técnicas geoquímicas como a amostragem de fluido do próprio reservatório alvo em poço de monitoramento profundo também podem ser aplicadas para acompanhamento da característica hidrogeoquímica da água de formação e análise do processo interativo CO_2-água-rocha (Figura 1.7). Entretanto, há técnicas que não dependem de poços e são executadas exclusivamente em terra (*onshore*), como sísmica superficial 2D/3D, métodos eletromagnéticos (*EM*), tomografia de resistividade elétrica (*ERT*) e gravimetria superficial.

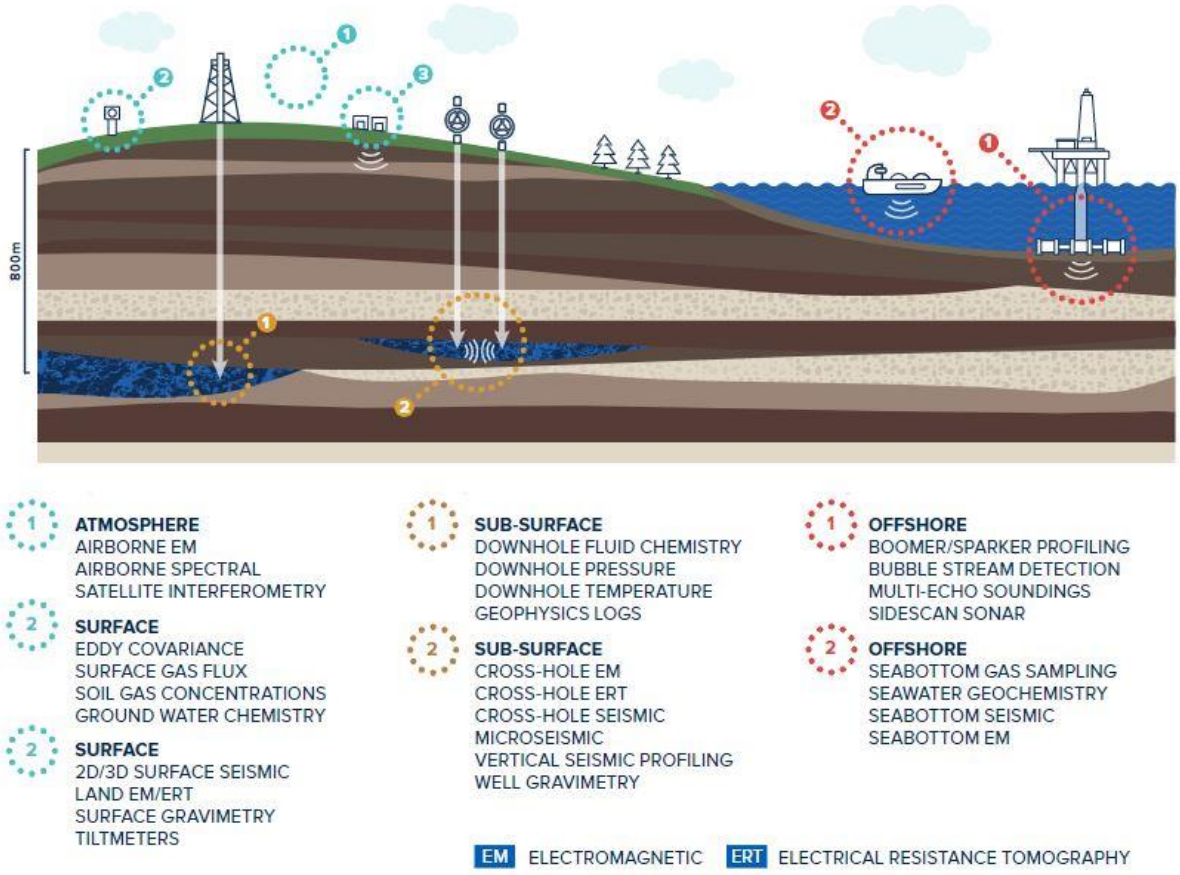

Figura 1. 7. *Técnicas de MMV onshore e offshore aplicados em diferentes compartimentos geológicos. Fonte: Global Status of CCS 2019.*

No entanto, as técnicas de MMV de *alcance raso* (< 500 m) dependerão se o local de injeção está localizado em terra ou no mar. Como as tecnologias aplicadas são normalmente utilizadas para a confirmação adicional do aprisionamento no ambiente planejado e observância regulatória (*compliance*), elas são fundamentais para a garantia da efetividade socioambiental do processo e servem como ferramenta de comunicação pública. Por isso, em ambiente *offshore* aplicam-se técnicas geofísicas acústicas, como a sísmica rasa de alta resolução (realizadas com equipamento do tipo *boomer* e *sparker*), sonar de varredura lateral (*sidescan sonar*) e a ecobatimetria multifeixe (*multi-echo soundings*), além de sismógrafos de fundo oceânico (OBS, *ocean bottom seismometers*) e medidores eletromagnéticos de fundo oceânico (OBEM, *ocean bottom eletromagnetic meters*). Adicionalmente, técnicas geoquímicas como amostragem de água e gás da coluna d'água próximos a zonas de possível escape de CO_2 também são métodos aplicados.

Em ambientes *onshore*, distinguem-se as técnicas aplicadas na superfície do terreno e atmosféricas. Entre as primeiras, destacam-se técnicas como o

monitoramento hidroquímico da água subterrânea, concentração do gás do solo e fluxo de gás superficial (interface solo-atmosfera). Dentre as técnicas atmosféricas, além do acompanhamento por meio de estações *Eddy Covariance*, métodos satelitais, como interferometria (*InSAR*) e monitoramento espectral do terreno, também podem ser aplicados.

O monitoramento do impacto hidroquímico do vazamento de CO_2 em aquífero raso próximo à superfície (poucos a dezenas de metros, foco desse trabalho), representa um dos principais desafios da aplicabilidade dessa técnica para confirmação pública de tal fenômeno. Essa complexidade resulta de diversos fatores, como a composição mineralógica do aquífero (silicático ou carbonático), natureza do confinamento (livre ou confinado), taxa de vazamento em relação a velocidade do fluxo subterrâneo, composição química do gás vazado, composição química da salmoura (*brine*) do reservatório e o caminho de migração (Jones et al., 2015).

Nesse caso, a compreensão do processo interativo CO_2-água-mineral e o planejamento da distribuição da rede de poços de monitoramento deve respeitar as características geológicas e hidrogeológicas do *site* onde se planeja fazer a atividade de injeção de CO_2. O objetivo é minimizar a possibilidade de não detecção do vazamento pela técnica em função: i) do posicionamento à montante do ponto de vazamento (‘*well 1’*, Figura 1. 8a); ii) do posicionamento muito afastado do ponto de vazamento e possível atenuação de modificações hidrogeoquímicas (‘*well 2*’, Figura 1.8a); iii) da diferença na velocidade de migração dos elementos conforme natureza química reativa ou conservativa (Figura 1.8b); iv) da migração preferencial do CO_2 em direção à atmosfera e respectiva baixa solubilização na água subterrânea em aquíferos livres (Figura 1.8c); e v) do acúmulo do CO_2 em fases gasosa no topo de um intervalo confinado e sua ação como fonte de acidez prolongada e permanência no aquífero, promovendo extensa pluma dissolvida (Figura 1.8d).

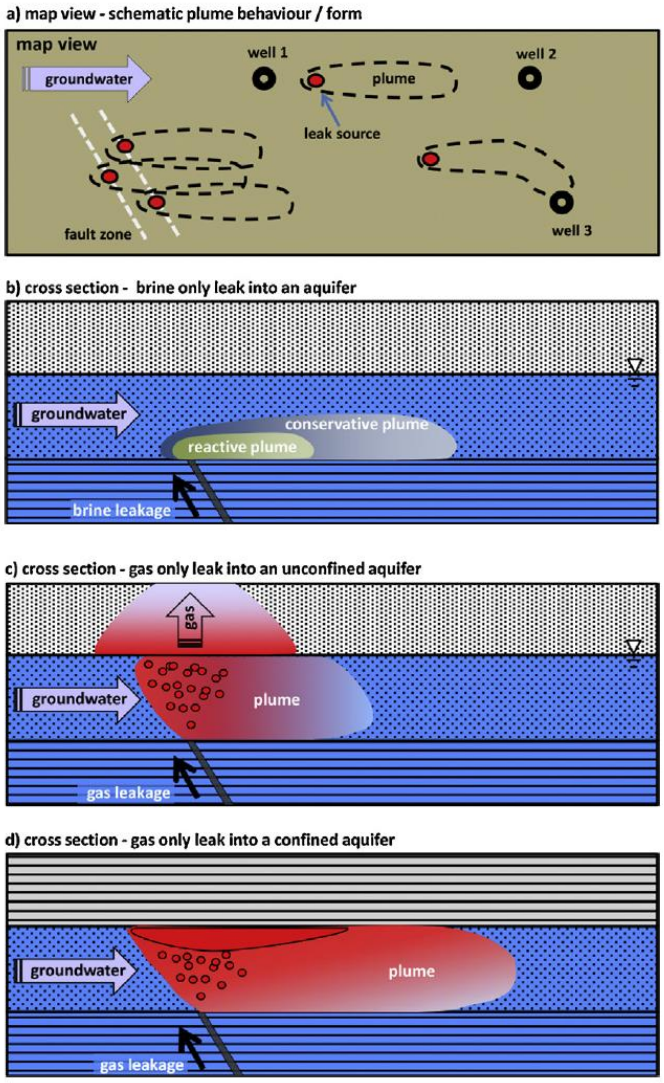

***Figura 1. 8**. Diagrama esquemático da distribuição da pluma de CO_2 (e da salmoura), posicionamento espacial dos poços e comportamento dinâmico em diferentes aquíferos (livre e confinado). Modificado de Jones et al. (2015).*

1.4. Diretrizes ambientais de CCS e justificativa da tese

Alguns países já possuem leis e diretrizes técnicas nacionais vigentes que contribuem para a regulação ambiental das atividades. Dentre as obrigatoriedades dos operadores de projetos CCS está a apresentação e execução do plano de MMV, que visa assegurar que as técnicas e os processos seguidos são capazes de detectar ou minimizar a migração ou vazamento do CO_2. De acordo com a IEA (2022), um plano MMV deve detalhar, no mínimo, um programa de monitoramento cujos métodos sejam suficientes para:

- Estabelecer e manter uma pesquisa de linha de base (*background*) para o local de armazenamento até o início da injeção;

- Monitorar as instalações de injeção, o local de armazenamento (incluindo a pluma de CO_2) e o ambiente adjacente;
- Comparar os resultados do monitoramento contínuo com a linha de base (background) para o local de armazenamento;
- Comparar o comportamento real do CO_2 no local de armazenamento com seu comportamento antecipado (simulado) baseado nos resultados do processo de caracterização do site e do monitoramento prévio;
- Detectar, atribuir e avaliar vazamentos significativos, migração não intencional ou outra irregularidade no local de armazenamento;
- Quantificar, conforme exigido pela autoridade competente, os volumes de CO_2 associados a vazamentos significativos ou migração não intencional;
- Detectar migração de CO_2;
- Detectar efeitos adversos significativos no ambiente adjacente;
- Avaliar a eficácia de quaisquer medidas corretivas tomadas.

Nesse contexto, há duas diretrizes relevantes e consolidadas em escala global. A primeira corresponde à *Diretriz 2009/31/EC* da União Europeia (EUROPEAN PARLIAMENT AND COUNCIL, 2009), na qual os operadores devem apresentar um relatório às autoridades competentes pelo menos uma vez por ano com detalhes dos resultados do monitoramento, além das quantidades e propriedades do CO_2 injetado. No caso específico dessa regulamentação, em termos ambientais, é obrigatório: i) detectar irregularidades significativas, migração ou vazamento; e ii) detectar efeitos adversos significativos sobre o meio ambiente. Portanto, há explícito respaldo legal que define a necessidade de apresentar relatórios específicos de monitoramento ambiental do site de armazenamento, independentemente do compartimento geológico/ambiental, e que abranja o meio ambiente na sua integralidade.

A segunda corresponde à diretriz dada pela EPA (*Environmental Protection Agency*) dentro do programa '*Underground Injection Control Class VI*' (US EPA, 2021), cujo principal objetivo corresponde à proteção de fontes subterrâneas de água potável e que, por isso, está sob as disposições do '*Safe Drinking Water Act*', a principal legislação dos EUA destinada a garantir água potável segura para a população. Nesse caso, a EPA deixa claro que os operadores devem atender à requisitos de monitoramento abrangentes que contemplem "todos os aspectos sobre a integridade do poço, injeção e armazenamento de CO_2 e qualidade da água subterrânea durante

a operação de injeção e o período de cuidados pós-injeção", cujos resultados devem ser reportados anualmente à agência (IEA, 2022). Nesse caso, a regulamentação americana se mostra fundamentalmente protetiva dos recursos hídricos subterrâneos, trazendo o tema sob a guarda da mais importante lei de proteção à água potável.

Aqui no Brasil, no entanto, a regulamentação geral do tema ainda se encontra em fase incipiente. O documento mais avançado corresponde ao Projeto de Lei (PL) nº 1.425/2022 (BRASIL, 2022), que contou com o suporte científico do Centro de Pesquisa para Inovação em Gases do Efeito Estufa (*Research Center for Greenhouse Gas Innovation – RCGI*) da Universidade de São Paulo (USP). Embora esteja em sua primeira versão, o texto já define - assim como as diretrizes europeia e americana - a obrigatoriedade da apresentação do plano de monitoramento por parte do operador, que deverá seguir o princípio de proteção ao meio ambiente. Além disso, o PL também define que o plano deve ser atualizado e encaminhado para homologação da autoridade de regulação competente quando houver mudanças no risco avaliado para o meio ambiente, e define a responsabilização objetiva do operador por quaisquer danos causados pelo projeto, incluindo os danos ao meio ambiente e à saúde humana (BRASIL, 2022). Por fim, o texto legal também já indica que a atividade deverá ser, futuramente, passível de licenciamento ambiental conforme trata a Lei nº 6.938/1981(BRASIL, 1981).

Dessa forma, nota-se como imprescindível que projetos e estudos científicos sobre os possíveis impactos de um vazamento não intencional de CO_2 decorrente da atividade de CCS devam ser executados considerando as especificidades geológicas, hidrogeológicas, ambientais e climáticas do território brasileiro, até mesmo para criar uma base científica sólida para respaldar tecnicamente as prováveis diretrizes ambientais mais específicas que deverão nortear os planos de MMV e as condicionantes do licenciamento ambiental. Assim, a presente tese justifica-se como uma contribuição científica e socioambiental ao tema, especialmente visando elucidar as consequências diretas do processo interativo CO_2-água subterrânea-mineral, descrevendo alterações possíveis de acontecer em aquífero próximo à superfície e apontando ferramentas de auxílio ao diagnóstico ambiental desse fenômeno.

1.5. Objetivos da tese

O objetivo geral desse projeto é avaliar e analisar a interação CO_2-água subterrânea-mineral, em aquífero raso, procurando identificar alterações

hidrogeoquímicas na água subterrânea e determinar parâmetros indicativos da ocorrência desses processos de interação.

Adicionalmente, pode-se estabelecer como objetivos específicos:

a. Definir um modelo hidrogeológico conceitual, caracterizando as unidades hidroestratigráficas e as respectivas propriedades hidráulicas considerando a característica de um aquífero freático multicamadas;
b. Caracterizar a variabilidade hidroquímica e isotópica sazonal ($\delta^{13}C$-DIC) de referência ao longo de três anos (*background* longo), antes da realização do experimento de liberação controlada de CO_2;
c. Avaliar a evolução dos parâmetros de campo (pH, temperatura, CE, OD, ORP) e da alcalinidade/espécies carbônicas na água subterrânea, correlacionando-os com o processo de interação CO_2-água subterrânea-mineral;
d. Investigar a concentração de elementos maiores, menores e traços na água subterrânea e suas modificações ao longo do tempo como resultado da interação com o CO_2;
e. Quantificar a PCO_2 na água subterrânea e correlacioná-la com os parâmetros hidrogeoquímicos anômalos identificados;
f. Estabelecer a trajetória evolutiva das alterações dos parâmetros hidrogeoquímicos associadas à reação com a pluma de CO_2 e quantificar os índices de saturação mineral para determinar o estado de saturação das águas; e
g. Discutir as possíveis implicações ambientais decorrentes do processo de vazamento de CO_2 na área de estudo

CAPÍTULO 2: Breve fundamentação teórica do tema

2.1. Processos hidrogeoquímicos relacionados

Ao longo dos últimos 15 anos, os experimentos de injeção controlada em escala de campo têm sido executados por pesquisadores de todo o mundo para realizar estudos representativos e de baixo custo sobre como o CO_2 se comporta quando interage com águas subterrâneas de aquíferos rasos e seu arcabouço mineral. Assim, diversos estudos serviram de base para esta tese visando entender em que condições esses experimentos foram desenvolvidos, quais eram as características hidrodinâmicas e geoquímica dos aquíferos, quanto de CO_2 havia sido deliberadamente vazado, por quanto tempo e quais foram as mudanças observadas na água subterrânea.

Nesse contexto, apesar de algumas revisões bibliográficas já terem sido publicadas (Feitz et al., 2014; Lee et al., 2016; Jeong et al., 2017; Gupta & Yadav; 2020), até onde se tem conhecimento, nenhum estudo compilou os resultados coletivos das mudanças químicas das águas subterrâneas em aquífero raso resultantes do vazamento controlado do CO_2 em experimentos de campo buscando enquadrar os resultados em mecanismos geoquímicos que representam o espectro completo de possíveis reações em relação à composição mineral (variável V1), aos parâmetros hidráulicos do aquífero (variável V2), o volume de CO_2 vazado (variável V3), o tempo do experimento (variável V4) e as características hidrogeoquímicas (variável V5) em cada local de pesquisa.

Assim, para suprir essa lacuna científica, foi elaborado um artigo de revisão específico (Zielinski et al., 2023; Capítulo 4), cujo objetivo foi ampliar a compreensão dos processos geoquímicos (troca de íons, adsorção/dessorção, reações redox e dissolução/precipitação mineral) vinculados aos experimentos analisados nesta revisão e como estão qualitativamente relacionados a essas cinco ‘macro variáveis’. Neste contexto, este estudo servirá como um resumo geoquímico baseado em processos das descobertas científicas de experimentos relevantes em escala de campo realizados até agora sobre a resposta de águas subterrâneas rasas a elevados níveis de CO_2.

2.2. Isótopos do carbono inorgânico dissolvido (δ^{13}C-DIC)

Diferentemente dos artigos envolvendo análises hidrogeoquímicas, estudos abordando o uso de isótopos estáveis de carbono da água subterrânea para monitoramento da interação CO_2-água subterrânea-mineral em aquífero raso são relativamente mais restritos. SCHULZ et al. (2012) foram os primeiros a utilizar a técnica no experimento de Wittstock/ALE, utilizando o CO_2 cuja razão isotópica fosse simbolicamente próxima ao esperado em projetos de CCS cujo carbono é de origem fóssil (−30.5 ± 0.4 ‰). Três campanhas para acompanhamento da assinatura natural do $\delta^{13}C$-$_{DIC}$ foram realizadas previamente à injeção do CO_2, sendo reportado uma média de −21.9 ± 1.4 ‰, sem variação sazonal significativa. Apenas 4 dias após o início da injeção de CO_2, a razão isotópica da água no poço mais próximo (2.5 m de distância, 1C-3 da Figura 2. 1a) apresentou valores de −29.9 ‰ ± 0.32 ‰, após 10 dias o equilíbrio isotópico foi verificado no poço distante 5 m (−29.1‰ ± 0.20 ‰).

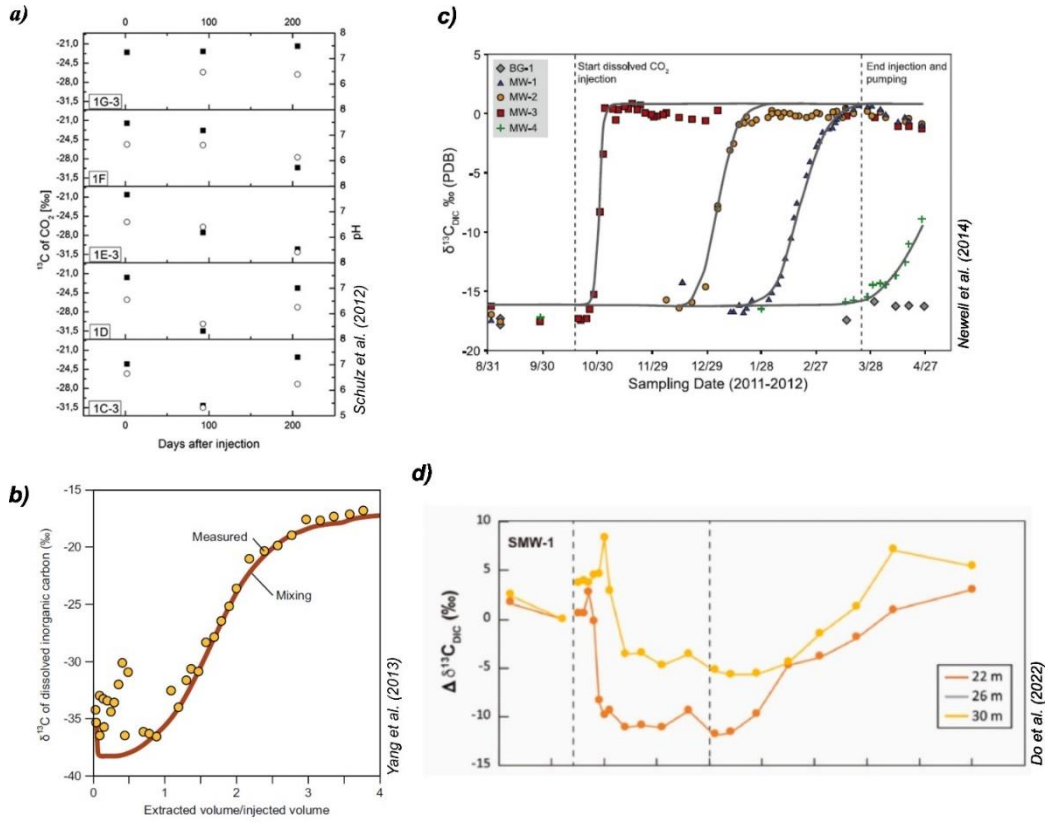

***Figura 2. 1**. Resultados reportados de $\delta^{13}C$-$_{DIC}$ de (a) Schulz et al. (2012), onde os círculos representam a assinatura isotópica e os quadrados o pH para diferentes poços (de 1C-3 a 1G-3); (b) Yang et al. (2013), cujos pontos simbolizam os valores medidos de isótopos de $^{13}C/^{12}C$ e a linha o modelo calculado; (c) Newell et al. (2014), que demonstra os valores isotópicos para os poços BG-1 a MW-4; e (d) Do et al. (2022), exemplificado pela alteração*

isotópica do $\delta^{13}C_{\text{-DIC}}$ em relação ao background $\Delta\delta^{13}C_{\text{-DIC}}$ para o poço SMW-1 (mais próximo e correspondentes à direção de fluxo).

Os poços mais distantes (1F da Figura 2.1a), mesmo após 204 dias (>190 dias após o fim da injeção), demonstraram valores de até −29.8 ‰ (± 0.11 ‰), período no qual os poços mais próximos já haviam retornado ao valor próximo ao *background* (−23.7 ± 1.46 ‰.). Essa mudança observada seguiu o fluxo subterrâneo do local (orientado ao Oeste), enquanto os poços localizados fora do range de influência do CO_2 não apresentaram alteração da razão isotópica. Dessa forma, por mais que a diferença entre a razão isotópica natural e a do CO_2 injetado não fosse tão discrepante (aprox. 5 ‰), os autores consideraram que a quantidade injetada de CO_2 foi suficiente para promover a alteração, indicando a utilidade do método isotópico para traçar a área de influência em aquíferos de mineralogia silicática.

YANG et al. (2013) avaliaram a aplicabilidade do método no estudo experimental de Cranfield/EUA. De acordo com os dados publicados, o valor médio do $\delta^{13}C_{\text{-DIC}}$ correspondente ao *background* é equivalente a −16.8‰, porém demonstra variação entre −11‰ e −21‰ no período entre 2009 e 2012. No decorrer do teste de '*push-pull'*, no entanto, o valor do $\delta^{13}C_{\text{-DIC}}$ foi gradualmente decaindo até atingir patamar abaixo de −38‰, refletindo a predominância de uma fonte empobrecida em ^{13}C (Figura 2.1b). Embora não tenha sido medido o $\delta^{13}C$ do CO_2 injetado, os autores assumiram que a resposta isotópica induzida pela injeção é correspondente à da solução incubada com CO_2 utilizada, em virtude do grande desvio gerado em relação à variabilidade espaço-temporal natural e que nenhuma outra fonte de carbono existia no aquífero. Assim, concluíram que a técnica demonstrou resultado, pois se houvesse vazamento de CO_2 cujo $\delta^{13}C$ fosse suficientemente diferente do $\delta^{13}C_{\text{-DIC}}$ da água subterrânea presente no aquífero, esse processo seria detectado pelo método.

NEWELL et al. (2014) reportaram os resultados obtidos no experimento de Jackson County/EUA. Segundo os autores, os valores de *background* (de apenas poucos dias antes do teste de injeção) do $\delta^{13}C_{\text{-DIC}}$ variaram de −17.6 a −15.2 ‰. Após início da injeção do CO_2, os resultados mostraram que os poços mais próximos (aprox. 5 m de distância, MW-3 da Figura 2.1c) apresentaram mudança na assinatura do $\delta^{13}C_{\text{-DIC}}$, cujos valores subiram para 0.16 ‰ (± 0.30 ‰) dezesseis dias após o início na campanha, indicando um enriquecimento de ^{13}C em comparação ao valor de base. Os poços mais à jusante foram gradualmente assumindo resposta isotópica similar com

o passar do experimento (MW-2, MW-1 e BG-1 da Figura 2.1c), indicando o aumento progressivo à medida que o fluxo subterrâneo progredia. Nesse caso, os autores não realizaram a medição da δ^{13C} do CO_2 injetado, e assumiram que este poderia ser inferido ao tomar como base o valor médio do δ^{13C}-$_{DIC}$ (0.16 ‰) durante o completo equilíbrio isotópico verificado no poço mais próximo (MW-3). Assim, chegaram ao valor do δ^{13C} do CO_2 injetado correspondente a +1.03 (± 0.30 ‰), tendo como premissa a não ocorrência de fracionamento isotópico significativo. Nesse sentido, embora o valor analítico da fonte não tenha sido analisado, os autores consideram que a assinatura do δ^{13C}-$_{DIC}$ demonstra claramente as curvas de *breakthrough* que representam a chegada e a migração do CO_2 injetado nos pontos de monitoramento, corroborando a efetividade da técnica.

DO et al. (2022) apresentam os resultados obtidos durante experimento no site experimental EIT/KOR, cujo arcabouço litológico também corresponde à um solo residual de granito (com mineralogia próxima ao site experimental dessa tese). De acordo com os autores, os valores de *background* do δ^{13C}-$_{DIC}$ demonstraram valores médios entre -14.3 ‰ (± 2.1 ‰) e -16.7 ‰ (± 1.3 ‰). Esses resultados são isotopicamente diferentes dos valores da solução carbonatada (CO_2 + água) injetada que possuía assinatura de isotópica de -24.7 ‰ (± 1.8 ‰). Nesse estudo, os pesquisadores divulgaram os resultados da alteração isotópica do δ^{13C}-$_{DIC}$ em relação ao valor natural de base ($\Delta\delta^{13C}$-$_{DIC}$). Assim, considerando o período de injeção do CO_2, houve notável alteração do parâmetro, sendo mensurado o $\Delta\delta^{13C}$-$_{DIC}$ de aproximadamente -5 ‰ apenas dois dias após o início da injeção no poço localizado a menos de 2.5 m dos poços de injeção e perpendicular à direção de fluxo de CO_2 (BS-5, não exibido na Figura 2.1), mostrando espalhamento da pluma de CO_2 dissolvido. Mudança similar foi observado no poço a 2.5 m na direção correspondente ao fluxo subterrâneo apenas no 6º dia após o início da injeção (SMW-1, da Figura 2.1d). No entanto, os poços localizados na direção principal da água subterrânea exibiram maior alteração isotópica no decorrer do experimento (principalmente no SMW-2, SMW-3 e SMW-4), apresentando valores de $\Delta\delta^{13C}$-$_{DIC}$ abaixo de -10 ‰. Dessa forma, os autores consideraram que a utilização do δ^{13C}-$_{DIC}$ foi efetiva, mas sugerem que esse método é válido somente para valores significativamente diferentes entre a assinatura natural do reservatório e o δ^{13C}-$_{DIC}$ do CO_2 injetado e desde que não haja fonte de carbono adicional.

CAPÍTULO 3: Materiais e métodos aplicados

Para o desenvolvimento deste trabalho, foi adotada uma metodologia que abrange uma série de atividades, incluindo:

i) revisão bibliográfica sobre os subtemas da tese;

ii) caracterização física da área de estudo (topografia, geologia e geofísica);

iii) caracterização e compreensão do comportamento hidrogeológico das camadas aquíferas;

iv) característica hidroquímica da água em diferentes estágios sazonais;

v) avaliação da interação CO_2-água subterrânea-mineral decorrente da injeção controlada de CO_2 em aquífero raso.

Para sintetizar essas etapas, a Figura 3.1 apresenta o fluxo de trabalho seguido na tese. Os detalhes específicos, pertinentes ao escopo de cada artigo científico e as técnicas adotadas, estão descritos nos capítulos correspondentes.

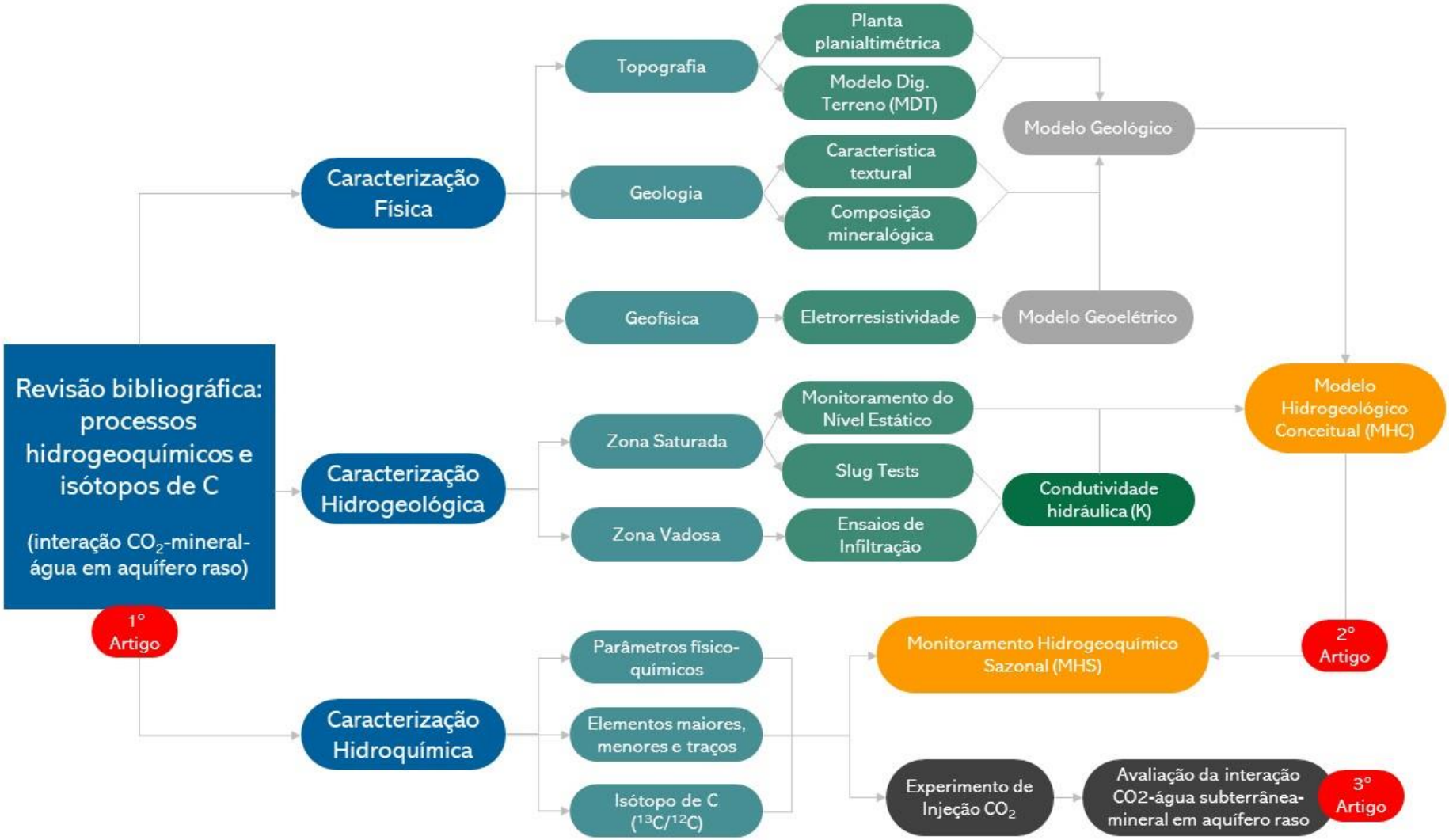

Figura 3. 1 *Fluxograma de desenvolvimento dos trabalhos, métodos aplicados e relação entre as etapas, bem como os resultados de cada uma das etapas (artigos produzidos).*

CAPÍTULO 4: CO_2-shallow groundwater interaction and related hydrogeochemical mechanisms: A review on reduced-scale CO_2 release field experiments

*Esse capítulo foi publicado na revista '**Greenhouse Gases: Science and Technology**'.*

Zielinski JPT, Melo CL, Iglesias RS, Reginato PR (2023) CO_2-shallow groundwater interaction and related hydrogeochemical mechanisms: A review on reduced-scale CO_2 release field experiments. Greenhouse Gases: Science and Technology.

https://doi.org/10.1002/ghg.2205

Abstract

Carbon Capture and Storage (CCS) has been highlighted as a crucial technology for reducing carbon emissions, yet CO_2 leakage from the reservoir is still a matter of great public concern, especially because of water pollution reasons. Hence, reduced-scale CO_2 release experiments have been conducted worldwide to study hydrogeochemical response in shallow groundwaters. Although other reviews have been previously published, this study reviews critical data to establish a geochemical process-based framework of the scientific findings. Following this, four mechanisms were found to be responsible for hydrogeochemical behavior: i) ion-exchange are mainly responsible for short-lived increase in Mg, Ca, Ba and Sr concentrations; ii) sorption and desorption processes were related to heavy metal and trace element variations, seemingly due to the presence of oxyhydroxides and clay minerals; iii) silicate and carbonate dissolution played different roles as a function of specific aquifer mineralogy, releasing metals or influencing divalent cations response; iv) conservative, mixing and oxidation processes were pointed out as possible mechanisms regulating variations of Cl^-, SO_4^{2-} and NO_3^-. Although studies suggested no parameter exceeded potable limits, most experiments were short-lived, possibly overlooking the CO_2 leakage response in a long-term exposure. Hence, further work is still needed specially to support relevant environmental legislation.

***Keywords**: CCS; groundwater; CO_2 monitoring; leakage; hydrogeochemistry*

4.1. Introduction

Greenhouse gases (GHG) emissions continue to grow despite continuous warnings from scientific authorities, environmental regulators and concerned citizens from around the world. Although the global COVID-19 pandemic forced daily CO_2 emissions to decline by 17% by early April 2020 compared with the mean 2019 levels (LE QUÉRÉ et al., 2020), this reduction was only temporary and CO_2 emissions bounced back to growing levels (LIU et al., 2020), reaching the global average concentration of 412.5 ppm by the end of 2020 (LINDSEY, 2021), which represents an increase of 2.6 ppm in relation to 2019 levels.

For this reason, serious carbon mitigation approaches are now more necessary than ever, as short-lived actions and measures are clearly not enough to curb emissions at the global scale. One way of doing this is by implementing Carbon Capture and Storage (CCS) projects (IPCC, 2005b) to abate CO_2 emission from stationary sources, like heavy industries (steel & cement), power plants, Oil & Gas refineries and bioenergy plants, followed by long-term geological storage. The working principle is that CO_2 is captured, compressed, and transported for injection into deep geological formations where it should remain permanently confined (KETZER; IGLESIAS; EINLOFT, 2012a). This injection can be done in at least four different environments (deep saline aquifers, depleted O&G reservoirs, coal seams and basaltic rocks), in which CO_2 is either stored as a supercritical phase, in the form of a soluble carbonic compound ($HCO_3^-{}_{(aq)}$ or $CO_3^{2-}{}_{(aq)}$) or as a solid mineral such as calcite ($CaCO_3$) or magnesite ($MgCO_3$) (GALE, 2004; IPCC, 2005b).

Hence, the essence of CCS is that CO_2 must remain contained in the subsurface to be considered a viable and reliable geoengineering technique to combat climate change. Nonetheless, unintended CO_2 (or brine) leakage from the reservoir could happen if the risks are not properly assessed, potentially causing societal, economic and environmental impacts near the injection sites (HA-DUONG; LOISEL, 2009; HARVEY et al., 2013a; JONES et al., 2015a; LEMIEUX, 2011a). Hepple & Benson (2005) consider an annual seepage rate of 0.01% still tolerable to ensure the effectiveness of geological carbon storage, whereas the (IPCC, 2005b) recommends that CCS projects should operate with less than 1% CO_2 leakage to the surface for a 1000 years' time scale. The US Department of Energy (US DOE) states that a rate of 99% storage permanence is acceptable (BIELICKI et al., 2015). Following the IPCC

premise, Roberts et al. (2018) calculated that a lower-bound commercial CCS project storing at least 0.4 Mt of CO_2 per year (Mt CO_2/y) operating for 40 years would inject 16 Mt CO_2 and thus could allow a maximum CO_2 loss rate to the atmosphere of 160 t CO_2/y.

Under this scope, improperly sealed wells represent the most probable leakage pathway to surface (IPCC, 2005; Roberts & Stalker, 2020), even though such events are until now very rare. Nevertheless, as already regulated by the United States Environmental Protection Agency ((EPA), 2013) and European Union CCS Directive (PARLIAMENT, 2009), CO_2 containment in the reservoir complex must be monitored, verified, and accounted in several compartments, including in the near-surface and surface environments (JENKINS; CHADWICK; HOVORKA, 2015b; JONES et al., 2015a). However, as the number of CCS projects are still relatively low and the likelihood of CO_2 reaching the surface is small, researchers started looking at other options on how CO_2 leakage would be manifested in the underground.

There are four ways of doing this: i) studying natural analogues (KEATING et al., 2014, 2010a; LEWICKI; BIRKHOLZER; TSANG, 2006); ii) developing laboratory-scale experiments (HA et al., 2020; HUMEZ et al., 2013; JEONG et al., 2020; KHARAKA et al., 2018; LU et al., 2010; SHAO et al., 2015; VARADHARAJAN et al., 2013; WANG et al., 2016a); iii) performing geochemical modelling studies (CAHILL; JAKOBSEN, 2015a; ZHENG et al., 2012a, 2016); and iv) developing reduced-scale controlled release field experiments (GUPTA; YADAV, 2020a; LEE et al., 2016a; ROBERTS; STALKER, 2020b). The latter one follows the ‘learn-by-doing’ approach and have proved to be extremely valuable as a base to develop monitoring, measurement and verification (MMV) guidelines to fulfil environment regulation in countries where CCS is already a reality (USA, Canada, Australia and Norway), and for this reason it will be the focus of this work, as it can be used as a precedent for other countries where CCS is in its infancy and needs more scientific basis, especially for environmental regulation.

4.1.1. Simulating CO_2 leakage at reduced scale experiments

As experimental tests at full scale are usually expensive, researchers have been exploring the idea of developing leakage experiments in small field sites as a way of mimicking the process of CO_2 reaching the near surface drinking water reservoirs in

order to understand the hydrogeochemical reactions that could be developed in these circumstances (Figure 4.1). The purpose of this approach is to gain hands-on experience on how groundwater chemistry alteration would be manifested and what is the magnitude of this change.

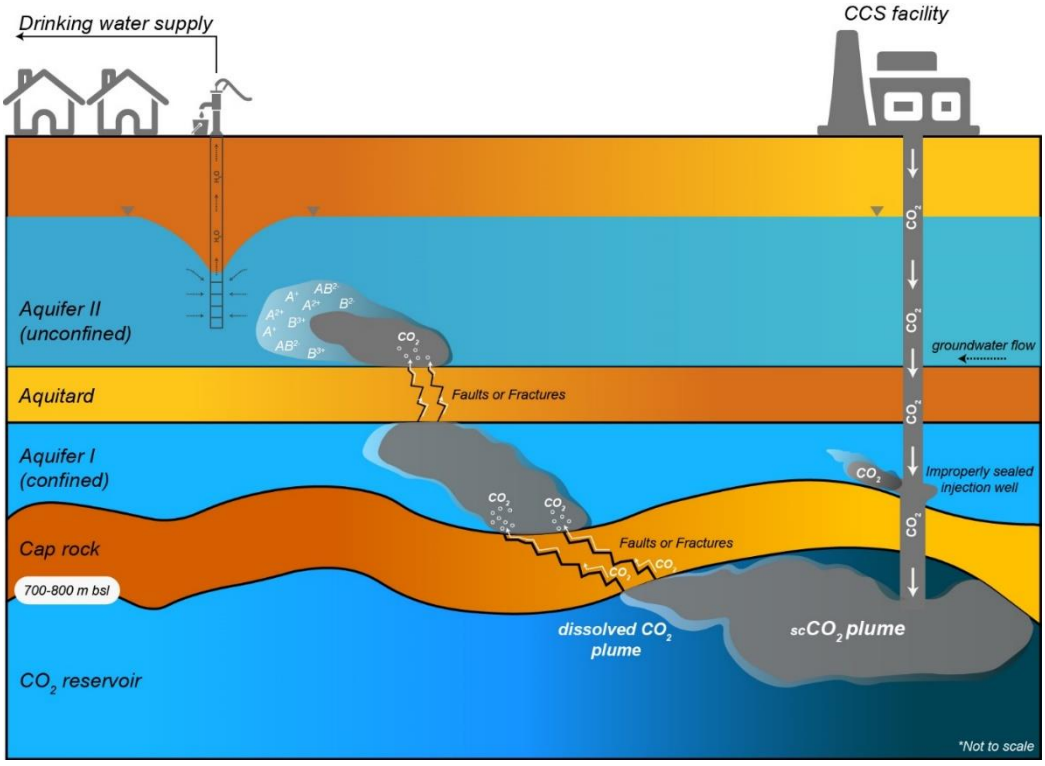

Figure 4. 1. *Representative illustration of CO_2 reaching near surface zones through possible leakage routes and its interaction with groundwater and aquifer minerals.*

For at least 15 years, field-scale controlled release experiments have been preferred by researchers from around the world to conduct site-specific, reduced-cost studies on how CO_2 behaves when it interacts with shallow groundwater aquifers and their mineral framework. A recent research led by Roberts & Stalker (2020) found that 15 different field experiments have already been carried out in almost all continents, in a variety of geological, hydrogeological and climatic conditions. This study has compiled and synthesized the experimental parameters used (e.g. injection rate and quantity, depth of CO_2 release, etc.) and summarized the fate of the CO_2 and leakage quantification, detailing aspects of the design, implementation, and technical development of the studies.

Feitz et al. (2014) were the first to publish a review on field test sites studies, comparing experimental setups, methods applied for monitoring and general findings at four locations (Ginninderra/AUS, ZERT/USA, Ressacada Farm/BRA and CO_2Field Lab/NOR), but had not discussed any groundwater chemistry change as a result of the CO_2-groundwater-rock interaction.(Lee et al., 2016), on the other hand, were the first to publish a comprehensive review on field experimental methods detailing shallow groundwater chemistry changes at eight sites (Cranfield/USA, Brackenridge/USA, Wittstock/GER, Vrøgum/DEN, Escatawpa/USA), showing their characteristics, geological/hydrogeological settings, sampling procedures and hydrogeochemistry parameters studied in each case. However, the authors have limited the study to show the general trends and had not thoroughly discussed the geochemical mechanisms responsible for modifying groundwater quality. Later, (JEONG; LEE; YOON, 2017) launched a review on the analytical procedures applied in five field experiments (ZERT/USA, Wittstock/GER, Western Texas/USA, Escatawpa/USA, CO_2FieldLab/NOR), summarizing all the field and laboratory parameters quantified in each case together with the used methods (ISO, USEPA and USGS), recommended detections range and required equipment to reliably measure the analytes.

More recently, Gupta & Yadav (2020) showed an extensive list of numerical and laboratory studies, together with the field-scale experiments of ZERT/USA, Escatawpa/USA, Wittstock/GER and Vrøgum/DEN, but limited the analysis by mentioning the shifts and trends of groundwater chemistry during the CO_2 release experiments without discussing in detail all the geochemical processes involved and the geological and technical specificities of each case. Hence, as far as we know, no specific review article has ever compiled the collective results of shallow groundwater chemistry changes resulting from the controlled released CO_2 in field experiments and frame them into geochemical mechanisms that represent the full spectrum of possible reactions regarding the mineral composition (variable V1), the hydraulic aquifer parameters (variable V2), the volume of leaked CO_2 (variable V3), the time of the experiment (variable V4) and the hydrogeochemical characteristics (variable V5) in each research site.

Therefore, the objective of this work is to give a better understanding of the geochemical processes (ion exchange, adsorption/desorption, redox reactions and

mineral dissolution/precipitation) linked to the experiments analyzed in this review and how they are qualitatively related to these five macro variables. In this context, this study will serve as geochemical process-based summary of the scientific findings of relevant field-scale experiments carried out so far about shallow groundwater response to high CO_2 levels.

4.2. Methods and premises followed

For this work, a dataset of reduced-scale field experiments has been compiled from the '*Web of Science*' platform. In this case, *Web of Science Core Collection* was the main search network in which all the citation indexes were employed. The focus of this review is on publicly available peer-reviewed articles published up to August 2022, which dealt with injected/released CO_2, either with the purpose of keeping CO_2 'locally' stored or releasing it to surface, into near-surface underground environments, where shallow groundwater chemistry data is clearly discussed. In this case, a list of 23 general and specific keywords (Table 4.1) was used in the queries, returning hundreds of papers that were broadly analyzed and classified. Those studies dealing exclusively with numerical geochemical simulation/modelling, laboratory experiments and natural analogues were excluded from the selection.

Table 4. 1*. List of keywords used to find peer-reviewed research papers dealing with shallow release of CO_2 and groundwater monitoring.*

General keywords used	***Specific keywords used***
CCS	*Field test*
Carbon	*Pilot*
Storage	*Site*
CO_2	*Controlled*
CO_2 plume	*Release*
Leakage	*Inject**
MMV	*Shallow*
Impact	*Groundwater monitoring*
Intrusion	*Geochem**
	Hydrogeology
	Aquifer
	*Geologic**

	Chemistry
	Mineral

Note: the asterisk symbol (*) was used as a wildcard to broaden the searching procedure, retrieving variations staring with the same typing but ending with different letters.

As there was no standard form for displaying the data, a spreadsheet containing all the relevant information fitting the scope of this work was populated and organized. This full dataset is available as a Supplementary Material (Table S1). Variables listed in the file were either directly extracted from the original paper or converted using specific metrics. For instance, mineral composition quantitatively displayed reflect the result of XRD analysis and hence constitutes a weight percentage of the mineral in the bulk aquifer material. Those that were not analytically determined are marked with an 'X' followed by 'minor' or 'major' to indicate its relative abundance in the material.

Hydraulic conductivity data followed the same principle, and most data were collected in the original form and converted to m/day unit. When available only as transmissivity (m^2/s), the original data was divided by the aquifer thickness and latter to m/day. Total mass or average rate of release CO_2 was considered as kg/day (or kg/h, for those experiments lasting less than 1 day). When applicable, as in the case of CO_2-rich water injection, CO_2 mass was calculated based on the assumption that CO_2 solubility at 20ºC is 1,600 mg/L, and latter converted to symbolize kg of CO_2/day. Groundwater concentration of chemical elements or species are displayed either in mg/L (major and minor elements) or µg/L (trace elements), being converted in relation to each element atomic mass when needed. CO_2 leakage time is represented by the duration of the injection phase in days or hours. Incomplete information results from the unavailability of public data.

4.3. Results on selected studies

After applying the search criteria, a total of 16 field-scale experiments were found. Out of these, 10 studies were conducted in unconsolidated (UC) aquifer materials (CAHILL; JAKOBSEN, 2013a; CAHILL; MARKER; JAKOBSEN, 2014a; DO et al., 2022b; GAL et al., 2014; HUMEZ et al., 2014a; JU et al., 2019; LEE et al., 2017; MYERS et al., 2020; PETER et al., 2012a; PEZARD et al., 2016a; SCHULZ et al.,

2012a; SHIN et al., 2020; SPANGLER et al., 2010; TRAUTZ et al., 2013a), 5 were entirely performed in consolidated rock (R) aquifers (Gal et al., 2014; Gombert et al., 2014; Myers et al., 2020; Petit et al., 2021; Rillard et al., 2014; Yang et al., 2014; Zhu et al., 2015) and one was done both in unconsolidated and consolidated aquifer (GAL et al., 2014), reflecting different geological contexts. For the purpose of this review, we decided to focus only on the UC aquifers (Table 4.2) as the number of the papers analyzed were higher and because the scientific content is more numerous than the other papers. Besides, the interaction of CO_2-groundwater-mineral is more pronounced in UC aquifers, since the intergranular space between sediment is higher, the groundwater flows at a faster pace and the surface area of the minerals is greater, which is expected to be the most recurring setting in near-surface environments worldwide.

Table 4. 2*. Summary of selected studies, injection types and depth of releasing CO_2 and water table.*

Experimental site	***Injection type/strategy***	***Injection depth – bsl (m)[a]***	***Water table – bsl (m)***	***Reference***
ZERT - Bozeman, MT (USA)	Multiple-well/Free-gas phase	3	1-1.5	Kharaka et al. (2010)
Wittstock - Brandenburg (GER)		20	2.8	Peter et al. (2012)
CO_2 Field Lab - Svelvik Ridge, Oslo (NOR)		24	0.6-1	Humez et al. (2014)
Vrøgum (DEN)		10	1.5-2	Cahill et al. (2014)
SiMEX - Maguelone (FRA)		20	*NS*	Pezard et al. (2016)
Jackson County/Escatawpa - Mississipi (USA)	Multiple-well/ CO_2-saturated groundwater	56.7	*NS*	Trautz et al. (2013)

Brackenridge - Austin, Texas (USA)	[1]Push-pull/ CO_2-rich groundwater [2]Pulse-like test (CO_2 bubbled into groundwater)	6	2.4	[1]Mickler et al. (2013) [2](Yang et al., 2014)
Cranfield - Adams County, Mississipi (USA)	Push-pull/ CO_2-rich groundwater	73	27	Yang et al. (2013)
Environmental Impact Evaluation Test – EIT (South Korea)	CO_2-saturated groundwater	21-24	15	(DO et al., 2022b)

[a] *bsl = below surface level*
[b] *NS = Not Specified*

Table S1 (Supplementary Material) presents all the information gathered from the original papers, from Roberts & Stalker (2020) and Lee et al. (2016), that fit into the macro variables described above. In our analysis, push-pull tests (injection and withdrawal from the same well) and multiple-well experiments (injection and withdrawal from different wells) were included, although some considerations have been made to each case. The injection strategy, either as carbonated water (CO_2-rich groundwater) or gaseous phase CO_2 are both considered.

4.3.1. Mineral composition (V1)

The ZERT/USA field site (Kharaka et al., 2010; Spangler et al., 2010; Zheng et al., 2012) is composed of a deposit of coarse sandy gravel from 5m to 1.2m deep, where the injection of CO_2 occurred (~ 2.5m deep via a perforated horizontal pipe), with gravels comprising 70% of the rock volume, and andesite being the most recurring rock fragment among them, although some amounts of detrital limestone and dolostone had also been observed. From 1.2 m to 0.2 m there is a topsoil layer of organic-rich silt and clay with some sands, in which a caliche (hard subsoil encrusted with calcium-carbonate, in this case with 15% calcite) layer also occurs between 50-80 cm deep. X-Ray Diffraction (XRD) quantification of the sand and silt sized fraction

of the sediment revealed that 40% is quartz, 40% is magnetite and magnetic rock fragments, and the rest of the 20% is constituted by particles of amphibole, biotite/chlorite and feldspar (Kharaka et al., 2010).

In this case, although the mineralogy of the bulk rock volume is primarily composed by rock-forming silicate minerals, the existence of a caliche layer (representing an impervious material cemented by Ca/Mg carbonates) above the CO_2 injection horizon forces the gaseous CO_2 plume to spread laterally over the area. Consequently, with time the CO_2 starts to dissolve into the groundwater and to interact with the caliche layer, which is located just above the first set of monitoring wells. Hence, although most of the background mineralogy of this site is of silicate nature, this characteristic geologic setting makes the groundwater of this example to be considered a *lato sensu* representative of a carbonate aquifer.

Differently, the field site at Wittstock/GER represent a carbonate-free aquifer, whose geological origin relates to glacial periods (Peter et al., 2011; Peter et al., 2012). In this case, there are two aquifers in the area: a) the upper aquifer (Aquifer 1) occurs between 2.5/3 m and 9.5 m bsl, and is characterized by a heterogeneously distributed sequence of interbedded sand and silt-sized particles; b) the lower aquifer (Aquifer 2) occurs between 10.5 m to 19 m bsl and is composed of homogenously distributed sand-sized (medium to coarse) sediments. These two aquifers are partially disconnected by a glacial loam that forms an aquiclude, which disappears towards the west of the area. Below the depth of 19.5 m bsl a glacial till was found, forming another aquiclude limiting the lower boundary of the Aquifer 2, where the CO_2 injection point is located.

Although Peter et al. (2012) had not carried out any mineralogical characterization, data gathered from Peter et al. (2011) shows that TIC (wt. %) from both aquifers is usually < 0.1% or hardly exceeds 1.5% in some intervals (clay layer at the top and till layer at the base). Besides, main cations concentration of retrieved samples indicate that Ca and Mg content represent approximately only 5% to 7% of the sum of Na, K, Fe, Mn and Al, suggesting that these two elements do not form part of the majority of the chemical composition of the aquifer layers. Hence, it is plausible to assume that the mineral framework of both aquifers is silicate-dominated.

Another experimental site, the CO_2FieldLab/NOR, which is located in the Svelvik Ridge, is mainly composed of fluvioglacial-glaciomarine gravel resulted from a

deglaciation process. The sediments that comprise this area are well-sorted coarse-grained sand with gravel (pebble) and cobble lenses sporadically appearing throughout the deposit (BARRIO et al., 2014; HUMEZ et al., 2014a). XRD analysis of the main groundwater monitoring well revealed that the aquifer sediment is dominated by quartz (35-50%), plagioclase (albite 23-33%), k-feldspar (orthoclase 8-12%), mica (annite 1%, muscovite 3-6%), chlorite (nimite 3-9%), amphibole (Mg-hornblende 2-6%) and calcite (2-4%). Illite and smectite have also been reported as minerals present in the clay fraction. Cation exchange capacity (CEC) from the recovered samples showed a mean value of 1 meq/100 g (± 0.15 meq/100 g), indicating a very low capacity of the aquifer mineral framework to exchange cations with groundwater.

Moreover, the Jackson County-Escatawpa/USA field site has two important aquifers within circa (ca.) 60 m of the stratigraphic interval relevant to this study. The shallowest unit, which is 30 m thick, is the Citronelle Formation, which is mainly composed of light brown to gray silty sands interbedded with a relatively thick (~5 m) layer of olive-gray clay. The upper section of this formation is formed by a cover of Quaternary alluvium, composed of silt and clay-sized sediments ranging in color from green to brown with organic material. The lower unit is the Graham Ferry Formation, which on top of the section is formed by a 15 m-thick green clay interval that confines the gray-green silty sand (with minor clay content defining 'black laminations'). This silty sand comprises the CO_2 injection interval and is located in the last ~10 m of the analyzed section. XRD and petrographic analysis determined that these last two units, the silty sand and the confining green clay, are both formed by similar mineral content. The silty sand is dominated by large grains of quartz and minor amounts of albite, plagioclase, illite and pyrite, while the green clay exhibited less quartz and more kaolinite. X-Ray Fluorescence (XRF) also showed a small proportion of Fe oxyhydroxides in this unit. Selective chemical extraction performed in the 'black laminations' (an organic-rich layer found in the tested interval) revealed that this material can be regarded as the source of Ca, Mg, Sr, Mn and Fe content even in mild acidic conditions (Trautz et al., 2013).

The Vrøgum/DEN site is formed by two distinct units: a) the upper 5-6 m bsl of the stratigraphic record is formed by a fine aeolian sand; and b) the lower 6-12 m bsl is comprised of medium to coarse glacial outwash layer of sand-sized sediment (Cahill et al., 2014; Cahill & Jakobsen, 2013). Both layers have extremely low carbonate content,

with TIC 0.1% in the aeolian sand and 0.01 % in the glacial sand. Semiquantitative XRD analysis showed that quartz is the dominating mineral both in the aeolian and glacial sand (88 wt% and 95 wt%, respectively), with minor amounts of K-feldspar (5.6 wt% in the aeolian sand and 1.5 wt% in the glacial), plagioclase (1.5 wt% in the aeolian sand and 3.8 wt% in the glacial) and clay (5 wt% in the aeolian sand) comprising the rest of the mineralogy of the area. CEC of both layers indicates a very low capacity to exchange cations with the surrounding solution, with the aeolian sand showing a measured value of 3.64 meq/100 g and the glacial sand 1.31 meq/100 g. In both cases, Ca and Mg respond to more than 79% as the equivalent fractions on the exchanger (Cahill et al., 2014).

Another European experiment, the SIMEX-Maguelone/FRA test field, is comprised of two distinct geological units: i) the first, which occurs from surface down to 9 m bsl, is composed by lagoonal sediments from the Holocene age; ii) the second, which extends from 9 m up to the base of the drilled wells (ca. 20 m deep), is formed by fluvial deposits of the Pliocene age. In the lower unit, from 13 m to 16 m deep occurs a permeable gravel rich interval (named R1) that is capped both at the base and at the top by clay-rich layers. The shallowest unit comprises a basal 1m-thick (from 8 to 9 m bsl) gravel-rich interval (named R2) that is topped by two thick clay and sand layers. The mineral composition of the reservoir two (R2), which is where CO_2 remains trapped and interacts with groundwater, was quantified by XRD coupled with XRF and indicates that the sediment has 57.5% calcite, 19.3% quartz, 18.08% clay minerals (muscovite, kaolinite and chlorite), 4.28% plagioclase (albite) and 0.84% pyrite (Pezard et al., 2016).

Brackenridge/USA site is a silicate-dominated aquifer, which is located in an alluvial plain of the Colorado River. The 6 m-thick unit that comprises the test interval is composed of sand (medium to coarse-grained) and gravel size sediments interbedded wit clay-rich horizons that can reach up to ~0.2 m thick. Below this unit, a carbonate (limestone) bedrock was encountered. Quantitative XRD analysis revealed that the bulk mineralogy of the CO_2 injection interval is formed by 50% quartz, 17% calcite, 14% plagioclase (albite), 13% K-feldspar (microcline), 4% illite, <2% kaolinite and <2% dolomite (MICKLER et al., 2013a). Complementarily, the Cranfield/USA site is also a silicate-dominated aquifer formed by clay-rich and sandy intervals that represents the upper portion of the Catahoula aquifer (Yang et al.,

2013). Geological distribution of the layers indicate that the CO_2 injection horizon is predominantly composed of sand-sized sediments from 66 to 73 m deep, capped by a very thick clay unit of 38m. XRD analysis of the sediments indicate that the average mineral composition of the bottom sandy interval is 56% quartz, 16% k-feldspar (microcline), 19% kaolinite, 6% illite and 2% plagioclase (albite). On the other hand, the clay-rich layer that lies on top of the injection horizon has 38.8% quartz, 20.9% kaolinite, 19.7% illite, 17.5% k-feldspar (microcline) and 3.2% albite (Yang et al., 2013). All discussed data is represented at Table 4.3.

The Environmental Impact Evaluation Test – EIT (South Korea), hereafter referred to as EIT/KOR, is formed by 40m-thick biotite granite weathering zone, whose main minerals are quartz, plagioclase, microcline and biotite (Do et al., 2022). Whitin this altered interval, illite and Na-montmorillonite are also present, and they account to approximately 6% vol. in the aquifer. According to the authors, the texture of this interval is classified as loamy sand to sand, with a measured CEC between 6-9 meq/100g. Carbonate minerals were detected in very small amounts (~0.1%), especially in portions deeper than 24m (below CO_2 injection point). Jun et al. (2017) mentioned the development of XRD and XRF analysis, but these quantitative results were not found in the literature.

According to Cahill et al. (2013), even aquifers with small amounts of carbonate (i.e., 0.16% weight) might exert some protection against acidification if exposed to CO_2. Moreover, the authors also found that aquifer types dominated by silicate sediments that contain little or no carbonate, possess the smallest surface area and therefore show generally small increases in concentrations of major ions after CO_2 interaction. Nevertheless, these sediments revealed the highest concentrations of pH-dependent (amphoteric) elements such as Al and Fe. Additionally, mixed mineralogy aquifer types containing silicate, carbonate and clay minerals may threaten water quality by dissolution of carbonates and silicates, sorption/ion exchange processes and dissolution of clay minerals. Hence, in their study it is acknowledged that quantitative sediment compositions should be evaluated. However, even though we agree with that argument, the accuracy of the mineral composition quantification (or the lack of it) in the published studies used in this review could not be assessed as not all papers expressed the results quantitatively. Thus, no further discussion on this matter will not be made in the next sections.

***Table 4. 3**. Summary of mineral composition of each experimental investigation site.*

Experiment	***V1) MINERAL COMPOSITION (wt. %)***											
	Quartz	***K-Feldspar (Microcline; Orthoclase)***	***Plagioclase (Albite)***	***Illite***	***Kaolinite***	***Mica (annite, muscovite or biotite)***	***Calcite***	***Dolomite***	***Chlorite***	***Amphibole***	***Magnetite***	***Others (specified)***
ZERT - Bozeman, MT (USA)	*40*	*-*	*-*	*-*	*-*	*-*	***	*-*	*-*	*-*	*40*	*20 (amphibole, biotite, chlorite, feldspar)*
Wittstock - Brandenburg (GER)[a]	*NA*	*NA*	*NA*	*NA*	*NA*	*NA*	*NA*	*NA*	*NA*	*NA*	*NA*	*NA*
CO_2 Field Lab (NOR)	*35-50*	*8-12*	*23-33*	*-*	*-*	*1-6*	*2-4*	*-*	*3-9*	*2-6*	*-*	*-*
Vrøgum (DEN)	*92*	*3*	*5*	*-*	*-*	*-*	*-*	*-*	*-*	*-*	*-*	*-*
Jackson County/Escatawpa - Mississipi (USA)[b]	*X (major amount)*	*-*	*X (minor amount)*	*X (minor amount)*	*X (minor amount)*	*-*	*-*	*-*	*-*	*-*	*-*	*X (pyrite; Fe oxyhydroxides)*
SiMEX - Maguelone (FRA)	*19.3*	*-*	*4.28*	*-*	*-*	*18.08*	*57.5*	*-*	*-*	*-*	*-*	*0.84 (pyrite)*
Brackenridge - Austin, Texas (USA)	*50*	*13*	*14*	*4*	*<2*	*-*	*17*	*<2*	*-*	*-*	*-*	*-*
Cranfield - Adams County, Mississipi (USA)	*52*	*17*	*2*	*9*	*20*	*-*	*-*	*-*	*-*	*-*	*-*	*-*
EIT (KOR)[b]	*X*	*X*	*X*	*X*	*-*	*X*	*0.1*	*-*	*-*	*-*	*-*	*Na-Montmorillonite*

[a] *Mineral composition was neither determined nor qualitatively mentioned at Wittstock/GER. NA = Not available.*

[b] *Mineral composition was only qualitatively mentioned at Jackson County/Escatawpa/USA and EIT (KOR), although carbonate composition was mentioned to be ~0.1% in the latter case.*

** A caliche layer is reported to cap the CO_2 injection horizon, clearly influencing chemical composition of groundwaters as indicated by the authors and showed in the data.*

4.3.2. Hydraulic aquifer parameters (V2)

Regarding the hydrodynamic parameters of the field sites, most of the studies reported the hydraulic conductivity of the aquifers either calculated by *in situ* slug or pumping tests (CAHILL; JAKOBSEN, 2013a; CAHILL; MARKER; JAKOBSEN, 2014a; DO et al., 2022b; PETER et al., 2012a; TRAUTZ et al., 2013a), by percolation tests (Kharaka et al., 2010; Spangler et al., 2010) or using tracers (MICKLER et al., 2013a). Others presented calculated transmissivity data obtained from pumping tests (GAL et al., 2013; HUMEZ et al., 2014a). Pezard et al. (2016) did not mention how hydraulic conductivity was calculated, even though its value is reported in the study. Yang et al (2013) was the only one who did not report any hydrodynamic parameter (Table 4.4).

Table 4. 4. Hydraulic conductivity measured at each site and its classified aquifer type based on mineralogy and flow characteristics.

Experiment	***Reference***	***V2) HYDRAULIC CONDUCTIVITY (m/day)***		***Aquifer type***
		Min.	***Max.***	
ZERT - Bozeman, MT (USA)	Kharaka et al. (2010)	*1.4*	*2*	*Mixed mineralogy (low-HC)*
Wittstock - Brandenburg (GER)	*Peter et al. (2012)*	*<0.1*	*1*	*Silicate (low-HC)*
CO_2 Field Lab (NOR)	*Humez et al. (2014)*	*1.87*	*169.34*	*Mixed mineralogy (high-HC)*
Vrøgum (DEN)	*Cahill et al. (2014)*	*10.97*	*19.87*	*Silicate (intermediate-HC)*
Jackson County/Escatawpa - Mississipi (USA)	*Trautz et al. (2013)*	*14.68* [a]		*Silicate (intermediate-HC)*
SiMEX - Maguelone (FRA)	*Pezard et al. (2016)*	*345.6* [a]		*Carbonate (high-HC)*
Brackenridge - Austin, Texas (USA)	*Mickler et al. (2013)* *Yang et al. (2014)*	*1.0* [a]		*Mixed mineralogy (low-HC)*
Cranfield - Adams County, Mississipi (USA)	*Yang et al. (2013)*	*NA* [b]		*Silicate*
EIT (KOR)	*Do et al. (2022)*	*0.18* [a]		*Silicate (low-HC)*

[a] Average or reported values found at the original papers. For details the reader is referred to the cited works.; [b] NA = Not Available

Among all the reported hydraulic conductivities, the SIMEX-Maguelone/FRA and CO_2 Field Lab/NOR have the highest flow rates (345.6 m/day and up to 169.34 m/day, respectively). These results are in agreement with the reported sediment composition of the sites and indicate that the gravel-rich intervals that forms the CO_2 injection horizon allows a very rapid displacement of groundwater and gaseous CO_2 plume. Vrøgum/DEN and Jackson County-Escatawpa/USA also have a relatively high hydraulic conductivity, but one order of magnitude lower than the abovementioned sites (19.87 m/day and 14.68 m/day, respectively), equally suggesting good capacity for fluid flow and advection transport of the solutes/dissolved CO_2.

ZERT/USA and Brackenridge/USA show more modest values, ranging from 1.4 to 2 m/day and 1 m/day, respectively. In these cases, the values are influenced by the heterogeneity of the sediment composition in both cases and are related to the interbedded nature and textural complexity of the aquifer. Wittstock/GER is the field test with the lowest range of hydraulic conductivity (<0.1 to 1 m/day). This characteristic seems to be related with occurrence of interbedded layers of fine-grained particles (especially silt-sized ones) that hinders groundwater flow and, consequently, reduce the relative spatial dispersion of solutes and gases.

Average hydraulic conductivity for EIT/KOR is computed taken into consideration the data obtained from slug and pumping tests performed in the loamy sand to sand interval of the weathered granite zone where injection took place, resulting in a value of 0.18 m/day (Do et al., 2022).

To simplify the results and to understand the relation between the variables, injection experiments were grouped in aquifer types regarding their mineralogy and hydraulic conductivity. Hence, field experiments majorly composed by aluminosilicate minerals, with minimum amount of carbonate minerals (<1% volume), were categorized as silicate aquifer type, while others with carbonate minerals greater than 2% volume but with varying amounts of aluminosilicate minerals were classified as mixed mineralogy aquifer type. Lastly, aquifers with more than 50% of carbonate minerals were considered as carbonate aquifer type.

Moreover, aquifers with hydraulic conductivity of up to 2 m/day are considered low-HC (Hydraulic Conductivity), those between a few m/day and ~20 m/day are grouped as intermediate-HC, while aquifers with higher flow velocities (> 20m/day and a few hundreds of m/day) were categorized as high-HC. For the Cranfield/USA

experiment only the mineralogy is mentioned, thus flow rate categorization was not possible for this case.

4.3.3. Total mass and rate of leaked CO_2 (V3)

Mass and rate of released CO_2 is reported differently in the analyzed studies. In this article, total mass of CO_2 is shown in kilograms (kg), while injection/release rates are represented by kg/day (even though some studies lasted less than one day). In this case, to simplify any variations on the rates caused by technical problems or flow rate adjustments, an average rate was calculated based on total mass of released CO_2 divided by the period of injection in days/hours. In the experiments where CO_2 was injected as dissolved phase in water, CO_2 mass was calculated based on the assumption that its solubility at 20°C was 1,600 mg/L. Hence, as can be later seen, total CO_2 mass and average rate in these cases were significantly lower than in those where it was released as a gaseous phase.

By far, ZERT/USA has the highest total mass of injected CO_2 (9,000 kg) and average leaked rate (300 kg/day), which was performed via a 70 m-long horizontal pipe (Figure 4.2a). However, groundwater monitoring was only carried out in the vicinity of a 10 m-long interval (Kharaka et al., 2010). Assuming an even distribution of CO_2 along the pipe, 128.6 kg were injected in the section where CO_2-groundwater interaction was monitored, with an average rate of approximately 4.3 kg/day. At CO_2FieldLab/NOR site, a total mass of 1,670 kg of CO_2 was leaked at 18 m deep bsl through an 45° inclined well, with a flowrate of 278 kg/day (Figure 4.2b), although the hourly injection rate varied from 5 to 17.5 kg/h (BARRIO et al., 2014). Vrøgum/DEN follows almost the same total leaked CO_2 mass, with 1,600 kg. Nevertheless, considering the longer period of injection, the average rate was 22 kg/day, much lower than the Norwegian study.

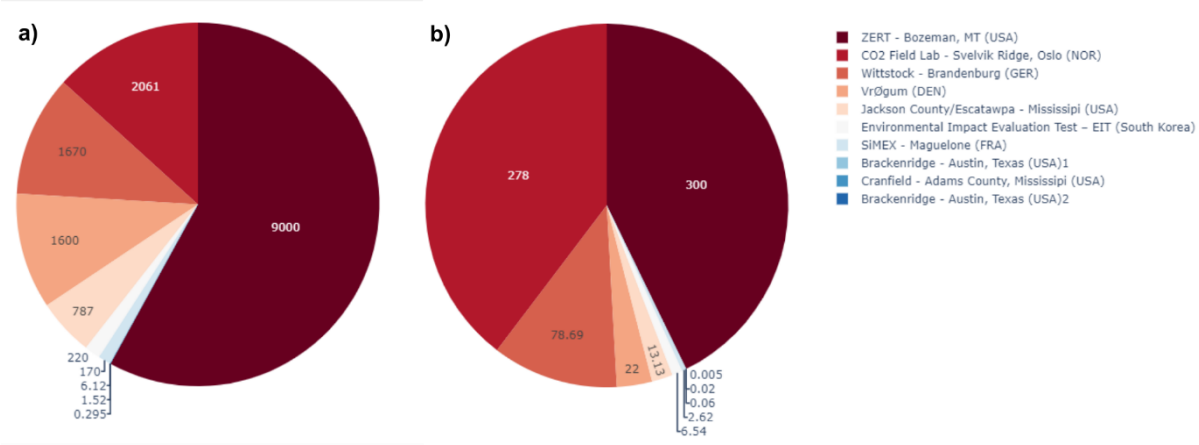

Figure 4. 2. *Total mass (a) and average rate (b) of CO_2 (kg) release in each experiment, either as gaseous phase or CO_2-saturated groundwater.*

At Wittstock/GER, the amount of CO_2 released at least 50% less than these later cases, with a total mass of 787 kg of CO_2 leaked over the course of the experiment. This was done by injecting this amount through three wells, which results in an average of 26.23 kg of CO_2 per day at each well, or 78.69 kg/d in total. At SIMEX-Maguelone/FRA, the researchers released even less CO_2, with a total amount of 220 kg. However, considering the characteristics of the experiment, which consisted in a single CO_2 release over less than one day, the leaking rate was very high, calculated to have been approximately 62.85 kg/h.

In those cases where CO_2 was injected dissolved in groundwater, the Jackson County-Escatawpa/USA represents the situation where the biggest amount was released. In this case, a total of 1,288,656 L of CO_2-saturated water has been injected. Therefore, it is assumed that a total mass of 2,061 kg of CO_2 was injected into the aquifer, which results in an average rate of 13.13 kgCO_2/day (as the injection lasted for 157 days). In the Brackenridge/USA study, two different tests were performed. In the first, Mickler et al. (2013) reported that a total of 950 L of CO_2-saturated H_2O were injected, therefore it is presumed that only 1.52 kg of CO_2 has interacted with the aquifer. In this condition, the average flow rate was 0.06 kg of CO_2/day.

Another test was carried out by Yang et al. (2014) at the same site, in which a very small gas-phase CO_2 (only 0.295 kg) was bubbled through the well for a short time (2.5 hours). Thus, the calculated injection rate was 0.118 kg/h. At the Cranfield/USA site, 3,825 L of CO_2-saturated H2O have been released to the aquifer, which means

that 6.12 kg of dissolved CO_2 interacted with groundwater. As the test ran for 10 hours, the average leaked rate was 0.2 kg/day of CO_2. In the EIT/KOR study, the authors reported a total of 170 kg of CO_2 injected as CO_2-saturated water which, considering the experiment length, represents an average release rate of ca. 6.5 kg/day.

In order to facilitate an intercomparison, average CO_2 leaked rate has been normalized by average hydraulic conductivity (Figure 4.3), symbolizing the amount of CO_2 (kg) per unit meter (m) through time (day). As can be seen, there is no homogenous distribution of the amount of CO_2 release in each aquifer type in comparison with their flow characteristics. Mixed mineralogy aquifer (low-HC) type has been exposed both to very low and high amount of CO_2/m, while mixed mineralogy aquifer (high-HC) only experienced low amount of CO_2/m. Silicate (low-HC) aquifer types has been subjected to high and intermediate amount of CO_2/m, whereas silicate (intermediate-HC) aquifer types to very low amount of CO_2/m. Carbonate (high-HC), on the other hand, has been only expose to very low amount of CO_2/m. Further discussion of the role of this parameter on the promoted hydrogeochemical changes has been included in section 3.5.

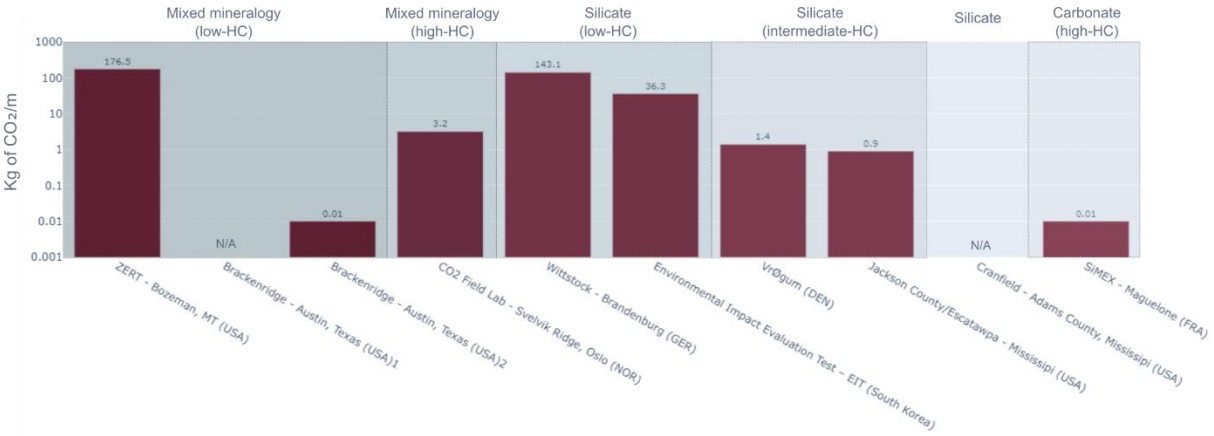

Figure 4. 3. *Average CO_2 leakage rate normalized by average hydraulic conductivity of each experimental study grouped by aquifer type.*

4.3.4. Length of injection experiment (V4)

Apart from the abovementioned characteristics of the studies, the experiments also had completely different lifespans (Figure 4.4). While some lasted a few hours, others

nearly completed or have exactly completed a whole year if background, injection and post-injection are considered. Background was monitored for as little as a few minutes or hours before CO_2 injection in some cases to months prior to CO_2 release in others. The same occurred in the post-injection phase. As for the injection phase, time varied from just one hour at Brackenridge/USA (MICKLER et al., 2013a) to 157 days (5 months) at Jackson County-Escatawpa/USA (Trautz et al., 2013).

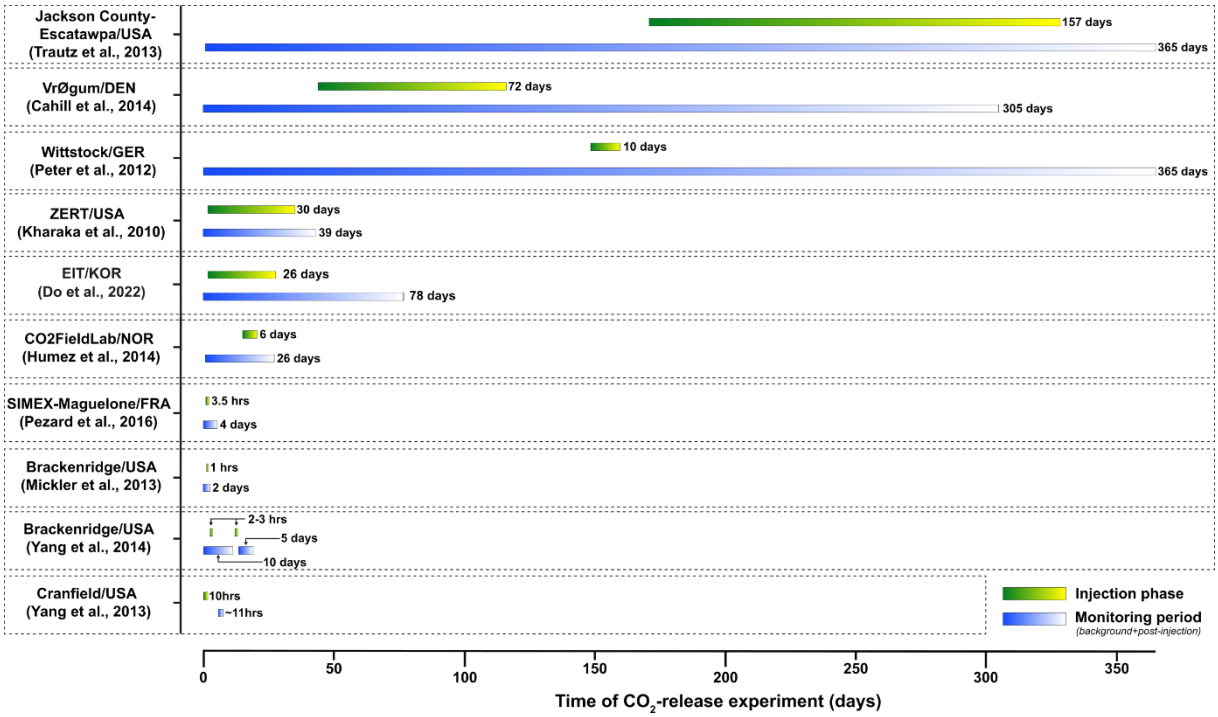

Figure 4. 4. *Length of injection and monitoring phases of analyzed experimental sites.*

Between these end-members, from the shortest to the longest, are the following projects: a) Brackenridge/USA (Yang et al., 2014), which injected for just 2 to 3 hours; b) SIMEX-Maguelone/FRA (Pezard et al., 2016), with an injection period that lasted 3.5 hours; c) Cranfield/USA (Yang et al., 2013), whose injection time was 10h; d) CO_2 Field Lab/NOR (HUMEZ et al., 2014a), that took 6 days to completely inject CO_2; e) EIT/KOR (Do et al., 2022), where the injection campaign lasted 26 days; f) Wittstock/GER (PETER et al., 2012a), where injection took 10 days; g) ZERT/USA (Kharaka et al., 2010), which continuously released CO_2 to the aquifer for 30 days; and finally h) Vrøgum/DEN (Cahill et al., 2014), where injection endured for 72 days.

This shows that some studies are so short-lived that some slow kinetic hydrogeochemical mechanisms (e.g., dissolution in silicate aquifers) are not even accounted for, although others long-lived ones can better represent situations where

CO_2 persistency in the aquifer can be relevant. Moreover, brief experiments (less than few days) might not mimic a possible real leakage from CO_2 reservoir to the aquifer neither from a style perspective (as CO_2 outflow would happen more continuous, but not as a fixed flow rate) nor for a monitoring purpose point of view (as CO_2 induced hydrogeochemical changes would be missed in a relatively time spaced MMV campaign).

Additionally, as will be seen in the next section, background, injection and post-injection values used in this study are average values calculated from the original papers. Hence, if each of these periods are short or include only a few monitoring points, used data could not be representative and would imply more uncertainty. Although acknowledged, this study will not analyze the effects of such characteristics.

4.3.5. Hydrogeochemical characteristics (V5)

Considering all explored studies, at least 54 hydrogeochemical parameters have been analyzed. Among the field parameters, pH, temperature and electrical conductivity (EC) had been the most assessed physicochemical *in situ* indicators of CO_2-mineral-groundwater interaction, followed by dissolved oxygen (DO), total dissolved solids (TDS) and oxidation-reduction potential (ORP). Regarding the inorganic compounds, alkalinity, major ions (mostly Na, Mg, Ca and K) and anions (mainly Cl^- and SO_4^{2-}) had also been monitored. NO_2^-, NO_3^- and PO_4^{3-} were included in less than half of the studies. Amid the minor elements, Fe, Mn, Ba and Sr were the most analyzed. Trace elements were measured in all cases at varying spectrums. Half of the studies included only one or two elements (mostly Al and Zn), while the rest involved at least seven elements (Al, As, B, Co, Li, Ni and Zn). In the present study, indicated changes represent those observed at the nearest groundwater monitoring well and considering the highest modification from background values. Gathered information is showed in Table S1 (Supplementary Material).

Although almost all cited temperature monitoring, only four studies have explicitly mentioned the values in degrees Celsius. In those, temperature varied from <10°C (Wittstock/GER) up to >25°C (Brackenridge/USA), clearly indicating different conditions in which CO_2 dissolved (Table S1). Considering the length of the experiments, little variations have been observed from background to post-injection phase. The pH was the most tracked field parameter, being determined for

background, injection and post-injection in all studies. In nearly all of them the background value was observed to be in the range of natural waters (6.5-8.5), except for Vrøgum/DEN and Cranfield/USA, which exhibited more acidic conditions (5.5 and 6.1, respectively).

Electrical conductivity was the second most followed parameter, not been included in only two studies (SIMEX-Maguelone/FRA and Brackenridge/USA). As with temperature, EC values showed a considerable range, from <180 µS/cm to 850 µS/cm, indicating different content of ionic species dissolved in groundwater. Alkalinity, which is strongly related to the distribution of carbonic species in groundwater (Clark, 2015a), has been measured in nearly all sites (except at SIMEX-Maguelone/FRA), but was only traced from background to post-injection in five of them. Dissolved oxygen was only mentioned in Wittstock/GER (0.6 mg/L) and Vrøgum/DEN (7.9 mg/L), but completely tracked from background to post-injection only at the Danish site. Oxidation-reduction potential had been measured just in the German study (276 mV) and TDS at ZERT/USA (614 mg/L).

Following CO_2 injection, all studies reported a pH decrease in the order of 1.1 to 3.9 units, with a median value of 1.23 units. The highest changes were observed in silicate (intermediate-HC) aquifer types, which also corresponds to those field tests were injection length was greater. Similarly, mixed mineralogy (high-HC) aquifer types experienced the second-most decrease, as can be seen in Figure 4.5a. These changes do not seem to be largely influenced by the amount of CO_2 (kg) per unit meter (m) through time as experiments developed in silicate (low-HC) aquifer types had more CO_2 (kg)/m and still exhibited less proportional modification.

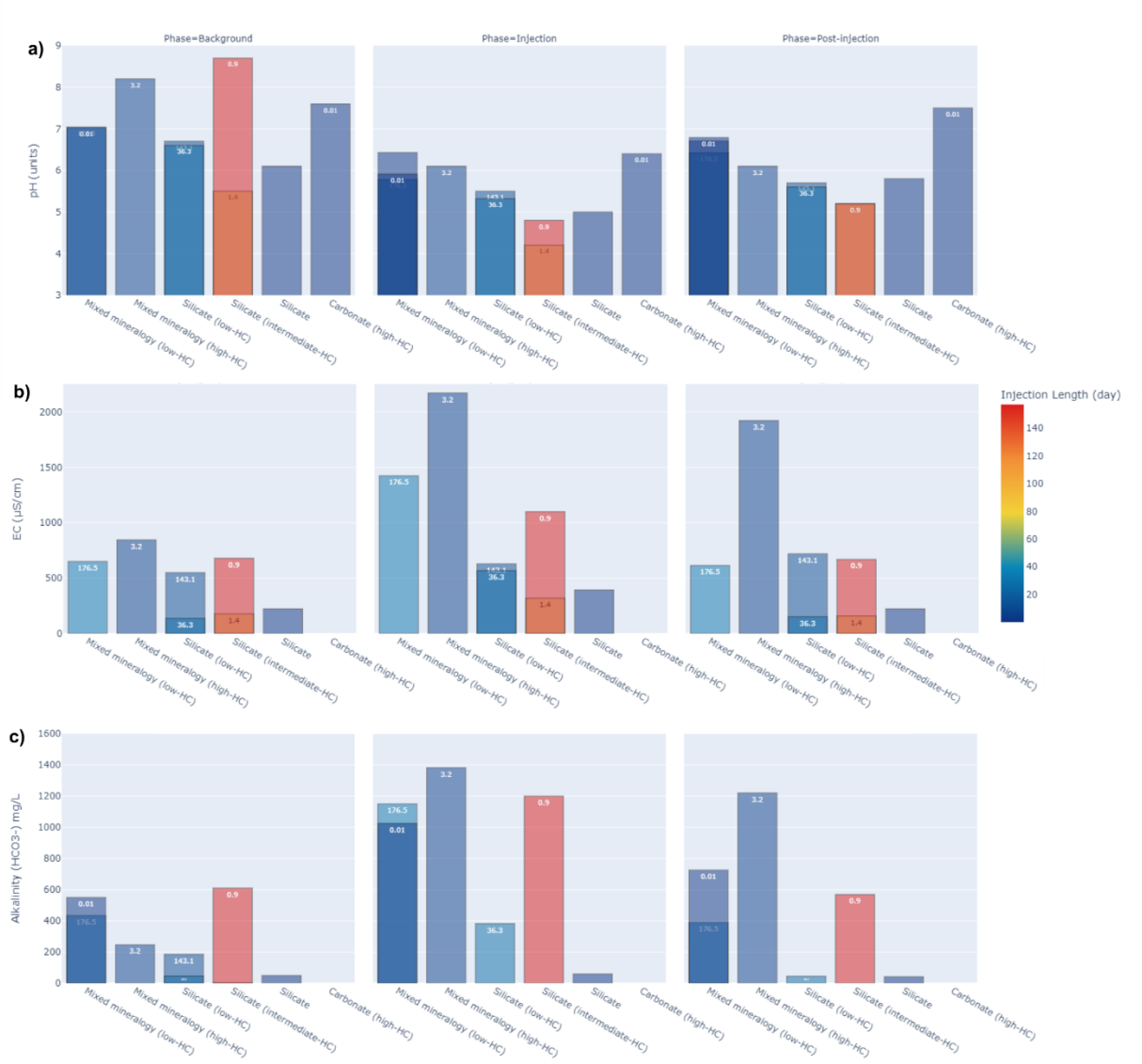

Figure 4. 5. *Observed physicochemical changes for pH (a), EC (b) and alkalinity (c) from background to post-injection considering both injection length (days) and average leaked normalized by average hydraulic conductivity (kg of CO_2/m). Bar colors represent injection length and numbers inside the bars symbolize kg of CO_2/m.*

Conversely, EC has been seen to increase at least 15%, but surpassed >100% in some cases, with a median value of 295 µS/cm. Greatest increases were noted in mixed mineralogy aquifer types, both with low and high-HC, irrespective of amount of CO_2 (kg)/m (Figure 4.5b). Although, one case of silicate (low-HC) aquifer type (EIT/KOR) also showed a great increase in EC (ΔEC=309%), not observed in other aquifers of the same type. This change is probably related to a larger amount of cations release from the aquifer framework (which has higher CEC and larger

percentage of clay minerals), as suggested by the authors. EC did not change much in silicate (intermediate-HC) aquifer types even tough exposed to CO_2 for longer time.

Alkalinity (here adjusted to mg/L of HCO_3^-) has shown an overall increase because of CO_2 injection, from as little as ca. 20% increase in rich silicate aquifers (+ 10 mg/L) up to 460% (+ 1,135 mg/L) rise in mixed mineralogy (high-HC) aquifers (Figure 4.5c). An average value of relative increase of 589.1 mg/L HCO_3^- was calculated, showing that most sites experienced a significant positive response for this parameter. In this case, even though longer injection length helped alkalinity to increase in silicate (intermediate-HC) aquifers in comparison to short-lived experiments in silicate (low-HC) aquifers, greatest changes are clearly related to mixed-mineralogy aquifer types, indicating a more significant role of mineralogy.

After CO_2 injection stopped, in most cases pH demonstrated a clear pattern of returning to values of background conditions, although it remained low in some cases of mixed mineralogy (high-HC) and silicate (intermediate-HC) aquifers, indicating a more persistent acidic condition (though post-injection monitoring lasted only a few days and recovery to background could not be observed). EC followed the same behavior, but in some mixed mineralogy (high-HC) and silicate (low-HC) aquifers the parameter remained at least hundreds of µS/cm above background values, suggesting different capacity to dilute the ionic content and to renew the groundwater in the aquifer.

Dissolved oxygen measurements in Vrøgum/DEN (intermediate-HC silicate aquifer) showed a decrease from approximately 7.9 to 5.5 mg/L (2.4 mg/L reduction), and TDS monitored in ZERT/USA (low-HC mixed mineralogy aquifer) followed the same pattern of EC for that case. Dissolved oxygen in Vrøgum/DEN exhibited a gradual return to background values as the CO_2 plume dispersed, and even a final minor increase (approx. 1.1 mg/L) in comparison to initial situation after more than 250 days since injection ended.

These physicochemical changes could also be related to the amount of CO_2 dissolved in groundwater, as the experiments were carried out in different depth conditions. Nonetheless, analyzed data do not show a clear relationship between pH, EC and alkalinity changes (ΔpH, ΔEC and ΔAlkalinity, respectively), kg of CO_2/m and depth (Figure 4.6). As can be seen, the highest changes are related to low amount of CO_2/m regardless of depth and are mainly linked to mixed mineralogy (high-HC) and

silicate (low-HC) aquifer types. Average amount of CO_2 (kg)/m seems to play a limited role, indicating that a larger injected CO_2 mass in a low hydraulic conductivity aquifer do not necessarily promote significative physicochemical alteration.

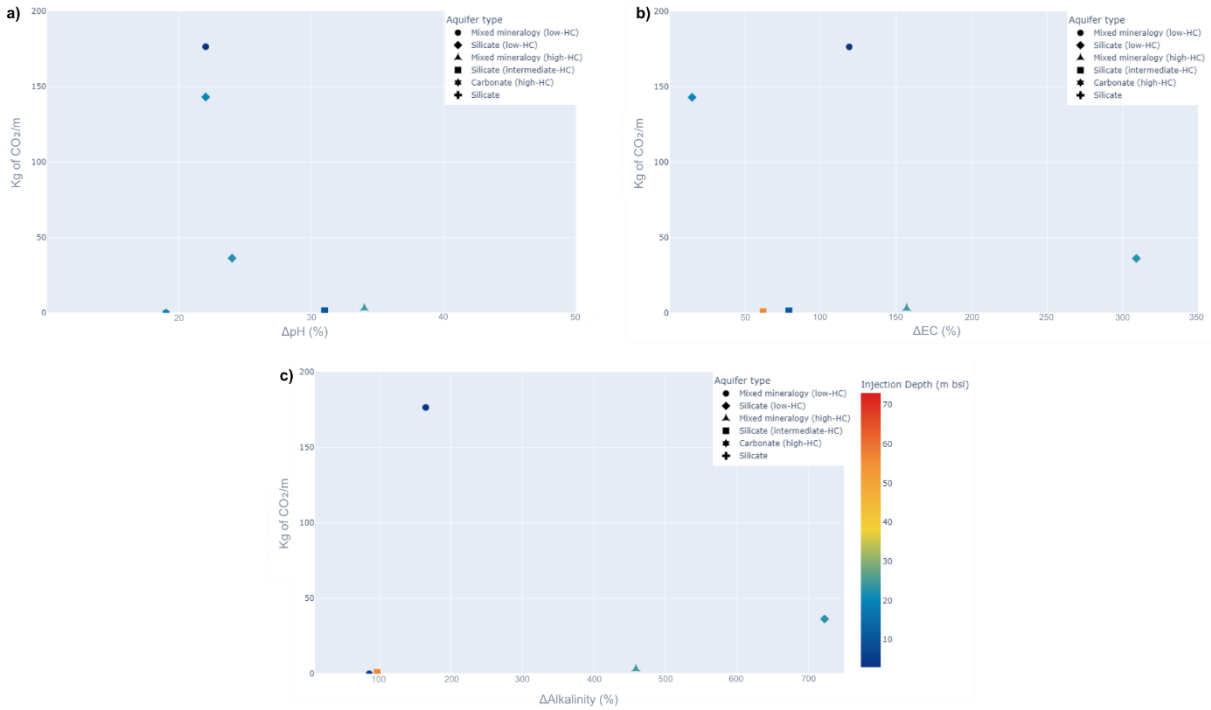

Figure 4. 6. *Observed relative physicochemical changes for pH (a), EC (b) and alkalinity (c) from background to injection considering both injection depth (m bsl) and average leaked normalized by average hydraulic conductivity (kg of CO_2/m) in each aquifer type.*

Among major ions, Ca and Mg were the only ones quantified in all nine experiments, followed by Na, K, Cl^- (eight experiments), SO_4^{2-} (six experiments) and NO_3^- (four experiments). Regarding minor elements, Mn, Fe, Si, Sr and Ba were completely tracked in at least five sites, rendering valuable data about the geochemical behavior in each experiment. On the other hand, as far as trace elements are considered, eleven elements were thoroughly traced from background to post-injection in at least three studies. In order of appearance, Al (6 studies), As and Zn (5 studies), B, Co, Cr, Cu and Pb (4 studies), and Mo, U and Ni (3 studies) were included in this paper to evaluate the tendency in each case. Although more chemical elements were measured in some cases, the analysis in this paper only included those whose concentration in groundwater was measured in at least three field tests, with data representative of each phase (background, injection and post-injection).

Table S1 brings all the information with respect to representative wells or sample points where groundwater was analyzed in every study, as well as the number of sampled events for each experiment phase and the literature reference used to extract the data. In all cases, observed numbers represent concentrations at the nearest groundwater monitoring well or at the same injection well in the case of push-pull tests. As only one value is shown for each phase, background values are usually a calculated or indicated average, while the injection values are regarded as the highest alteration from background for that parameter and post-injection values generally represents an indicative value of the parameter when it reaches a steady state condition. Nonetheless, when the element shows an irregular behavior in post-injection recovery, its median was chosen to characterize it. Additionally, values below informed detection limits (DL) were calculated as DL/2.

In this situation, at least three behaviors can be observed: (1) pulse-like, when elements increase during injection and then decrease and usually return to background levels during post-injection; (2) unaffected/negligible change, when elements remain practically unaltered or experienced insignificant change during all phases of the experiment; and (3) irregular, when elements show a combination of behaviors (pulse-like, unaffected and persistent increase/decrease) depending on the study in case.

4.3.5.1 Pulse-like behavior

Divalent cations such as Mg, Ca, Ba and Sr, and also Si (to a lesser extent), exhibited the same pulse-like trend (with few exceptions for silicon), where element concentration in groundwater increased from background to injection in a similar manner as pH decreased and EC/Alkalinity increased. This pattern is observed to happen regardless of experiment length, amount of CO_2/m or aquifer type (Figure 4.7). However, compared to mixed mineralogy aquifer types, in silicate aquifer types (both low and intermediate-HC) this effect is less pronounced, but occurred in short-lived and long-lived experiments.

On average, concentration of these elements increased 189% from background to injection, and then decreased 30% from injection to post-injection. Besides, post-injection values remained on average 45% above background, showing that the concentration of these elements stayed a little higher than their original for at least

the duration of the post-injection monitoring (although the number of sampling events and the frequency of it during injection campaigns are completely heterogenous and could potentially influence this analysis).

Co, Cr, Ni and Zn are the trace elements that also showed this trend. On average the concentration increase from background to injection was 1,312%, while it decreased 65% in post-injection relative to the injection phase, but remained 288% above natural background values during post-injection. Nonetheless, this high increase during post-injection relative to background was biased due to persistent presence of Co, Ni and Zn in the CO_2 Field Lab/NOR experiment. If this value is ruled out, the average goes down to 39%, which is more consistent with the other cases.

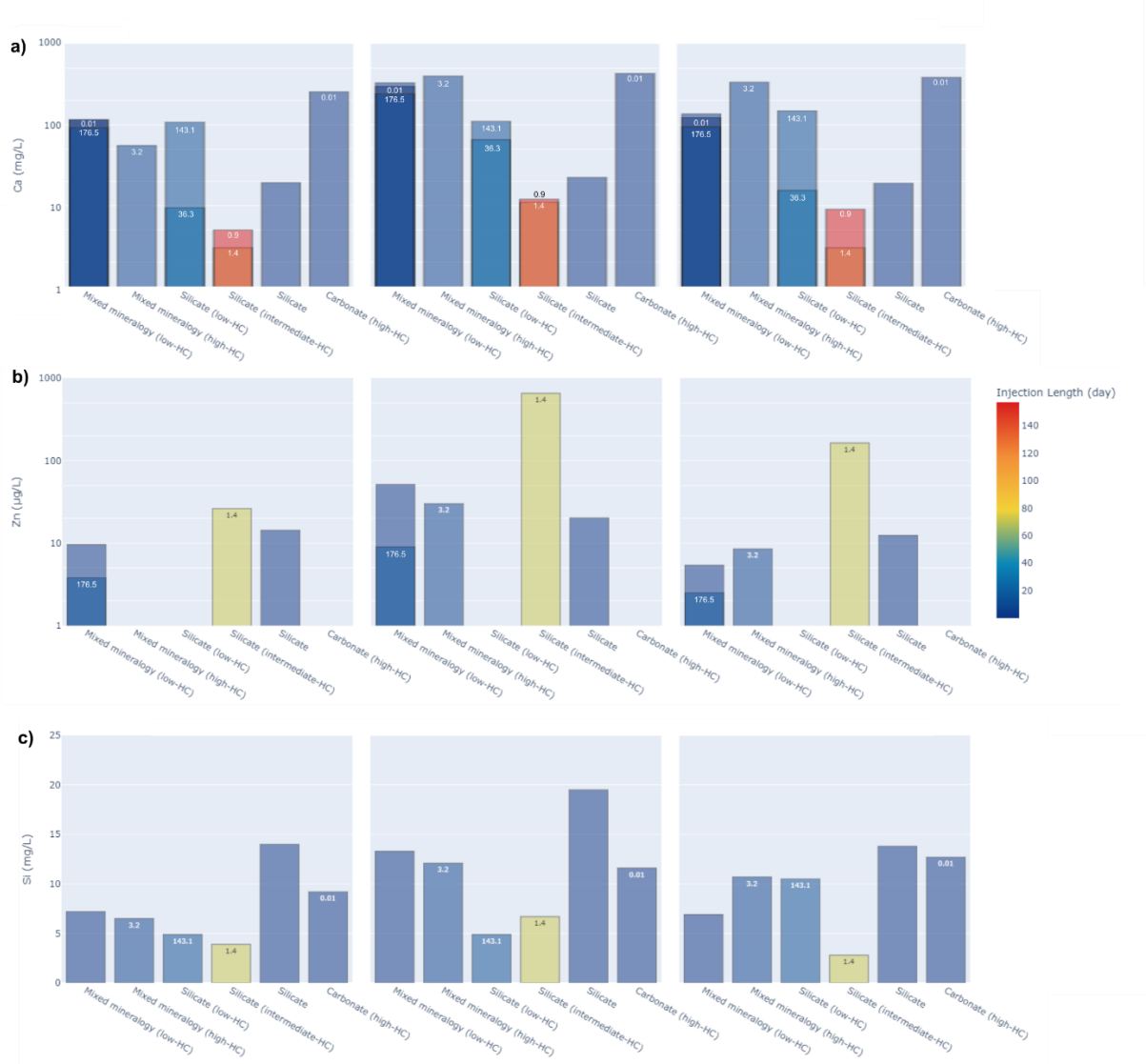

Figure 4. 7. *Example of three elements with a pulse-like behavior from background to post-injection in different studies: a) Ca (mg/L); b) Zn (µg/L); and c) Si (mg/L). Bar colors represent injection length (days) and numbers inside the bars symbolize kg of CO_2/m.*

4.3.5.2. Unaffected/negligible change

Ions like K, Cl^- and to a lesser extent SO_4^{2-} were generally unaffected or showed insignificant variation in response to CO_2-groundwater-mineral interaction (Figure 4.8), except for the mixed mineralogy (high-HC) aquifer type represented by the CO_2 Field Lab/NOR experiment (and for K in one mixed mineralogy low-HC aquifer - ZERT/USA). On average, groundwater concentration of these elements and compounds increased only 21% during injection in relation to background, and then decreased just 0.4% from injection to post-injection. Moreover, post-injection values stayed on average ca. 1% above background, evidencing that these chemical species are less prone to significant changes when the general trend of all performed studies are considered.

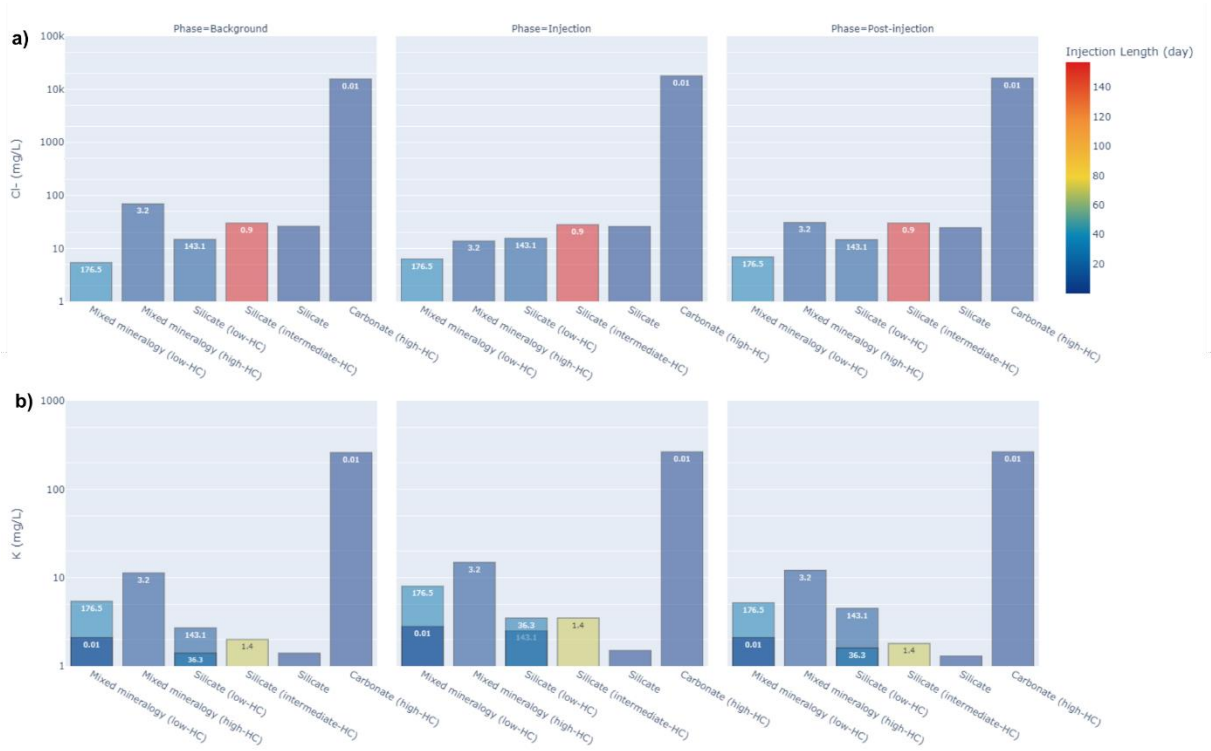

Figure 4. 8. *Concentration variation of two chemical species with an unaffected or negligible change behavior from background to post-injection in different studies: a) Cl^- (mg/L); and b) K (mg/L). Bar colors represent injection length (days) and numbers inside the bars symbolize kg of CO_2/m.*

4.3.5.3. Irregular pattern

The majority of the elements tracked in the experiments revealed an irregular behavior before, during and after injection, that seems to be site-dependent (Figure

9). Major and minor ions such as Na, NO_3^-, Fe (total) and Mn have all shown increasing/decreasing pulse-like, unaffected, or continuous increasing/decreasing trends considering different groups of experiments. For example, in mixed mineralogy (low-HC) aquifer types Na showed a slightly pulse-like increase, resembling the behavior of the first category elements. However, in mixed mineralogy (high-HC) aquifer type Na exhibited a pulse-like decrease, following a similar tendency for Cl^- in the CO_2 Field Lab/NOR field test. In other aquifer types such as silicate (low-HC) and carbonate (high-HC) this parameter remained almost unchanged (Figure 4.9a).

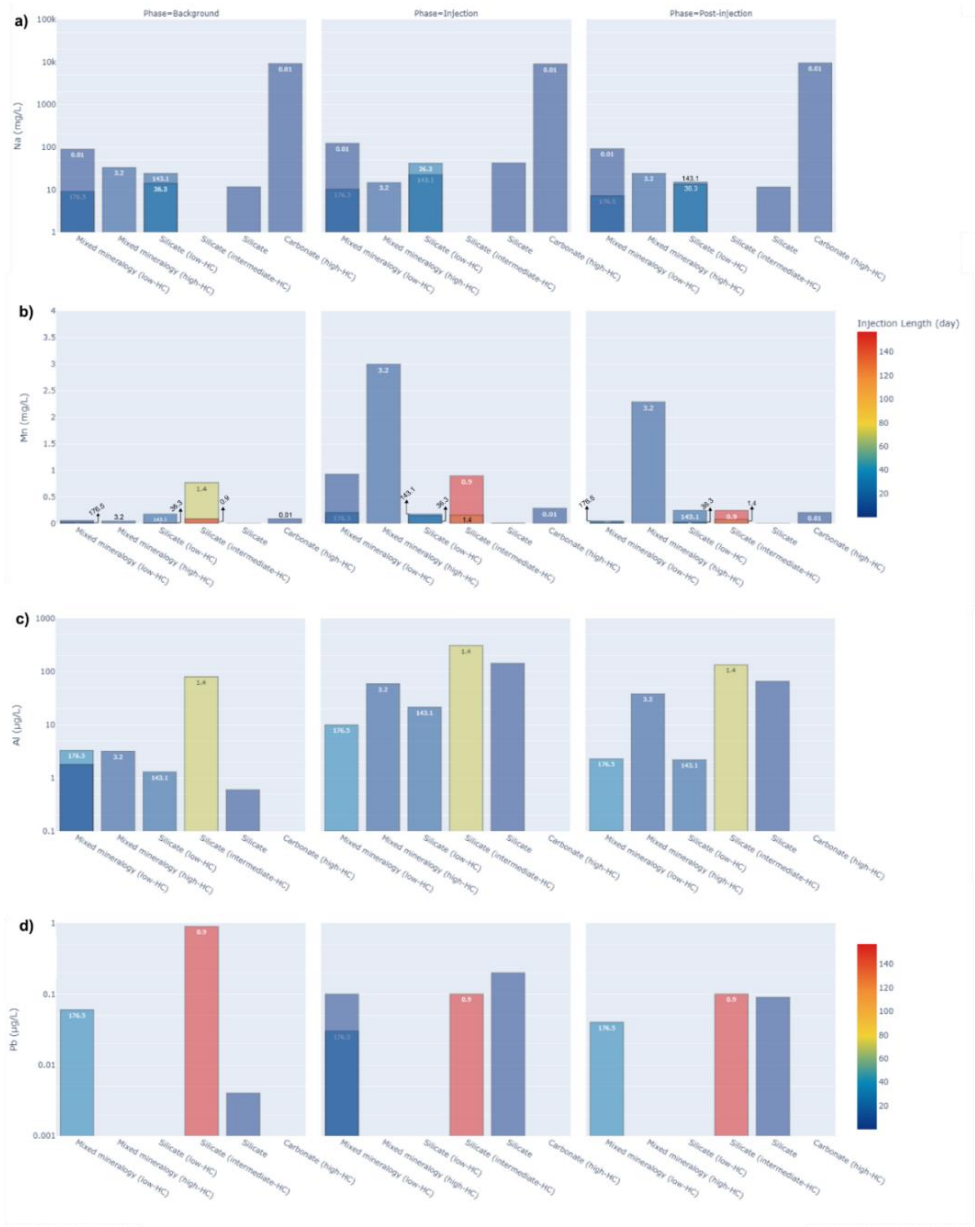

Figure 4. 9. *Concentration variation of four elements with an irregular behavior from background to post-injection in different studies: a) Na*

(mg/L); b) Mn (mg/L); c) Al (µg/L); and d) Pb (µg/L). Bar colors represent injection length (days) and numbers inside the bars symbolize kg of CO_2/m.

Complementarily, Mn also revealed a complex pattern. In mixed mineralogy (high-HC) Mn concentration showed a sharp pulse-like trend, while in one experiment conducted in a silicate (intermediate-HC) aquifer its value decreased during injection and stayed low even after a long period of post-injection monitoring, whereas in other it also increased following a pulse-like trend. In silicate (low-HC) aquifer it remained unaffected during injection but experienced a slightly increase in post-injection phase (Figure 4.9b).

As far as trace elements are regarded, Al, As, B, Cu, Mo, Pb and U comprise the rest of the tracked hydrogeochemical parameters. Among these, Al represents the most complex behavior – while in one mixed mineralogy (low-HC) aquifer type experiment its concentration has experienced a persistent decrease (0.1 µg/L in the graph), in other it has demonstrated a more pulse-like pattern. Besides, in mixed mineralogy (high-HC), silicate and silicate (intermediate-HC) aquifer types it clearly exhibited a persistent increase (Figure 9c).

As another example, Pb also showed an intriguing behavior. In silicate (intermediate-HC) and mixed mineralogy (low-HC) aquifer types it displayed a decrease during injection and post injection, but in other silicate aquifer type (Cranfield/USA) its concentration increased during the same phases, clearly indicating a contrasting evolution due to CO_2 reaction with groundwater (Figure 9d). For the full list of groundwater chemical concentration measurements and trends during all phases of the experiments see Table S1.

4.4. Hydrogeochemical mechanisms

Dissolved elements in natural waters may be present as different chemical species such as cations, anions, neutral molecules or complexes (KORETSKY, 2000), which can undergo a series of process or reactions such as aqueous speciation, ion exchange, surface complexation (sorption and desorption) and mineral dissolution/precipitation that are responsible for different mechanisms of groundwater geochemical alteration (CAHILL, 2013). In the context of CCS, the CO_2-induced hydrogeochemical changes are fundamentally related to the acidification of the

solution as a result of increased CO_2 partial pressure (pCO_2) in groundwater, causing the equilibrium of the carbonate system to shift to new conditions (Figure 4.10).

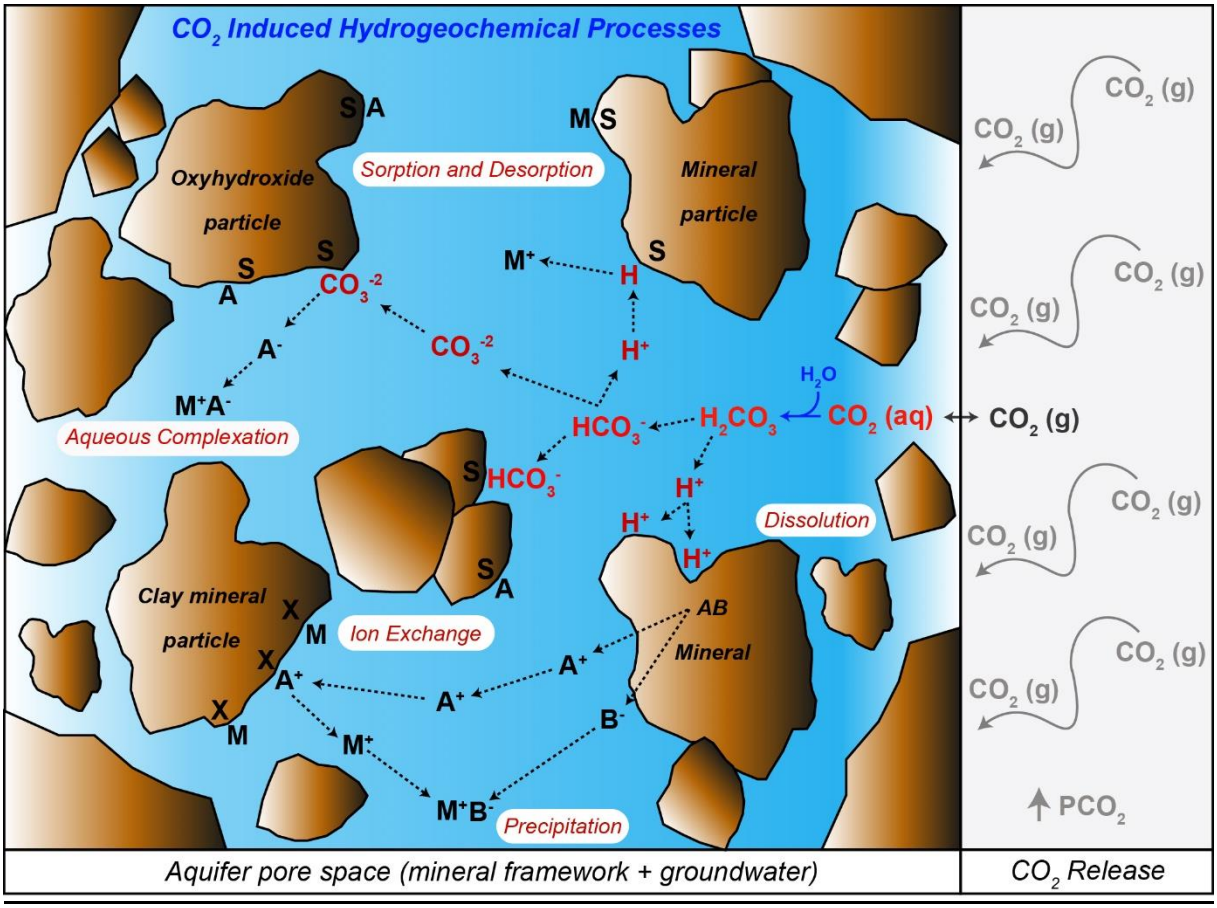

Figure 4. 10. *Hydrogeochemical mechanisms related to induced higher pCO_2 as a result of CO_2 release in the aquifer. Modified from* Cahill (2013).

All these processes are more pronounced in aquifers with reactive minerals, especially in those whose composition include carbonate minerals (e.g., calcite and dolomite), clay minerals, amorphous iron, manganese and aluminum oxyhydroxides, colloidal particles and organic matter, which possess high electrostatic charges on their surfaces (CLARK, 2015a). As previously mentioned in this paper, almost all analyzed sites have some degree of reactive materials (except at Wittstock/GER) that contributed to the observed hydrogeochemical changes.

4.4.1. Ion exchange

Ion exchange processes, which represent a class of reversible chemical reactions wherein an ion from a solution is exchanged for a similarly charged ion attached to a solid particle, are largely controlled by hydroxyl ions coordinated with Si, Al or Fe

cations, that gives a negative electrostatic potential to the surface that can be explored by protons and cations (CLARK, 2015a). As these species are weakly bonded, they can be displaced by other cations that have a greater electrostatic charge or are more concentrated in the aqueous solution, for example. The capacity of each cation to attach to a charged surface depends on their selectivity coefficient. In this case, cations with greater charge and smaller hydrated radii will exhibit a superior tendency to attach onto a particle surface and expel to the solution the ions previously adsorbed. According to Merkel & Planer-Friedrich (2008), the order of selectivity for adsorption is (in decreasing intensity): $Ba^{2+}>Sr^{2+}>Ca^{2+}>Mg^{2+}>Be^{2+}/Cs^{+}>K^{+}>Na^{+}>Li+$. Hence, divalent cations tend to attach more easily than monovalent ones, except for H^{+}. Due to its elevated charge density and small atomic radius, this element is preferably attached to surfaces.

In the context of the analyzed studies, during the injection phase, CO_2 (g) is rapidly hydrated to form carbonic acid (H_2CO_3), which in turn dissociates to form bicarbonate ions (HCO_3^-) by releasing H^+ to the solution, reducing its pH. As more protons become available, H^+ tends to migrate towards the surface of mineral particles, attaching to them and releasing back to solution any cations hitherto adsorbed. Considering the data presented here, concentration of Mg, Ca, Ba and Sr increased in almost all cases where the pulse-like behavior has been observed, even in those silicate-dominated with the presence of clay minerals, and whose carbonate minerals are absent or nearly undetected (Table 3).

As can be seen in Figure 7, this behavior is observed regardless of aquifer type, experiment duration or amount of CO_2/m, indicating that a similar geochemical mechanism (ion exchange processes) could be controlling this response. However, in the case of mixed mineralogy and carbonate aquifer types, the increase magnitude is higher than those observed in the free-carbonate silicate (low and intermediate-HC) aquifer types, suggesting that an additional (or prevailing) geochemical process such as carbonate dissolution is significant. Moreover, considering the slow dissolution kinetics of silica (Appelo & Postma, 2005; Hem, 1985; Lasaga, 1984), increased concentration of Si noted in practically all studies where this parameter has been tracked is most likely explained by Al^{3+} substitution in easily accessible sites (e.g., tetrahedral sheet in clay minerals). An indicative proof of this process is that average

percentage increase of Mg, Ca, Ba and Sr from background to injection phase was calculated to be 189%, while for Si this value was 51%.

Na and K also participate in the cation exchange process, especially in the silicate-dominated aquifer types (Figure 4.9a and Figure 4.8b), usually increasing during CO_2 injection as the result of a weaker interaction compared with divalent cations (HEM, 1985a). Even so, their concentration variation during the experiments was found to be one order of magnitude lower than that of other cations, suggesting a highly competing cationic process. In the silicate aquifer types of Cranfield/USA and EIT/KOR, and one mixed mineralogy (low-HC) aquifer type (Brackenridge/USA), sodium and potassium increased more than other sites, which made the authors suggest that some degree of mineral dissolution of plagioclase (specially albite) and K-feldspar detected in the aquifer mineral framework could be happening (Yang et al., 2013, 2014). In the carbonate aquifer type (SIMEX-Maguelone/FRA) and in one mixed mineralogy (high-HC) aquifer (CO_2 Field Lab/NOR) Na decreased, indicating another geochemical mechanism. A possible explanation of this will be detailed in the next section, as it is more related to sorption processes.

4.4.2. Sorption and desorption

Sorption and desorption process, unlike ion exchange, remove ions from solution without releasing other ions back in equivalent proportion, and the mineral surface charge can be either positive or negative depending on the pH and the solution composition (APPELO; POSTMA, 2005). Most clay minerals have a permanent negative charge due to isomorphous substitutions or vacancies in their structure (BERKOWITZ; DROR; YARON, 2014a), hence favoring adsorption of positively charged ions, while Al, Fe, Mn, and Si oxides and hydroxides are considered amphoteric materials, meaning they have no permanent surface charge. Therefore, these solid solutions have different affinities for H^+ and OH^- ions and thus exhibit various points of zero charge (PZC).

In this framework, the PZC is associated to certain pH intervals, and each mineral has its own specific range. For example, K-feldspar and albite have pH_{pzc} between 2.0-2.4, while clay minerals like kaolinite and montmorillonite exhibit pH_{pzc} around 2.0-4.6, whereas in Al/Fe/Mn oxyhydroxides pH_{pzc} usually ranges from more than 7 up to 9.4 (CORNELIS et al., 2014). Based on this, when the solution pH is higher than the

pH_{pzc} of the mineral, surface particles tend to adsorb cations, and when the solution pH is lower than the pH_{pzc} of the mineral, surface particles are prone to adsorb anions. As the pH of background groundwater in the analyzed field experiments varied from 5.5 to 8.7, it is likely that K-feldspar, plagioclase, kaolinite, illite, smectite and other clay minerals observed in various sites were responsible for adsorbing cations or positively charged complexes in their surfaces.

On the other hand, Al/Fe/Mn oxyhydroxides reported in some studies might control the adsorption of anions or negatively charged complexes from solution, even though in some of them (Jackson County-Escatawpa/USA, SIMEX-Maguelone/FRA and CO_2 Field Lab/NOR) background groundwater showed a pH > 7, meaning that some Al/Fe/Mn oxyhydroxides could also be adsorbing cations or positively charged complexes, instead of anions. When pH reached values lower than 6.5 during the injection phase, and even below 5 in some cases, these ions and complexes had to adapt to new acidic conditions, forcing some elements to desorb or others to adsorb. Metals (notably heavy metals) are usually controlled by this geochemical mechanism and tend to be desorbed from particle surfaces when pH reach lower values (Appelo & Postma, 2005).

This behavior has been clearly observed in both mixed mineralogy (low and high-HC) and silicate aquifer types for As, Cr, Co, Ni and Zn (and to a lesser extent for U), as can be check on Table S1, where concentration of these elements achieved a maximum during injection and then returned to background values afterwards. As arsenic occur as $As(OH)_{3(aq)}$ or negatively charged complexes ($H_2AsO_4^-$ or $HAsO_4^{2-}$) at pH between 5-7 and oxic conditions (TAKENO, 2005), we assume that it is most likely that this element had been released to solution from oxyhydroxides in most cases, except from the abovementioned cases where oxyhydroxides could potentially be adsorbing cations.

Additionally, since Co, Ni and Zn occur exclusively as positively charged free species (CO_2^+, Ni^{2+} and Zn^{2+}), while Cr have both positive free species (Cr^{3+}) and complex form ($CrOH^{2+}$), and U appears mainly as positive complexes (UO_2^+, UO_2^{2+} and UO_2OH^+), we consider that it is plausible to assume that the desorption of these ions and complexes has occurred from K-feldspar, plagioclase or most likely from clay minerals. As an example of how species can affect the behavior of the elements, Zheng et al. (2012) pointed out that arsenic species usually compete for sorption

sites, with $H_2AsO_4^-$ usually adsorbing as pH drops, whereas $HAsO_4^{2-}$ tending to be desorbed when carbonate (CO_3^{2-}) is adsorbed, leading to a net effect that can demonstrate either a desorption or adsorption of As.

On the other hand, the observed irregular patterns for Al, B, Cu, Fe, Mn, Mo and Pb (Figure 4.9 and Table S1) variations difficult the establishment of a unique and clear explanation for this group of elements, in part due to the absence of clearly demonstrated analytical detection limits for some cases. Table 4.5 shows a simplified view of the relative changes from background to CO_2 injection for these elements in the analyzed experiments.

Table 4. 5. *Apparent relative change of element concentration in groundwater from background to CO_2 injection in each field experiment, as reported in the original papers.*

↑ ***Pb***	↓ ***Pb***	↑ ***Mn/Fe***	↓ ***Mn/Fe***	↑ ***Cu***	↓ ***Cu***
Cranfield/USA	*Jackson County-Escatawpa/USA*	*All others*[a]	*Vrøgum/DEN*	*Cranfield/USA*	*Jackson County-Escatawpa/USA*
	ZERT/USA			*Brackenridge/USA*	*ZERT/USA*
↑ ***Al***	↓ ***Al***	↑ ***Mo***	↓ ***Mo***	↑ ***B***	↓ ***B***
All others	*Brackenridge/USA*	*Cranfield/USA*	*ZERT/USA*	*Brackenridge/USA*	*CO_2 Field Lab/NOR*
			Brackenridge/USA	*ZERT/USA*	
				Cranfield/USA	

[a] *Fe remained apparently stable at Wittstock/GER.*

According to pH-pe diagrams (TAKENO, 2005) and considering all field experiments conditions analyzed here, Pb occurs both as free species (Pb^{2+}) and forming a complex ($Pb(OH)^+$), Fe, Mn and Cu possibly appears exclusively as Fe^{2+}, Mn^{2+} and Cu^{2+}, as Fe^{3+} and Mn^{4+} is most common in highly oxidizing states or under alkaline pH, respectively, which is not the case of the analyzed studies. Molybdenum, on the other hand, is found as MoO_4^{2-} and MoO_4^- and B as $B(OH)_3$ (aq).

Sorption and desorption of Pb and Cu are related to both the relative chemical bond's strength with respect to different sorbent materials and the competition with H^+ under more acidic conditions. For instance, Cu is more strongly attached than Pb in clay minerals, hence it can be assumed that in clay-rich aquifers Pb can be more easily desorbed from these minerals than Cu, making its presence in the solution more pronounced. The opposite happens when Fe/Mn oxyhydroxides, organic matter and humic/fulvic acids are present in the aquifer. Under these circumstances, Pb is

more strongly attached than Cu, leaving Cu to be easier desorbed than Cu (Merkel & Planer-Friedrich, 2008).

Nonetheless, Pb and Cu are normally desorbed as pH decreases (Appelo & Postma, 2005; Fetter, 1992), thus its concentration reduction at ZERT/USA and Jackson County-Escatawpa/USA (mixed mineralogy and silicate low-HC, respectively, in Figure 9d) is intriguing, and no straightforward explanation is envisioned. One possible reason we envision is that they could be adsorbed onto colloidal-sized metal hydroxides and, as the hydroxide moves through the aquifer as a colloidal particle, both Pb and Cu would also move with groundwater flow, reducing its concentration at the sampling points.

Molybdenum has a different behavior in relation to most heavy metals in soils (GOLDBERG et al., 2007). Under increasing acidic conditions MoO_4^{2-} adsorbs on amorphous Al and Fe, decreasing its concentration in solution. In this situation, Mo is more tightly bound to Fe oxide than to Al oxide, which could explain its behavior in both mixed mineralogy (low-HC) aquifer types of ZERT/USA and Brackenridge/USA. Nonetheless, in the silicate aquifer of Cranfield/USA, Mo and B are highly correlated to Ca (correlation coefficient >0.9), which according to Yang et al. (2013) may suggest that both elements can be associated with carbonate dissolution, even though these minerals were not detected using XRD and SEM analysis.

Boron is an accessory constituent of biotite, amphiboles (Hem, 1985) and occur in many types of clay-rich marine sediments (BUTTERWICK; DE OUDE; RAYMOND, 1989). Besides, as the more important boron dissolved species are anionic or uncharged, its adsorption on other mineral surfaces is unlikely. Hence, we assume that a possible reason why B increased in the mixed mineralogy (low-HC) aquifer type of ZERT/USA could be tied to the dissolution of already altered biotite, but its increase in the mixed mineralogy (low-HC) aquifer type of Brackenridge/USA and the silicate aquifer of Cranfield/USA might be linked to other mechanisms, as biotite or amphibole are not present. In these cases, we believe that B could be dissolved under more acidic conditions from borate salts present in the aquifer pore-space (STAMATAKIS; TZIRITIS; EVELPIDOU, 2009). In the mixed mineralogy (high-HC) of the CO_2 Field Lab/NOR, B concentration decreased during CO_2 injection, revealing a surprising effect. This is because even though dissolved boron can be partly removed by adsorption on the aquifer matrix (NÉGREL et al., 2012), Goldberg et al. (2000) demonstrated that under increasing acidic environment B is expected to desorb, not

the opposite. Hence, B behavior in the mentioned case is unclear and still a matter of debate.

Sorption and desorption of Na can also play a significant role in the distribution of this species, having a different behavior in saline groundwaters, as is the case of CO_2 Field Lab/NOR and SIMEX-Maguelone/FRA. At both cases, Na has been seen to decrease under more acidic conditions, contrasting with the trend observed in freshwater aquifers. Based on a PHREEQC modeling study, Humez et al. (2014) suggested that Na is the predominant cation fixed on the exchanger after the sudden salinity rise. In this case, when salt water displaces freshwater in an aquifer, an exchange of cations takes place and Na is taken up by the exchanger while Ca is released. According to these authors, this reaction is reversible during a freshening phase, explaining why after CO_2 injection and a slightly salinity decrease, Na started to recover to its background concentration or even increased.

Therefore, we can see that sorption and desorption affected aquifer types differently with no clear distinction of geochemical behavior in relation to a higher amount of CO_2/m or injection length. Instead, it seems that the aquifer mineralogy (specially clay minerals and some oxyhydroxides) and the physicochemical characteristics of the groundwater majorly control the process that can develop heterogeneously according to each site.

4.4.3. Silicate and carbonate dissolution

Dissolution of silicate minerals is a slow process (Appelo & Postma, 2005; Lasaga, 1984) and because of this, aquifers in silicate rocks are more prone to acidification, as minerals are not able to counter-balance pH decrease, and geochemical reactions occurs incongruently. Thus, increased acidification due to CO_2 release tend to increment chemical weathering, favoring ions to be released to groundwater. This process follows the Goldich sequence (GOLDICH, 1938), where olivine, augite, hornblende, biotite and plagioclase have a higher tendency to dissolution than K-feldspar, muscovite and quartz.

Even so, as the dissolution kinetics of the most unstable of them still requires some thousands of years of action (Lasaga, 1984), its unlike that dissolution of these primary minerals played a significant role in the analyzed studies where silicate minerals are dominant in the aquifer. In fact, dissolution of clay minerals (kaolinite,

chlorite, muscovite, smectite and illite), which have faster dissolution kinetics (CAMA; GANOR, 2015), reported in almost all studies at varying proportions and even poorly crystalline Al/Fe/Mn oxyhydroxides are undoubtedly more important considering the length of the experiments. Nonetheless, partial dissolution of more unstable primary minerals is not totally discarded.

Under oxidizing environment settings of the investigated shallow aquifers, Fe and Mn have seen their concentration increase significantly in groundwater in almost all aquifer types (Figure 4.9b and Table S1), except in the silicate (low and intermediate-HC) aquifers of Wittstock/GER and Vrøgum/DEN. At ZERT/USA, Fe could reflect dissolution of several Fe(II) and Fe(III) minerals, including siderite and ferrihydrite (GUPTA; YADAV, 2020a), but according to Kharaka et al. (2010) it most likely caused by dissolution of iron oxyhydroxides. At Jackson County-Escatawpa/USA, a dissolution model including illite, Fe-smectite, ferrihydrite (as Fe(OH)3(s)) and amorphous iron sulfide (mackinawite, FeS(m)) was developed by Trautz et al. (2013), and the results indicated a good agreement with field data, supporting the argument that Fe could be dissolved from these mineral phases. Additionally, Mn followed the same behavior at both sites, indicating a similar process.

Even tough in the aquifers of Brackenridge/USA, CO_2 Field Lab/NOR, Cranfield/USA, EIT/KOR and SIMEX-Maguelone/FRA the authors have not explicitly discussed possible origins for Fe and Mn increase, it is reasonable to assume that considering the similar behavior observed in the other studies, both elements are related either to oxyhydroxides dissolution or carbonate dissolution (as Fe and Mn are sometimes also present as impurities in calcite and dolomite). Differently than the other species, Fe and Mn concentration in Wittstock/GER showed very little or practically no alteration. As the authors have also not clearly showed mineralogical data or even discussed this chemical behavior, we presumably believe that Fe and Mn exhibited this trend because neither Fe/Mn-bearing clay mineral nor oxyhydroxide are present in the aquifer, and thus predominating a virtually inert mineralogy.

Nonetheless, Fe and Mn unexpectedly decrease during injection at Vrøgum/DEN. According to Cahill et al. (2014), targeted extractions of core samples after post-injection indicated an increase in elements related with amorphous and poorly crystalline Fe and Al oxides (mainly gibbsite), suggesting the precipitation of these

minerals as a likely mechanism for the decrease in dissolved concentrations in groundwater.

Aluminum concentration was shown to increase in all sites (Figure 9c and Table S1), except for Brackenridge/USA. Even though included in an exchange process with Si, as already cited, this mechanism alone could not explain the behavior of aluminum. Under the prevailing pH-pe conditions of the considered studies, Al must appear in solution predominantly as the anion $Al(OH)_4^-$ when pH > 6 (Hem, 1985; Takeno, 2005), the dominant condition of almost all background groundwaters (except at Vrøgum/DEN, pH = 5.5). As pH decrease during CO_2 injection, the prevalent species of Al become the cationic forms $Al(OH)_2^+$, $AlOH^{2+}$ and Al^{3+} (when pH < 4.8) and aluminum solubility starts to increase due to more acidic settings.

Cahill et al. (2014) pointed out that at Vrøgum/DEN, this pattern is most likely a result of dissolution of a microcrystalline or amorphous form of gibbsite, while Humez et al. (2014) explained that at CO_2 Field Lab/NOR, the saturation state of gibbsite remained at equilibrium/supersaturated, and hence attributed the Al increase to dissolution of K-feldspar and plagioclase (albite), showing a distinct behavior in silicate (intermediate-HC) and mixed mineralogy (high-HC) aquifer types. Yang et al. (2013) mentioned that the dominant dissolution of silicate minerals (without detailing which group) in the aquifer sediments elevated Al concentration in groundwater at Cranfield/USA. Operating geochemical mechanisms at ZERT/USA and Wittstock/GER, although not discussed by the original authors, are possibly related to some or all of these aforementioned processes considering their aquifer types category. On the other hand, Al decrease at Brackenridge/USA suggests some type of precipitation/adsorption mechanism still unclear and undiscussed by the authors.

Dissolution kinetics of carbonates are much faster than silicates (MORSE; ARVIDSON, 2002), and aquifers with calcite/dolomite present, such as the mixed mineralogy aquifers of ZERT/USA, CO_2 Field Lab/NOR and Brackenridge/USA, and the carbonate aquifer of SIMEX-Maguelone/FRA, showed a more pronounced response to increasing pCO_2 due to carbon dioxide injection. Although the presence of calcite is low at EIT/KOR (0.1 wt. %), Do et al. (2022) argued that this process is responsible for Ca, Mg, Sr and Ba increase as the concentration of these elements grew faster than SiO_2 and follow $Ca+Mg/HCO_3^-$ trendline consistent with calcite/dolomite dissolution.

Besides, calcite dissolution can also induce cation exchange as a result of Ca increase in solution, affecting the distribution of major species in groundwater (ZHENG et al., 2012a). Thus, we believe that this geochemical process is responsible for Mg, Ca, Ba, Sr and K increase at ZERT/USA and CO_2 Field Lab/NOR, although at SIMEX-Maguelone/FRA and Brackenridge/USA it majorly affected the response of Ca, Mg, Ba and Sr. However, the lack of Sr and Ba data for SIMEX-Maguelone/FRA hinders a more conclusive assumption.

4.4.4. Mechanisms regulating Cl^-, SO_4^{2-} and NO_3^-

Although Cl^- remained practically unaltered in most studies, due to its conservative nature, in two sites its behavior showed a different pathway. SO_4^{2-} also exhibited discrepant trends that do not seems to be related to any hydrogeochemical process mentioned earlier in this paper. For example, according to Humez et al. (2014), variations of SO_4^{2-} and Cl^- concentration observed at CO_2 Field Lab/NOR are not related to geochemical reactive mechanisms but to a conservative mixing of meteoric-derived groundwater and seawater (associated with CO_2 injection and subsequent flow through the aquifer), causing the dilution of both species, displayed as a concentration decrease during the experiment.

Furthermore, chloride concentration showed a different trend at SIMEX-Maguelone/FRA, increasing during injection and returning to the initial state immediately after the end of injection. According to Pezard et al. (2016), some desorption exchange with clay minerals may explain the chloride release during CO_2 injection due to acidification and promoting the clay particles decohesion as observed by Andreani et al. (2009; Berrezueta et al., 2013; Pèpe et al., 2010).

Additionally, NO_3^- and SO_4^{2-} increased concentrations observed at ZERT/USA, Cranfield/USA and Wittstock/GER were not investigated in the original papers but, as showed by Clark (2015), both anionic species are also generated by bacteria mediation through sulfide and ammonia (usually present in soils) oxidation process. In this case, although CO_2 injection can partially cause O_2 depletion by its removal from solution, depending on the CO_2 injection rate, this gas could also be acting as an oxygenation mechanism through physical bubbling of groundwater, and thus favoring NO_3^- and SO_4^{2-} production. Table 4.6 presents a qualitative summary of all discussions above.

Table 4. 6. *Summary of observed chemical species concentration patterns in groundwater and probable geochemical mechanisms responsible for their alteration in each analyzed study.*

Experimental site	***Aquifer type***	***Chemical species***	***Groundwater concentration trend***	***Geochemical process***
ZERT - Bozeman, MT (USA)	Mixed mineralogy (low-HC)	Mg, Ca, Ba, Sr and K	↑	Carbonate dissolution and induced Ca^{+2} ion exchange
		Cl	±	Conservative process
		NO_3^- and SO_4^{2-}	↑	H_2S and NH^{4+} oxidation (?)
		Mo	↓	Adsorption
		B	↑	Silicate dissolution
		Pb and Cu	↓	Unknown mechanism
		Fe, Mn	↑	Dissolution of siderite and ferrihydrite
		Na, K	↑	Ion exchange
		Al	↑	Most likely dissolution of silicate minerals
Wittstock - Brandenburg (GER)	Silicate (low-HC)	Mg, Ca, Ba, Sr and Si	↑	Ion exchange
		Cl^-	±	Conservative process
		NO_3^- and SO_4^{2-}	↑	H_2S and NH^{4+} oxidation (?)
		Fe, Mn	±	Practically inert mineralogy
		Al	↑	Most likely dissolution of some silicate minerals
		Na, K	↑	Ion exchange
CO_2 Field Lab - Svelvik Ridge, Oslo (NOR)	Mixed mineralogy (high-HC)	Mg, Ca, Ba, Sr and K	↑	Carbonate dissolution and induced Ca^{+2} ion exchange
		Cl^-, SO_4^{2-}	↓	Mixing process (dilution)
		Mn	↑	Dissolution of oxyhydroxides

		B	↓	Unknown mechanism
		Al	↑	K-feldspar and plagioclase (albite) dissolution
		Na	↓	Preferential adsorption (saline conditions)
Vrøgum (DEN)	Silicate (intermediate-HC)	Mg, Ca, Ba, Sr and Si	↑	Ion exchange
		Fe, Mn	↓	Precipitation of amorphous and poorly crystalline Fe and Al oxides
		Al	↑	Gibbsite dissolution
		K	↑	Ion exchange
SiMEX - Maguelone (FRA)	Carbonate (high-HC)	Fe (minor), Mn	↑	Dissolution of Fe-bearing clay minerals
		Mg, Ca	↑	Carbonate dissolution
		Si, K	↑	Feldspar and clay dissolution
		Cl	↑	Desorption (clays)
		Na	↓	Preferential adsorption (saline conditions)
Jackson County/Escatawpa - Mississipi (USA)	Silicate (intermediate-HC)	Mo	↓	Adsorption
		Cl^-	±	Conservative process
		Pb and Cu	↓	?
		Fe, Mn	↑	Dissolution of Fe-bearing clay minerals, oxyhydroxides and amorphous iron sulfide (?)
Brackenridge - Austin, Texas (USA)	Mixed mineralogy (low-HC)	Mg, Ca, Ba and Sr	↑	Carbonate dissolution
		Cu	↑	Desorption
		B	↑	Dissolution of borate salts (?)
		Fe, Mn	↑	Dissolution of Fe-bearing clay minerals and oxyhydroxides
		Al	↓	Unknown mechanism

		Na, K	↑	Ion exchange and mineral dissolution
Cranfield - Adams County, Mississipi (USA)	Silicate	Pb, Cu	↑	Desorption
		B and Mo	↑	Dissolution of borate salts (B) Carbonate dissolution
		Fe, Mn	↑	Dissolution of Fe-bearing clay minerals and oxyhydroxides
		Al	↑	Dissolution of silicate minerals
		Na, K	↑	Ion exchange and mineral dissolution
		Cl^-	±	Conservative process
		NO_3^- and SO_4^{2-}	↑	H2S and NH4+ oxidation (?)
EIT (KOR)	Silicate (low-HC)	Mg, Ca, Ba and Sr	↑	Carbonate dissolution
		Na and K	↑	Ion exchange
		Si and Mn	↑	Dissolution of silicate minerals

Symbology:

± indicate stable or a slightly increase/decrease;

↑ indicate concentration increase in groundwater; and

↓ indicate concentration decrease in groundwater.

4.5. Conclusions

Many CCS projects have historically failed to advance from conception to operation phase in part due to public perception about the technology. A common argument is that a possible leakage of CO_2 from storage reservoirs represent a primary risk and could potentially affect the groundwater quality of aquifers in the surrounding area of the project, usually a freshwater source for humans, animals and plants. Hence, all the efforts employed to develop the studies analyzed in this review are duly justified as they intended to demonstrate possible changes in shallow groundwater as a result of CO_2 presence in near-surface environment in the event of an unintended leakage.

Although some previous reviews have demonstrated some aspects of these studies, in this review the behavior of chemical elements, compounds and water quality parameters have been collectively gathered and related to each site-specific mineral composition, hydraulic parameters, mass of leaked CO_2, hydrogeochemical characteristics and CO_2 leakage time. Regarding this, at least three valid results were compared to each parameter analyzed, giving a more representative meaning about the interpretation. Taking that into account, groundwater alterations were framed into geochemical mechanisms most likely responsible for the processes.

After analyzing the integrated data from the selected studies, it was observed that:

(1) Ion-exchange is mainly responsible for short-lived increased concentration of Mg, Ca, Ba and Sr in almost all cases where the pulse-like behavior (sudden increase followed by a decrease during injection) has been observed, especially in the silicate-dominated aquifers with presence of clay minerals, and where carbonate minerals are nearly undetected or even absent. Na and K concentrations also suffered a mild response to increased CO_2 concentration related to cation-exchange in some cases, although weaker than observed with divalent cations.

(2) Sorption and desorption process were related to heavy metals and trace elements variations, being regulated by mineral composition of the aquifer, presumably due to the presence of Al/Fe/Mn oxyhydroxides and clay minerals. As these elements are sensitive to the groundwater pH (and to the pH_{pzc} of the minerals), they showed different patterns. As, Cr, Co, Ni and Zn (and to a lesser extent for U) achieved a maximum concentration during injection and then returned to background values afterwards. On the other hand, Al, B, Cu, Fe, Mn, Mo and Pb showed irregular patterns, and each response to CO_2 injection demonstrated a strongly dependence on mineral

composition of the aquifer, with clay minerals, oxyhydroxides and primary silicate most likely regulating each element through their own specific mechanism.

(3) Silicate and carbonate dissolution played different roles in each case, as aquifers in silicate background are more prone to persistent acidification and shows slower dissolution kinetics. Therefore, Fe, Mn and Al increase were related to dissolution of Fe-bearing clay minerals, gibbsite and ferrihydrite in some studies, and attributed to minor K-feldspar and plagioclase (albite) dissolution in others. Dissolution of carbonates on the other hand influenced a fast response of Mg, Ca, Ba, Sr and K (to a lesser extent) in some studies and potentially an Fe and Mn increase due to siderite dissolution in a particular case.

(4) Conservative mixing and oxidation processes were also pointed out as possible mechanisms regulating the response of Cl^-, SO_4^{2-} and NO_3^-. While Cl^- remained mostly unaltered in practically all studies, in those where it did change, authors argued that its behavior was not related to geochemical reactive mechanisms, but to a conservative mixing of meteoric-derived groundwater and seawater. Nonetheless, Cl^- desorption exchange with clay minerals was not discarded in one specific case. NO_3^- and SO_4^{2-} increased concentrations observed in three sites were not specifically discussed in the original papers, even though studies indicate that this trend could be potentially generated by bacteria mediation through sulfide (H_2S) and ammonia (NH_4^+) oxidation.

Overall, this review has shown how the collective learning at the field experiments conducted so far has advanced current knowledge of near-surface groundwater impact pathways framing them into the possible geochemical mechanisms, yet there are still some unknown processes and parameters that need to be further investigated. For instance, dissolved oxygen (DO) and oxidation-reduction potential (ORP) were poorly traced from background to post-injection, thus considerably affecting the interpretation of some redox sensitive elements' behavior. Isotope signature and dissolved gas composition are other parameters lacking properly measurement and further discussion. Moreover, although studies demonstrated that no parameter has exceed the freshwater potable limit, very few of them have been conducted over extended periods of time, most being very short-lived (a few hours or days). This could potentially affect how CO_2 leakage would manifest during long, persistent exposure to groundwater aquifer or soil dynamics. Hence, although fewer field experiments have

been carried out recently, further work is still needed for understanding the particular behavior of some elements in support for the development of relevant environmental legislation.

CAPÍTULO 5: Hydrogeological assessment and seasonal hydrogeochemical monitoring of the TECNOPUC-Viamão CO_2 controlled-release experimental site, Rio Grande do Sul state, Southern Brazil

*Esse capítulo foi publicado na revista '**Environmental Earth Sciences**'. Zielinski, J.P.T., Hamerski, F., Vecchia, F.D. et al. Hydrogeological assessment and seasonal hydrogeochemical monitoring of the TECNOPUC-Viamão CO_2 controlled-release experimental site, Rio Grande do Sul state, Southern Brazil. Environ Earth Sci 83, 459 (2024). https://doi.org/10.1007/s12665-024-11775-z*

Abstract: *Reduced-scale CO_2 release experiments in shallow aquifers serve as crucial monitoring strategies for detecting unintended CO_2 leakage into potable aquifers within Carbon Capture and Storage (CCS) projects. Understanding site-specific geological, hydrogeological, and climatic features is essential. However, accurately tracing changes in groundwater quality due to this process and using hydrochemical parameters for CO_2 leakage diagnosis require establishing a solid, seasonally relevant baseline to avoid misinterpretation. This study focuses on detailing the geological, hydrogeological, and geophysical characteristics of the TECNOPUC-Viamão CO_2 controlled-release experimental site in Rio Grande do Sul, Brazil. It presents a comprehensive three-year investigation into the seasonal natural background hydrochemistry. Field characterization involved recognition boreholes, in-situ infiltration and Slug Tests, topographic surveys, DC resistivity measurements, and groundwater sampling campaigns for physicochemical, major, minor, trace elements, and δ^{13}C-DIC evaluation. Results indicate the area comprises a granite-derived multilayer phreatic aquifer with two distinct hydrostratigraphic units (St and Aa). These units differ in lithological composition, hydraulic conductivities (St: 10-4 m/s, Aa: 10-8 m/s), apparent resistivities, and physicochemical and hydrochemical compositions. The St unit shows slightly neutral pH, higher temperature, EC, ORP, DO, Ca, Mg, K, Fe, Mn, Sr, B, HCO3-, and DIC concentrations, with δ^{13}C-DIC between -3 to -8 ‰. Conversely, the Aa unit displays slightly acidic pH, lower temperature, EC, ORP, higher DO fluctuation, Na, SO42-, Cl-, NO3-, Zn, Al, Ni concentrations, lower HCO3-, DIC levels, with δ^{13}C-DIC ranging between -6 to -11 ‰. Additionally, seasonal monitoring campaign revealed that there is a clear temperature-related influence on K, Na and*

trace elements (Fe, Ba, Mn, Al, B, and Zn) behavior (but not in Ca, Mg, Sr and Ni), which could impact further interpretation of the results during the upcoming CO_2 injection phase, and that the Control Charts can confidently serve as a valuable tool in understanding the inherent natural hydrochemical trends.

***Keywords**: CCS; CO_2 monitoring; leakage; hydrogeochemistry; isotopes*

5.1. Introduction

Carbon Capture and Storage (CCS) technology, especially with the aim of permanent CO_2 storage (geological storage), is gaining increasing global relevance. According to the latest survey conducted by the Global CCS Institute (GCCSI, 2023), there are currently over 392 facilities worldwide at various stages of commercial development, collectively capturing and sequestering 361 million metric tons per annum (Mtpa) of CO_2. This number represents a 102% increase in the number of CCS facilities since the Global Status of CCS 2022 (GCCSI, 2022), a percentage increase unprecedented in history. This increase could gain further momentum as several countries included mentions of CCS technology in the most recent updates of their respective Nationally Determined Contributions (NDCs), a step that was largely taken before COP-26 (Glasgow). However, even with this reference included, the latest analysis conducted by the Climate Action Tracker (CAT, 2023) shows that only 28% of global emissions are covered by new NDC submissions, with only a few Paris Agreement (2015) member countries increasing their ambition. This suggests that although CCS may be on the rise, there are still numerous actions that need to be pursued.

One of the major challenges is the absence of a national regulatory framework that clearly and objectively defines the guidelines to be followed by operators and regulatory bodies. Most countries in the Middle East and North Africa (MENA) region, Asia-Pacific, and the Americas do not have specific legislation, and those who intend to have are in the policy discussion phase (GCCSI, 2022). This is the case of Brazil, where since May 2022, the bill number 1425 has been under consideration in the country's legislative houses. The bill aims to regulate the exploration of the activity of permanent carbon dioxide storage for public interest in geological or temporary reservoirs, and its subsequent reuse (AGÊNCIA FAPESP, 2022; GCCSI, 2022; SENADO FEDERAL, 2023). Considering the maturity of the topic in the country, even

though this bill represents a significant and innovative advancement, from an environmental perspective, the presented document still contains gaps that will need to be filled in the future by specific guidelines from Brazilian environmental agencies. Looking at global examples, one of the topics that should receive greater attention will encompass the activities of Monitoring, Measurement and Verification (MMV) of CO_2 in various geological compartments (deep, intermediate, and near-surface environments).

Within this context, monitoring the hydrochemical quality of groundwater near CCS sites is commonly used to demonstrate the project's environmental compliance and the expected containment of CO_2 in the reservoir (BRYDIE et al., 2014; IRANMANESH; LOCKE; WIMMER, 2014; KLAPPSTEIN; ROSTRON, 2014). In this case, despite significant advancements in recent years (since 2010) in understanding the hydrogeochemical mechanisms involved in the CO_2-water-mineral framework interactive process (Lemieux 2011; Humez et al. 2014; Lions et al. 2014; Jones et al. 2015; Mayer et al. 2015; Lee et al. 2016; Gupta and Yadav 2020; Roberts and Stalker 2020), there are still scientific gaps to be filled. One of these challenges corresponds to the scientific support for monitoring plans for potential unintentional CO_2 leakage tracking, considering the specific geological, hydrogeological, and climatic characteristics of the locations where the projects are planned. Furthermore, much of the knowledge about changes in groundwater due to CO_2 injection is based on short-duration field experiments (Lee et al. 2016; Roberts et al. 2018; Zheng et al. 2021; Zielinski et al. 2023), with only few examples where groundwater alterations are compared with an extended study of the natural baseline (CAHILL; JAKOBSEN, 2013b; PETER et al., 2012b; TRAUTZ et al., 2013b), which is especially relevant for seasonal variations in unconfined aquifers.

Additionally, as highlighted by Jones et al. (2015), the resulting plume of CO_2-impacted water within a shallow potable aquifer will tend to be long and narrow due to a constant groundwater flow direction. These characteristics makes monitoring much more challenging, as the network of groundwater monitoring wells is typically spatially limited. Hence, seasonal and more frequent monitoring becomes even more necessary to effectively detect the presence of an unplanned CO_2 leakage in the subsurface. Zheng et al. (2021) proposed an 8-step site assessment procedure after analyzing over 139 papers and reports. Included in this proposal is the need to evaluate the

mineralogical composition, conduct a comprehensive geological-hydrogeological site characterization, and establish groundwater monitoring campaigns for an extended period before conducting the test in order to provide a solid baseline data.

Another critical factor, as mentioned in various studies (Gupta and Yadav 2020; Zheng et al. 2021; Zielinski et al. 2023), is the presence of chemically reactive minerals (primarily clay minerals, Fe-Al-Mn oxides and hydroxides, and sulfides) in the mineralogy of the impacted aquifer. These minerals can serve as sources of, for example, Ba, Zn, Cu, Cd, Pb, and As. Therefore, studies in aquifers with reactive minerals become relevant in understanding the release of potential contaminants. Within this context, Do et al. (2022) developed a controlled release test of CO_2 in an aquifer characterized by the alteration of granitic rock (which contains various clay minerals, Fe-Al-Mn oxides, and hydroxides), providing a valuable comparative scenario for the research presented in this study.

Therefore, the objective of this study was to develop and present a robust topographical, geological, and hydrogeological characterization of the controlled CO_2 leakage experimental field located at TECNOPUC/Viamão (Rio Grande do Sul state, southern Brazil) and to conduct extended seasonal monitoring (>3 years) of the natural hydrochemical and isotopic (δ^{13}C-DIC) characteristics to support the observations to be verified in the CO_2 injection test to be carried out at the same location in the next months. This study also provides a statistical framework based on control charts to establish the lower and upper limits of natural hydrochemical variation observed during the monitoring period, offering a more appropriate context for future comparisons. Ultimately, the most ambitious intention of the study is to serve as a supplementary source of technical and scientific information to contribute to the creation of national legislation based on research conducted in a representative (yet reduced) environment of the national territory.

5.1.1. Study area

5.1.1.1. Field site location

The study area is located at the Scientific and Technological Park of Pontifical Catholic University of Rio Grande do Sul (PUCRS), known as ‘TECNOPUC’, in the municipality of Viamão, in Rio Grande do Sul, the southernmost state of Brazil (IGLESIAS et al., 2019; MELO et al., 2017). In this place, a small-scale CO_2 release

experimental site was established in 2015 (coordinates: 22J 494315 mE/6671940 mN), covering an area of approximately 6,000 m^2 (Figure 5.1).

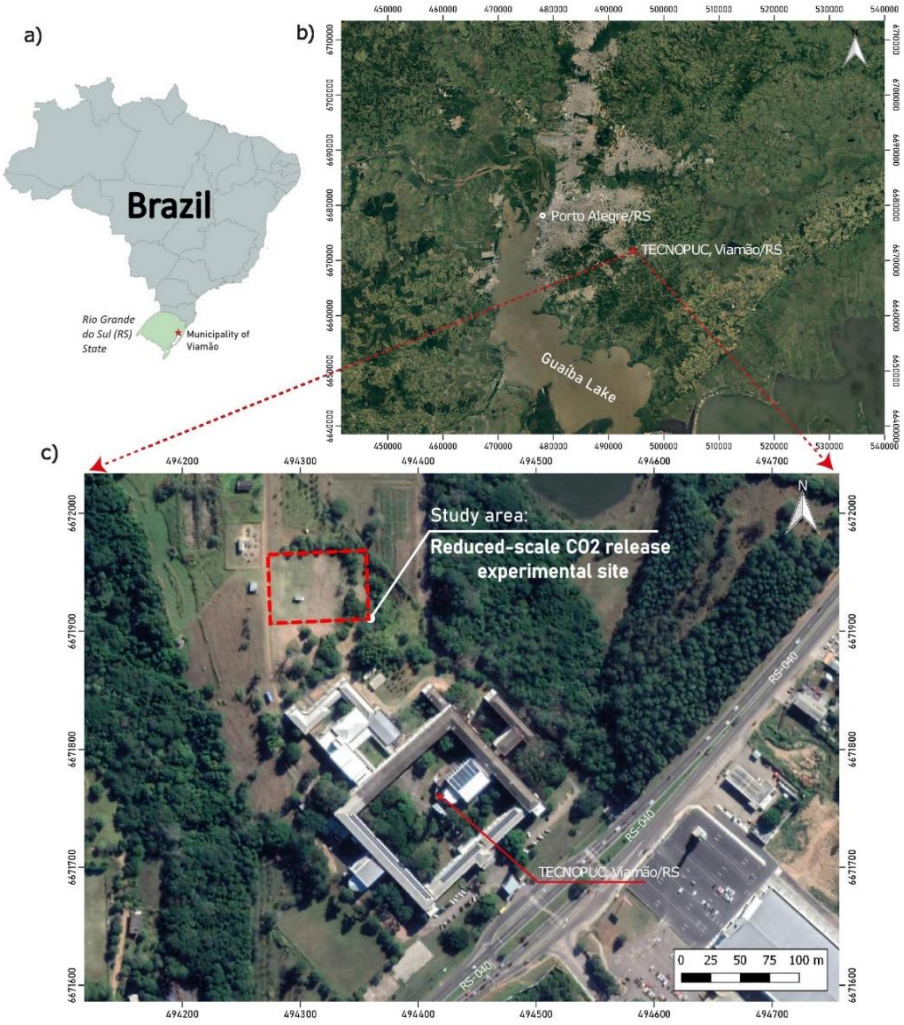

Figure 5. 1. *Location map of the experimental small-scale CO_2 release site: a) location in relation to Brazil; b) situation in relation to capital of Rio Grande do Sul (RS) state, which is the municipality of Porto Alegre; c) detailed vision of the study site.*

5.1.1.2. Regional and local geology

From a geological perspective, the site is located in the Pre-Cambrian Granitic-Gneiss Basement Complex (Neoproterozoic age, 609±17 Ma (FRAGOSO CESAR et al., 1986).This granitic-gneiss complex is part of the Pelotas batholith, a large plutonic body of approximately 2,500 km^2, formed by rock of calc-alkaline to alkaline geochemical affinity (FIANCO, 2011). Structurally, this geological unit exhibits NE and NW faults (RAMAGE, 2005), with riolitic and diabase dykes associated.

The granites and gneisses that compose this complex are divided in six distinct lithological units (PHILIPP, 1988; PHILLIP et al., 2002; PHILLIP; DE CAMPOS, 2004): Porto Alegre gneiss; b) Viamão granite; c) Independência granite; d) Canta Galo granite; e) Ponta Grossa granite; and f) Santana granite. The study area is totally established in the Viamão granite (Figure S1, Supplementary Information), which is characterized as the most outcropped spatially distributed unit. Its mineralogical framework is constituted by tabular K-feldspars megaphenocrysts dispersed in a coarse matrix of granodioritic composition, forming rocks of biotite monzogranite to granodiorite composition.

The mineralogy of the granites is mainly composed of quartz, K-feldspars (microcline) and plagioclase, while biotite and metallic oxides (e.g., magnetite) are less frequently observed (RAMAGE, 2005). Apatite, titanite, allanite, zircon and metallic minerals compose the accessory mineralogy, whereas chlorite and epidote form the secondary mineralogy (FIANCO, 2011). These rocks exhibit a pronounced magmatic foliation, vertically oriented, marked by the alignment of the K-feldspars phenocrysts and biotite. Subordinately, they also present a subparallel tectonic foliation superimposing the magmatic one, being identified by the occurrence of quartz ribbons, formation of subgrains and curved planes of crystal twinning of plagioclases (FIANCO, 2011).

5.1.1.3. Groundwater monitoring setup

The experimental site has eighteen installed monitoring wells and piezometers. Twelve of them are multilevel wells that were designed for water sampling campaigns, and they have three distinct depths, designated by their prefix ‘M’ and suffix according to installed depth as follows: i) A wells are 1 m deep; ii) B wells are 2.5 m deep; and iii) C wells are 3.5 m deep. Apart from these, six other wells are considered piezometers, as they are only used to monitor the water levels and evaluate the recharge response of the studied multilayer shallow phreatic aquifer (Table S1 and Figure S2, Supplementary Information).

These wells are specially distributed in the lowland area of the site, which can be topographically described as a ‘mini’ watershed, with a higher portion (‘catchment area’) located in the western side of the field, closest to the inner access road (between 111 to 112 m altitude); and the lower (‘drainage area’) situated in the eastern region,

with altitude levels of 107 to 106 m, where an artificial drainage pond is located (Figure 5.2).

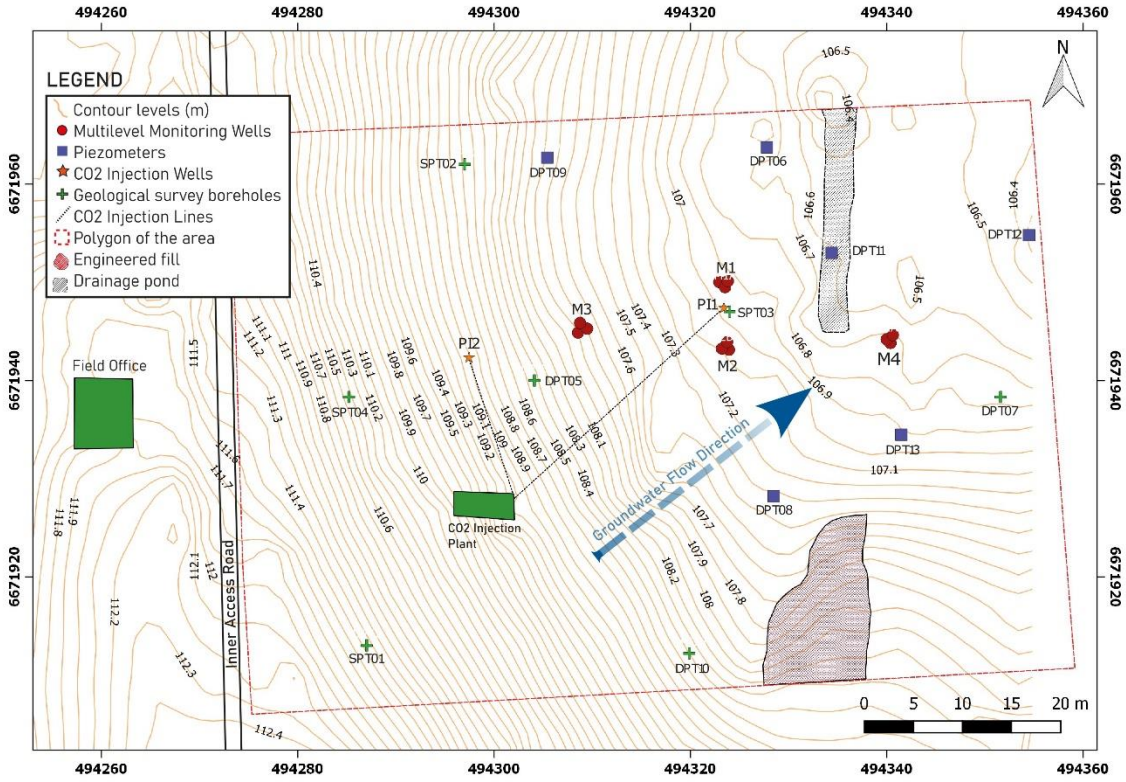

Figure 5. 2. *Topographic map of the site with location of water level monitoring wells and sampling wells along with the general groundwater flow direction (towards NE).*

5.2. Materials and methods

5.2.1. Topographic survey

Around 3,000 points were collected to characterize the area's topography using a GNSS (Global Navigation Satellite Systems) with RTK (Real-time Kinematic) equipment (model F90-RTK, Tecnosat®), ensuring accuracy below 4 mm. Interpolating the collected points - which was done by applying the Nearest Neighbor method - resulted in contour lines with a vertical equidistance of 10 cm. Additionally, Surfer® software was utilized to create a high-quality Digital Terrain Model (DTM) with a dense point distribution, providing a detailed three-dimensional perspective of the terrain's topographic configuration.

5.2.2. Geological characterization (texture and mineralogy)

An extensive investigation was conducted to characterize the geological strata and hydrogeological properties of the site using thirteen direct boreholes. Initial lithology reconnaissance boreholes (SPT01 to SPT04) were drilled to depths of 8.5 m to 10 m using the Standard Penetration Test (SPT) technique. Further, nine additional boreholes (DPT05 to DPT13) were executed with an automatic hollow stem auger drill, followed by piezometer installation for hydraulic property monitoring.

Undisturbed samples were obtained using the Direct Push Technology (DPT) system with a disposable liner sampler. Comprehensive logging descriptions were performed in the field to document the geological attributes. Each borehole yielded six to seven sampled packs, with intermittent ca. 35 cm segments without core recovery. The samples were analyzed for grain size (conventional sieve method), chemical composition, mineralogical identification using binocular microscopy, SEM, and XRD analyses. Data integration and visualization were accomplished using Rockworks® software. Binocular microscope analysis was conducted using a Zeiss® stereomicroscope, while mineralogical identification employed SEM with EDS. XRD analysis was carried out using a Bruker® D8 Advance diffractometer with the powder method. All analyses took place at PUCRS.

5.2.3. Geoelectric survey (DC resistivity)

In addition to on-site direct drilling, 2D electrical resistivity (geoelectrical) surveys were conducted using the SuperSting R8/IP equipment (Advanced Geoscience Inc.®). The chosen technique was horizontal profiling with the Dipole-Dipole array, known for identifying lateral resistivity variations and mapping CO_2-related subsurface anomalies (AUKEN et al., 2014; DAFFLON et al., 2013; LAMERT et al., 2012; LE ROUX et al., 2013; OLIVA et al., 2018; OLIVAA et al., 2014; STRAZISAR et al., 2009; YANG et al., 2015). Multiple surveys were performed to assess equipment sensitivity, investigate subsurface characteristics, and remove interfering materials like the grounding bar of the injection plant container and CO_2 injection lines to enhance data quality.

For data acquisition, 2D lines were spaced at 1 m intervals, offering an approximate resolution of 30 cm for shallow layers and a lower resolution for deeper layers. The investigation area covered a 55 m x 60 m (3,300 m2) polygon between the access road to the west and the drainage pond to the east. This confined area was necessary to

eliminate data noise caused by excessive water volume in the pond, affecting geoelectrical imaging quality. The imaging depth reached approximately 16.5 m. Data processing utilized EarthImager 2D/3D® software with a smoothness-constrained inversion routine (de Groot-Hedlin and Constable 1990) to achieve low Root Mean Square error (RMS) values below 5% in all conducted surveys.

5.2.4. Water table monitoring

To address significant lithological variation observed during initial surveys in the area and evaluate the hydrogeological behavior of different layers in relation to the water recharge, a water table monitoring plan was devised. In April 2019, automated level meters (model M5, Solinst®) were installed in six selected wells to monitor static water level (WL). Episodic cross-checks were conducted using a manually operated water level reader (HSIF-30 model, Hidrosuprimentos®) to confirm hydrodynamic behavior. This extensive monitoring span allowed for a comprehensive understanding of the seasonal dynamics of hydrostratigraphic units, their response to precipitation events (recharging episodes), and prolonged drought periods (low or no recharge). The monitoring approach facilitated differentiation of aquifers' sensitivity to these phenomena. Precipitation data were collected from the database of Brazil's National Institute of Meteorology (INMET). The closest station (geographically) covering the entire analyzed period was used for reference.

5.2.5. Permeability tests and slug tests

To estimate infiltration rate and groundwater flow capacity, two types of tests were conducted: i) an *in situ* permeability (infiltration) test using the Guelph Permeameter (model 2800K1, SoilMoisture®) for the shallowest unit (So) - vadose zone (for spatial distribution see Figure S3, Supplementary Information); and ii) Slug Tests for the other units (St, Aa, and Ga) using monitoring wells (M1, M2, M3, and M4) and piezometer DPT08 in the saturated zone.

The infiltration test followed procedures outlined in the manufacturer's manual (SOILMOISTURE, 2012), based on ASTM D5126 (ASTM, 2016). The Slug Tests involved introducing a known volume of water to induce instantaneous water level rise. Pressure transducers were used for precise data acquisition during the tests. Data was organized into spreadsheets and analyzed using AQTESOLV®, evaluating the results

with Hvorslev (1951) Bouwer and Rice (1976) and Butler (1998) methods to obtain average hydraulic conductivity values for the hydrostratigraphic units.

5.2.6. Hidrochemistry characterization (sampling campaings and analysis)

Groundwater sampling campaigns were conducted seasonally to study the chemical variation of water during different climatic seasons. The goal was to understand natural changes resulting from the open communication of the aquifer with the atmosphere and a deeper aquifer (fractured granite). Eight campaigns were conducted but not uniformly or regularly due to technical, health (COVID-19 pandemic), and financial reasons (Table 5.1).

Table 5. 1. *Sampling campaigns carried out for seasonal monitoring of the hydrochemical characteristic of groundwater.*

Sampling campaing	Date	Season
S1	*21/03/2019*	*Summer/2019*
S2	*14/05/2019*	*Fall/2019*
S3	*13/08/2019*	*Winter/2019*
S4	*22/10/2019*	*Spring/2019*
S5	*15/01/2020*	*Summer/2020*
S6	*14/10/2020*	*Spring/2020*
S7	*21/06/2021*	*Winter/2021*
S8	*04/02/2022*	*Summer/2022*

During all monitoring campaigns, groundwater sampling was conducted using the low-flow method as specified in the NBR 15847 standard (ABNT, 2010), which is based on ASTM's D6452 (ASTM, 2018) and D4448 (ASTM, 2019) guidelines. A Millipore® Easy-Load peristaltic pump integrated into a closed system flow cell equipped with a QED® MP-20 multiparameter probe facilitated field measurements of various physicochemical parameters: i) Groundwater temperature; ii) Hydrogen Potential (pH); iii) Electrical Conductivity (EC); iv) Redox Potential (ORP); and v) Dissolved Oxygen (DO).

Samples were collected with a syringe immediately after indicative stabilization of the parameters and passing through the probe sensors. These samples were then filtered through a 0.22 µm hydrophilic acetate filter to more efficiently retain colloidal material and bacteria responsible for isotopic carbon fractionation. For chemical

analysis of metals, samples were acidified with HNO3 in the field until pH ≤ 2 and stored in 50 mL polypropylene (PP) Falcon-type tubes. Samples for anion analysis underwent only filtration without acidification. Samples for C isotopes (^{13}C /^{12}C) and Dissolved Inorganic Carbon (DIC) analysis were stored in 10 mL Exetainer® vials. These vials were pre-treated with two drops of benzalkonium chloride ($C_{21}H_{38}NCl$) for bacterial sterilization, and the air inside the vials was removed using a vacuum pump.

Chemical analyses were performed at IPR/PUCRS using different techniques. Anions were analyzed with Thermo Scientific® Dionex ICS-5000 Ion Chromatograph (CI), while metals were assessed with the Optima 7000 DV Inductively Coupled Plasma Optical Emission Spectrometer (ICP-OES) from Perkin Elmer®. Analytical errors varied for each analyte, ranging from 0.1 µg/l (Cu) to 0.82 mg/L (Ca). The Limit of Quantification (LQ) varied across parameters, reaching 0.1 µg/l (toxic metals) and 0.005 mg/L (nonmetals and metals). In some cases, the LQ value was conventionally substituted by LQ/2 for quantitative interpretation.

Using the obtained results, the ionic balance was calculated with Aqion®, estimating the error in charge balance (CBE) under the assumption of water electroneutrality. Typically, the maximum tolerable CBE for groundwater is 5%. However, for low ionic strength waters (I < 0.1 mol/L) like those in this study, errors above 10% are more likely (FRITZ, 1994). Additionally, since the H_2CO_3 and HCO_3- species distribution are pH-dependent, a small variation in pH can significantly impact CBE. Hence, for non-restrictive purposes, a maximum error value of 15% (±0.1) was adopted.

Chemical speciation of solutes, carbonic species distribution (H_2CO_3, HCO_3^-, CO_3^{2-}), partial pressure of CO_2 (pCO_2), and mineral saturation index (SI) calculations were performed using PHREEQC INTERACTIVE 3.7 (PARKHURST; APPELO, 2013), considering physicochemical parameters at the time of collection. Chadha's diagram was developed using WQChartPy application (YANG et al., 2022). DIC analyses utilized a prepared sample aliquot added to 12 mL vials with a screw cap and rubber septum. The analytical procedure followed the method described in Xie et al. (2018) with a Shimadzu® Gas Chromatograph (GC), model GC-2010 Plus, employing a Na_2CO_3 solution calibration curve. Reported DIC results are expressed in ‘ppm C’, considering the mass contribution of carbon and its molar mass.

Carbon stable isotope ($^{13}C/^{12}C$) analyses were conducted using the GasBench II equipment, connected to the Isotope Ratio Mass Spectrometer (IRMS) model Delta V

Plus from Thermo Scientific®. The NBS18 primary standard was employed for calibration, anchored to the original VPDB standard (NBS18 = -5.014‰ VPDB) as per Friedman et al. (1982) and Coplen et al. (2006). Results are reported as the ratio between the abundance of the heavy isotope (^{13}C) and the light isotope (12C) in the sample, compared to the abundance ratio of the standard used (as mentioned in Faure and Mensing (2004) and Hoefs (2021).

The isotopic ratio of $^{13}C/^{12}C$ in DIC within water samples is represented as $\delta^{13}C$-DIC and reported in per mil (‰). The average analytical error for the analyses was 0.1 ‰. Besides, considering the unknown isotopic ratio values of soil gas ($\delta^{13}C$-CO_2) in the study area, theoretical enrichment factor (ε) equations from Clark and Fritz (1997) were used to calculate the DIC source's isotopic ratio. Additionally, isotopic mass balance calculations from (2015) were employed to account for the contribution of H_2CO_3 and HCO_3^- species to the CO_2 source's isotopic fractionation in the DIC response. Detailed calculation steps (equations 1 to 7) can be found in the Supplementary Information.

5.3. Results

5.3.1. Lithology, mineral composition and hydrostratigraphic units

Analysis of the SPT and DPT drillings revealed a significant variation in lithology, indicating a prevalence of silty-clay grains mixed with coarser materials. In the upper few centimeters of the lithological profile, the particles are brownish and easily penetrates down to a depth of 1.45 meters. Below this layer, the material shows a silty aspect with a significant occurrence of clay in many areas, especially at lower elevations. The colors vary from light gray to reddish-brown, reaching depths ranging from 2.85 to 3.8 meters.

Further down, up to depths between 4.15 and 4.9 meters clayey material is predominant, but with a significant silt fraction in some areas. The colors are light gray to reddish-brown, with an increase in sandy grains towards the deeper portions of the profile, and the presence of quartz-feldspar minerals and mica near the base. Beyond this interval, down to a depth of 8.1 to 8.9 meters, there is heavily weathered rocky material with disintegrated quartz and feldspar-K grains, along with the occurrence of kaolinite, which has a reddish to whitish color. This lithology was grouped into 4 (four) hydrostratigraphic units (Table 5.2), considering the average hydraulic conductivity values (detailed in a specific section below).

Table 5. 2. *Classified hydrostratigraphic units and properties used to segment the geological profile of the studied area.*

Hydrostratigraphic Unit (HU)	Primary material	Secondary material	Depth range (m)	Color	Hydraulic Conductivity (m/s)	Observations
Organic Soil (So)	Sandy-silty clay	Organic matter and vegetal remains	0.35 – 1.45	Dark brown	10^{-7}	Few centimeters thick at higher elevations to a few meters thick (≤ 1.5m) at lower elevations
Silt (St)	Silt	Clay (especially at lower elevations), with dispersed sandy fraction	2.85 – 3.8	Light gray to reddish-brown	10^{-4}	Varied colors reflect different oxidative states depending on water table fluctuation
Sandy Clay (Aa)	Clay	Silt (some locations) and sandy grains towards the deeper portions	4.15 – 4.9	Light gray to reddish-brown color	10^{-8}	Presence of quartz-feldspar minerals and mica near the base
Altered Granite (Ga)	Disaggregated quartz and feldspar-K grains	Clay (kaolinitization)	8.1 – 8.9	Reddish to whitish coloration	10^{-5}	Larger granite fragments maybe preserved

Note*: The lithology was grouped into hydrostratigraphic units to understand the distribution of distinct layers in the study area, especially the more groundwater-conductive lithologies (St and Ga units) in the complex context of a residual granite soil (regolith/saprolite). It is essential to recognize that the actual geological framework is much more intricate beyond this simplification.*

Figure 5.3 illustrates a fence diagram representing the spatial distribution and variation of soil thickness in various regions of the study area, as well as the geometry of the hydrostratigraphic units based on the conducted boreholes and their descriptions.

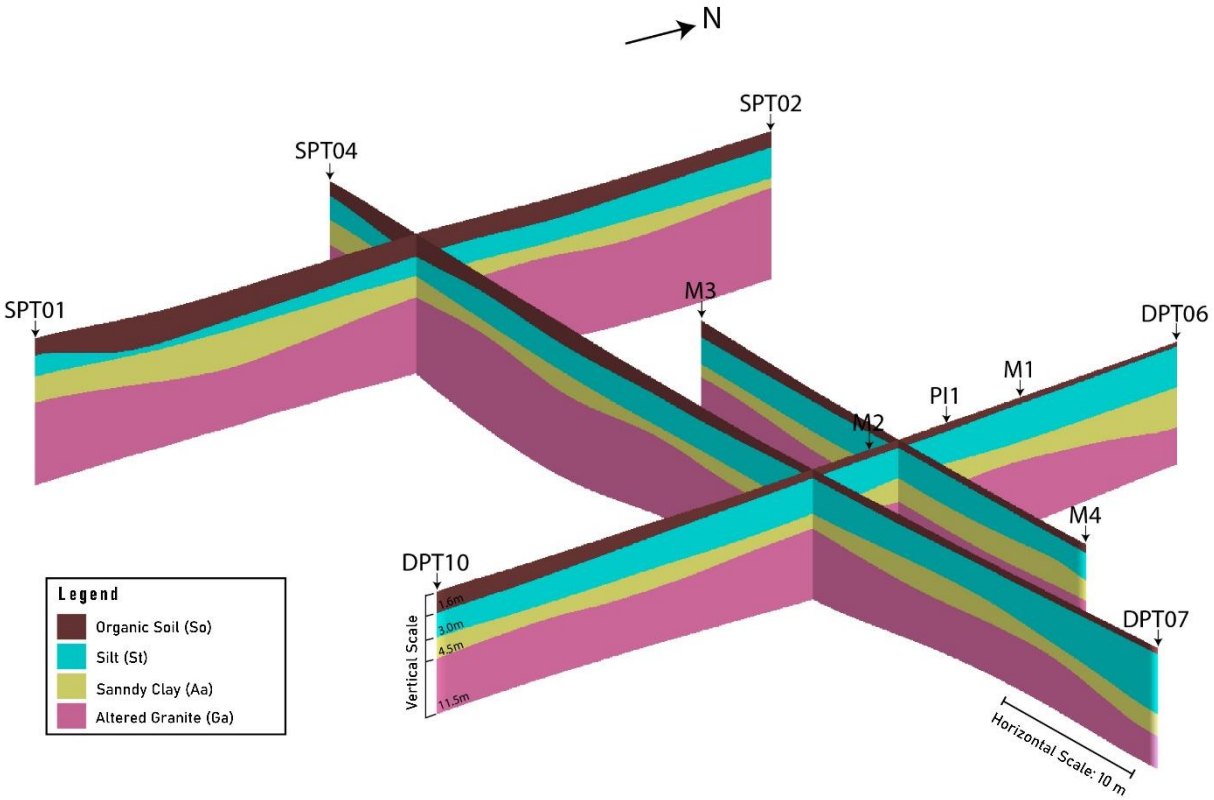

Figure 5. 3. *Fence diagram illustrating the lateral and vertical distribution of described hydrostratigraphic units.*

Analysis of the sandy fractions of the samples show a mineralogical composition dominated by feldspars, micas, quartz, amphibole, and opaque minerals, with K-feldspar being the most prevalent. Orthoclase is more abundant than microcline and displays a range of colors, contributing to variations in sandy fraction coloration. Plagioclase (albite - oligoclase) is also present but in lesser proportions compared to K-feldspar. Muscovite is the dominant mica variety, with biotite occurrences. Micas impart a vitreous appearance, resulting in distinctive greenish tones.

Amphibole and opaque minerals are less common but found in specific contexts. Some samples exhibit partial grain coatings of clay minerals and iron oxides, adding complexity. Figure S4 A and B (Supplementary Information) illustrates the principal mineralogical constituents of the coarse fraction (sandy) from the Sandy Clay (Aa) and Altered Granite (Ga) units. SEM investigation confirms identified minerals, including iron oxide-covered K-feldspar and alteration minerals like smectite (Figure S4C and D, Supplementary Information). The silt and clay fraction, in addition to the sandy fraction, was characterized using XRD. Kaolinite is the major constituent in most samples, with illite as the secondary clay mineral. Interstratified clay minerals (smectite/illite) occur in

smaller quantities, along with trace amounts of goethite and lepidocrocite (Figure 5SA and B). In the shallower intervals (0 to 3m), Organic Soil (So) and Silt (St) units, kaolinite is the most abundant clay mineral, while illite and interstratified clay minerals constitute a secondary fraction. DPT07 is an exception, where goethite and lepidocrocite are also present between 1.5 and 2.65m. In the intermediate intervals (3 to 6m), there is a predominance of kaolinite and illite, with goethite becoming more common, especially between 4.5 and 5.65m. In the deepest portion of the profile (> 6m to 10.15m), kaolinite and illite prevail, with rare occurrences of lepidocrocite, while goethite was not observed (Figure 5S C, Supplementary Information).

Granulometric analyses, due to the homogenization of a reasonable length of the recovered core (1.15m), do not differentiate the layers satisfactorily, as they blend the grain size ranges at the contacts between the four defined units. However, by analyzing the clay percentage in the sampled intervals, it is possible to identify that there is a higher concentration of the clay fraction at a depth between 1.50 and 2.65m (Figure S6, Supplementary Information), reaching values above 40%. In zones above and below this interval, the percentage decreases, predominantly constituting between 20 and 33% of the total. Thus, the occurrence of clay in this portion suggests the existence of a very fine-grained interval that contributes to the development of an overlying hydrostratigraphic unit with higher hydraulic conductivity, as will be seen later.

5.3.2. Geoelectric model of the study area

After processing the data, the apparent resistivity (ρa) was observed to span a range from approximately 0 to 1000 ohm.m. However, values very close to zero were considered undesirable anomalies and were consequently excluded from the hydrogeological interpretation. Nevertheless, the majority of the data was deemed representative of the area's resistivity and provided valuable insights into the subsurface characteristics. The results indicated that the deeper zones generally exhibited more resistive units, while the portions interpreted as hydrostratigraphic units (HU) displayed less resistive characteristics. The apparent resistivity (ρa) ranges (Ohm.m) for each unit, as shown in Figure 5.4, are as follows: a. Organic Soil (So) - 70 to 120 Ohm.m; b. Silt (St) - 10 to 40 Ohm.m; c. Sandy Clay (Aa) - 40 to 80 Ohm.m; d. Altered Granite (Ga) - 120 to 400 Ohm.m; and e. Unaltered Granite (Gr) - 400 to 1000 Ohm.m.

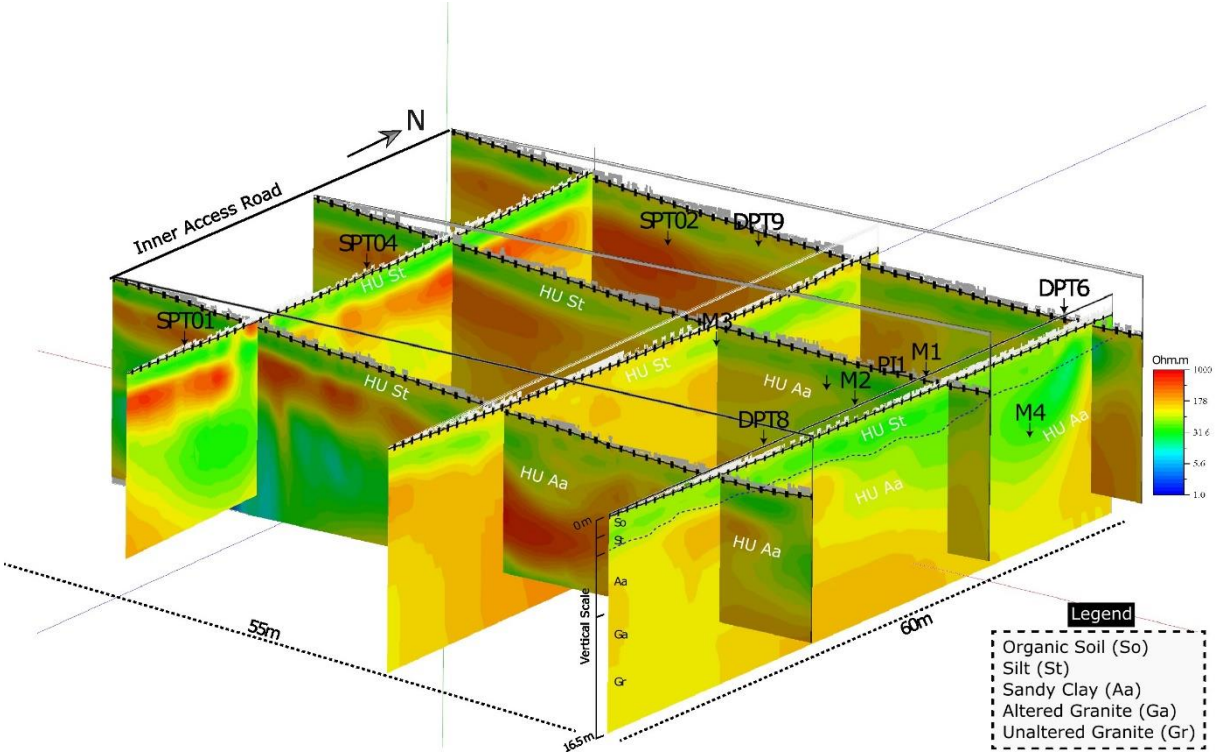

Figure 5. 4. *Diagram depicting the 2D geoelectric cross-sectional profiles acquired, along with the interpretation of hydrostratigraphic units.*

The color ranges from light blue to darker green in the depicted zones indicates lower resistivity, which corresponds to layers with abundant groundwater occurrence and high saturation. These layers represent the HU St. On the other hand, the areas with shades ranging from light green to yellow depict transition zones between less resistive (wet) and more resistive (dry) layers. The varying saturation levels within this unit create a heterogeneous pattern, and these regions are indicative of the HU Aa. Interestingly, in some locations, the Aa seems to be connected with the St, emphasizing the complex interplay between these units.

Furthermore, it can be observed that the distribution of the aquifers is not homogeneous, and in some areas, the units are laterally disconnected, with non-aquiferous layers between them. It should also be noted that in the higher topographic areas, the resistive portion is shallower, with a more common occurrence of zones with resistivity >400 Ohm.m, indicating a thinner layer of units resulting from granite alteration (So and St) and proximity of the granite top to the surface. The opposite occurs in the lower topographic zones, where a greater thickness of the So, St, and Aa units can be observed, and the resistivities of the altered granite zone (Ga) range

between 200 and 400 Ohm.m, indicating a higher occurrence of groundwater compared to the higher regions.

5.3.3. Hydraulic aquifer parameters and water level fluctuation

Infiltration tests revealed that hydraulic conductivity for the So unit varied from 10^{-6} to 10^{-9} m/s. This variation was mainly attributed to higher sandy fractions in some regions of the study area, especially between points GP06, GP07, GP08, and GP09 (near the injection plant) and GP06 and GP10 (further east near the drainage pond). In other points, hydraulic conductivity consistently remained around 10^{-8} m/s, except for point GP05 (10^{-9} m/s) with a higher abundance of silty-clayey material.

Slug Test results for the saturated zone (St, Aa, and Ga units) showed global variations between 10^{-4} and 10^{-9} m/s, indicating significant heterogeneity in hydraulic conductivity. Tests developed in the well's intervals A and B exhibited relative consistency, with values between 10^{-4} and 10^{-5} m/s, mainly representing the St lithology. The values in interval C, however, ranged between 10^{-8} and 10^{-9} m/s, indicating significantly lower hydraulic conductivity, which is indicative of the Aa unit. This layer acts as a barrier, isolating groundwater in the overlying St unit. Tests on the well DPT08, which penetrates only the Ga unit (filter section between 5.5 m and 9.5 m depth), showed an average value of approximately 10^{-5} m/s due to the presence of altered coarse material from the granite. Figure S7 (Supplementary Information) illustrates the different hydraulic conductivity values among the wells where the tests were conducted.

Groundwater levels were monitored using leveloggers from April 2019 to February 2022, corroborating sporadic manual measurements (Figure 5.5). The piezometric level's dynamic behavior clearly distinguishes between the identified aquifer layers. The dynamic behavior of the piezometric level of the hydrostratigraphic units demonstrates a clear distinction between the identified aquifer layers. The St unit, represented by wells A and B (M1A, M1B, M2B, and M3B) and indicated by the green arrow, exhibits a clear behavior, oscillating together and consistently with each other, depending on the recharge from rainfall.

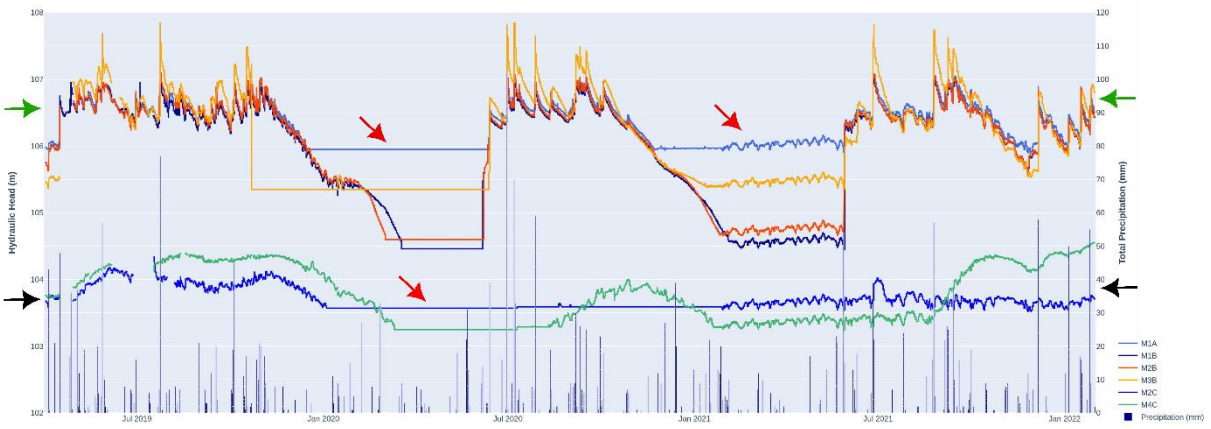

Figure 5. 5*. Variation of hydraulic head (m) of multilevel monitoring wells from April 2019 to February 2022 with total precipitation data (mm). Green arrows indicate the HU St, while the dark arrow indicates the HU Aa.*

In general, the St unit is completely saturated in almost all seasons, except during prolonged drought periods, like the one in summer and autumn of 2020. During this time, the aquifer experienced a complete depletion from late March until early June 2020. A similar but less intense behavior was observed in summer and autumn of 2021, with the monitoring wells not completely exhausted (events indicated by the red arrows). These atypical occurrences can be attributed to the severe drought experienced in the southern region of Brazil during those periods. The area suffered from scarce rainfall and significantly below-average precipitation linked to the effect of the La Niña phenomena (BARBOSA et al., 2021; GRIMM et al., 2020; PEIRIS; GOURDJI; PANDEY, 2022).

The Aa unit, represented by wells C (M2C and M4C, dark arrow in Figure 5), exhibits irregular behavior. This pattern is especially notable when there is higher recharge from rainfall and infiltration from the St unit, which occurs in certain areas where they are connected (Figure 4). During months of reduced recharge, the Aa unit shows low levels, remaining only a few centimeters above the bottom of the wells representing it. In contrast, during autumn, winter, and spring months, the Aa level rises, coinciding with a water table increase of more than 50 cm. However, during the summer of 2020 and 2021, precisely when the water table in the St declines and reaches depletion, the Aa level decreases again, leading to well depletion during that period.

5.3.4. Hydrogeochemical and δ^{13}C-DIC characteristics

After conducting 8 (eight) seasonal monitoring campaigns of the hydrogeochemical background of the area, a total of 54 (fifty-four) samples were collected for major, minor, trace elements, carbon isotopes ($^{13}C/^{12}C$), and DIC (Dissolved Inorganic Carbon), representing an average of approximately 7 (seven) samples per sampling campaign. However, it is worth noting that the number of sampled wells was twice as high during periods of high aquifer recharge, which occur during autumn, winter, and spring, compared to the predominantly dry season (summer).

5.3.4.1. Field physicochemical parameters

Temperature, pH, electrical conductivity (EC), ORP and DO fluctuations from campaigns S1 to S8 revealed distinct patterns (Figure 5.6). Shallower wells (M1A, M1B, M2A, M2B, M4A and M4B) experienced larger temperature variation (nearly 12 °C) than relatively deeper wells (M3B, M3C, M4C), which exhibited a 6 ºC difference. On the other hand, pH showed a maximum difference of approximately 1 unit for shallow wells and a greater difference for the deep set (up to 1.5 units). EC exhibited a greater amplitude for the shallower wells (> 120 µS/cm) and below 80 µS/cm for the deeper ones. ORP data displayed the most significant heterogeneity, with values spanning from approximately -175 to +175 mV for the whole set of wells, indicating a temporal oxidizing-reducing interplay. DO demonstrated a general variation between 0.5 and 3.5 mg/L for shallow wells and between approximately 2 and 7 mg/L to the deeper set of wells. Table 5.3 summarizes the seasonal amplitude and median value for all wells.

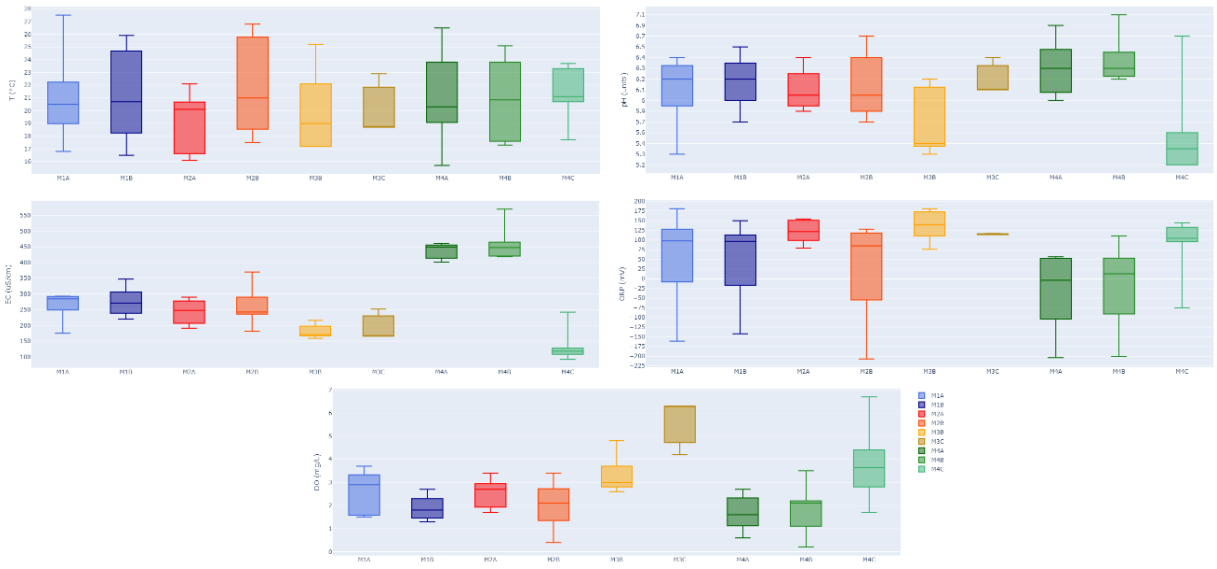

Figure 5. 6. *Representative boxplot of the seasonal variation of the physicochemical parameters measured in the field, individually grouped by sampled well.*

Table 5. 3. *Summary of the amplitude and median values of physicochemical parameters, categorized into shallow and deeper wells.*

Parameter	**Shallower wells (M1A, M1B, M2A, M2B, M4A and M4B)**	**Deeper Wells (M3B, M3C, M4C)**
Temperature amplitude	15.7°C - 27.5°C	17.7°C - 23.7°C
Temperature (median)	20.4 to 20.8 °C	19 to 21°C
pH amplitude	5.3 - 6.4	5.2 - 6.7
pH (median)	6.1 to 6.3	~ 5.4
EC amplitude	170 – 360 µS/cm (M1A to M2B) 400 - 560 µS/cm (M4A and M4B)	100 – 250 µS/cm
EC (median)	250 to 280 µS/cm (M1A to M2B) 450 µS/cm (M4A and M4B)	120 to 170 µS/cm
ORP amplitude	-175 - +175 mV	-75 - +175 mV
ORP median	100 to 125 mV (M1A to M2B) 0 mV (M4A and M4B)	100 to 125 mV
DO amplitude	0.5 - 3.5 mg/L	2 - 7 mg/L
DO (median)	1.5 to 3 mg/L	3 to 6 mg/L

5.3.4.2. Chemical analysis of groundwater

Anion and cation concentrations relative to major elements were quantified. Samples with an ion balance error >15% (± 0.1) were discarded, which includes samples from campaign S1 and some samples that exceeded this limit. Analyzed data revealed that shallow wells M1A to M2B displayed consistent data throughout all seasons, while wells M4A and M4B exhibited enriched concentrations than the former shallow wells. Deeper wells M3C and M4C usually follow the same pattern, whereas well M3B represent an intermediate case between these two sets considering its chemical characteristics (Figure 5.7 and 5.8).

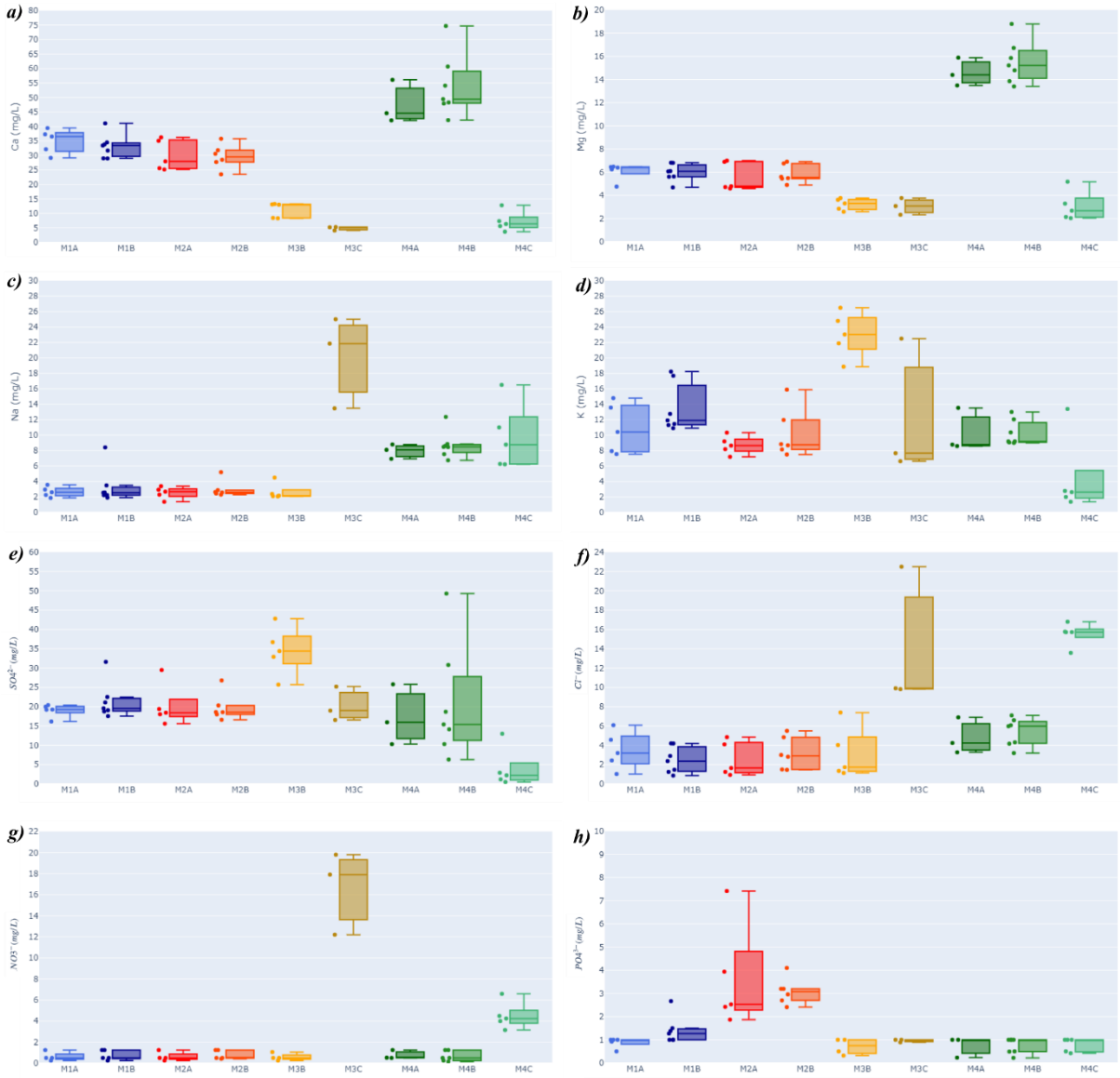

Figure 5. 7. *Boxplot showing the overall variation of cations and anions (major elements) per well.*

In this context, calcium (Ca) and magnesium (Mg) concentration followed a similar pattern, as they showed the greatest seasonal amplitude (Figure 5.7a and 5.7b). Shallow wells M1A to M2B exhibited Ca concentration from 23.5 to 41 mg/L and Mg varying between 4.6 and 7 mg/L, while Ca oscillated from 42 to 75 mg/L and Mg from 13.4 to 18.8 mg/L in M4A and M4B. Deep wells M3B, M3C, and M4C displayed Ca variation from 3.6 to 13.25 mg/L and Mg from 2 to 5.2 mg/L in. Sodium (Figure 5.7c) only exhibited significant variation in wells M3C and M4C (ranging from 6 to ca. 25 mg/L), while showing a consistent amplitude in the shallower wells (<2 mg/L in M1A to M2B, and between 6.9 to 8.8 mg/L in M4A and M4B).

Potassium (K) and sulfate (SO_4^{2-}) have showed the most intricate parameters among all seasons. Shallow wells showed a general K distribution between 7.2 and 15 mg/L (with occasional outliers) and SO_4^{2-} showed a dominant range of 15.5 to 22.5 mg/L, with a similar pattern observed in well M3C (16.5 to 25.2 mg/L). Deeper well M4C frequently exhibits lower K (1.3 to 2.7 mg/L) and SO_4^{2-} (0.5 to 2.9 mg/L) concentrations. Differently than observed in other parameters, well M3B showed the higher concentrations of both K and SO_4^{2-}, varying seasonally between 18.8 to 26.5 mg/L and 25.7 to 42.8 mg/L, respectively (Figure 5.7d and 5.7e).

For chloride (Cl^-), most shallow wells consistently have values below 7.4 mg/L in all sets of multilevel wells, usually ranging between 0.8 and 7 mg/L, except for wells M3C and M4C, where concentrations can exceed 9.8 mg/L and reach up to 22.5 mg/L (Figure 5.7f). Nitrate (NO_3^-) and phosphate (PO_4^{3-}) are generally low in almost all cases (Figure 5.7g and 5.7h), often below the LQ (2.5 mg/L and 1 mg/L, respectively), except for wells M3C and M4C, which show higher levels of NO_3^- (12.2 to 19.8 mg/L in M3C and 3.1 to 6.5 mg/L in M4C) and for those wells where PO_4^{3-} are above 1.2 mg/L (mainly M2A and M2B).

Analysis of minor and trace elements indicated that Ba, Fe (total), Mn, and Sr have relatively higher concentration ranges, usually >75 µg/L. On the other hand, Al, B, Ni, and Zn showed lower concentration ranges (<75 µg/L). Most wells show Fe concentrations ranging from a few tens to approximately 690 µg/L, with some outliers. However, wells M4A and M4B stand out with frequent values above 830 µg/L (0.83 mg/L) and, in certain situations, up to 8230 µg/L (8.23 mg/L) (Figure 5.8a). Similarly, Mn distribution follows a comparable pattern. Most wells (particularly M3B and M3C) range from the LQ (5 µg/L) to 75 µg/L or lower (<10 µg/L). However, wells M4A and

M4B frequently exceed 123 µg/L, and M4C occasionally shows elevated levels (Figure 5.8b).

Strontium (Sr) concentration behaves similarly to Ca and Mg. Wells M1A to M2B show values between 110 and 200 µg/L, while wells M4A and M4B range from 250 to 340 µg/L, and wells M3B, M3C, and M4C range from 32 to 100 µg/L (Figure 5.8c). Barium numerical pattern is somewhat similar to Mn. Wells M1A to M3C have values between 50 and 120 µg/L, while the M4 group (A, B, and C) predominantly display values above 120 µg/L, reaching levels near 300 µg/L (Figure 5.8d). Zinc distribution in the wells centers around the median, approximately 25 µg/L, for most cases (with rare exception, as in S6 campaign). Notably, wells M3B and M4C exhibit relatively higher values, ranging from 25 to 325 µg/L (Figure 5.8e).

Aluminum concentration, similar to Fe, mostly ranged consistently between 25 and 100 µg/L, with some outliers. However, well M3C displayed anomalous behavior, showing a wide range from 32 µg/L to nearly 1800 µg/L (1.8 mg/L) (Figure 5.8f), which could be linked, to some degree, to the presence of unavoidable particulate material in the sampled water. Boron and nickel had the lowest concentrations, with Ni frequently below the quantification limit (<LQ). Boron showed usual variations between 20 and 55 µg/L for shallow wells (M1A-M2B and M4A-M4B), and slightly lower, between 3 and 28 µg/L, for wells M3B, M3C, and M4C (Figure 5.8g). Nickel, when quantified, ranged from 18 to 49 µg/L in most wells, except for well M3B, which consistently had concentrations ≤11 µg/L (Figure 5.8h). As for Cd, Co, Cr and Pb, their concentrations remained below LQ in all campaigns, with no manifestation in any of the seasons. Cu also showed a similar behavior, except for an isolated concentration of 12 µg/L (±0.1) in well M3C during the S3 campaign, for an unknown reason.

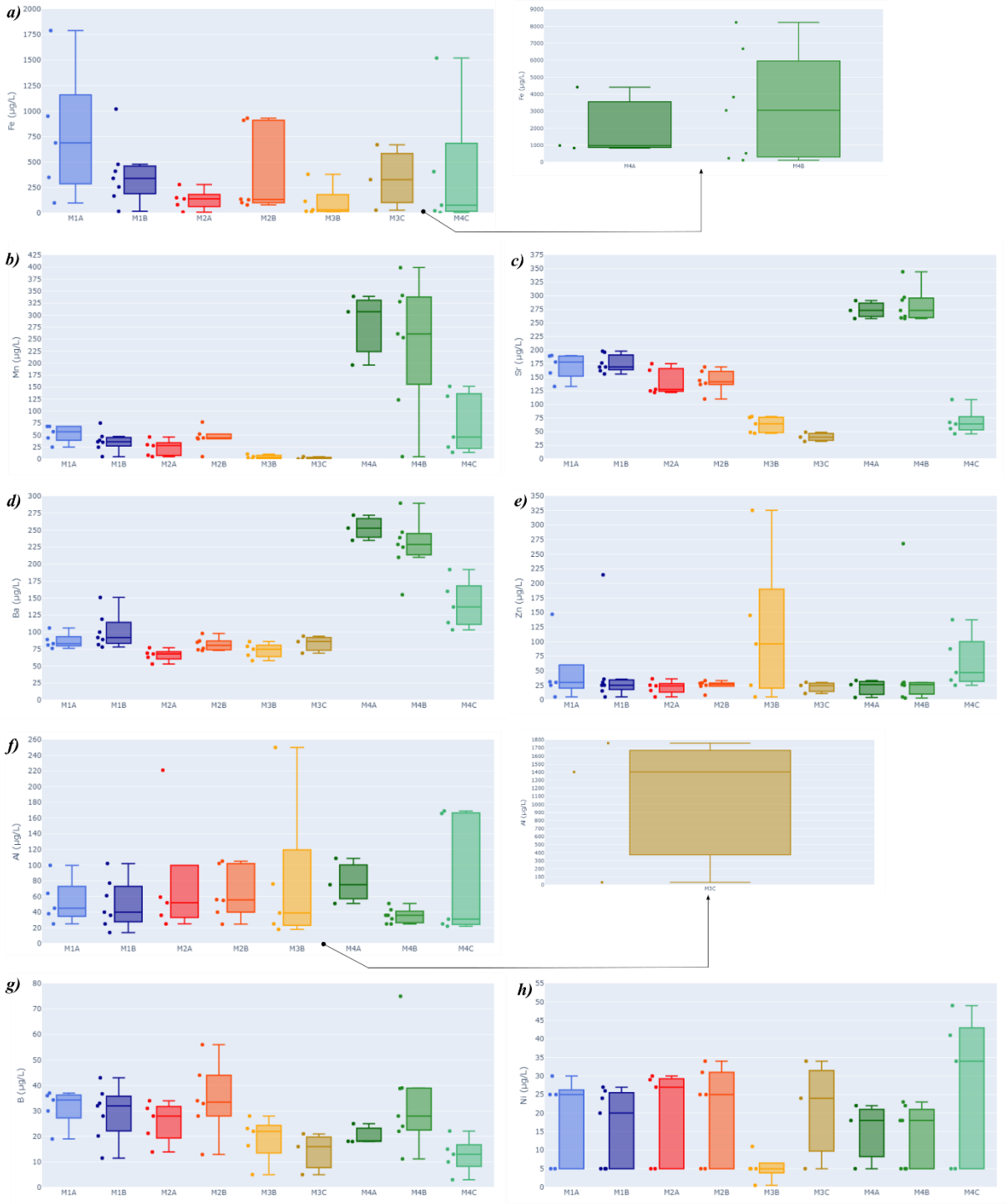

Figure 5. 8. *Boxplot showing the overall variation of minor elements and traces per well.*

5.3.4.3. Mineral saturation indices (SI)

To determine the SI, PHREEQC uses diverse thermodynamic databases. Initially, we examined databases containing minerals found in SEM and XRD analyses or expected to occur in the granite-derived lithological context (even if not explicitly

identified). To ensure technical coherence, we assessed potential discrepancies in mineral saturation data across databases. In total, 16 (sixteen) minerals present in the study area were selected, including Fe and Al oxides and hydroxides, some of which may amorphous forms. Table 5.4 summarizes the statistical data for the wells closest to the pretended CO_2 injection point (controlled leakage). This includes the depth level immediately above the gas release point and the most representative stratigraphic unit (wells M1B and M2B). Additionally, it covers the farthest well horizontally (well M3B) and a well at a similar or relatively lower depth interval compared to the injection well (well M4C), which exhibit different hydrochemical characteristics, as previously shown.

Table 5. 4. *Statistical summary of the mineral saturation index (SI) for the representative wells M1B, M2B, M3B, and M4C.*

Mineral	M1B				M2B				M3B				M4C			
	Min.	Max.	μ	σ	Min.	Max.	μ	σ	Min.	Max.	μ	σ	Min.	Max.	μ	σ
$Al(OH)_3(a)$*	-0.56	-0.20	-0.40	0.15	-0.74	-0.38	-0.52	0.19	-1.71	-0.31	-1.01	0.99	-1.62	-1.19	-1.46	0.23
Al_2O_3†	-3.04	-2.27	-2.66	0.32	-3.22	-2.61	-2.82	0.35	-4.28	-2.47	-3.38	1.28	-4.52	-3.68	-4.20	0.45
$Fe_3(OH)$ (a)*	-3.15	-2.54	-2.95	0.28	-3.73	-2.98	-3.47	0.42	-6.40	-1.76	-4.08	3.28	-6.06	-4.75	-5.41	0.93
Gibbsite ($Al(OH)_3$)*	2.21	2.54	2.33	0.15	2.01	2.35	2.20	0.17	1.05	2.41	1.73	0.96	1.10	1.52	1.27	0.22
Goethite (FeOOH)*	2.43	3.20	2.80	0.32	1.90	2.76	2.31	0.43	-0.80	4.03	1.62	3.42	-0.44	1.08	0.32	1.07
Lepidocrocite (FeOOH)†	0.40	1.02	0.61	0.28	-0.18	0.57	0.09	0.42	-2.89	1.78	-0.56	3.30	-2.55	-1.24	-1.90	0.93
Kaolinite ($Al_2O_3.2SiO_2.2H_2O$) *	5.27	6.36	5.71	0.49	5.04	5.76	5.45	0.37	1.97	5.22	3.60	2.30	3.71	5.24	4.26	0.85
Illite ($K,H_3O)(Al, Mg, Fe)_2(Si, Al)_4O_{10}[(OH)_2,(H_2O)]$*	1.65	3.15	2.30	0.69	1.13	2.46	1.85	0.67	-3.59	1.43	-1.08	3.55	-1.27	0.92	-0.41	1.17
K-feldspar ($KAlSi_3O_8$)*	-1.05	-0.10	-0.62	0.43	-1.39	-0.58	-0.96	0.41	-4.25	-1.32	-2.79	2.07	-2.91	-1.35	-2.29	0.83
Albite ($NaAlSi_3O_8$)*	-4.06	-3.21	-3.61	0.37	-4.40	-3.46	-3.82	0.51	-7.73	-4.64	-6.19	2.18	-4.64	-3.09	-4.04	0.83
Anorthite ($CaAl_2Si_2O_8$)*	-4.30	-3.05	-3.65	0.61	-5.01	-3.28	-4.06	0.88	-9.94	-4.43	-7.19	3.90	-8.14	-6.58	-7.46	0.80
Muscovite ($KAl_2Si_3AlO_{10}$)*	9.01	10.55	9.63	0.72	8.20	9.71	9.03	0.77	3.42	9.09	6.26	4.01	4.89	7.29	5.85	1.27
Phlogopite ($KMg_3AlSi_3O_{10}(OH)_2$)•	-17.25	-14.83	-16.10	1.05	-18.20	-15.00	-16.94	1.70	-25.76	-17.35	-21.56	5.95	-24.43	-22.60	-23.54	0.92
Hydroxyapatite ($Ca_{10}(PO_4)_6(OH)_2$)*	-7.33	-5.19	-6.06	1.03	-6.89	-3.97	-5.80	1.59	-15.08	-8.22	-11.65	4.85	-16.37	-13.82	-15.49	1.45
Quartz (SiO_2)*	0.00	0.24	0.12	0.10	0.11	0.13	0.12	0.01	-0.47	-0.21	-0.34	0.18	0.32	0.69	0.45	0.21
Hematite (Fe_2O_3)*	6.82	8.40	7.58	0.66	5.77	7.52	6.61	0.88	0.38	10.05	5.22	6.84	1.10	4.16	2.63	2.16

Notes:

*[1] PHREEQC thermodynamic databases used to calculate mineral saturation indexes: *phreeqc.dat; •wateq.dat; †minteq.dat; The symbol 'μ' represents the sample mean of the parameter, while the notation 'σ' identifies the calculated standard deviation.*

[2] Although the most common mica variety in granite is biotite (K(Mg,Fe)3(AlSi3O10)(F,OH)2), the thermodynamic databases used only consider the more magnesian variety (phlogopite). Therefore, the hydrogeochemical stability of biotite is inferred to be similar to that of phlogopite.

The results show that amorphous and poorly crystalline Al and Fe oxides and hydroxides (Al(OH)3(a), Al2O3, and Fe3(OH)(a)) are unsaturated in the aquifer, meaning they are more likely to dissolve. More crystalline Al and Fe oxyhydroxides (gibbsite, goethite and lepidocrocite) are generally saturated, but can be unsaturated in some wells. Kaolinite is supersaturated in all wells, but illite may occasionally become unsaturated. Among the primary mineral phases, K-feldspar, albite, anorthite, phlogopite, and hydroxyapatite are consistently undersaturated. Muscovite is saturated, and quartz is in equilibrium with the aquifer water.

Hematite is consistently supersaturated and does not serve as a possible source of Fe for the aquifer. The inclusion of hematite in the analysis is to demonstrate that more stable and highly crystalline Al and Fe mineral phases are rarely found in an undersaturated condition, unlike more common oxyhydroxides found in soil environments. Nonetheless, it cannot be discarded that some fraction of Fe and Al could come from complexes that passed through the 0.22 µm filter (even after taking all precautions), and therefore, their presence might be associated with moving colloids. This is a limitation inherent to the technique.

5.3.4.4. Dissolved inorganic carbon (DIC) and carbon isotopes (δ^{13}C-DIC)

DIC levels for wells M3B, M3C, and M4C consistently remained below 42 ppm C across all seasons, maintaining an average of 19.5 ppm C. In contrast, the shallower wells (M1A to M4B) consistently exhibited values exceeding 37 ppm C, with an average of 56.7 ppm C. When considering factors such as pH, temperature, and ambient pressure, these values align with average dissolved CO_2 concentrations of 56.5 mg/L and 112.3 mg/L, respectively. The isotopic signature of DIC (δ^{13}C-DIC) in the sampled wells displayed a global variation ranging from -2.9 ‰ (observed in well M1B) to -10.7 ‰ (representative of well M4C), indicating significant differences in the area. Wells M1A to M2B and well M3C had medians between -4 and -5 ‰, reflecting slightly enriched ^{13}C waters. On the other hand, wells M4A, M4B, and M3B exhibited relatively depleted ^{13}C values, with medians between -6 and -6.95 ‰. Notably, well M4C showed the lowest values, with a median equivalent to -9.15 ‰, indicating even greater ^{13}C depletion (Figure 5.9). This variation suggests that different processes are responsible

for the natural isotopic signature, rather than a single carbon source for DIC, which will be further discussed.

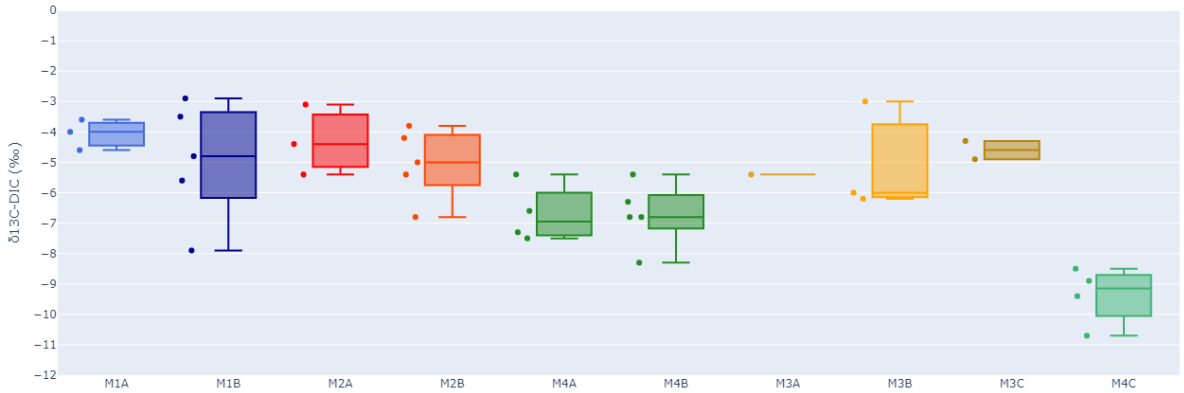

***Figure 5. 9**. Global variation of δ¹³C-DIC background of all sampled wells.*

5.4. Discussion

5.4.1. Hydrochemical type of groundwaters

Analyzed groundwaters have been plotted using Chadha's diagram (CHADHA, 1999) to classify samples into different water types (Figure 5.10). In this diagram, the difference in milliequivalent percentage between alkaline earths (Ca^{2+} + Mg^{2+}) and alkali metals (Na^{+} + K^{+}) is plotted against the difference between weak acidic anions (CO_3^{2-} + HCO_3^{-}) and strong acidic anions (Cl^{-} + SO_4^{2-}), allowing the classification of water types into eight sub-types. In this study, it is possible to note that samples from the St unit (M1A to M4B) are grouped in field 5, indicating that alkaline earths and weak acidic anions exceed both alkali metals and strong acidic anions (Ca-Mg-HCO_3 type). This zone is usually attributed to recharging waters.

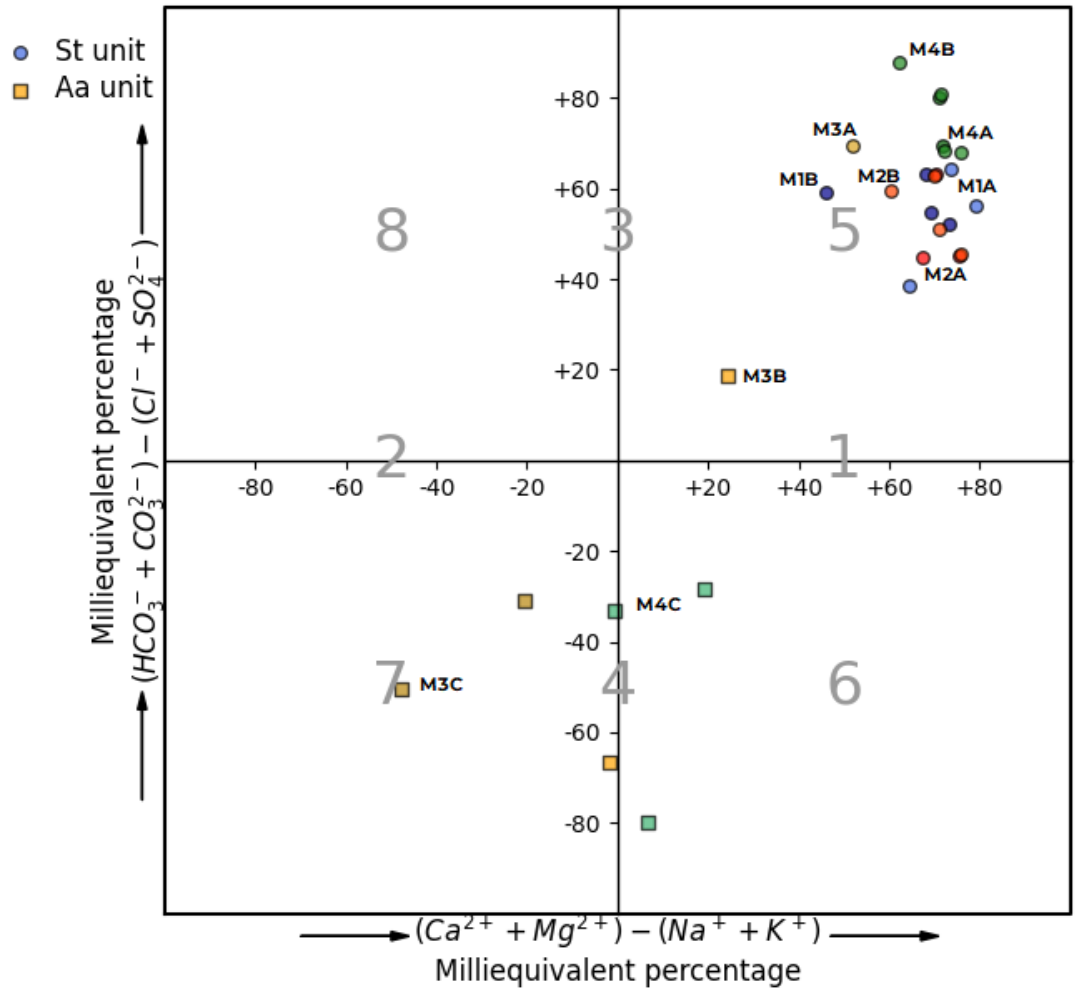

***Figure 5. 10**. Chadha's diagram showing the distribution of samples and its hydrochemical facies in the studied area.*

On the other hand, samples from the Aa unit (mainly M3C and M4C) do not form a concentrated cluster confined to a specific group, plotting either in sub-fields 7 (Na-Cl type) or 6 (Ca-Mg-Cl type), but close to field 4, a region which indicates that strong acidic anions (SO_4^{2-} and Cl^-) exceed weak acidic anions (HCO_3^- and CO_3^{2-}). In this case, the waters from this study area become slightly enriched in Na^+ and Cl^-, which is interpreted as a pronounced effect of Na-feldspars (albite) hydrolysis (a process already noted by Roisenberg et al. (2003)) and the accumulation of Cl^- in deeper zones of the soil profile (a process recognized by Renaud et al. (2023)). Water from M3B plots between these two zones.

5.4.2. Seasonal variation of physicochemical parameters

As can be observed in Figure 5.11, the temperature exhibits a "V" pattern, generally ranging from 23 to 27°C in the summer (represented by campaigns S1, S5, and S8) and between 18 and 16°C in the winter (S3 and S7), with intermediate values (18 to 21°C) in the autumn (S2) and spring (S4 and S6). Additionally, the data show corresponding trends between shallower and deeper wells, as described earlier, with a greater propensity for seasonal variation in the former. Regarding pH, it is noted that it tends to fluctuate in the range corresponding to a neutral to slightly acidic characteristic, regardless of the climatic season. For shallow wells (M1A, M1B, M2A, M2B, M4A, and M4B), the pH varied relatively consistently between 5.7 and 6.5, remaining nearly in that range from S1 to S6, with a slight increase in the last campaign (S8). Alternatively, the pH of wells M3B and M4C tended to stay within the range of 5.2 to 5.6 during most campaigns, except for the last one, when it showed an increase above 6.1.

EC exhibited a more homogeneous behavior throughout all campaigns, with a slightly higher level during the summer of different years. Among wells M3B, M3C, and M4C, this variation remained in the lower range, between 100 and 200 µS/cm, while for wells M1A to M2B, it generally ranged between 200 and 300 µS/cm. For wells M4A and M4B, this level was mostly between 400 and 500 µS/cm. The ORP data showed a variation in an inverted "V" pattern, with predominantly oxidizing conditions - highlighted by values above 0 (zero) mV - between campaigns S2 and S7, and reducing situations (with negative values) in campaigns S1 and S8. Overall, the values remained relatively constant between +85 and +180 mV for almost all wells, except for M4A and M4B. In these wells, the values frequently fluctuated between -50 and +100 mV during S2 and S7, while they had values below -70 mV in campaigns S1 and S8.

Lastly, DO presents slightly higher values during the winter months (S3 and S7) and, to a lesser extent, in the spring (S4). During the summer months (S1, S5, and S8) and autumn (S2), the values are slightly lower. However, the values fluctuate in the range between 2 and 3 mg/L of O2. This behavior is more evident in shallow wells (M1A to M2B) but imperceptible in deeper wells (especially M3C and M4C), where the values show a decreasing pattern between S2 and S8, transitioning from values between 6 and 7 mg/L to values below 4 and 2 mg/L, respectively.

Although this behavior is not straightforward, and the higher concentration of dissolved oxygen in deeper sampled intervals might appear incoherent at first glance, the transport of oxygen to the phreatic zone from the vadose is a theme already documented (ROSE; LONG, 1988; WINOGRAD; ROBERTSON, 1982). In this study's case, some factors could be contributing to this cause: i) wells M3B, M3C, and M4C display colder water temperatures than shallower ones (meaning they can hold more dissolved oxygen comparatively), which is an inverse correlation already shown by Foulquier et al. (2009); ii) these wells experience moments of less recharge and depletion of water during dry periods, causing the screened interval to be exposed to oxidizing conditions (their ORP values are constantly above 100 mV, Figure 5.6), which could also implicate in a higher DO; and iii) DO is especially higher during winter and spring (Figure 5.11), which coincides with seasons of heavy rain (high rainfall rate in a short time, Figure 5.5), and this colder rain could transport dissolved oxygen to deeper portions as already shown by Datry et al. (2004) and Foulquier et al. (2010).

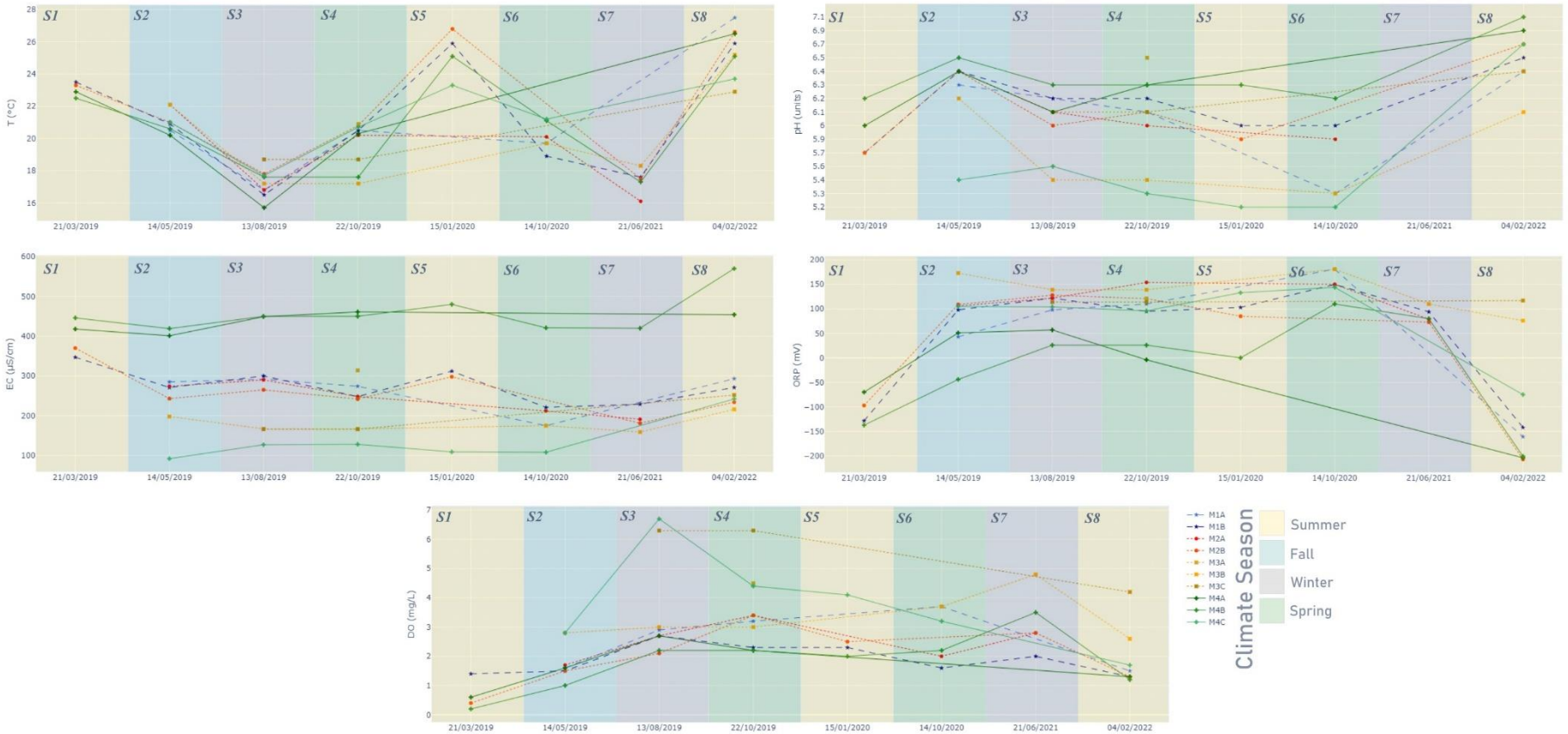

Figure 5. 11. *Seasonal variation of physicochemical parameters of the sampled wells across the representative climatic seasons of each campaign.*

5.4.3. Seasonal influence on groundwater geochemistry and mineral saturation indices

From a seasonal perspective, the concentrations of major cations K and Na, and trace elements (Fe, Ba, Mn, Al, B, and Zn) are proportionally higher in the summer, spring, and autumn periods (S2, S4, S5, S6, and S8) compared to winter (S3 and S7) in both St and Aa units, although this is more noticeable in the St unit. This pattern can be seen in Figure 5.12, where the upper right dashed square appears more populated by data from these climatic seasons. This behavior suggests that secondary alteration minerals, predominant in the upper St unit, might be chemically weathered due to higher temperatures, which favor the increase of dissolved ions in groundwater (RIEDEL, 2019). It is also possibly linked to higher PCO_2 (lower pH), which enhances the release of ions present in the aquifer matrix (KEATING et al., 2010b). Although less significant, the solute concentration increase due to a higher evaporation rate during summer cannot be totally discarded as another mechanism influencing the results(ZHU; SCHWARTZ, 2011).

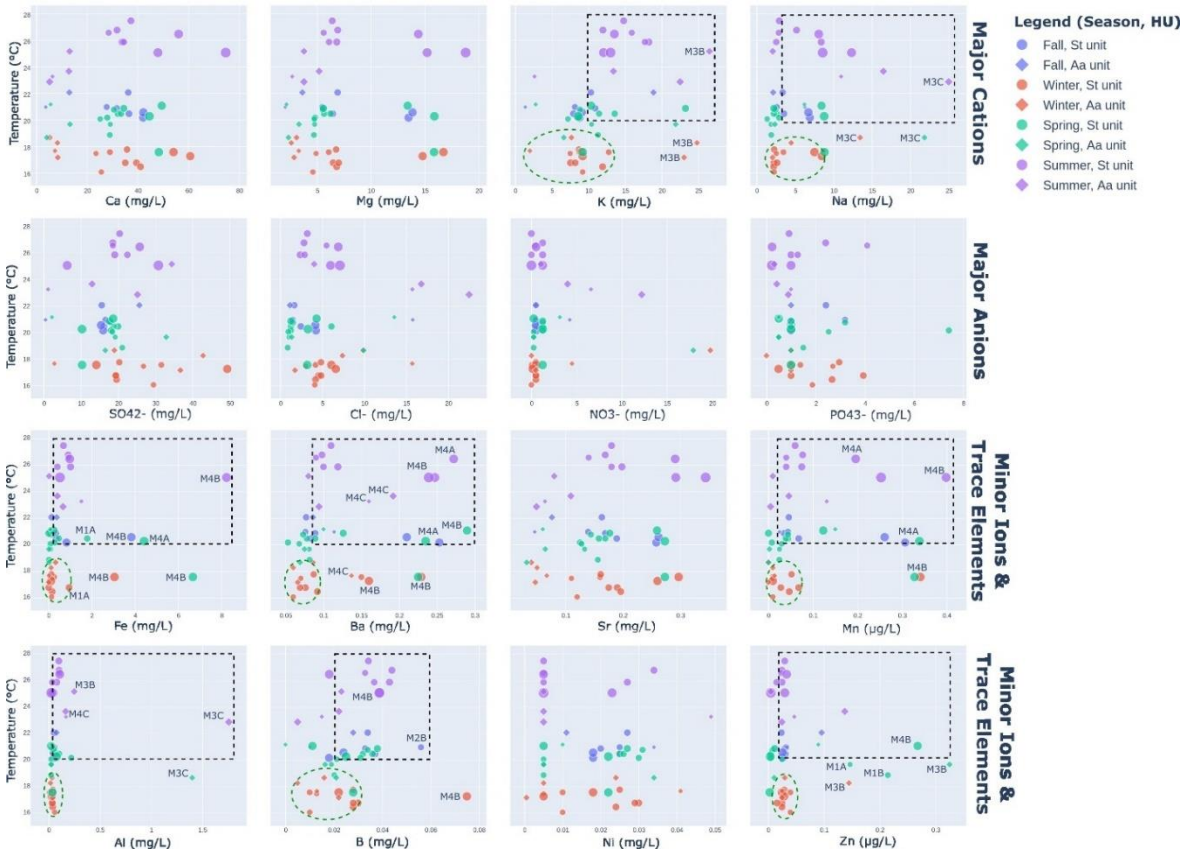

Figure 5. 12. *Scatter plot illustrating the relationship between major ions (cations and anions) and minor ions & trace elements concentrations with temperature across different climatic seasons according to each hydrostratigraphic unit. Dashed black squares symbolize a set of samples that show a relative increase in concentration (even if slightly) in the warmer seasons compared to winter (dashed green circles). Note that some wells have been highlighted to emphasize well-by-well increases that might not be clear at first.*

On the other hand, major cations Ca and Mg, and minor ions Sr and Ni, do not show an evident increase in the warmer seasons. This suggests that under the conditions of this case study and the observed temperature and pH variations over the seasons, these elements do not significantly differ from one season to another. Assuming the main source of these elements is the Ca-rich feldspar anorthite (since lime application for pH correction has not been carried out for at least the past 10 years), the dissolution rate of this mineral might remain nearly constant or insignificantly changed under the observed variations during the monitoring period.

Higher NO_3^- concentrations during this period are primarily related to the Aa unit wells (M4C and M3C) connected to the deeper fractured crystalline aquifer. These align with values reported by (ROISENBERG; VIERO; ROISENBERG, 2003), who attributed the origin of this compound to either contamination, decomposition of organic matter and rain water, with no direct relation with the granite. Elevated NO_3^- levels can also result from organic fertilizer degradation and nitrogen residues, especially at higher temperatures (PASTÉN-ZAPATA et al., 2014). Abnormal concentrations of cations and trace elements (especially Ca, Mg, Na, K, Fe, Mn, Sr, and Ba) in wells M4A and M4B - compared to other wells in St unit - can be explained by the accumulation of dissolved ions in topographically low areas, where there is convergence of surface runoff and groundwater flow (ADAMS et al., 2001; DELIN; LANDON, 2002; YAN et al., 2017), causing a local hydrochemical anomaly.

Conversely, concentrations of the anions SO_4^{2-}, Cl^-, and PO_4^{3-} remain elevated across all seasons, exhibiting weak correlation with temperature. This pattern suggests that these solutes originate independently from the aquifer's mineralogy, indicating external sources. The most plausible origins for these elements are atmospheric deposition, residual NPK fertilizer dissolution, and/or decomposition of organic matter from animal sources (DOMAGALSKI; JOHNSON; SURVEY, 2012; POROWSKI;

POROWSKA; HALAS, 2019; ROISENBERG; VIERO; ROISENBERG, 2003; TORRES-MARTÍNEZ et al., 2020).

As the increase in dissolved CO_2 will contribute to the acidity of groundwater, this factor is expected to alter the hydrogeochemical stability of minerals present in the aquifer. Therefore, understanding SI in background water establishes a baseline to assess climate-driven changes. The data show that although seasonal influence affects SI, shifts from undersaturation to supersaturation are rare, except for wells M3B and M4C (goethite, lepidocrocite, and illite). During the CO_2 injection phase (which will be carried out in a future phase), the alteration of saturation conditions and the interactive process with the aquifer mineralogy will be comprehensively examined.

5.4.4. Carbon isotopes ($\delta^{13}C_{\text{-DIC}}$) and CO_2 sources

Due to the complexity of the isotope signature in background groundwaters, the Miller-Tans plot (MILLER; TANS, 2003) Figure 5.13), which plots δ^{13}C-DIC x DIC against DIC concentration (Table 5.5), were used to differentiate possible CO_2 sources to the DIC of the groundwater. The line depicting the overall linear trend of data (R^2=0.76) effectively segregates two groups: i) those above the line, mostly comprising wells with a δ^{13}C-DIC median around -6 ‰ or higher, and ii) those below the line, primarily including wells with a δ^{13}C-DIC median below -6 ‰. Applying the analytical data of δ^{13}C-DIC and referring to the equations by Clark and Fritz (1997) and Clark (2015) (Equations (1) to (7), Supplementary Information), the isotopic ratio of the DIC source ($\delta^{13}C\text{-}CO_2$) could be deduced, considering an isotopic equilibrium between them.

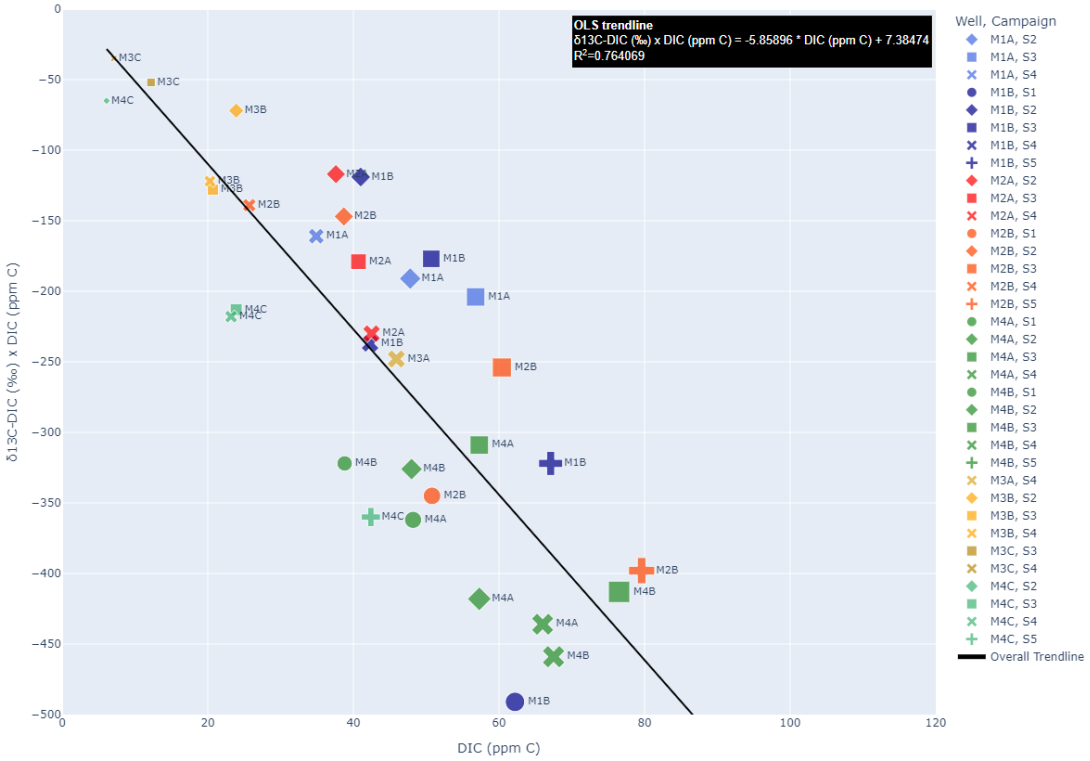

***Figure 5. 13**. Miller-Tans plot demonstrating the relationship between δ¹³C-DIC x DIC as a function of DIC concentration in the samples.*

***Table 5. 5.** DIC concentration (ppm C) and δ¹³C-DIC (‰) isotopic signatures of samples evaluated.*

Well	Sampling Campaing	DIC (ppm C)	δ13C-DIC (‰)
M1A	S2	47.84	-4.04
M1A	S3	56.78	-3.643
M1A	S4	44.31	-4.61
M1B	S2	40.99	-2.85
M1B	S3	50.71	-3.484
M1B	S4	42.33	-5.621
M1B	S5	67.06	-4.777
M2A	S2	37.6	-3.05
M2A	S3	50.03	-4.356
M2A	S4	42.48	-5.425
M2B	S2	38.67	-3.82
M2B	S3	60.42	-4.216
M2B	S4	37.6	-5.44

M2B	S5	79.61	-5.015
M3A	S4	45.91	-5.371
M3B	S2	23.92	-2.99
M3B	S3	20.73	-6.166
M3C	S3	12.23	-4.287
M3C	S4	7.1	-4.918
M4A	S2	57.34	-7.25
M4A	S4	71.03	-6.559
M4B	S2	48.01	-6.84
M4B	S3	76.48	-5.387
M4B	S4	75.24	-6.835
M4B	S5	115.09	-6.327
M4C	S2	6.14	-10.68
M4C	S3	23.87	-8.874
M4C	S5	42.45	-8.455

As can be noted, $\delta^{13}C\text{-}CO_2$ values for wells M1A, M1B, M2A, M2B, and M3B generally fall between -6 and -8 ‰. This range corresponds to the isotopic ratio of atmospheric CO_2 (Sharp 2017; Hoefs 2021), implying these shallow wells maintain isotopic equilibrium with the atmosphere. However, M4A, M4B, M4C, and occasionally M3C exhibit slightly depleted $\delta^{13}C\text{-}CO_2$ values, spanning from -8.1 to 11.3 ‰, aligning with CO_2 produced in soil through C4 plant decay (VIETH; WILKES, 2010). Though these samples show a somewhat enriched ratio compared to C4 plants, it can be attributed to the diffusive effect of ^{12}C towards the atmosphere, causing a slight ^{13}C enrichment in the soil. This results in a $\delta^{13}C$ value less negative than -10 ‰. These findings corroborate the pattern observed in the Miller-Tans plot, revealing two main carbon sources influencing the two hydrostratigraphic units differently, although not exclusively to the St or the Aa unit.

5.4.5. The importance of seasonal background monitoring

The usefulness of groundwater monitoring in CCS projects relies on the potential of a leakage signal detection using conventional hydrogeochemistry, which offer a well-established, usually low-cost, and reliable set of approaches. Nonetheless, as pointed

out by Jones et al. (2015), tracking CO_2-impacted groundwater plume is complex due to its spatially restricted nature (as they tend to be long and narrow due to a constant groundwater flow direction of the overlying aquifer), which makes the monitoring and the discovery of its presence much more difficult. Zielinski et al. (2023) also showed in a thorough review that numerous studies on controlled-release CO_2 in shallow groundwater exhibited the detection of elements freed from the aquifer mineral framework in a high frequency sampling setting, which is not always the case. Besides, they also found that seasonal background monitoring is usually not considered in this type of studies, making its reproducibility in real cases not straightforward.

One possible approach to overcome these issues is to monitor the natural range of seasonally influenced overlying shallow aquifers and establish the upper and lower limits within which groundwater parameters usually fall. A similar idea was proposed by Berger et al. (2019), although they argued in favor of creating statistically determined limits that depend on each parameter's sensitivity to CO_2. Here, the data regarding the seasonal hydrochemical variation of the analyzed parameters in the two aquifer units were assessed using individual control charts, also known as Shewhart Charts (IGLESIAS et al., 2016; SWAMIDASS, 2000). The aim was to observe the data points collected at specific time intervals to comprehend variations and trends in the background and establish the upper and lower bounds (Upper Control Limit – UCL and Lower Control Limit - LCL, respectively) of the hydrogeochemical processes involving water-mineral matrix interaction.

Hence, the study conducted by Do et al. (2022), which carried out CO_2 injection tests in a lithological and hydrogeological context that is very similar to the study area of this paper (granite-derived setting) was used as a reference. In their study, the main parameters seen to vary were Ca, Mg, Na, K, HCO_3^-, Mn, Sr, Ba, pH and EC (apart from pCO_2 and $\delta^{13}C$-DIC). Assuming that the variation (increase or decrease) from the average background values were the same as in their case, these parameters would display the following behavior (seen in yellow dashed lines in Figure 5.14): Ca (+56.10 mg/L), Mg (+9.72 mg/L), Na (+28.74 mg/L), K (+2.15 mg/L), HCO3- (+3,355 mg/L), Mn (+148.18 µg/L), Sr (+9.19 µg/L), Ba (+65.99 µg/L), pH (-1.28 unit) and EC (+488 µS/cm).

Tacking this example, depending in which season the CO_2 controlled release would occur (or, in a real case, when the CO_2 leakage might be manifested), K, Sr and Ba

could not be used as hydrochemical tracers as they fall within the natural variation range and could not be reliably used as indirect indicators of CO_2 leakage. On the other hand, Ca, Mg, Na, HCO3-, Mn, pH and EC could potentially be used since their natural seasonal variation are restricted to their respective UCL and LCL, and theoretically expected increase and decrease are at least some units out of this range (Figure 5.14).

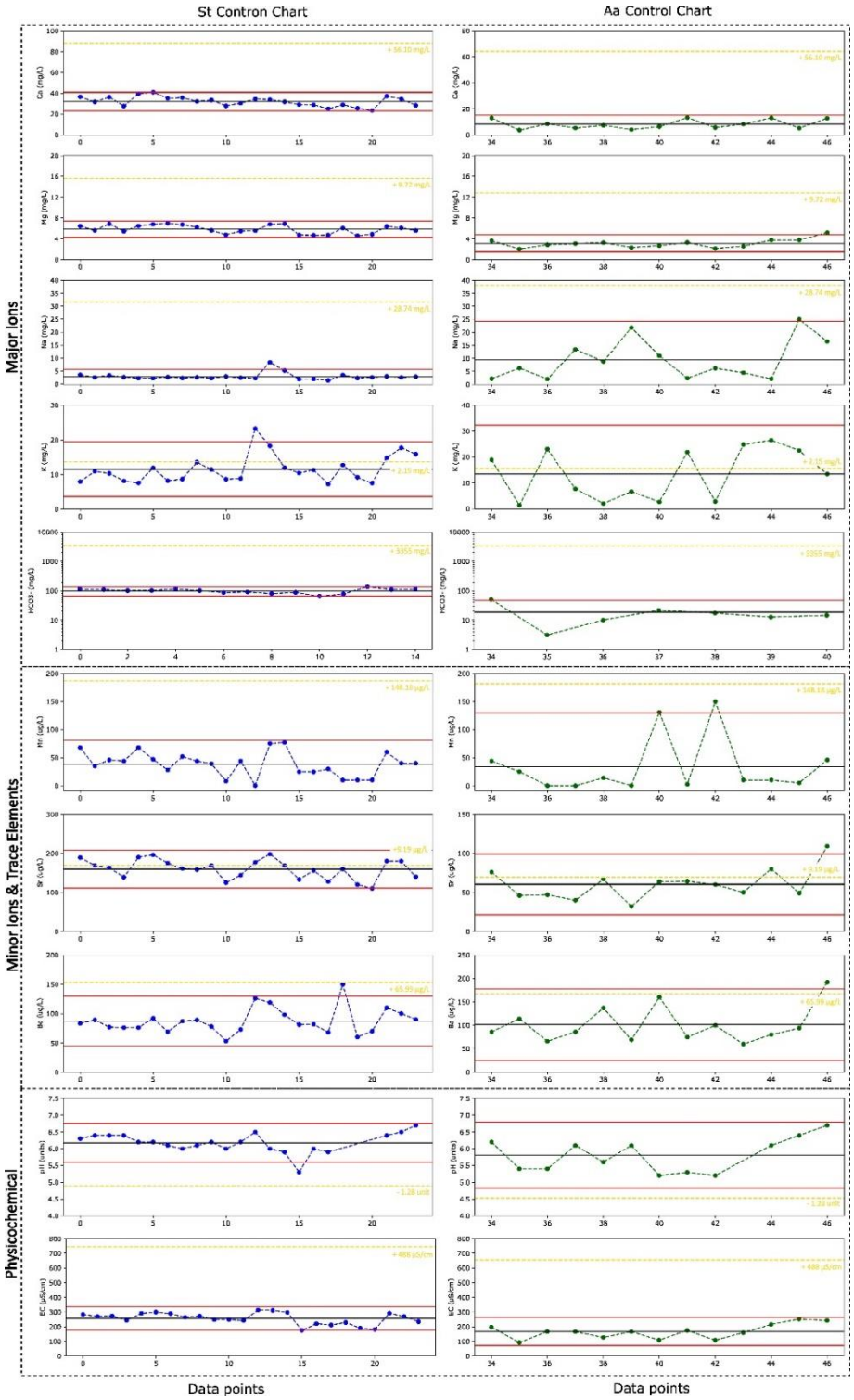

Figure 5. 14. *Individual control chart of some hydrochemical parameters showing natural seasonal variation observed in wells M1 and M2 (St unit) and M3 and M4 (Aa unit). Center line (solid black) indicate the mean value. Solid red lines represent both the Upper Control Limit (UCL) and Lower Control Limit (LCL). Dashed yellow line indicate maximum alteration values either at 22 or 26m-distance wells described in* Do et al. (2022)*.*

5.5. Conclusions

In summary, this study has uncovered crucial insights into the importance of the hydrogeological site characterization and the development of an extended hydrogeochemical baseline survey for the purpose of establishing CO_2 MMV plans in order to track unintended leakage to shallow aquifers in CCS project locations. Multilayer aquifers systems can pose particular difficulties for a correct diagnostic of hydrochemical patterns, specially in contexts with open connection to recharge waters and underlying aquifers. Hence, after presenting the results and discussion outlined in this study, the following conclusions can be drawn:

1. Although the study area is set in a simple geological context (granite-altered setting), an in-depth investigation revealed that a multilayer phreatic aquifer is present in the first 9 to 10m of the altered soil horizon with two units clearly exhibiting distinct lithological, hydraulic, geophysical and hydrochemical characteristics;
2. The St unit is mainly composed of a silty-sized material, with hydraulic conductivity in the order of 10-4 m/s, and with apparent resistivities usually lower than 40 Ohm.m. This unit is notably more prone to recharge fluctuations and exhibit a water level pattern that clearly shows this behavior. Hydrochemically, this unit shows a slightly neutral pH, and higher amplitudes of temperature, EC, ORP and DO, apart from the higher concentrations of Ca, Mg, K, Fe, Mn, Sr, B, HCO3-, and DIC, and the water's isotopic signature (δ^{13}C-DIC) varies from approximately -3 to -8 ‰;
3. The Aa unit is mainly composed of a sandy clay material, with hydraulic conductivity in the order of 10-8 m/s, and with apparent resistivities usually between 40 to 80 Ohm.m. This unit is less prone to recharge fluctuations and exhibit a water level that sometimes reach the bottom of the well in dry periods. Hydrochemically, this unit shows a slightly acidic pH, and lower amplitudes of temperature, EC and ORP, but higher DO fluctuation. Additionally, it displays higher concentrations of Na, SO_4^{2-}, Cl^-, NO_3^-, Zn, Al, Ni, and lower levels of HCO_3^- and DIC, and the water's isotopic signature (δ^{13}C-DIC) appears slightly more depleted (ranging between -6 to -11 ‰);
4. A 3-year long seasonal monitoring campaign revealed that K, Na and trace elements Fe, Ba, Mn, Al, B, and Zn) are clearly affected by temperature-derived

seasonal interferences (higher dissolution rate and PCO_2), as their concentrations are proportionally higher in the summer, spring, and autumn compared to winter. On the other hand, Ca, Mg, Sr and Ni do not appear to be influenced by seasonal differences in temperature or slightly higher PCO_2 (lower pH). This dynamism will be taken into consideration during the CO_2 injection phase and further interpretation of the results; and

5. Control Charts serve as valuable tools in comprehending the natural hydrochemical trends inherent in the background. When assessing past studies in a comparable hydrogeological context and preparing for future CO_2 injection at this site, these charts provide the chance to selectively consider or exclude certain parameters (such as K, Sr, and Ba, as discussed in the study by Do et al. (2022) and referenced here).

CAPÍTULO 6: Hydrogeochemical changes in a silicate-dominated aquifer during a controlled CO_2 release: insights for monitoring unintended CO_2 leakage at CCS sites

*Esse capítulo será submetido à revista '**Applied Geochemistry**'.*

Abstract: Groundwater quality alteration due to potential unintended CO_2 leakage at carbon capture and storage (CCS) sites is a critical environmental concern and is often cited as a socio-environmental barrier to public acceptance. Although CO_2 itself is not a contaminant, its excessive concentration can induce geochemical reactions with aquifer mineralogy, making it essential to evaluate these potential consequences. Despite recent advances in understanding the geochemical imprint of CO_2-impacted aquifers, there remains a limited number of studies focused on silicate-dominated aquifers rich in altered minerals under near-surface conditions, where precipitation can significantly influence these processes. Thus, this study aims to evaluate the CO_2-groundwater-mineral interactions within a shallow aluminosilicate porous aquifer, derived from granite, at the TECNOPUC-Viamão CO_2 experimental site in Southern Brazil. The primary objectives are to identify hydrogeochemical alterations and to determine key indicators that signal these processes. Gaseous CO_2 was injected at varying rates (5, 10, and 12.5 kg/day) at approximately 3 meters below ground level, with groundwater samples frequently collected from multilevel monitoring wells within a 5-meter radius. The CO_2 injection spanned 46 days, following a background monitoring campaign, and was succeeded by a two-week post-injection phase, culminating in a final sampling campaign conducted 137 days after the injection ceased. Hydrochemical evolution of the CO_2-groundwater-mineral interaction was tracked through physicochemical and chemical analyses of major, minor, and trace elements. Despite the influence of atmospheric precipitation on certain parameters, a strong correlation ($R^2 > 0.60$) was observed between the partial pressure of CO_2 (PCO_2) and variables such as Electrical Conductivity (EC), pH, ORP, Total Alkalinity (TA), Ca, Mg, K, Na, Si, Ba, Sr, Fe, Mn, PO_4^{3-}, and HCO_3^- in the impacted wells. A linear chronological evolution pattern with increasing injection rates was noted for EC, TA, Ca, Mg, K, Na, Si, Ba, Sr, Fe, and HCO_3^- in the closest wells. Taking into account the natural seasonal hydrogeochemical variability and the control chart constructed for

the hydrostratigraphic unit, the sensitivity to CO_2 interaction, including seasonal effects, indicates that EC, Ca, Mg, Fe, HCO_3^-, Ba, Sr, and Mn provided a consistent diagnosis of the interaction. Concerning the risk to water quality, Fe and Mn concentrations exceeded the limits set by both national and international regulations. This study suggests that this suite of variables enables an effective diagnosis and assessment of the impact of unintended CO_2 leaks in CCS projects, provided they are adequately monitored within a well-established seasonal background.

Keywords: CO_2 leakage, hydrogeochemistry, silicate, monitoring, release experiment

6.1. Introduction

Carbon Capture and Storage (CCS), sometimes also referred as Geological Carbon Storage (GCS), is increasingly recognized as a critical strategy for mitigating climate change by reducing CO_2 emissions to the atmosphere (AZAR et al., 2006; BENSON; COLE, 2008; IPCC, 2005a; NELSON et al., 2005; OELKERS; COLE, 2008). This technology aims to securely store CO_2 in deep underground formations, preventing its release and thus alleviating stress on the Earth's climatic system. However, the geological complexity of storage sites, which may include faults, fractures, and small cracks in caprocks, introduces significant challenges. Should CO_2 leakage occur at a CCS site, the solubility of CO_2 in water can lead to the formation of carbonic acid, resulting in localized acidification of shallow groundwater above the storage site (ASSAYAG et al., 2009). This acidification can have profound impacts on groundwater quality by enhancing the dissolution of aquifer rocks, thereby increasing the concentrations of cations and potential trace metals (BENSON et al., 2002; LAWTER et al., 2016; QAFOKU et al., 2017; WANG et al., 2016b; XIAO et al., 2017).

Further geochemical reactions, such as ion-exchange, surface complexation, and the precipitation of secondary minerals, can also alter groundwater chemistry due to CO_2 leakage (CAHILL; JAKOBSEN, 2015b; ZHENG et al., 2012b). The potential migration of CO_2 and CO_2-rich fluids into freshwater aquifers can degrade drinkable groundwater, highlighting the importance of comprehensive environmental monitoring systems. A previously shown, hydrochemical and isotopic analyses have proven essential for detecting CO_2 leakage and assessing its impact on groundwater quality (HUMEZ et al., 2014c; KHARAKA et al., 2010c; NEWELL et al., 2014b; SCHULZ et

al., 2012c). Understanding the pattern and degree of geochemical changes at specific sites is crucial not only for detecting leakage but also for managing the undesirable effects, such as the mobilization of toxic elements and the reduction of the aquifer's buffering capacity (LIONS et al., 2014b). Addressing these risks through rigorous monitoring, including the use of hydrochemical indicators and environmental sensors, is vital for the safe, long-term, and effective storage of CO_2. These measures are necessary to mitigate public concern and to ensure the successful demonstration and commercialization of GCS technology (CUÉLLAR-FRANCA; AZAPAGIC, 2015).

Consequently, implementing effective Monitoring, Measurement, and Verification (MMV) strategies is crucial for ensuring the safe storage of CO_2 in deep geological formations and for gaining public acceptance of these technologies. A key and cost-effective approach to better understand the interactions between CO_2, groundwater, and minerals is the controlled injection of CO_2 into the subsurface. This method allows researchers to track hydrogeochemical changes within the aquifer, providing valuable insights into the processes governing CO_2 behavior and its potential impacts on groundwater quality.

Several studies employing this approach have been published over the past 15 years (LEE et al., 2016c; ZIELINSKI et al., 2023), documenting changes in groundwater chemistry resulting from interactions with CO_2 and aquifer mineralogy, including carbonate, mixed-mineralogy, and silicate-dominated systems. These studies have been conducted under a range of hydraulic conductivities - low (≤ 2 m/day), intermediate (2–20 m/day), and high (≥ 20 m/day). Additionally, they have varied the total mass and rate of leaked CO_2, the duration of injection, and the timing of pre- and post-injection monitoring campaigns. This variation in parameters allows for the simulation of a broader range of hydrogeochemical responses that might occur in different leakage scenarios. While still limited in number, these studies have collectively advanced the understanding of potential impacts of CO_2 leakage on groundwater quality. However, only a limited number of studies have assessed the effects of silicate-dominated aquifers rich in altered minerals, such as clays and oxides (DO et al., 2022d), under shallow conditions (KHARAKA et al., 2010d). These conditions are particularly important as they influence the geochemical signature of CO_2-impacted groundwater during precipitation events.

Furthermore, to the best of the author's knowledge, no studies have yet conducted experiments that combine these characteristics within a humid subtropical climate. Thus, the primary objective of this study was to design and implement a controlled CO_2(g) leakage experiment within a shallow groundwater aquifer located in a silicate formation resulting from granite alteration, at TECNOPUC/Viamão in Rio Grande do Sul, southern Brazil (ZIELINSKI et al., 2024). The experiment was conducted under varying CO_2 leakage rates and precipitation events to explore the hydrogeochemical responses and interactions within this geological setting. Spatiotemporal physicochemical and chemical parameters (major ions and trace elements), were monitored through groundwater samples collected from wells positioned both upstream and downstream of the groundwater flow. Multivariate statistical techniques, such as Principal Component Analysis and Correlation Analysis, were employed to identify CO_2-impacted groups and track changes in hydrochemical variables relative to the partial pressure of CO_2 (PCO_2). Additionally, anomalous hydrochemical parameters were compared with long-term (>3 years) natural background variations to assess their sensitivity to CO_2 injection. Parameters exceeding contaminant levels were evaluated against regulatory guidelines and existing studies to assess potential environmental risks to groundwater quality.

6.2. Materials and methods

The TECNOPUC-Viamão controlled-release experimental site (UTM Zone 22, Southern Hemisphere, 494315 mE & 6671940 mN), Rio Grande do Sul state, Southern Brazil, comprehends a practical research field facility of the Pontifical Catholic University of Rio Grande do Sul (PUCRS), which is composed of a granite-derived weathered soil profile, located 20 km away from the state's capital Porto Alegre (Melo et al. 2017; Iglesias et al. 2019; Zielinski et al., 2024). Established in 2015 and covering an area of ca. 6,000 m^2, the field facility – maintained and operated by the Institute of Petroleum and Natural Resources (IPR) - has four sets of three multilevel wells each (Figure 6.1), totaling twelve groundwater monitoring wells (MW) that were designed for water sampling campaigns. Wells are named by the prefix M and a suffix according to their installed depth (Table 6.1).

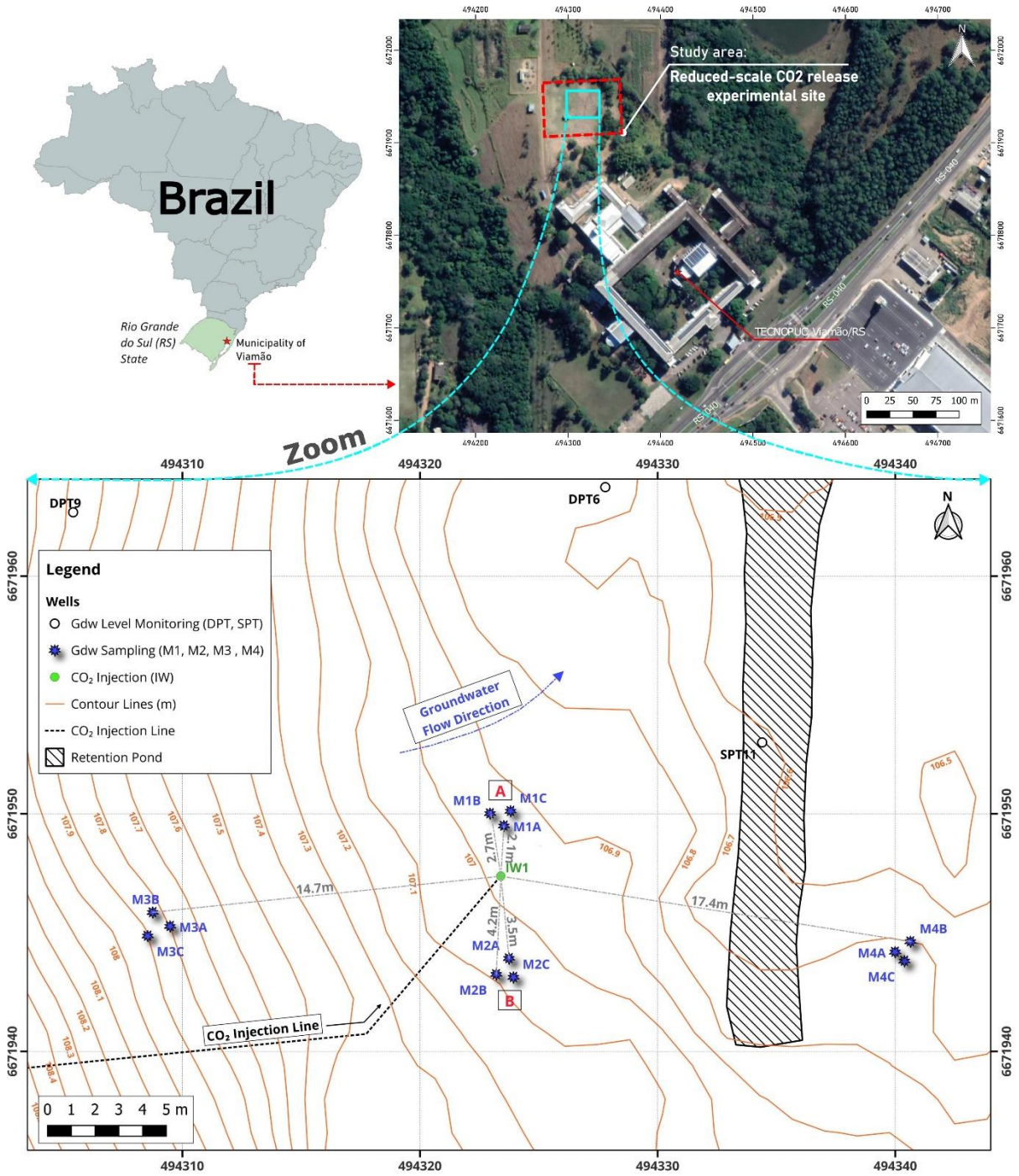

Figure 6.1. *Location map of the small-scale TECNOPUC-Viamão experimental CO_2 release site and the installed infrastructure. Multilevel sampling wells are shown in blue, with gray dashed line symbolizing the linear distance between the injection well (IW1) and each sampling well. Groundwater general trend flow is towards the northeast (NE). Letters A and B (in red) illustrates the transect between M1 and M2, detailed in Figure 6.2.*

***Table 6.1**. Installed water sampling wells and their corresponding screened intervals. Sampling depth indicates the distance from the surface to the point of water extraction, where samples were collected during each sampling campaign.*

Well	Installed depth (m)	Screened Interval (m)	Sampling depth (m)
M1A	1	0.5 - 1	0.75
M2B	2.5	1 - 2.5	2
M2C	3.5	2.5 – 3.5	NS
M2A	1	0.5 - 1	0.75
M2B	2.5	1 - 2.5	2
M2C	3.5	2.5 – 3.5	NS
M3A	1	0.5 - 1	NS
M3B	2.5	1 - 2.5	2
M3C	3.5	2.5 – 3.5	NS
M4A	1	0.5 - 1	NS
M4B	2.5	1 - 2.5	2
M4C	3.5	2.5 – 3.5	NS

Note: depths are referenced by surface (ground) level not the by the tip of the wellhead, and therefore represent depth below ground level (bgl); NS means Not Sampled.

In this study, MW M1A, M1B, M2A, M2B, M3B and M4B were selected and used for hydrochemical and isotopic evaluation of the CO_2-groundwater-mineral interaction evaluation as they were either near the CO_2 injection well or upstream/downstream of the groundwater flow direction.

Based on the described mineralogical composition, vertical soil texture distribution, and characterized hydraulic conductivity, the geological strata were classified into four hydrostratigraphic units (from top to bottom): i) Organic Soil (So); ii) Silt (St); iii) Sandy Clay (Aa); and iv) Altered Granite (Ga). CO_2 injection was conducted within the Sandy Clay (Aa) unit in its gaseous state. Given the natural groundwater flow and the lower density of CO_2 (g), groundwater samples were collected from levels A and B (Figure 6.2).

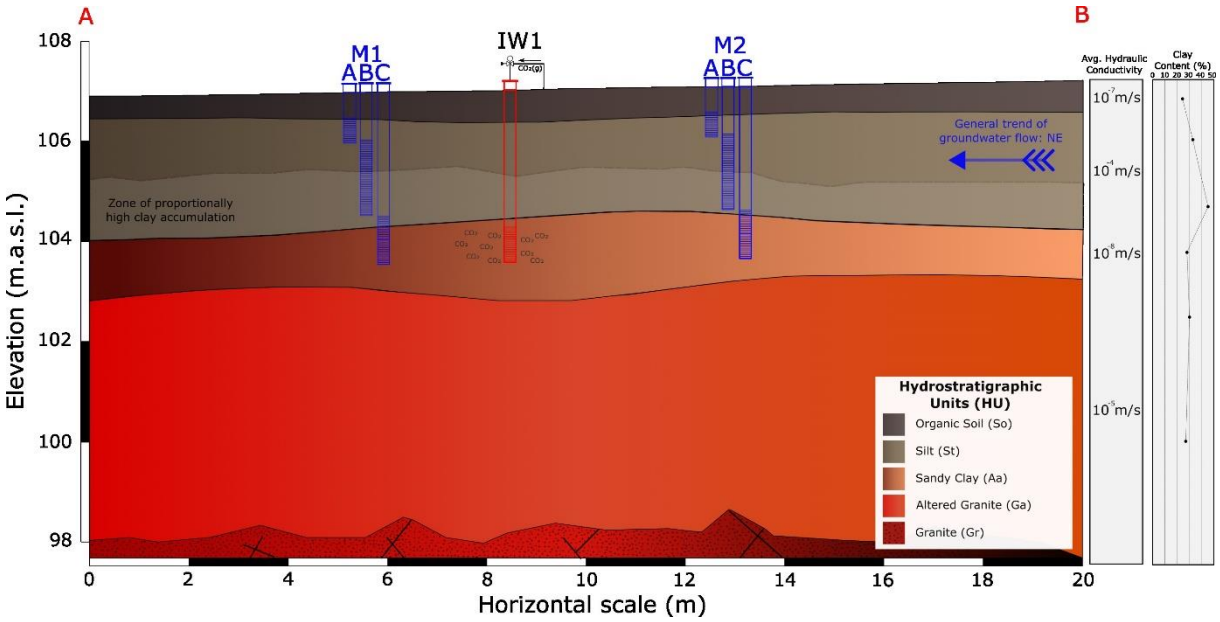

Figure 6.2. *Hydrostratigraphic units and constructive characteristics of the monitoring wells (M1 and M2) and injection well (IW1). Letters A and B correspond to the section referenced in the location map of Figure 6.1.*

The sampled wells within the HU St unit are primarily composed of feldspars, micas, quartz, amphibole, and opaque minerals, with K-feldspar being the most prevalent. Orthoclase is more abundant than microcline and exhibits a range of colors, contributing to variations in the sandy fraction's coloration. Plagioclase (albite-oligoclase) is also present but in lower proportions compared to K-feldspar. Muscovite is the dominant mica, with some occurrences of biotite. Kaolinite is the most abundant clay mineral, while illite and interstratified clay minerals form a secondary fraction, along with trace amounts of goethite and lepidocrocite. For a more detailed discussion on the geological and hydrogeological characteristics, as well as the geoelectrical model of this area, see Zielinski et al. (2024).

6.2.1. Design and execution of the controlled-release CO_2 experiment

The experiment was planned to have three main phases: i) a background, that consisted of three samplings campaigns (SB); ii) an injection phase composed of sixteen samplings (SI); and iii) a post-injection which comprised of five samplings (SP). The first previous one-week immediate background campaign, which defined the groundwater baseline composition and natural hydrochemical range, included the samplings SB1, SB2 and SB3, carried out from January 8 to January 12. The injection

phase took place between January 15 to March 1 (46 days), and included SI4 to SI20. The concentrated post-injection phase occurred between March 5 to March 15 (SP21 to SP24), followed by a final sampling campaign 124 days after March 15 (SP25) to check for groundwater background attainment.

CO_2(g) has been released to the subsurface at the IW1 between 2.7 to 3 m deep, which is at least 0.7 m below the first sampling point of the nearest MW (M1B and M2B). The injection system is composed of an injection plant actionable by an electronic device (backed up by a manual control system) that is directly connected to CO_2 cylinders through a manifold. A Mass Flow Controller (MFC) regulates the injection rate according to a set value. After passing through the release valve, the CO_2 get into the tracer chamber before reaching the injection well, which is equipped with a gas sampling port at the well head (Figure 6.3).

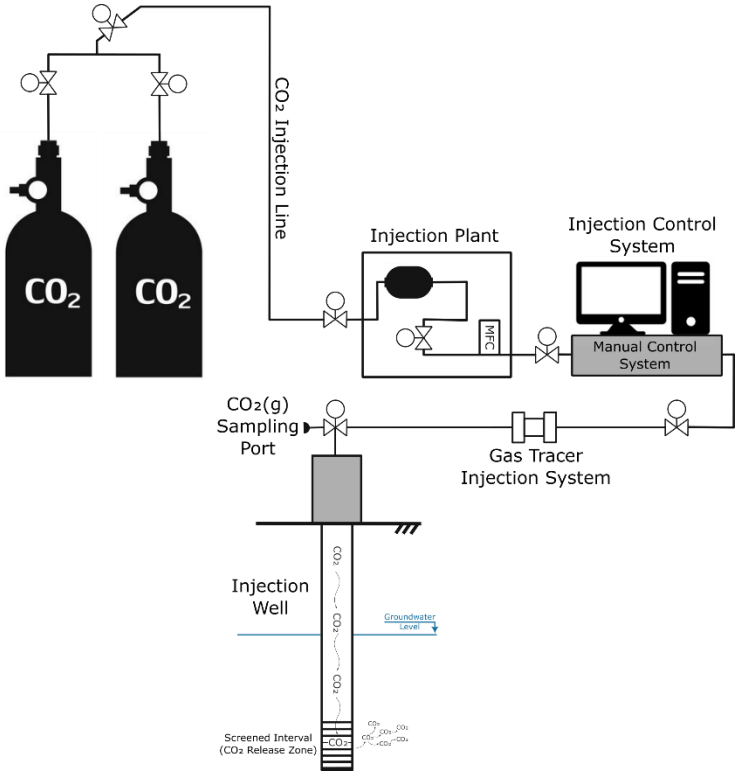

Figure 6.3.*Simplified schematic sketch of the CO_2 injection system and its associated components from the cylinder to the injection well.*

The CO_2 controlled release (injection) started on January 15 with a nominal injection rate of 5 kg of CO_2/day, which was increase to 10 kg of CO_2/day on January 29 due to subtle chances on physicochemical parameters observed onsite during the sampling procedure and to compensate possible dilution caused by rainwater recharge events

that occurred in the period. On February 15 the release rate was again increase to 12.5 kg of CO_2/day for the last two weeks of the experiment to increment CO_2-groundwater-mineral interaction. Injection stopped on March 2 approximately at midnight. Based on the calculations performed, approximately 430 (± 5%) kg of CO_2 was released throughout the injection phase. Precipitation data were obtained from an automated weather station (Plugstation® WS22, Plugfield) installed near the field office (between 50-60 m away from the wells).

6.2.2. Sampling procedure and chemical analysis

Groundwater sampling operations were conducted periodically to track for hydrochemical and carbon isotopic variations as the CO_2 release progressed. A total of 25 sampling campaigns were conducted (Table 6.2), yielding a total of 116 samples: a) M1A (n=17 samples); b) M1B (n=25 samples); c) M2A (n=2 samples); d) M2B (n=25 samples); e) M3B (n=25 samples); and f) M4B (n=22 samples). Sampling was conducted according the low-flow method as specified in the NBR 15847 standard (ABNT, 2010), which is based on ASTM's D6452 (ASTM, 2018) and D4448 (ASTM, 2019) guidelines. A Millipore® Easy-Load peristaltic pump integrated into a closed system flow cell equipped with a QED® MP-20 multiparameter probe provided field measurements for groundwater temperature, hydrogen potential (pH), Electrical Conductivity (EC), redox potential (ORP) and Dissolved Oxygen (DO). Total alkalinity was measured in the lab by titration with a 0.1N H_2SO_4 solution.

***Table 6.2**. Sampling campaigns conducted during background (BG), injection, and post-injection (PI) periods, indicating the number of wells sampled and the relative timing of each campaign with respect to the start date of CO_2 injection.*

Sampling Campaign	***Campaign Phase***	***Days before/since injection***	***Date***	***N° of sampled wells***
SB1	*BG*	*-7*	*Jan 8, 2024*	*3*
SB2		*-5*	*Jan10, 2024*	*4*
SB3		*-3*	*Jan 12, 2024*	*5*
SI 4	*Injection*	*0**	*Jan 15, 2024*	*4*
SI 5		*+3*	*Jan18, 2024*	*4*
SI 6		*+4*	*Jan 19, 2024*	*5*
SI 7		*+7*	*Jan 22, 2024*	*5*
SI 8		*+9*	*Jan 24, 2024*	*4*

SI 9		*+11*	*Jan 26, 2024*	*5*
SI 10		*+14*	*Jan 29, 2024*	*4*
SI 11		*+16*	*Jan 31, 2024*	*5*
SI 12		*+21*	*Feb 05, 2024*	*4*
SI 13		*+23*	*Feb 07, 2024*	*5*
SI 14		*+25*	*Feb 09, 2024*	*5*
SI 15		*+30*	*Feb 14, 2024*	*5*
SI 16		*+32*	*Feb 16, 2024*	*4*
SI 17		*+36*	*Feb 20, 2024*	*5*
SI 18		*+39*	*Feb 23, 2024*	*5*
SI 19		*+44*	*Feb 28, 2024*	*5*
SI 20		*+46†*	*Mar 1, 2024*	*5*
SP21	*PI*	*+50*	*Mar 5, 2024*	*5*
SP 22		*+53*	*Mar 8, 2024*	*5*
SP 23		*+57*	*Mar 12, 2024*	*5*
SP 24		*+60*	*Mar 15, 2024*	*5*
SP 25		*+184*	*July 17, 2024*	*5*
Total sampling campaigns: 25			***Total samples: 116***	

*Note: *First sampling day of the injection campaign; †Last sampling day of the injection campaign. CO_2 injection stopped on Mar 2, 2024.*

Samples were collected with a syringe immediately after indicative physicochemical parameters stabilization, filtered through a 0.22 µm hydrophilic acetate filter (to retain colloidal material) and transferred to 50 mL polypropylene (PP) Falcon-type tubes or 10 mL Exetainer® vials. For dissolved metals analysis, samples were acidified with 50% HNO_3 in the field until pH ≤ 2 and stored to ≤10ºC using a portable cooler. For anion analysis samples underwent only filtration without acidification.

Chemical analyses were either performed at IPR's Laboratory for Chemical Analysis (LAQ) at PUCRS or at NSF Laboratories Brasil. Anions were analyzed with Thermo Scientific® Dionex ICS-5000 Ion Chromatograph (CI), while metals were assessed with the Optima 7000 DV Inductively Coupled Plasma Optical Emission Spectrometer (ICP-OES) from Perkin Elmer®. Analytical errors generally varied from 0.004 to 0.03 mg/L. The Limit of Quantification (LOQ) varied across parameters, reaching 0.3 µg/l (toxic metals, like Cr and Cd) and 0.01 mg/L (nonmetals and metals). In some cases, the LOQ value was conventionally substituted by LOQ/2 for quantitative interpretation. The aforementioned sampling procedures and analyses are accredited according to

ISO/IEC 17025:2017 by the ANSI National Accreditation Board (ANAB) under certificate number AT-3169.

The error in charge balance (CBE), chemical speciation of solutes, partial pressure of CO_2 (PCO_2) and mineral saturation index (SI) calculations were made using PHREEQC INTERACTIVE 3.7 (PARKHURST; APPELO, 2013). The average CBE was -1.4% (20.2% maximum; 0.1 minimum), and those above 10% (only 7 samples) were discarded and not considered in further statistical evaluation shown in the discussion section. Hydrochemical graphs and geochemical diagrams were generated by using Plotly or WQChartPy Python libraries (Yang et al., 2022). PCA analysis was accomplished using the freely available *pca* Python package (Taskesen, 2020). Spearman's non-parametric correlation analysis was conducted after confirming the non-normal distribution of selected representative data using the Shapiro-Wilk test ($p \leq 0.05$). No data transformations were applied, and the correlation coefficient is represented by the Greek letter ρ (CONOVER, 1999; SHAPIRO; WILK, 1965).

6.3. Results

The results from field measurements and laboratory analyses of the collected water samples are comprehensively summarized in Tables S1, S2, and S3. For additional details and a thorough dataset, please refer to the Supplementary Material.

6.3.1. Temporal evolution of physicochemical parameters

The monitoring of temperature, pH, EC, DO, and ORP started on January 8, proceeded regularly during injection (which started only on January 15 and ended on 3 March) and the concentrated post-injection, and was one last time measured on July 17 after a long period of intense rainfall. Immediate background showed that during this period, the pH varied from 5.4 (M3B) to 6.5 (M4B), EC from 190 µS/cm (M3B) to 493 µS/cm (M4B), DO from 1.6 mg/L (M1B) to 4 mg/L (M3B), and ORP from +202 mV (M3B) to -190 mV (M4B), as shown in Figure 6.4. Temperature varied from 23.9°C (M4B) to 26.3°C (M2B) and remained within this range for the whole duration of the concentrated field experiment, except for the last post-injection sampling campaign that took place during winter when temperatures were lower than 19ºC. During this period, pH decreased for all wells but remained within the observed range for the previous long background campaign carried out for 3 years (ZIELINSKI et al., 2024).

This is also true for the other physicochemical parameters, which had some high-amplitude changes before CO_2 was released.

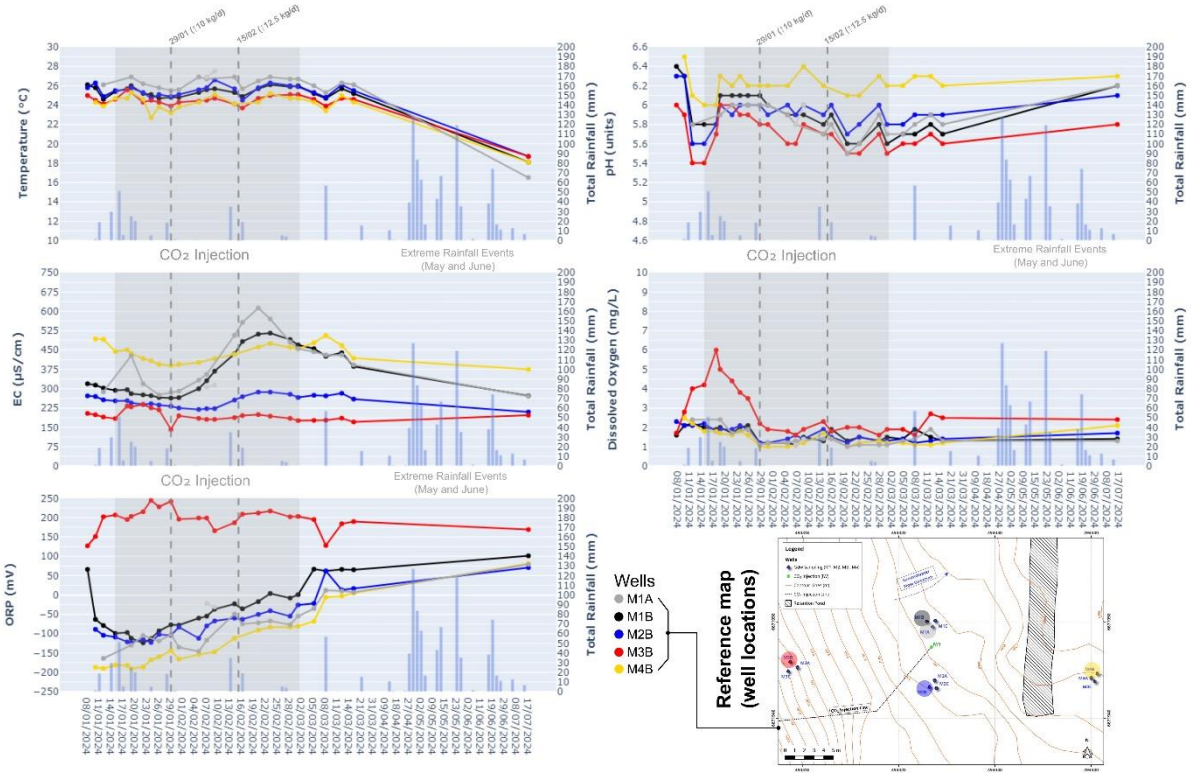

Figure 6.4. *Evolution of physicochemical parameters across different phases: background, CO_2 injection, and post-injection (immediate and long-term). The gray shaded area represents the CO_2 injection phase. Vertical dotted lines indicate the increase in CO_2 injection rate on January 29 (10 kg/day) and February 15 (12.5 kg/day).*

After CO_2 injection started, pH actually slightly increased until January 19 and remained nearly constant for all wells up to January 29 (14 days after CO_2 began to be released to the aquifer). It only showed an observable decrease after January 31, two days after the decision to increase the injection rate from 5 to 10 kg/day had been made. During this period, pH had fallen from 6 to 5.5 for M1A, from 6.1 to 5.6 for M1B, and from 6 to 5.7 for M2B, the closest to the injection well, all showing some levels of slight rebounds. This event coincided with breakdowns in the CO_2 injection system on February 5 and 8, and with two precipitation events that showed an accumulated amount of ~54.3 mm. M3B showed a decrease in pH from 6 to 5.5 five days earlier, but apparently without any connection to CO_2 injection, as will be seen later. M4B oscillated from 6 to 6.4 units throughout the injection period. Electrical conductivity increased simultaneously, with values rising from 285 µS/cm on January 29 to 613 µS/cm on February 20 for M1A (115% increase) and from 264 µS/cm to 515 µS/cm on

February 23 for M1B (95% increase). Well M2B only saw its EC start to rise on February 14, reaching its highest point also on February 23, although its percentage increase was lower than the other two (an increase of 28.6%). EC for M4B also started to rise on January 29 but continued rising slowly until March 8 (29.7% increase).

DO began to drop after CO_2 injection for all wells, even for M3B, which had increased right before the injection started, although not homogeneously. From January 15 to January 26, DO stood between 1.8 to 2.1 mg/L. On January 29, the levels dropped to 1.1 mg/L and remained lower than 1.5 mg/L until the end of the injection phase. Minor rebounds to higher levels were observed after February 9, coinciding with periods of heavier rainfall and injection malfunctions. In general, ORP began to increase seven days after the beginning of CO_2 injection for all wells except for M3B, which oscillated between +166 to +245 mV. Nonetheless, for M1A, M1B, M2B, and M4B, ORP started to gradually rise on January 22 from a reduction condition (< -120 mV) towards higher ORP values at the end of the injection campaign (between +1 to -81 mV), reaching oxidizing conditions at the end of the post-injection phase.

6.3.2. Alkalinity and PCO_2 behavior

The evolution of total alkalinity (measured as mg/L of CaCO3) and CO_2 partial pressure (PCO_2, in atm) can be observed in Figure 6.5. During the background period, the alkalinity of M1A, M1B, and M2B varied from 100.6 to 135.2 mg/L, while for M3B it remained between ~28.0 to 47.1 mg/L, and for M4B between 218.7 to 249 mg/L. During CO_2 injection, these values increased at the beginning, between January 15 to January 19 for M1A and M3B, promoting an increase of approximately 38.5% and 115%, respectively. This is possibly linked to the 132.6 mm of rain accumulated between January 8 and the sampling date, which may have washed down naturally produced CO_2 from soil microbial activity and organic matter degradation. This process can lead to a decrease in pH, while total alkalinity increases due to a concurrent rise in cations released from mineral dissolution and bicarbonate (HCO_3^-) formation (DREVER, 1997; LASAGA, 1984a). Stumm and Morgan (1996) note that once the buffering capacity is overwhelmed, pH decreases despite rising alkalinity, which could explain this observation. Afterward, the total alkalinity began to drop even with the CO_2 injection still happening. This was not clearly observed in the other wells.

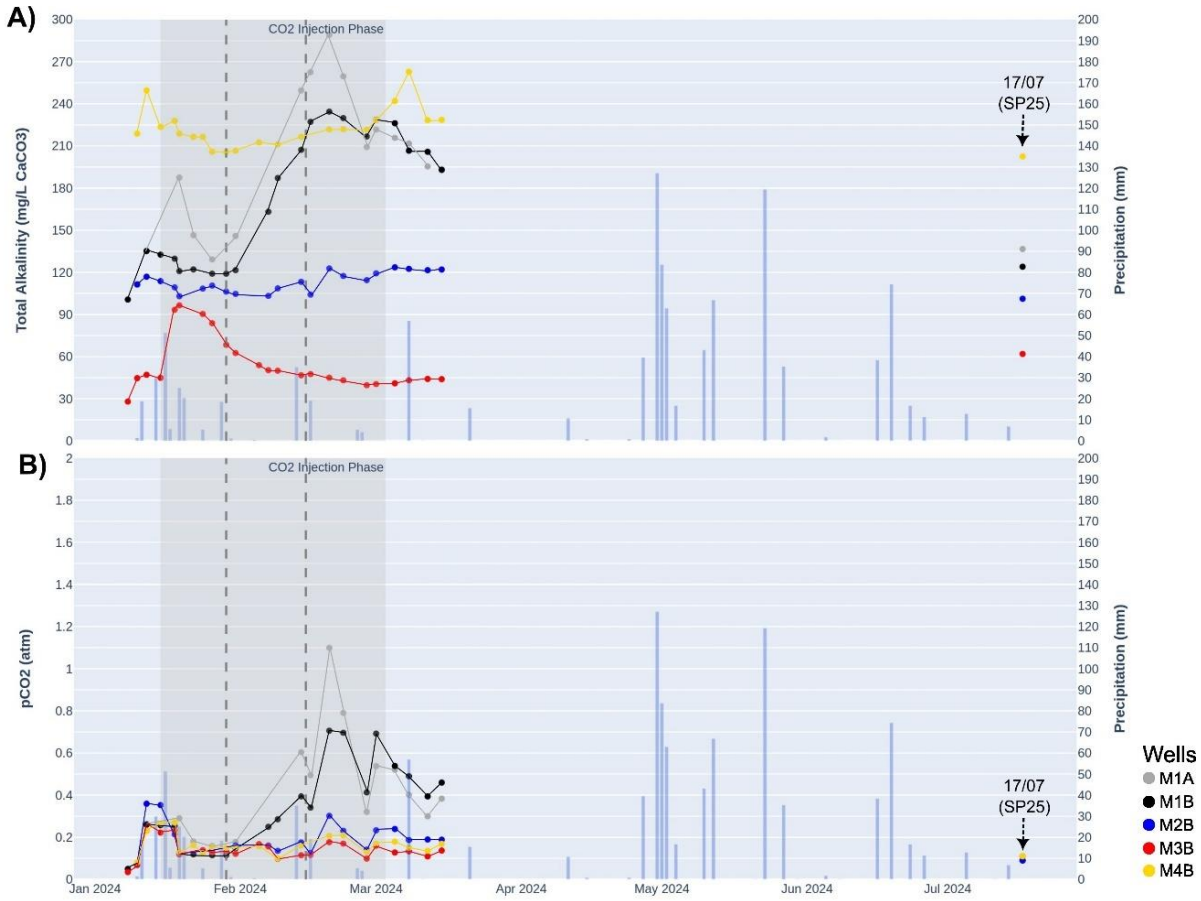

Figure 6.5. *Evolution of total alkalinity (measured in mg/L as CaCO3) and partial pressure of CO_2 (in atm) across the background, CO_2 injection, and post-injection (immediate and long-term) phases. The gray shaded area indicates the CO_2 injection phase. Vertical dotted lines indicate the increase in CO_2 injection rate on January 29 (10 kg/day) and February 15 (12.5 kg/day).*

No significant changes were seen in wells M1B and M2B until the injection rate increased to 10 kg/day and later to 12.5 kg/day. On January 26 and 31, total alkalinity started to climb from 129.2 to 289.2 mg/L (almost a 124% increase) for M1A and from 121.5 to 234.4 mg/L (almost a 92.3% increase) for M1B, respectively. This level of change visibly only occurred in these two wells during the most critical phase of CO_2 injection, as alkalinity for M3B continuously decreased throughout the experiment and M4B showed only a 24% increase after 9 February.

In addition, PCO_2, which varied from 0.03 to 0.35 atm during background and initial injection phases for all wells in general, sharply increased to approximately 1.1 atm (M1A) and 0.7 atm (M1B) on February 20, a growth of 541% and 545%, respectively. After this period, it started to decrease to lower values but remained above the levels

observed in the background phase during immediate post-injection. Apart from M2B, which showed a somewhat similar but more subtle behavior, PCO_2 for wells M3B and M4B varied within a restricted interval and did not exhibit a clear rising trend.

6.3.3. Dissolved ions time series trend

Observed changes in dissolved ions aligned with the evolution of physicochemical parameters, such as alkalinity and PCO_2, as CO_2-impacted groundwater progressed through the field. As illustrated in Figure 6.6, wells M1A and M1B exhibited a gradual increase in concentrations of Ca, Mg, K, Na, Sr, Ba, Fe, and Si during CO_2 injection, particularly after the injection rate was increased to 10 kg/day and subsequently to 12.5 kg/day. Concentrations peaked on February 20 or 23 (depending on the parameter) and then began to decline progressively. However, they did not return to background levels within two weeks post-injection, with recovery occurring in the weeks following the final immediate post-injection sampling campaign (SP24), as confirmed by the subsequent SP25 campaign. Manganese (Mn) concentrations in these wells exceeded quantification levels only after February 20, with values of 0.14 and 0.11 mg/L for M1A and M1B, respectively. Although Mn concentrations in M1A decreased to low levels, they remained above 0.1 mg/L (100 µg/L) in M1B.

Well M2B also showed increased concentrations for some parameters (Ca, Mg, K, Na, Fe, and Si), though not as consistently as the previously discussed wells. Additionally, chemical species such as Ba and Sr did not exhibit a noticeable increase. Manganese (Mn) concentrations in M2B peaked during the same period as in M1A and later decreased to low levels. In well M3B, concentrations of Ca, Mg, K, Sr, Na, and Si initially showed a sharp increase during the background or low injection rate period but subsequently decreased even during CO_2 injection, indicating a possible lack of correlation with the injection process. Finally, concentration levels in M4B exhibited either oscillating behavior or a relatively stable pattern with no apparent relationship to the progression of CO_2 injection.

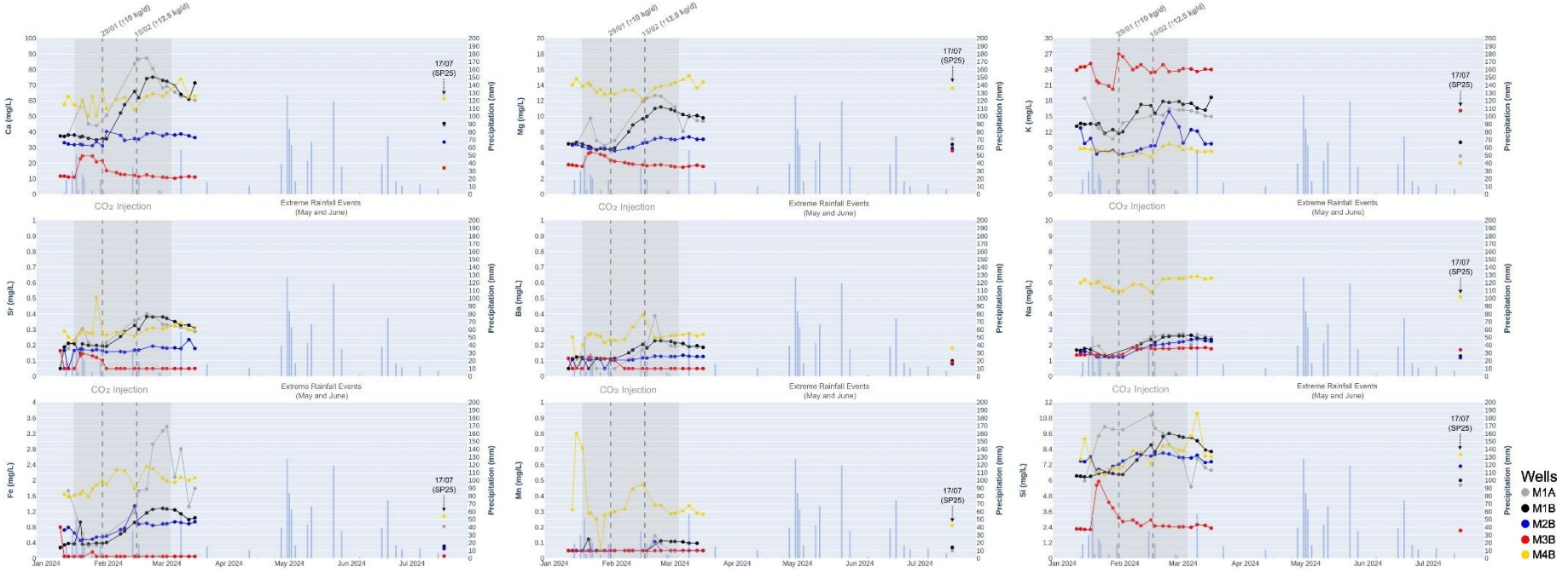

Figure 6.6. *Time series of dissolved cation concentration trends for the sampled wells throughout the experimental period. The gray shaded area denotes the CO_2 injection phase. Vertical dotted lines mark the increases in CO_2 injection rate on January 29 (to 10 kg/day) and February 15 (to 12.5 kg/day).*

Additionally, Cl^- and HCO_3^- concentrations exhibited patterns similar to those of cations in wells M1A and M1B, with a gradual increase during CO_2 injection (Figure 6.7). However, a similar Cl^- behavior was also observed in wells M2B and M4B, while HCO_3^- consistently followed the trend of major cations across all wells. Phosphate (PO_4^{3-}) generally remained at low quantification levels in wells M3B and M4B, but showed a notable peak in wells M1A, M1B, and M2B during the initial days of CO_2 injection, up until the injection rate was increased to 10 kg/day, after which it began to decline.

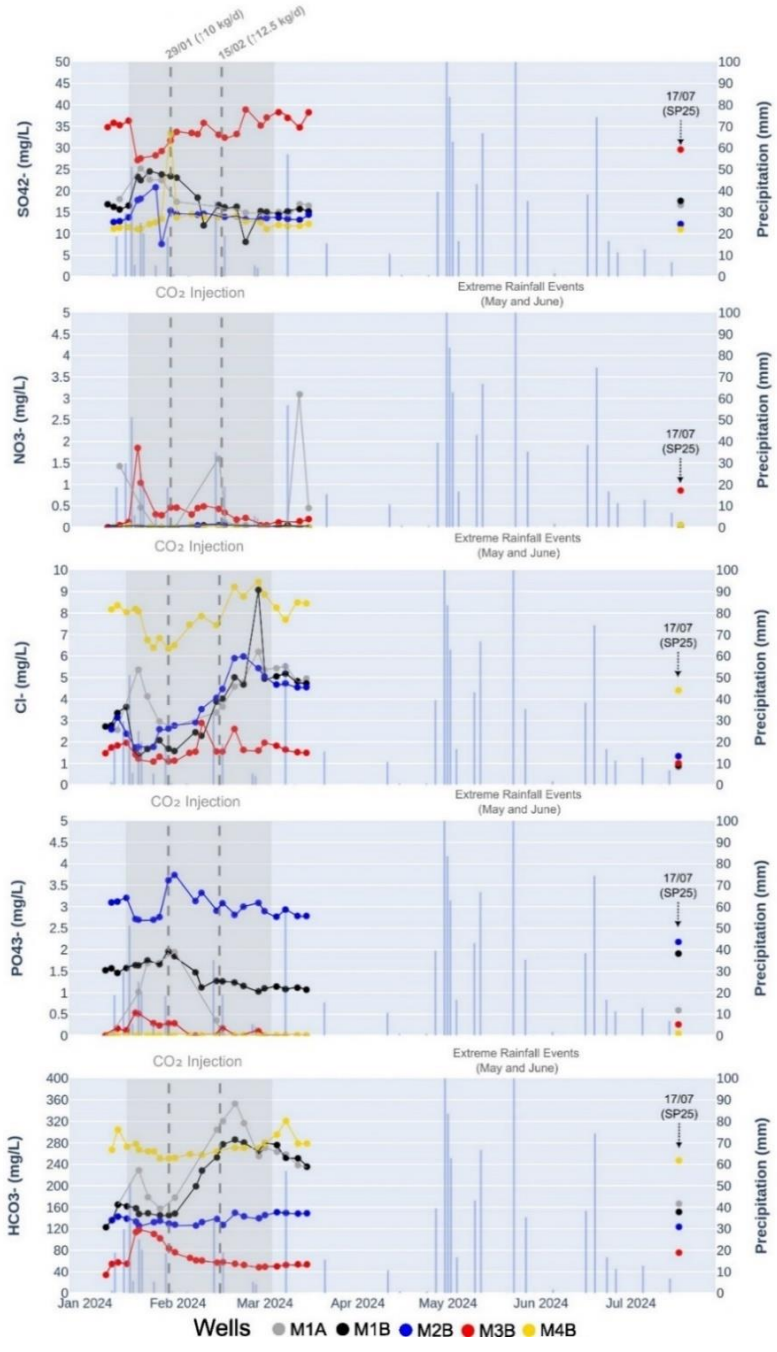

Figure 6.7. *Time series of dissolved anions concentration trends for the sampled wells throughout the experimental period. The gray shaded area denotes the CO_2 injection phase. Vertical dotted lines mark the increases in CO_2 injection rate on January 29 (to 10 kg/day) and February 15 (to 12.5 kg/day).*

Sulfate (SO_4^{2-}), on the other hand, initially increased during the early stages of CO_2 injection, but subsequently decreased in wells M1A, M1B, and M2B as injection progressed. In well M3B, SO_4^{2-} showed a progressive increase after an initial decrease at the beginning of CO_2 injection, while in well M4B, SO_4^{2-} exhibited minimal change. Nitrate (NO_3^-) concentrations displayed an irregular pattern across all wells throughout the experiment, with sudden increases followed by sharp decreases that appeared unrelated to CO_2 release in the aquifer. However, peaks observed in well M1A occurred immediately after significant precipitation events. All other dissolved ions like Al, B, Cd, Pb, Co, Cu, Cr, Li, Ni and Zn were either not detected (below Limit of Detection) or remained below the LOQ.

6.3.4. Mineral Saturation Indexes

The mineral saturation indices (SI) for wells M1A and M1B are presented in Figure 6.8. The data indicate that SI values reached their lowest levels on January 12 (M1A) and January 15 (M1B) for oxide and oxyhydroxide phases ($Al(OH)_3$(a), Al_2O_3, $Fe(OH)_3$(a), gibbsite, goethite, and lepidocrocite), immediately preceding a series of three precipitation events during the final background campaigns and the initial days of low injection rates. Following this period and short subsequent small increase in SI, aluminum-rich phases $Al(OH)_3$(a), Al_2O_3 and Gibbsite exhibited a slight decline in SI, indicating a tendency toward dissolution, as CO_2 injection commenced and injection rates increased to 10 kg/day. After the peak in PCO_2, the SI values for these phases began to return to pre-injection conditions. After the peak in PCO_2, the SI values for these phases began to return to pre-injection conditions. In contrast, iron-rich phases such as $Fe(OH)_3$(a), goethite, and lepidocrocite demonstrated a progressive increase in SI, moving toward saturation, which suggests a shift in hydrochemical conditions favoring precipitation. However, among these, only gibbsite actually achieved SI > 0.

Although there were occasional oscillations in SI values, the overall trend remained clear.

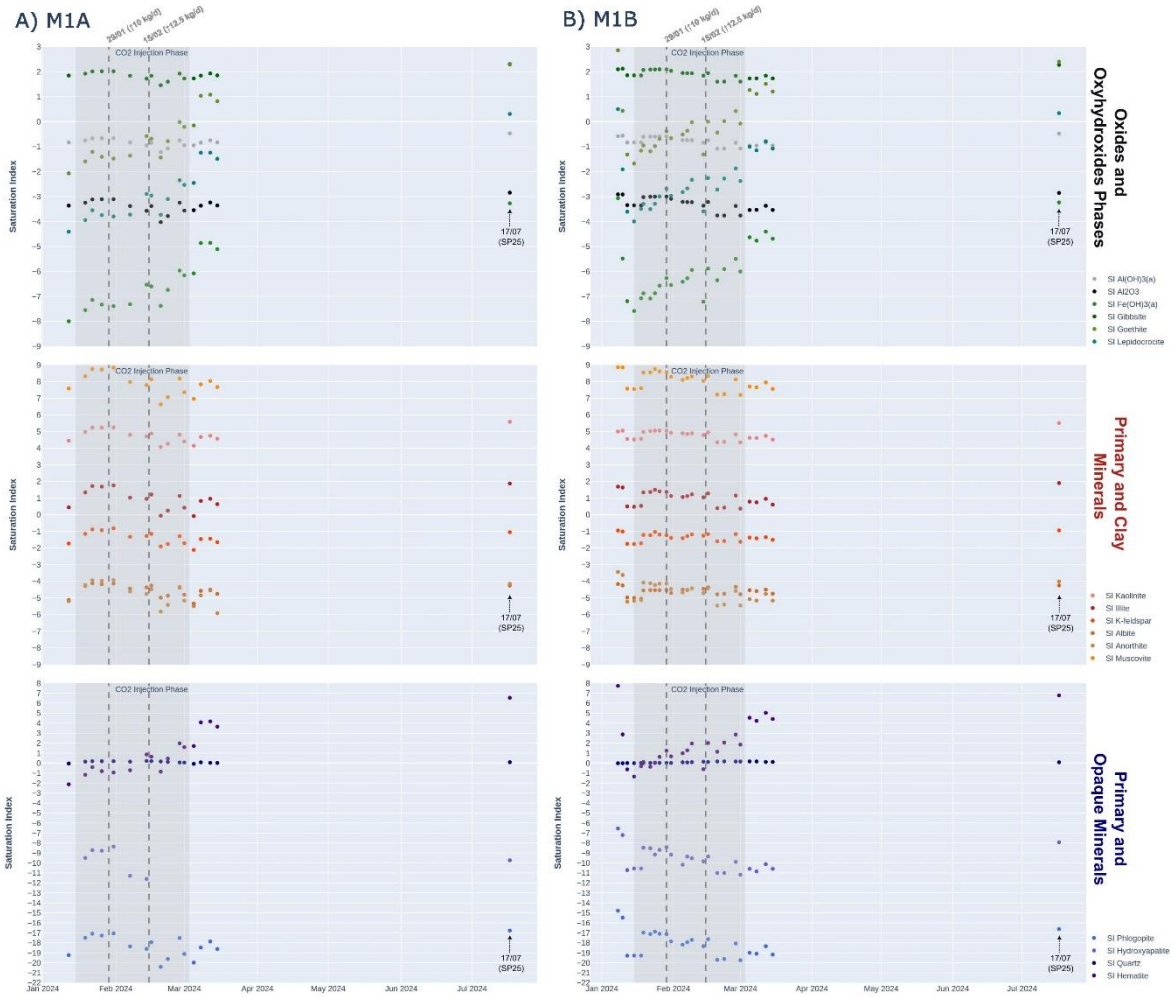

***Figure 6.8**. Observed trends and patterns in the saturation indices (SI) of secondary minerals, oxyhydroxide phases, and primary minerals observed during the CO_2 injection experiment in wells M1A (A) and M1B (B).*

Primary and clay minerals exhibited a progression in their SI toward conditions more prone to precipitation - either enhancing favorability or indicating shifts in environmental conditions that would facilitate this process - up until January 31. Following this date, a consistent decrease in SI was observed after the CO_2 injection rate increased to 10 kg/day, continuing until February 20, at which point SI values began to return to pre-injection levels. This trend was observed in both M1A and M1B, with a more pronounced response in M1A. Muscovite, kaolinite, and illite predominantly remained in the supersaturated field (SI > 0), while K-feldspar, albite,

and anorthite experienced increasingly negative SI values, suggesting these minerals were actively dissolving and releasing their constituent elements into the groundwater.

Phlogopite (used here as a thermodynamic representation for biotite) and hydroxyapatite also followed this pattern, shifting toward conditions favoring dissolution as CO_2 injection progressed to higher levels. In contrast, quartz remained largely unaffected, while hematite (used as a proxy for a kinetically slow oxide phase) transitioned from undersaturated to supersaturated conditions during the CO_2 injection phase and remained above SI > 0 until the final post-injection sampling campaign.

These results suggest that secondary phases such as $Fe(OH)_3$(a), goethite, lepidocrocite, kaolinite, and illite, along with primary minerals including K-feldspar, albite, anorthite, muscovite, biotite, and hydroxyapatite, exhibited shifts in their SI trends as CO_2 injection progressed. This behavior could be interpreted as indicative of these minerals acting as sources of elements whose concentrations increased in response to the CO_2 injection.

6.4. Discussion

6.4.1. PCA analysis and CO_2-impacted groups

To manage the large number of variables, the initial step involved reducing the dimensionality of the data set with minimal information loss. This analysis was conducted using Principal Component Analysis (PCA, Jolliffe, 1986) on all chemical species with significant concentrations (Ca, Mg, K, Na, Fe, Si, HCO_3^-, SO_4^{2-}, Cl^-, NO_3^-, PO_4^{3-}, Ba, Sr, and Mn), physicochemical field measurements (temperature, EC, DO, pH, and ORP), as well as Total Alkalinity and PCO_2. This approach has been shown to be effective, as demonstrated by DO et al. (2020). According to Figure 6.9A, wells M3B and M4B are clearly clustered separately from wells M1A, M1B, and M2B (and from each other) using PC1 and PC2, which collectively account for almost 68.6% of the total explained variance from the dataset. Additionally, it is possible to observe that they are homogeneously grouped and do not show any evident dispersion after CO_2 injection.

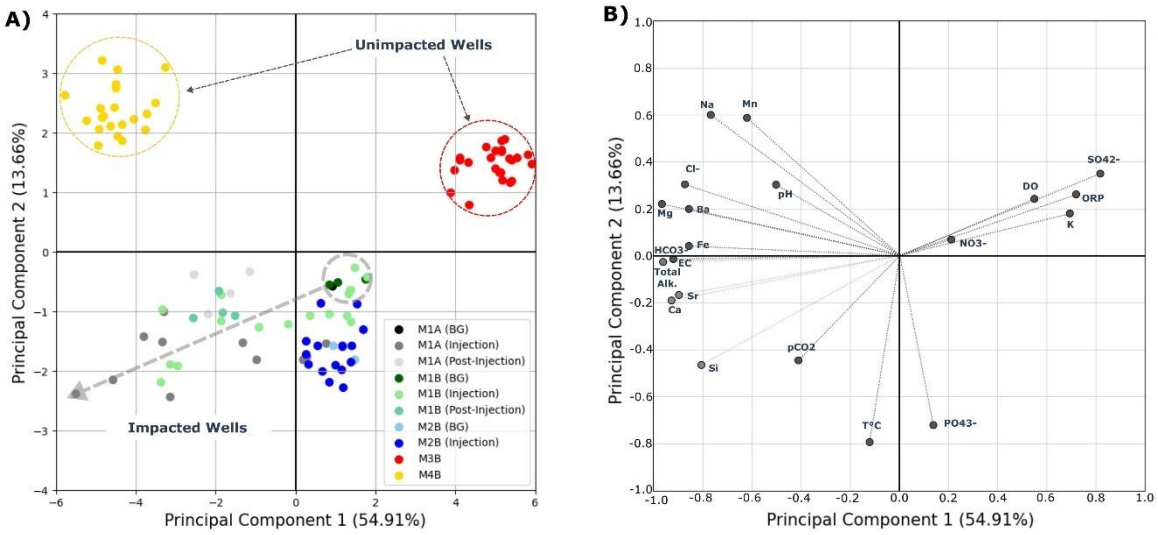

***Figure 6.9**. PCA analysis of all groundwater samples collected during background, CO_2 injection and post-injection: A) segmented groups base on scores of water samples by PC1 and PC2; and B) loadings of evaluated variables and their respective eigenvectors.*

Conversely, wells M1A, M1B, and M2B are clearly differentiated (majorly by PC1). While M2B remains primarily concentrated between PC1 0 to +2 and PC2 0 to -2.5, even during CO_2 injection, background data from wells M1A and M1B indicate an initial concentration between PC1 0 to +2 and PC2 0 to -1 (dashed grey circle) but display a regular data dispersion towards the lower left quadrant (dashed grey arrow), clearly indicating the influence of CO_2 as injection progressed.

After computing the loadings and eigenvectors (Figure 6.9B), it is possible to observe that the evolution of the CO_2-impacted wells is majorly regulated by PCO_2, total alkalinity, Si, Ca, Sr, HCO_3^-, and Fe, and secondarily by Mg, Ba, Na, pH, Mn, and Cl^-. Conversely, NO_3^-, DO, ORP, SO_4^{2-}, K, and PO_4^{3-} (to a lesser extent) show a negative contribution to the progression of the impacted group. Additionally, it is also possible to note that PCO_2 forms a relatively small angle (<90°) with Si, Ca, Sr, HCO_3^-, total alkalinity, EC, Fe, Mg, Ba, Cl^-, pH, Na, and Mn, implying they are positively correlated. This suggests that PCO_2 could be used as a proxy to characterize CO_2 interaction in the impacted wells and its expression in hydrogeochemical variables.

6.4.2. Correlation analysis and PCO_2 vs. dissolved ions evolution path

To assess the extent of the impact of CO_2 injection on the evaluated hydrochemical variables and identify those most strongly associated with this process, a correlation analysis was performed using Spearman's Correlation Coefficient (SCC). This analysis

examined the relationship between PCO_2 and nineteen variables, including EC, DO, pH, ORP, Total Alkalinity, Ca, Mg, K, Na, Fe, Si, HCO_3^-, SO_4^{2-}, Cl^-, NO_3^-, PO_4^{3-}, Ba, Sr, and Mn. As pointed out by Do et al. (2022), although PCO_2 cannot be directly used in this case as a tracer for diagnosing CO_2 leakage, since it is an indirect parameter calculated using PHREEQC - which uses temperature, pH, alkalinity, and ion concentrations to compute PCO_2-, the advancement of technology enabled the use of PCO_2 sensors to establish a direct correlation more accurately. Hence, we used the calculated PCO_2 as a reference point that could be quantitatively anchored with a sensing device, although this was not the focus of this study.

As shown in Table 6.3, which was build taking into consideration only the parameters monitored during the CO_2 injection phase, M1A and M1B showed the largest number of variables with a strong correlation with PCO_2 ($\rho > 0.60$), while M2B showed most of the parameters between a weak (0.20 to 0.39) to moderate (0.40 to 0.59) correlation, with some exceptions (WEIR, 2014). On the other hand, in both M3B and M4B, most variables exhibited either very weak or no correlation (0.00 to 0.19) and weak correlations. In this context, a more stringent statistical threshold was applied by restricting the analysis to variables with correlation coefficients greater than 0.70, even though the literature commonly considers values above 0.60 as indicative of strong correlations. Using this stricter criterion, the variables identified as strongly correlated in both M1A and M1B were EC, pH, ORP, Total Alkalinity, Ca, Mg, K, Na, Fe, HCO_3^-, PO_4^{3-}, Ba, Sr, and Mn.

Other variables, such as Si, SO_4^{2-}, Cl^-, showed higher correlations in M1B than in M1A, indicating a relatively lower relationship of these variables with PCO_2 in the shallower interval. This suggests that another factor is causing the correlation to become weaker, which we interpret to be the influence of rainfall, as will be further discussed. The correlation levels for EC, pH, Ca, Mg, Na, K, Sr, Ba, Si, and Mn are of the same order of magnitude as those reported by Do et al. (2022) for the most impacted well in their study, despite their use of Pearson's method. An exception is Li, which was not detected above the minimum quantification level in this study.

***Table 6.3**. Spearman's Correlation Coefficient (SCC) for PCO_2 and the corresponding variables, according to the degree of CO_2 impact: a) M1A and M1B are highly impacted wells; b) M2B is moderately impacted; and c) M3B and M4B are considered unimpacted wells.*

	EC	DO	pH	ORP	Total Alk.	Ca	Mg	K	Na	Fe	Si	HCO_3^-	SO_4^{2-}	Cl^-	NO_3^-	PO_4^{3-}	Ba	Sr	Mn
M1A	**0.94**	-0.64	**-0.99**	**0.83**	**0.93**	**0.90**	**0.96**	**0.72**	**0.76**	**0.70**	-0.22	**0.93**	-0.62	0.36	0.57	**-0.81**	**0.88**	**0.94**	**0.70**
M1B	**0.94**	-0.20	**-0.89**	**0.82**	**0.97**	**0.95**	**0.96**	**0.90**	**0.93**	**0.83**	**0.84**	**0.97**	**-0.85**	**0.83**	0.23	**-0.85**	**0.90**	**0.86**	0.61
M2B	0.37	-0.06	**-0.89**	0.41	**0.74**	0.50	0.46	0.50	0.42	0.39	0.37	**0.74**	-0.36	0.30	-0.00	-0.06	0.50	0.20	0.37
M3B	0.11	0.36	-0.54	0.26	0.00	0.04	0.01	0.09	-0.01	0.03	-0.06	0.00	0.06	0.07	-0.22	0.00	0.04	0.08	NC
M4B	0.49	0.07	**-0.89**	0.07	0.66	-0.15	0.28	0.50	0.35	-0.11	0.18	0.66	-0.31	0.38	0.327	NC	-0.18	-0.05	0.29

By plotting the variables against PCO_2 on a scatterplot and considering the chronological sequence of the sampling procedures alongside the incremental increase in injection rates, an evolutionary trend can be clearly identified for some parameters in the most impacted wells (Figure 6.10). As shown in Figure 6.10A (well M1B), the major cations Ca, Mg, K, Na, and Si, along with elements Fe, Ba, Sr, and the bicarbonate anion (HCO_3^-), exhibit a relatively linear progression from their baseline concentrations, or even during the low CO_2 injection rate of 5 kg/day, which is concentrated within the lower left quadrant of each graph. These concentrations increase with the injection rate, reaching peak levels at 12.5 kg/day in the upper right quadrant. Following this peak, the concentrations begin to return to baseline levels during the post-injection phase, ultimately approaching the cluster of background or nearly unaffected water compositions (lower left corner).

Manganese (Mn) remains below or near the limit of quantification (LOQ) for most of the time, except when the injection rate is increased to 12.5 kg/day. At this rate, its concentration rises by more than 100%, reaching detection levels greater than 0.1 mg/L (100 µg/L). A less clear correspondence is observed with SO_4^{2-}, Cl^-, and PO_4^{3-}, where a linear trend is not readily apparent, although an evolutionary path can be discerned. While SO_4^{2-} and PO_4^{3-} decrease with increasing PCO_2, Cl^- levels show a slight increase as the injection progresses.

Although M1A is clearly impacted, its evolutionary trend is not as distinct as that of M1B (Figure 6.10B). In this case, Ca, Mg, K, Na, Si, Fe, Ba, Sr, and HCO_3^- exhibit a more scattered distribution during background and low release rates, complicating the analysis. Even though their concentration levels increase as PCO_2 rises, a positive linear correlation is not clearly established, and sometimes a more complex pathway is needed to explain the evolution. For example, the highest Fe concentration in M1A is reached after the peak is attained for the other parameters, while Si reaches its highest concentration earlier than the other variables. As for SO_4^{2-}, Cl^-, and PO_4^{3-}, their behavior is even more intricate, and the traced evolution is nearly indistinguishable. Graphs for M2B, which displays a less distinct evolutionary pathway, as well as for M3B and M4B, which show a scattered relationship between PCO_2 and the evaluated variables, are presented in Figure S1, S2 and S3 (Supplementary Information).

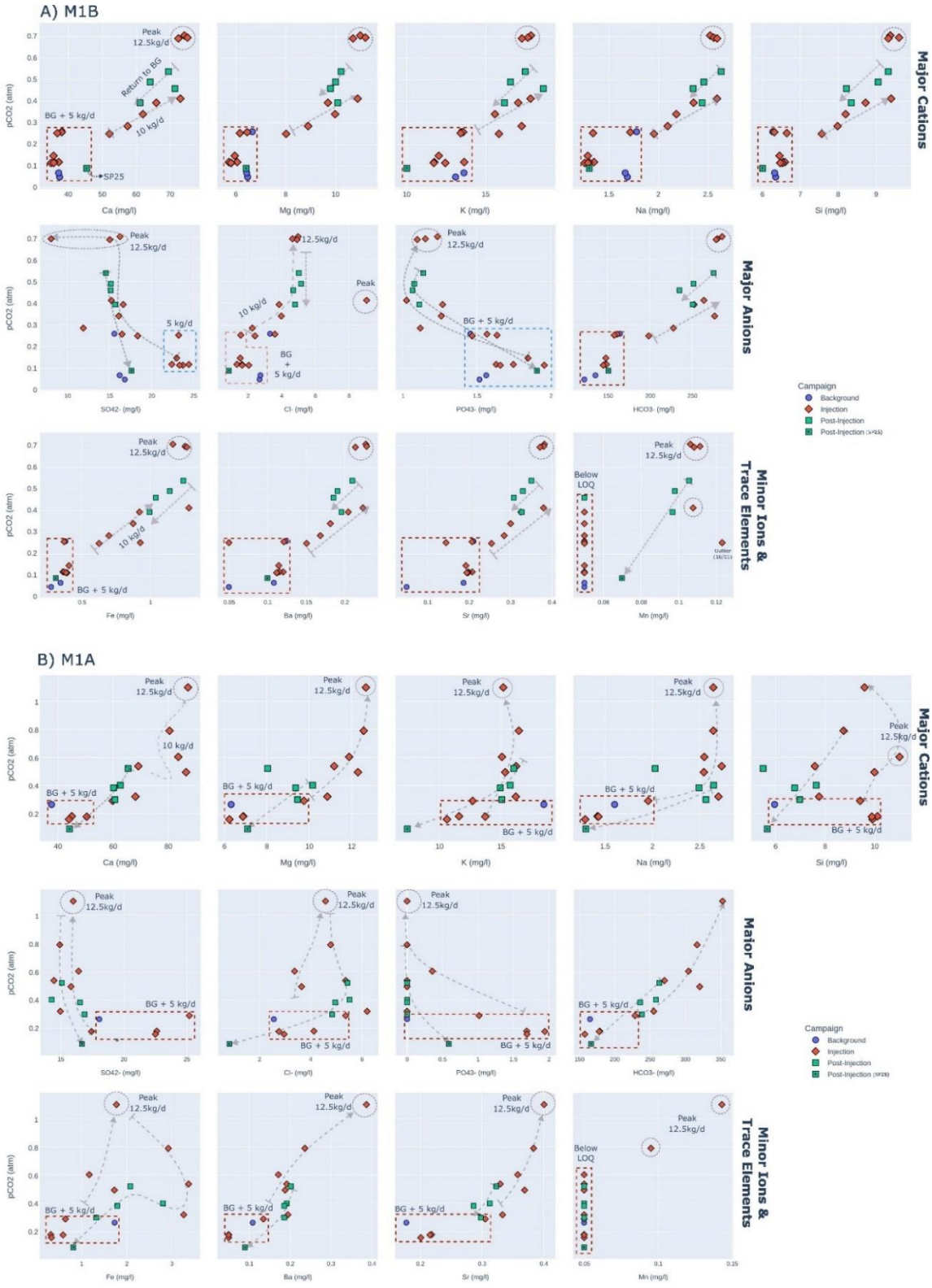

***Figure 6.10**. Evolutionary pathway of ion and trace element concentrations during background conditions, low CO_2 injection rates, increasing injection rates, peak levels, and subsequent return to background levels during both immediate and long-term post-injection phases.*

6.4.3. Bivariate plots and geochemical process

Groundwater chemistry data from all wells were used to recognize the geochemical processes and help identify the main mechanisms regulating the relation with CO_2. In this case, rock weathering and dissolution processes were identified through commonly-used bivariate plots (Figure 6.11). According to Gaillardet's plots (GAILLARDET et al., 1999), the majority of the samples falls within the silicate weathering field, which is characterized by an intermediate Ca/Na and HCO_3^-/Na ratios on a logarithmic graph (Figure 6.11A and B). Some samples have a higher tendency to approach carbonate dissolution field and eventually falls within the designated area, but this is restricted to samples from well M4B or an outlier from M1A. A further approach to the evaluate this process is by plotting the sum of Ca + Mg (meq/L) in relation to the total sum of cations (TC, in meq/L).

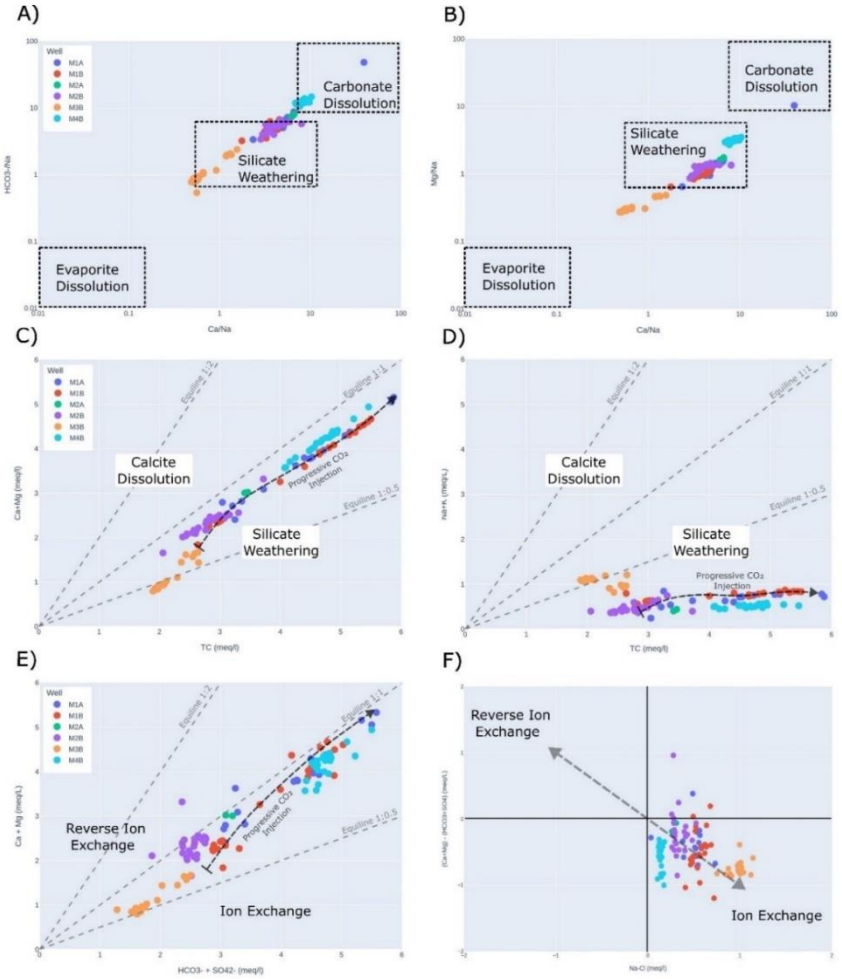

Figure 6.11. *Bivariate geochemical plots: (A) and (B) depict Gaillardet's sodium-normalized HCO_3^- and Mg versus Ca/Na relationship; (C) and (D) show Total*

Cations (TC) versus Ca + Mg and Na + K (in meq/L); and (E) and (F) evaluate ion exchange processes with Ca + Mg versus HCO_3^- + SO_4^{2-} (in meq/L) and (Ca + Mg) – (HCO_3^- + SO_4^{2-}) versus Na - Cl (in meq/L), respectively.

In this case, the dominance of Ca and Mg over Na and K is illustrated in the plots of TC versus Ca + Mg (Figure 6.11C) and TC versus Na + K (Figure 6.11D). The graphs reveal that groundwater samples are positioned between the 1:0.5 equiline and slightly below the 1:1 equiline for Ca + Mg, the latter line indicating conditions consistent with calcite dissolution. Additionally, the plot of Na + K versus TC indicates that most samples fall below or near the 1:0.5 equiline. As CO_2 injection progresses, an increasing contribution of Ca + Mg is observed alongside a rise in TDS, although still below the carbonate dissolution line, while the sum of Na + K remains relatively unchanged as the CO_2-water-mineral interactions advance. These relationships suggest that silicate weathering contributes to the presence of these ions in groundwater (KANAGARAJ; ELANGO, 2019; NETHONONDA; ELUMALAI; RAJMOHAN, 2019; SENTHILKUMAR; ELANGO, 2013; STALLARD; EDMOND, 1983).

Nonetheless, as previously discussed, a significant increase in Ca, Mg, Ba, and Sr—elements commonly associated with carbonate dissolution—has been observed. To elucidate the geochemical processes that may explain this mechanism, the plot of Ca + Mg versus HCO_3^- + SO_4^{2-} is used to assess the occurrence of ion exchange processes (Figure 6.11E and F). As shown in Figure 6.11E, most samples fall below the 1:1 equiline, indicating a direct ion exchange process (BRINDHA et al., 2020; MTHEMBU et al., 2020; REFAT NASHER; HUMAYAN AHMED, 2021). Typically, during ion exchange, Ca^{2+} cations are retained in the soil while Na^+ cations are released into groundwater. Conversely, in reverse ion exchange, Na^+ cations are retained in the soil while Ca^{2+} cations are released into groundwater. In our case, as CO_2 injection progresses, samples from wells M1A and M1B tend to approach and sometimes exceed the 1:1 equiline, entering the reverse ion exchange field. This behavior suggests that as CO_2 interacts with the mineral matrix, divalent cations are preferentially released from the aquifer material, leading to an increased presence in the groundwater.

This process has been attributed to the pulse-like behavior of Ca, Mg, Na, K, Sr, Ba, and HCO_3^- in various studies in aquifers dominated by silicate minerals (CAHILL; MARKER; JAKOBSEN, 2014b; PETER et al., 2012b; TRAUTZ et al., 2013c), including by Do et al. (2022), which corroborate our findings. Furthermore, although no carbonate minerals have been identified in our study area, the possible origin of carbonate minerals and associated elements could be related to the historical application of lime for soil pH correction. Even though the study area has not been used for agricultural practices in the past 10 years, Ca and other elements may still be adsorbed in the clay minerals, as documented by Cherian et al. (2018). These minerals are commonly found across all hydrostratigraphic units of the profile, particularly in the zones where groundwater samples were collected.

Iron and manganese concentrations can be significantly influenced by redox conditions and desorption processes, especially under increasing acidity (APPELO; POSTMA, 2005a; BERKOWITZ; DROR; YARON, 2014b). Iron, in its ferric form (Fe^{3+}), is generally insoluble under oxidizing conditions, whereas it becomes soluble as ferrous iron (Fe^{2+}) under reducing conditions. In this study, ORP measurements indicated a progressive increase in its values for almost all wells (with the exception of M4B) throughout the CO_2 injection phase, approaching more oxidizing conditions. ORP values eventually surpassed 0 mV only during the immediate post-injection period and SP25 (Figure 6.4). Concurrently, during this latter phase, Fe concentrations began to decline, which can be attributed to the precipitation of Fe^{3+} as Fe-oxyhydroxides (DREVER, 1997). However, the increase in Fe levels during the CO_2 injection phase, under mildly acidic conditions, may suggest an intermediate reaction pathway involving the desorption of Fe^{2+} from exchange and surface sorption sites, as previously discussed by Appelo et al., (1999) and Appelo and Postma (2005).

6.4.4. Influence of precipitation events

Given the very shallow nature of the experimental study area, subsoil CO_2(g) flux, dissolved CO_2 concentrations, and chemical changes in groundwater due to CO_2-mineral interactions are directly influenced by precipitation events. The impact of precipitation on CO_2(g) concentration and CO_2(g) flux in the soil has been previously studied by (DELSARTE et al., 2021) under conditions very similar to those in this study.

They observed that artificial rainfall events led to a reduction of more than 450% in CO_2 concentration levels (with concentrations dropping from 388 to 65 g/m³). Upward CO_2(g) fluxes also decreased significantly, from around 40-35 mg/m²/min to below 10 mg/m²/min, and in some cases, even below 1 mg/m²/min.

Furthermore, although rainwater samples were not collected onsite, Migliavacca et al. (2005) conducted an extensive study of bulk atmospheric precipitation over the hydrographic basin that encompasses the study area, spanning an entire year (January-December 2002). For comparison, the average (n=107) bulk precipitation composition revealed the following values: pH 6.13, EC 13.2 µS/cm, HCO_3^- 1.4 mg/L, Cl^- 0.66 mg/L, SO_4^{2-} 1.45 mg/L, Ca 0.66 mg/L, Mg 0.16 mg/L, Na 0.44 mg/L, and K 0.33 mg/L, indicating very dilute water compared to the groundwater analyzed in this study.

During the experiment, from January 8 to March 15, approximately 300 mm of accumulated precipitation was recorded. Between March 15 and July 17, a remarkable 1,100.04 mm of rainfall was registered. It is part of one of the most significant sequences of precipitation events ever observed in southern Brazil (CLARKE et al., 2024). Throughout the CO_2 injection phase, daily precipitation often exceeded 30 mm and occasionally surpassed 50 mm, as shown in the previous graphs. Thus, it is reasonable to conclude that the observed reductions in concentration increases and significant decreases in certain chemical species were likely due to the dilution effects of rainwater and the attenuation of dissolved CO_2(g). This dilution likely resulted in a diminished overall impact compared to findings reported in other studies, such as those summarized in Gupta and Yadav (2020), Lee et al. (2016), Roberts and Stalker (2020), Zheng et al. (2021) and Zielinski et al. (2023). However, fluctuations in water levels may also influence redox processes, contributing to the observed changes and explaining variations in parameters such as Fe and Mn.

6.4.5. Parameters variation and sensitiveness to CO_2 leakage

Although correlation analysis showed positive or negative association with PCO_2, and Figure 6.10 exhibited an evolutionary path during background, injection and post-injection phases, a leakage episode can be misinterpreted if natural longer-term background variation is unaccounted for (BEAUBIEN et al., 2015; MA et al., 2024;

UTLEY et al., 2023; WANG et al., 2023). Hence, to avoid considering possible parameters that might be equivocally interpreted as a leakage signal, an approach to evaluate sensitivity to CO_2 based on Choi (2019) was used. Nonetheless, instead of comparing the observed parameter to its immediate background level, this was compared to its Lower or Upper Control Limits (LCL and UCL) as shown in our previously publication (ZIELINSKI et al., 2024).

In this case, to account for the percentage increase of the parameter relative to this mentioned natural fluctuation, the following equation was applied:

$$Parameter\ Variation\ (PV, in\ \%) = \left(\frac{[Ci]CO_2 - [C_i]\ UCL\ or\ LCL}{[Ci]_{UCL\ or\ LCL}}\right) \text{x } 100 \qquad (1)$$

where $[Ci]CO_2$ represents the concentration of the i^{th} parameter during the CO_2 injection campaign, and [Ci]UCL or LCL the concentration of the respective i^{th} parameter during the 3-year long natural background. The LCL and UCL represent the average calculated for the respective hydrostratigraphic unit, minus or plus two times the observed standard deviation, respectively. In this study, PV that remained consistently equal to or greater than 20 % in the advanced stage of the CO_2 injection phase (injection rate ≥ 10 kg/day) were considered to be sensitive to CO_2 leakage (Table 6.4).

Table 6.4. *Parameter variations (%) of each evaluated variable consistently exhibiting either positive or negative correlation to PCO_2 (wells M1A, M1B and M2B), referenced to the UCL or LCL of the natural background level monitored for at least 3 years prior to the execution of the CO_2 injection experiment.*

Sample ID	Inj. Rate (kg/d)	Date	Phase	Parameter Variation (%)											
				ΔEC UCL	ΔpH LCL	ΔCa UCL	ΔMg UCL	ΔNa UCL	ΔFe UCL	ΔSi UCL	ΔHCO_3 UCL	ΔCl UCL	ΔBa UCL	ΔSr UCL	ΔMn UCL
M1A SB3	0	12/01	BG	-14.2	4.6	-7.9	-15.3	-71.4	**38.9**	-46.7	**23.0**	-57.1	-16.3	-15.4	-38.3
M1A SI6	5	19/01	Injection	**27.5**	6.2	**46.2**	**30.7**	-65.1	-48.4	-15.8	**70.7**	-10.2	3.9	**45.5**	-38.3
M1A SI7	5	22/01	Injection	-4.9	7.0	10.1	-7.6	-74.6	-74.2	-9.6	**33.3**	-31.0	-61.5	4.1	-38.3
M1A SI9	5	26/01	Injection	-17.7	8.2	7.5	-16.4	-77.0	-73.2	-11.4	17.6	-50.4	-61.5	-4.2	-38.3
M1A SI11	10	31/01	Injection	-13.3	6.8	**23.3**	-7.9	-74.5	-52.7	-11.6	**32.8**	-53.7	-61.5	2.8	-38.3
M1A SI15	10	14/02	Injection	**51.1**	1.9	**104.2**	**59.3**	-54.5	-6.2	-1.6	**127.1**	-43.5	**32.0**	**70.6**	-38.3
M1A SI16	12.5	16/02	Injection	**66.1**	3.6	**111.0**	**64.8**	-54.6	**38.6**	-10.7	**138.9**	-39.0	**44.8**	**76.0**	-38.3
M1A SI17	12.5	20/02	Injection	**82.6**	-1.0	**112.8**	**69.8**	-52.8	**42.0**	-14.3	**163.2**	-23.3	**197.8**	**90.9**	**76.7**
M1A SI18	12.5	23/02	Injection	**69.9**	0.9	**96.4**	**68.5**	-52.8	**134.2**	-21.8	**136.2**	-20.0	**82.1**	**82.9**	17.5
M1A SI19	12.5	28/02	Injection	**43.3**	4.7	**66.3**	**45.5**	-51.9	**161.4**	-30.7	**90.4**	3.8	**50.1**	**58.9**	-38.3
M1A SI20	12.5	01/03	Injection	**35.7**	2.1	**68.8**	**49.8**	-51.3	**170.1**	-32.2	**101.8**	-10.2	**48.0**	**57.1**	-38.3

M1A SP21	0	05/03	PI	**32.1**	2.7	**59.8**	7.8	-63.8	**66.8**	-50.9	**96.4**	-9.0	**55.6**	**54.0**	-38.3
M1A SP22	0	08/03	PI	**28.3**	3.0	**53.0**	**36.1**	-52.8	**124.4**	-31.8	**92.7**	-7.6	**48.0**	**49.1**	-38.3
M1A SP23	0	12/03	PI	**28.5**	4.9	**48.2**	**26.6**	-54.2	6.3	-37.6	**77.9**	-19.0	**43.1**	**42.1**	-38.3
M1A SP24	0	15/03	PI	16.9	3.9	**47.1**	**25.4**	-55.5	**43.6**	-39.5	**76.0**	-17.0	**43.2**	**36.6**	-38.3
M1A SP25	0	17/07	PI	-19.4	10.8	8.0	-5.0	-76.8	-34.4	-49.4	**24.3**	-86.1	-30.8	NM	-38.3
M1B SB1	0	08/01	BG	-5.0	13.8	-8.8	-13.5	-70.0	-77.9	-43.3	-8.4	-54.4	-61.5	-76.2	-38.3
M1B SB2	0	10/01	BG	-6.4	12.4	-9.5	-14.0	-70.3	-72.4	-43.6	1.4	-53.6	-16.7	-10.7	-38.3
M1B SB3	0	12/01	BG	-10.1	3.3	-7.1	-10.9	-68.3	-69.5	-44.0	**23.1**	-43.9	-4.6	0.7	-38.3
M1B SI4	5	15/01	Injection	-12.3	3.0	-7.3	-13.7	-69.4	-70.3	-43.7	**20.7**	-39.2	-6.6	-1.0	-38.3
M1B SI5	5	18/01	Injection	-11.8	3.6	-10.4	-17.6	-76.1	-25.8	-40.7	18.0	-73.2	-61.5	-30.9	52.1
M1B SI6	5	19/01	Injection	-16.3	8.9	-9.4	-19.1	-76.0	-71.0	-41.6	10.0	-76.9	-7.4	-0.8	-38.3
M1B SI7	5	22/01	Injection	-17.7	8.6	-12.6	-23.5	-76.9	-70.3	-41.2	11.1	-71.9	-11.1	-5.2	-38.3
M1B SI9	5	26/01	Injection	-20.6	9.1	-14.9	-22.3	-77.6	-68.6	-41.7	8.3	-65.1	-13.5	-5.7	-38.3
M1B SI10	5	29/01	Injection	-21.2	8.5	-13.0	-22.4	-77.1	-69.2	-42.3	8.3	-71.7	-13.9	-7.0	-38.3
M1B SI11	10	31/01	Injection	-21.0	7.7	-13.1	-20.4	-77.1	-67.4	-42.4	10.6	-73.6	-11.8	-8.0	-38.3
M1B SI13	10	07/02	Injection	-1.4	5.1	**27.0**	7.3	-65.2	-49.9	-32.5	**48.5**	-59.0	16.0	**21.5**	-38.3
M1B SI14	10	09/02	Injection	9.6	6.2	**40.1**	19.1	-62.7	-44.1	-28.8	**70.3**	-61.6	**29.7**	**36.0**	-38.3
M1B SI15	10	14/02	Injection	**29.6**	4.4	**60.7**	**29.7**	-58.0	-26.4	-22.2	**88.6**	-35.0	**57.6**	**55.3**	-38.3
M1B SI16	12.5	16/02	Injection	**44.0**	5.4	**51.1**	**33.6**	-61.1	-30.0	-26.9	**106.8**	-32.8	**39.7**	**43.4**	-38.3
M1B SI17	12.5	20/02	Injection	**52.5**	0.1	**80.9**	**47.1**	-55.1	-6.8	-16.3	**113.3**	-16.1	**75.1**	**82.2**	**31.3**
M1B SI18	12.5	23/02	Injection	**53.5**	0.4	**83.1**	**49.9**	-54.4	0.3	-14.3	**109.2**	-21.7	**76.0**	**81.5**	**37.6**
M1B SI19	12.5	28/02	Injection	**46.2**	3.5	**78.0**	**45.7**	-53.8	2.6	-16.1	**97.3**	**52.1**	**72.3**	**81.2**	**33.1**
M1B SI20	12.5	01/03	Injection	**40.0**	1.0	**76.6**	**43.2**	-53.8	1.4	-16.8	**108.1**	-17.1	**64.7**	**77.2**	**33.7**
M1B SP21	0	05/03	PI	**35.7**	1.8	**69.5**	**36.8**	-53.1	-0.6	-16.8	**105.8**	-15.3	**61.7**	**67.4**	**30.5**
M1B SP22	0	08/03	PI	**27.0**	2.4	**56.3**	**33.9**	-56.2	-8.6	-19.2	**88.0**	-13.2	**46.8**	**57.5**	21.1
M1B SP23	0	12/03	PI	**30.9**	2.9	**49.0**	**35.0**	-56.5	-20.4	-25.5	**87.3**	-19.2	**50.7**	**56.1**	19.5
M1B SP24	0	15/03	PI	15.2	2.0	**74.1**	**31.1**	-58.1	-16.8	-26.7	**75.6**	-20.8	**42.9**	**47.0**	-38.3
M1B SP25	0	17/07	PI	-19.0	10.1	10.7	-14.3	-76.8	-75.2	-46.4	12.9	-84.9	-23.1	NM	-13.6
M2B SB2	0	10/01	BG	-19.6	12.1	-19.4	-15.5	-72.3	-41.7	-33.0	1.4	-56.6	-13.4	-20.7	-38.3
M2B SB3	0	12/01	BG	-23.3	0.1	-21.4	-14.0	-71.5	-36.6	-33.6	6.4	-47.3	-61.5	-76.2	-38.3
M2B SI4	5	15/01	Injection	-24.6	0.4	-22.5	-17.9	-73.8	-47.8	-30.3	3.5	-60.1	-13.2	-21.0	-38.3
M2B SI5	5	18/01	Injection	-24.3	3.3	-21.7	-21.5	-77.5	-63.4	-39.8	-0.5	-70.8	-17.4	-16.7	-38.3
M2B SI6	5	19/01	Injection	-27.0	7.6	-22.7	-21.7	-77.8	-61.8	-38.8	-6.3	-70.4	-18.0	-17.7	-38.3
M2B SI8	5	24/01	Injection	-28.0	8.1	-23.9	-21.3	-78.0	-60.6	-41.1	-1.3	-70.3	-16.6	-20.6	-38.3
M2B SI9	5	26/01	Injection	-29.5	6.8	-17.7	-21.3	-77.8	-56.4	-36.8	0.6	-56.6	-61.5	-18.5	-38.3
M2B SI10	5	29/01	Injection	-31.0	8.2	-24.3	-23.9	-77.8	-55.4	-35.4	-3.3	-56.1	-21.7	-21.8	-38.3
M2B SI11	10	31/01	Injection	-33.0	5.3	-1.9	-25.4	-78.1	-54.5	-33.1	-4.7	-53.7	-21.0	-25.7	-38.3
M2B SI13	10	07/02	Injection	-33.6	6.0	-7.9	-20.7	-69.3	-41.3	-28.1	-6.1	-51.1	-19.1	-24.4	-38.3
M2B SI14	10	09/02	Injection	-33.5	7.9	-15.6	-19.5	-68.5	-38.1	-28.5	-1.2	-40.9	-18.6	-26.4	-38.3
M2B SI15	10	14/02	Injection	-23.6	4.8	-12.9	-12.3	-64.7	7.4	-29.7	3.1	-32.2	-8.6	-19.8	-38.3
M2B SI16	12.5	16/02	Injection	-19.8	7.0	-13.8	-11.1	-64.2	-29.5	-28.7	-5.2	-25.2	-9.9	-19.7	-38.3
M2B SI17	12.5	20/02	Injection	-14.6	1.5	-5.7	-5.0	-63.3	-28.2	-27.7	11.7	-1.2	-0.5	-100.0	**31.3**
M2B SI18	12.5	23/02	Injection	-14.4	3.2	-3.9	-2.9	-62.4	-32.4	-28.3	6.9	0.2	-1.3	-7.8	-38.3
M2B SI19	12.5	28/02	Injection	-17.0	7.3	-8.5	-5.4	-61.0	-29.3	-30.6	4.2	-8.9	-1.7	-12.6	-38.3
M2B SI20	12.5	01/03	Injection	-20.7	4.5	-5.8	-6.2	-60.4	-28.9	-30.8	8.6	-15.4	-2.1	-14.0	-38.3
M2B SP21	0	05/03	PI	-18.2	4.3	-7.3	-3.5	-58.1	-25.1	-31.0	12.5	-21.7	3.7	-12.8	-38.3

M2B SP22	0	08/03	PI	-19.0	5.7	-5.7	-1.5	-57.3	-26.6	-29.2	11.5	-20.8	-0.5	-15.4	-38.3
M2B SP23	0	12/03	PI	-15.9	5.8	-8.5	-5.6	-59.3	-28.9	-34.3	10.6	-23.8	-2.1	11.9	-38.3
M2B SP24	0	15/03	PI	-22.6	4.9	-11.4	-5.6	-59.9	-24.9	-33.7	11.0	-23.7	-2.3	-15.0	-38.3
M2B SP25	0	17/07	PI	-37.6	8.6	-18.3	-21.0	-78.6	-80.0	-36.7	-7.9	-77.6	-38.5	NM	-38.3

The parameters showing changes greater than 20% include EC, Ca, Mg, Fe, HCO_3^-, Ba, Sr, and Mn. Total alkalinity, though not listed in the table, should also be considered a sensitive parameter to CO_2 injection due to its direct relationship with HCO_3^-, a key chemical species. The observed behavior of most of these parameters (excluding Fe and Mn) aligns with the findings of Cahill et al. (2014), Do et al. (2022), Humez et al. (2014), Kharaka et al. (2010), Mickler et al. (2013), Peter et al. (2012), Pezard et al. (2016), Trautz et al. (2013) and Yang et al. (2013, 2014), supporting the conclusion that these hydrochemical variables are indeed sensitive to CO_2 injection, even at relatively low injection rates and under conditions of high interaction with recharge water (in this case rainfall). This pattern, consistent with the pulse-like response of these chemical species described in the literature, suggests that ion exchange is the dominant geochemical mechanism driving this process.

This suggests that, in the event of CO_2 leakage into a relatively deep monitored aquifer above the injection complex in a real industrial-scale CCS project, hydrochemical changes could still be monitored as indicators of leakage, even in the presence of an external water source (e.g., a leaky confined aquifer or proximity to a recharge zone), provided the long-term natural baseline is well established. Notably, pH changes were not consistently identified as sensitive indicators of CO_2 leakage in this study. This can be primarily attributed to the dilution effect of recharge water with pH values likely exceeding 6, which buffered the impact of CO_2 injection.

In contrast, the behavior of Fe and Mn across the referenced studies shows variability. While most studies report an increase in these elements due to CO_2 injection, some, such as Cahill et al. (2014), observed a decrease. In the present study, both elements showed elevated levels, particularly during the later stages of CO_2 injection, indicating their sensitivity to this process. This response is likely due to desorption and/or dissolution from Al/Fe/Mn oxyhydroxides (GUPTA; YADAV, 2020c; LEE et al., 2016c), which are common altered minerals or amorphous phases resulting from granite weathering. Given these factors and their percentage variation exceeding

20% during the injection phase, we believe these variables could serve as reliable hydrochemical tracers for detecting unintended CO_2 leakages in aquifers near carbon storage complexes.

6.4.6. Environmental risks to groundwater quality

Another major concerns among the public and environmental agencies is that an unintended CO_2 leakage from a carbon storage reservoir could lead to groundwater quality degradation or pose health risks to those consuming the affected water. In this context, Brazil has at least two relevant regulations, although they are not directly linked to a national CCS law, as bill 1425/2022 (SENADO FEDERAL, 2023) is currently under review in the country's legislative house. Resolution No. 396 (BRASIL, 2008) from the National Environmental Council (CONAMA) provides guidelines for the classification, prevention, and control of groundwater pollution. Based on this legislation and the results of this study, special attention should be given to iron (Fe) and manganese (Mn).

CONAMA's Resolution No. 396 sets the Maximum Contaminant Level (MCL) for Fe at 0.3 mg/L (300 µg/L) and for Mn at 0.1 mg/L (100 µg/L) for water intended for human consumption. Additionally, Ordinance No. 888/2021 from the Ministry of Health (BRASIL, 2021), which establishes procedures for monitoring and surveillance of water quality and its potability standards, also mandates that Fe and Mn should not exceed these limits, thereby ensuring compliance with the organoleptic potability standards outlined in Annex 11 of the regulation. These regulations and declared levels were based on the World Health Organization's guidelines for drinking-water quality (WHO, 2017).

During our field experiment, Fe concentrations in well M1A were naturally high but exceeded 3.0 mg/L during the period of greatest groundwater chemical alteration (February 28 and March 1) and surpassed the Mn concentration of 0.1 mg/L on February 20 and 23. While the Mn peak was short-lived, returning to undetectable levels shortly after, Fe concentrations remained above the Maximum Contaminant Level (MCL) for several days. A similar pattern was observed in wells M1B and M2B for both elements, although Fe concentrations were lower, at approximately 1.3 mg/L and 0.89 mg/L, respectively. This behavior is correspondent with observations found

in many other works (Cahill et al., 2014; Do et al., 2022b; Humez et al., 2014b; Kharaka et al., 2010; Mickler et al., 2013; Pezard et al., 2016; Trautz et al., 2013; Yang et al., 2013, 2014).

This experiment, which simulated CO_2 interaction in a small-scale environment within an aquifer rich in Fe and Mn oxyhydroxides and clay minerals, as described by Zielinski et al. (2024), with sampling wells located near the injection point, suggests that the CO_2 injection rate—and consequently the amount of CO_2 dissolved in groundwater—may facilitate the release of these elements into the groundwater. However, whether this phenomenon would occur in a full-scale CO_2 storage project depends on several factors, including the mineralogical composition of the aquifer (particularly in regions near the storage complex or within the overburden), hydrogeological conditions, the monitoring network, and the CO_2 leakage dynamics (BOUC et al., 2009b; HARVEY et al., 2013b; JONES et al., 2015e; ROBERTS; STALKER, 2020d). Should groundwater be impacted by elevated Fe and Mn levels, these elements could either be diluted within the aquifer on a larger scale or require appropriate treatment depending on the intended use of the water.

Even so, both (CHOI, 2019b) and (DO et al., 2020) assessed the potential impact of CO_2 leakage from deep storage reservoirs on shallow groundwater quality in South Korea, specifically in areas with naturally occurring CO_2-rich sources. Their studies revealed that Fe and Mn were mobilized from silicate bedrock formations, such as granite and gneiss, which have limited buffering capacity, leading to elevated concentrations exceeding acceptable levels due to prolonged CO_2 leakage. These studies underscore that this process has been observed in realistic settings and emphasize the need for thorough evaluation in future CCS projects.

6.5. Conclusions

In this study, we observed consistent spatiotemporal variations in physicochemical parameters, major ions, and trace elements during a controlled CO_2 release experiment in a silicate-rich, multilayer shallow aquifer. These variations were linked to the arrival of the CO_2-impacted groundwater plume at monitoring wells located in close geographic proximity. CO_2 injection was conducted at three distinct rates (5, 10, and 12.5 kg/day). The results demonstrated that higher release rates enhanced the

clarity of hydrochemical parameter detection, making it easier to observe changes in the groundwater chemistry. However, given the site's shallow nature, precipitation events were also observed to influence the magnitude of the hydrogeochemical changes, sometimes differing from the findings from other referenced studies.

The breakthrough point of the CO_2-impacted groundwater plume was distinctly identified in wells M1A and M1B by increases in EC, total alkalinity (and consequently HCO_3^-), PCO_2, and a range of elements and chemical compounds including Ca, Mg, K, Sr, Ba, Na, Fe, Si, and Cl^-. These changes became particularly pronounced when the CO_2 injection rate was increased to 10 kg/day. PCA and Correlation Analysis were instrumental in identifying groups of CO_2-impacted wells and tracking the evolution of dissolved ions in relation to PCO_2. PCA revealed that wells M3B, M4B, and M2B were either unaffected or only weakly impacted by CO_2. These analyses also reduced dimensionality by focusing on variables that exhibited a strong direct correlation with the proxy PCO_2, including EC, pH, HCO_3^-, Cl^-, total alkalinity, Ca, Mg, Na, Si, Ba, Sr, Fe, and Mn. Subsequent comparison of these variables with the calculated PCO_2 for each well enabled the establishment of a chronological evolutionary trend. This analysis indicated that certain variables exhibited clearer patterns during background conditions (BG) and low injection rates, with more pronounced changes at an injection rate of 10 kg/day, and peak changes at an injection rate of 12.5 kg/day.

Bivariate geochemical plots indicate that the majority of samples fall within the silicate weathering field. However, a more detailed comparison with other studies and an analysis of element behavior suggest that the dominant geochemical mechanism responsible for the release of Ca, Mg, Na, K, Sr, Ba, and HCO_3^- is direct or reverse ion exchange. In contrast, the behavior of Fe and Mn suggests an intermediate reaction pathway involving the desorption of Fe^{2+} from exchange and surface sorption sites.

Although precipitation events have clearly influenced CO_2(g) flux and the mixing with CO_2-impacted groundwater has altered the magnitude of physicochemical and chemical parameters, the sensitivity to CO_2 leakage could be assessed against the lower and upper control limits of each variable. In this context, a variation exceeding 20% indicates that EC, Ca, Mg, Fe, HCO_3^-, Ba, Sr, and Mn can be confidently used as indicators of leakage. Notably, the observed behavior of Fe and Mn warrants special attention, as their concentrations exceed maximum contaminant levels when

compared to national and international regulations. This is particularly concerning given that similar behavior has been reported in long-term, naturally CO_2-impacted groundwater in silicate bedrock formations (granite and gneiss) with limited buffering capacity.

CAPÍTULO 7: Conclusões finais da tese

Esta tese foi estruturada como uma coletânea de artigos, com as conclusões sendo apresentadas individualmente para cada um, seguidas por uma análise final abrangente. De modo geral, este trabalho buscou promover alguns avanços científicos:

i) consolidação do entendimento sobre os mecanismos geoquímicos que regulam a interação entre CO_2, água subterrânea e minerais em sistemas aquíferos monitorados sobrejacentes a sites de armazenamento geológico de (CCS). O foco recaiu sobre estudos de campo em escala reduzida, permitindo o controle mais rigoroso dos processos envolvidos e, consequentemente, a ampliação do conhecimento sobre este fenômeno;

ii) definição do contexto geológico, geofísico e hidrogeológico do campo experimental de liberação controlada de CO_2 do TECNOPUC-Viamão, que serviu como área de estudo para o experimento conduzido nesta tese, além de estabelecimento da linha de base (*background*) hidroquímica e isotópica sazonal, essencial para o diagnóstico mais preciso das mudanças hidroquímicas na água subterrânea resultantes da interação com o CO_2; e

iii) aprofundamento do entendimento da suíte hidroquímica aplicável no diagnóstico de vazamentos não intencionais de CO_2 em aquíferos rasos, particularmente aqueles de natureza aluminossilicática, e susceptíveis a influências de eventos de recarga, como método hidrogeoquímico de monitoramento ambiental.

7.1. Mecanismos geoquímicos vinculados ao processo interativo CO_2-água-mineral

Nesse contexto, em virtude de uma extensa revisão bibliográfica sobre o tema (primeiro artigo), foi analisado o comportamento de elementos e compostos químicos, parâmetros de qualidade da água relacionados à composição mineral específica de cada local, parâmetros hidráulicos (condutividade hidráulica), massa de CO_2 vazado, características hidrogeoquímicas e tempo de vazamento de CO_2. Para cada parâmetro analisado, ao menos três resultados válidos foram comparados,

proporcionando uma interpretação mais representativa. As alterações na água subterrânea foram enquadradas nos mecanismos geoquímicos mais prováveis responsáveis pelas alterações observadas.

A análise dos dados integrados dos estudos selecionados revelou que: (1) a troca iônica foi a principal responsável pelo aumento temporário das concentrações de Mg, Ca, Ba e Sr, especialmente em aquíferos dominados por silicatos com presença de minerais argilosos e baixa presença de carbonatos. As concentrações de Na e K também responderam ao aumento de CO_2, embora de forma menos intensa; (2) os processos de sorção e dessorção foram relacionados às variações de metais pesados e elementos-traço, sendo regulados pela composição mineral do aquífero. Elementos como As, Cr, Co, Ni e Zn atingiram concentrações máximas durante a injeção e retornaram aos valores de fundo posteriormente; (3) a dissolução de silicatos e carbonatos desempenhou papéis diferentes, com os aquíferos silicáticos mostrando acidificação mais persistente e cinética de dissolução mais lenta; e (4) os processos de mistura conservativa e oxidação foram apontados como possíveis mecanismos para a resposta de Cl^-, SO_4^{2-} e NO_3^-.

Em geral, o artigo publicado destacou como os experimentos de campo avançaram no entendimento das vias de impacto na água subterrânea próxima à superfície, enquadrando-as em mecanismos geoquímicos possíveis. No entanto, ainda existem processos e parâmetros cujo entendimento necessita ser aprofundado, como oxigênio dissolvido (OD), potencial de oxidação-redução (ORP), assinatura isotópica e composição de gases dissolvidos.

Além disso, embora na grande maioria dos casos nenhum parâmetro tenha excedido os limites de potabilidade para a água, poucos estudos foram realizados por períodos prolongados (escala de meses/anos), o que pode afetar como o vazamento de CO_2 se manifestaria em exposições prolongadas. Isso representa um ponto de avanço futuro, embora seja reconhecido que o custo elevado de um experimento dessa natureza possa impedir seu desenvolvimento.

7.2. Avaliação hidrogeológica e hidrogeoquímica sazonal do *site* experimental

Os resultados apresentados no segundo artigo revelaram *insights* cruciais sobre a importância da caracterização hidrogeológica do local e do desenvolvimento de uma

pesquisa de linha de base hidrogeoquímica ampliada, com o objetivo de rastrear vazamentos não intencionais em aquíferos rasos em locais de projetos de CCS. Sistemas aquíferos multicamadas podem apresentar dificuldades particulares para um diagnóstico correto dos padrões hidroquímicos, especialmente em contextos com conexão aberta com águas de recarga e aquíferos subjacentes.

Com base nos resultados e discussões apresentadas, foi possível chegar à algumas conclusões. Embora a área de estudo esteja inserida em um contexto geológico simples (ambiente granítico alterado), uma investigação aprofundada revelou a presença de um aquífero freático multicamadas nos primeiros metros do horizonte de solo alterado, com duas unidades exibindo características litológicas, hidráulicas, geofísicas e hidroquímicas distintas. A unidade St, onde acontece predominantemente o processo interativo com o CO_2, possui condutividade hidráulica da ordem de 10^{-4} m/s e é mais suscetível a flutuações no nível de água devido à recarga e apresenta um padrão de nível de água que reflete esse comportamento. Hidroquimicamente, a unidade mostra pH tendendo a neutro e maiores amplitudes de temperatura, CE, ORP e OD, além de concentrações mais elevadas de Ca, Mg, K, Fe, Mn, Sr, B, HCO_3^- e CID, com assinatura isotópica da água (δ^{13}C-DIC) variando entre aproximadamente -3 e -8 ‰.

A unidade Aa, onde o CO_2(g) é liberado controladamente no aquífero, apresenta condutividade hidráulica da ordem de 10^{-8} m/s e é menos suscetível a flutuações durante períodos de recarga e apresenta um nível de água que às vezes atinge o fundo do poço em períodos secos. Hidroquimicamente, apresenta pH ligeiramente ácido, menores amplitudes de temperatura, CE e ORP, mas maior flutuação de OD. Além disso, exibe concentrações mais altas de Na, SO_4^{2-}, Cl^-, NO_3^-, Zn, Al, Ni e menores concentrações de HCO_3^- e CID, com assinatura isotópica da água (δ^{13}C-DIC) ligeiramente mais depletada (variando entre -6 e -11 ‰).

Além disso, a campanha de monitoramento sazonal de três anos executada revelou que K, Na e elementos-traço (Fe, Ba, Mn, Al, B e Zn) são claramente afetados por interferências sazonais derivadas da temperatura (maior taxa de dissolução e PCO_2), com concentrações proporcionalmente mais altas no verão, primavera e outono em comparação com o inverno. Por outro lado, Ca, Mg, Sr e Ni não parecem ser influenciados por diferenças sazonais de temperatura ou PCO_2 ligeiramente mais

elevado (pH mais baixo). Por fim, conclui-se que Cartas de Controle (ferramenta utilizada para separar as variações de causas comuns das variações de causas especiais) são valiosas para compreender as tendências hidroquímicas naturais presentes no background. Ao avaliar estudos anteriores em um contexto hidrogeológico similar, essa ferramenta estatística ofereceu a oportunidade de considerar ou excluir seletivamente certos parâmetros. Os parâmetros de controle inferior e superior foram, inclusive, usados como patamares de comparação no experimento desenvolvido e detalhado no terceiro artigo.

7.3. Alterações hidrogeoquímicas em aquífero dominado por silicatos durante liberação controlada de CO_2

Por último, no terceiro artigo, foram observadas variações consistentes nos parâmetros físico-químicos, íons maiores e elementos-traço durante o experimento de liberação controlada de CO_2 na área de estudo. Essas variações foram associadas à chegada da pluma de água subterrânea impactada pelo CO_2 nos poços de monitoramento próximos ao local de injeção. A injeção de CO_2 foi realizada em três taxas distintas (5, 10 e 12.5 kg/dia), demonstrando que taxas de liberação mais altas aumentaram a clareza na detecção dos parâmetros hidroquímicos, facilitando a observação das mudanças na química da água subterrânea. No entanto, devido à natureza rasa do local, eventos de precipitação também influenciaram a magnitude das alterações hidrogeoquímicas, diferindo, em alguns casos, dos resultados de outros estudos referenciados. Isso precisa ser avaliado com casos futuros reais de projetos de CCS.

O avanço da pluma de água subterrânea impactada pelo CO_2 foi claramente identificado nos poços por meio de aumentos na CE, alcalinidade total (e consequentemente HCO_3^-), PCO_2 e em vários elementos e compostos químicos, incluindo Ca, Mg, K, Sr, Ba, Na, Fe, Si e Cl^-. Essas mudanças se tornaram mais evidentes quando a taxa de injeção de CO_2 foi aumentada para 10 kg/dia. A aplicação de estatística multivariada (PCA e Análise de Correlação) foi fundamental para identificar grupos de poços impactados pelo CO_2 e acompanhar a evolução dos íons dissolvidos em relação à PCO_2. Essas análises também reduziram a

dimensionalidade ao focar em variáveis com forte correlação direta com a PCO_2, incluindo CE, pH, HCO_3^-, Cl^-, alcalinidade total, Ca, Mg, Na, Si, Ba, Sr, Fe e Mn.

A comparação subsequente dessas variáveis com a PCO_2 calculada para cada poço permitiu estabelecer uma tendência evolutiva cronológica, indicando que certas variáveis apresentaram padrões mais claros durante as condições de background e em baixas taxas de injeção, com mudanças mais acentuadas a 10 kg/dia e picos a 12,5 kg/dia. Em comparação mais detalhada com outros estudos e uma análise do comportamento dos elementos sugerem que o mecanismo geoquímico dominante responsável pela liberação de Ca, Mg, Na, K, Sr, Ba e HCO_3^- é a troca iônica direta ou reversa. Em contraste, o comportamento de Fe e Mn sugere uma via de reação intermediária envolvendo a dessorção desses metais de locais de troca e sorção superficial.

Embora os eventos de precipitação tenham claramente influenciado o fluxo de CO_2(g) e a mistura com a água subterrânea impactada por CO_2 tenha alterado a magnitude dos parâmetros físico-químicos e químicos, a sensibilidade ao vazamento de CO_2 pôde ser avaliada em relação aos limites de controle inferior e superior de cada variável herdados dos limiteis (inferior e superior) da Carta de Controle sazonal. Nesse contexto, uma variação superior a 20% indica que CE, Ca, Mg, Fe, HCO_3^-, Ba, Sr e Mn podem ser usados com confiança como indicadores de vazamento. Ademais, o comportamento observado de Fe e Mn merece atenção especial, pois suas concentrações ultrapassam os níveis máximos permitidos quando comparados às regulamentações nacionais e internacionais. Dado o comportamento semelhante relatado em águas subterrâneas impactadas por CO_2 natural a longo prazo em formações rochosas ricas em silicatos reativos (argilas e óxihidróxidos) com capacidade de tamponamento limitada, isso sugere um ponto de atenção ambientalmente significativo.

7.4. Considerações finais e perspectivas futuras

Em conclusão, o mecanismo geoquímico inicial que provoca mudanças significativas nas concentrações de íons como Ca, Mg, Ba, Sr, Na e K (e, em alguns casos, Si) nos estágios iniciais da interação CO_2-água subterrânea-mineral é predominantemente a troca iônica, direta ou reversa. Esse processo tende a ser mais

acentuado em aquíferos com maior conteúdo de argilominerais e/ou presença de óxidos e hidróxidos. A liberação de metais pesados e elementos-traço, por sua vez, é fortemente controlada pelas condições do meio. A liberação de alguns elementos, como Fe e Mn, está associada à sorção e dessorção na matriz mineral do aquífero. A dissolução mineral, propriamente dita, torna-se mais representativa após um período de interação mais prolongado, o que dificulta sua observação em experimentos de curta duração.

Para que essas mudanças sejam detectáveis e monitoradas com eficácia, é imprescindível um conhecimento hidroquímico sazonal detalhado da área de estudo, aliado a uma caracterização geológica e hidrogeológica adequada. Além disso, o uso de ferramentas estatísticas, como Cartas de Controle, Análise de Componentes Principais (PCA) e Análise de Correlação, é essencial para uma interpretação mais precisa dos dados. Interferências, como a infiltração de água meteórica ou a mistura com águas de outros aquíferos, podem dificultar a caracterização do 'sinal de vazamento' de CO_2. Ademais, a quantidade de CO_2 vazada pode não ser suficiente para causar mudanças hidroquímicas detectáveis por análises convencionais, como observado no experimento de campo realizado durante as fases iniciais.

Por último, embora não tenha sido abordada em detalhe nesta tese, a assinatura isotópica da água subterrânea ($\delta^{13}C$-DIC) será objeto de avaliação mais aprofundada nas próximas etapas da pesquisa. Devido a problemas técnicos nas análises, os resultados obtidos até o momento não permitiram a consolidação definitiva desse parâmetro, que será incorporado no terceiro artigo. Além disso, nos próximos meses e anos, espera-se que esses resultados sejam comparados com um sistema de medição automática de pH, condutividade elétrica (CE) e, futuramente, com um sensor de PCO_2. Essa abordagem permitirá a correlação entre essas variáveis e as alterações hidroquímicas da água, viabilizando o desenvolvimento de uma ferramenta de monitoramento em tempo real para projetos de CCS em escala real.

Referências bibliográficas

ABNT. **Amostragem de água subterrânea em poços de monitoramento — Métodos de purga**. NBR 15847ABNT, , 2010.

ADAMS, S. et al. **Hydrochemical characteristics of aquifers near Sutherland in the Western Karoo, South Africa**. Journal of Hydrology, v. 241, n. 1–2, p. 91–103, jan. 2001.

AGÊNCIA FAPESP. **Studies on carbon storage supported by FAPESP contributed to legislative proposal**.

AJAYI, T.; GOMES, J. S.; BERA, A. **A review of CO2 storage in geological formations emphasizing modeling, monitoring and capacity estimation approaches**. Petroleum Science, v. 16, n. 5, p. 1028–1063, 2019.

ANDREANI, M. et al. **Experimental study of carbon sequestration reactions controlled by the percolation of CO2-rich brine through peridotites**. Geochim. Cosmochim. Acta, v. 73, p. A42, 2009.

APPELO, C. A. J. et al. **Modeling In Situ Iron Removal from Ground Water**. Groundwater, v. 37, n. 6, p. 811–817, 4 nov. 1999.

APPELO, C. A. J.; POSTMA, D. **Geochemistry, groundwater and pollutio**n. Geochemistry, groundwater and pollution, 2005.

ASSAYAG, N. et al. **Water–rock interactions during a CO2 injection field-test: Implications on host rock dissolution and alteration effects**. Chemical Geology, v. 265, n. 1–2, p. 227–235, jul. 2009.

ASTM. **Standard Guide for Comparison of Field Methods for Determining Hydraulic Conductivity in Vadose Zone 1**. 2016.

ASTM. **Standard Guide for Purging Methods for Wells Used for Ground Water Quality Investigations**. D6452-18, 2018.

ASTM. **Standard Guide for Sampling Ground-Water Monitoring Wells**. D4448-01(2019) ASTM, 2019.

AUKEN, E. et al. **Imaging subsurface migration of dissolved CO2 in a shallow aquifer using 3-D time-lapse electrical resistivity tomography**. Journal of Applied Geophysics, v. 101, p. 31–41, 2014.

AZAR, C. et al. **Carbon Capture and Storage from Fossil Fuels and Biomass – Costs and Potential Role in Stabilizing the Atmosphere**. Climatic Change, v. 74, n. 1–3, p. 47–79, 1 jan. 2006.

BARBOSA, P. et al. **GDO Analytical Report**. [s.l: s.n.]. Disponível em: <https://publications.jrc.ec.europa.eu/repository/bitstream/JRC125320/jrc125320_annual_droughts_report_final.pdf>.

BARRIO, M. et al. **CO2 Migration Monitoring Methodology in the Shallow Subsurface : Lessons Learned From the CO2 FIELDLAB Project**. Energy Procedia, v. 51, n. 1876, p. 65–74, 2014.

BEAUBIEN, S. E. et al. **The Importance of Baseline Surveys of Near-Surface Gas Geochemistry for CCS Monitoring, as Shown from Onshore Case Studies in Northern and Southern Europe**. Oil & Gas Science and Technology – Revue d'IFP Energies nouvelles, v. 70, n. 4, p. 615–633, 4 jul. 2015.

BENSON, S. M. et al. **Lessons Learned from Natural and Industrial Analogues for Storage of Carbon Dioxide in Deep Geological Formations**. Berkeley, CA: [s.n.].

BENSON, S. M.; COLE, D. R. **CO2 Sequestration in Deep Sedimentary Formations**. Elements, v. 4, n. 5, p. 325–331, 1 out. 2008.

BERGER, P. M.; WIMMER, B.; IRANMANESH, A. **Sensitivity thresholds of groundwater parameters for detecting CO2 leakage at a geologic carbon sequestration site**. Environmental Monitoring and Assessment, v. 191, n. 11, 1 nov. 2019.

BERKOWITZ, B.; DROR, I.; YARON, B. **Contaminant Geochemistry: Interactions and Transport in the Subsurface Environment**. Berlin: Springer Berlin Heidelberg, 2014. v. 2

BERREZUETA, E. et al**. Pore system changes during experimental CO2 injection into detritic rocks: Studies of potential storage rocks from some sedimentary basins of Spain**. International Journal of Greenhouse Gas Control, v. 17, p. 411–422, 2013.

BIELICKI, J. M. et al. **An examination of geologic carbon sequestration policies in the context of leakage potential**. International Journal of Greenhouse Gas Control, v. 37, p. 61–75, 2015.

BOUC, O. et al. **Determining safety criteria for CO2 geological storage**. Energy Procedia. Anais...fev. 2009.

BOUWER, H.; RICE, R. C. **A slug test method for determining hydraulic conductivity of unconfined aquifers with completely or partially penetrating wells**. Water Resources Research, v. 12, n. 3, p. 423–428, 1976.

BRASIL. Lei no 6.938. **Dispõe sobre a Política Nacional do Meio Ambiente, seus fins e mecanismos de formulação e aplicação, e dá outras providências**. Brasília, 1981. Disponível em: <http://www.planalto.gov.br/ccivil_03/Leis/L6938.htm>. Acesso em: 8 set. 2022

BRASIL. **Resolução CONAMA No 396/2008 - "Dispõe sobre a classificação e diretrizes ambientais para o enquadramento das águas subterrâneas e dá outras providências**." . . 3 abr. 2008, p. 66–68.

BRASIL. **PORTARIA GM/MS No 888, DE 4 DE MAIO DE 2021. Altera o Anexo XX da Portaria de Consolidação GM/MS no 5, de 28 de setembro de 2017, para dispor sobre os procedimentos de controle e de vigilância da qualidade da água para consumo humano e seu padrão de potabilidade** . . 7 maio 2021, p. 126–136.

BRASIL. **Projeto de Lei no 1425. Disciplina a exploração da atividade de armazenamento permanente de dióxido de carbono de interesse público, em reservatórios geológicos ou temporários, e seu posterior reaproveitamento**. BrasíliaSenado Federal, , 2022. Disponível em: <https://legis.senado.leg.br/sdleg-getter/documento?dm=9165480&ts=1660756497687&disposition=inline>. Acesso em: 8 set. 2022

BRINDHA, K. et al. **Trace metals contamination in groundwater and implications on human health: comprehensive assessment using hydrogeochemical and geostatistical methods**. Environmental Geochemistry and Health, v. 42, n. 11, p. 3819–3839, 29 nov. 2020.

BRYDIE, J. et al. **Assessment of baseline groundwater physical and geochemical properties for the Quest carbon capture and storage project, Alberta, Canada**. Energy Procedia. Anais...Elsevier Ltd, 2014.

BUTLER, J. J. **The Design, Performance, and Analysis of Slug Tests**. 1. ed. [s.l.] Lewis Publishers, 1998. v. 1

BUTTERWICK, L.; DE OUDE, N.; RAYMOND, K. **Safety assessment of boron in aquatic and terrestrial environments**. Ecotoxicology and Environmental Safety, v. 17, n. 3, p. 339–371, 1989.

CAHILL, A. G. et al. **Risks attributable to water quality changes in shallow potable aquifers from geological carbon sequestration leakage into sediments of variable carbonate content**. International Journal of Greenhouse Gas Control, v. 19, p. 117–125, 2013.

CAHILL, A. G. **Hydrogeochemical Impact of CO2 Leakage from Geological Sequestration on Shallow Potable Aquifers**. [s.l.] Technical University of Denmark, 2013.

CAHILL, A. G.; JAKOBSEN, R. **Hydro-geochemical impact of CO2 leakage from geological storage on shallow potable aquifers: A field scale pilot experiment**. International Journal of Greenhouse Gas Control, v. 19, p. 678–688, 2013.

CAHILL, A. G.; JAKOBSEN, R. **Geochemical modeling of a sustained shallow aquifer CO 2 leakage field study and implications for leakage and site monitoring**. International Journal of Greenhouse Gas Control, v. 37, p. 127–141, 2015.

CAHILL, A. G.; JAKOBSEN, R.; MARKER, P. **Hydrogeochemical and Mineralogical Effects of Sustained CO 2 contamination in a Shallow Sandy Aquifer : A field scale controlled release experiment.** p. 3–5, 2014.

CAMA, J.; GANOR, J. **Dissolution Kinetics of Clay Minerals**. [s.l.] Elsevier, 2015. v. 6

CARBONBRIEF. **Mapped: How climate change affects extreme weather around the world**. Disponível em: <https://www.carbonbrief.org/mapped-how-climate-change-affects-extreme-weather-around-the-world/>. Acesso em: 17 set. 2022.

CARMEN ANG. **The Accelerating Frequency of Extreme Weather.** Disponível em: <https://www.visualcapitalist.com/the-accelerating-frequency-of-extreme-weather/>. Acesso em: 17 set. 2022.

CAT. **CAT Climate Target Update Tracker**.

CHADE, J. **Eventos climáticos extremos se multiplicarão, diz painel científico global**. Disponível em: <https://noticias.uol.com.br/colunas/jamil-chade/2021/08/03/eventos-climaticos-extremos-se-multiplicarao-diz-painel-cientifico-global.htm>. Acesso em: 17 set. 2022.

CHADHA, D. K. **A proposed new diagram for geochemical classification of natural waters and interpretation of chemical data**. Hydrogeology Journal. [s.l.] Springer-Verlag, 1999.

CHERIAN, C. et al. **Calcium adsorption on clays: Effects of mineralogy, pore fluid chemistry and temperature**. Applied Clay Science, v. 160, p. 282–289, ago. 2018.

CHOI, B. Y. **Potential impact of leaking CO2 gas and CO2-rich fluids on shallow groundwater quality in the Chungcheong region (South Korea): A hydrogeochemical approach**. International Journal of Greenhouse Gas Control, v. 84, n. August 2018, p. 13–28, 2019.

CLARKE, B. et al. **Climate change, El Niño and infrastructure failures behind massive floods in southern Brazil**. London: [s.n.].

CLARK, I. **Groundwater Geochemistry and Isotopes**. [s.l.] CRC Press, 2015.

CLARK, I. D.; FRITZ, P. **Environmental Isotopes in Hydrogeology**. [s.l.] CRC Press, 1997.

CONOVER, W. J. **Practical nonparametric statistics**. 3rd. ed. New York: John Wiley & Sons, 1999.

COPLEN, T. B. et al. **New Guidelines for δ13C Measurements**. Analytical Chemistry, v. 78, n. 7, p. 2439–2441, 1 abr. 2006.

CORNELIS, G. et al. **Fate and Bioavailability of Engineered Nanoparticles in Soils: A Review**. Critical Reviews in Environmental Science and Technology, v. 44, n. 24, p. 2720–2764, 2014.

CRABTREE, B. **The Critical Role of CCS and EOR in Managing U . S . Carbon Emissions**. 2016.

CUÉLLAR-FRANCA, R. M.; AZAPAGIC, A. **Carbon capture, storage and utilisation technologies: A critical analysis and comparison of their life cycle environmental impacts**. Journal of CO2 Utilization, v. 9, p. 82–102, mar. 2015.

DAFFLON, B. et al. **Monitoring CO2 intrusion and associated geochemical transformations in a shallow groundwater system using complex electrical methods**. Environmental Science and Technology, v. 47, n. 1, p. 314–321, 2 jan. 2013.

DATRY, T.; MALARD, F.; GIBERT, J. **Dynamics of solutes and dissolved oxygen in shallow urban groundwater below a stormwater infiltration basin**. Science of the Total Environment, v. 329, n. 1–3, p. 215–229, 15 ago. 2004.

DEAN, M. et al. **Insights and guidance for offshore CO2 storage monitoring based on the QICS, ETI MMV, and STEMM-CCS projects**. International Journal of Greenhouse Gas Control, v. 100, p. 103120, 2020.

DEGROOT-HEDLIN, C.; CONSTABLE, S. **Occam's inversion to generate smooth, two-dimensional models from magnetotelluric data**. GEOPHYSICS, v. 55, n. 12, p. 1613–1624, dez. 1990.

DELIN, G. N.; LANDON, M. K. **Effects of topography on the transport of agricultural chemicals to groundwater in a sand-plain setting**. Hydrogeology Journal, v. 10, n. 4, p. 443–454, 22 ago. 2002.

DELSARTE, I. et al. **Soil carbon dioxide fluxes to atmosphere: The role of rainfall to control CO2 transport**. Applied Geochemistry, v. 127, p. 104854, abr. 2021.

DO, H.-K. et al. **Evaluation of Long-Term Impacts of CO2 Leakage on Groundwater Quality Using Hydrochemical Data from a Natural Analogue Site in South Korea**. Water, v. 12, n. 5, p. 1457, 20 maio 2020.

DO, H. K. et al. **Tracing CO2 leakage and migration using the hydrogeochemical tracers during a controlled CO2 release field test**. Applied Geochemistry, v. 143, 1 ago. 2022.

DOMAGALSKI, J. L.; JOHNSON, H.; SURVEY, U. S. G. **Phosphorus and groundwater: Establishing links between agricultural use and transport to streams**. Fact Sheet. Reston, VA: [s.n.]. Disponível em: <https://pubs.usgs.gov/publication/fs20123004>.

DREVER, J. I. **The Geochemistry of Natural Waters: Surface and Groundwater Environments**. [s.l.] Prentice Hall, 1997.

(EPA), U. S. E. P. A. **Geologic Sequestration of Carbon Dioxide: Underground Injection Control (UIC) Program Class VI Well Area of Review Evaluation and Corrective Action Guidance**. Disponível em: <https://www.epa.gov/sites/production/files/2015-07/documents/epa816r13005.pdf>.

EUROPEAN ACADEMIES' SCIENCE ADVISORY COUNCIL. **New data confirm increased frequency of extreme weather events**. Disponível em: <https://www.sciencedaily.com/releases/2018/03/180321130859.htm>. Acesso em: 17 set. 2022.

EUROPEAN PARLIAMENT AND COUNCIL. **Directive 2009/31/EC of the European Parliament and of the Council of 23 April 2009 on the geological storage of carbon dioxide and amending Council Directive 85/337/EEC**, European Parliament and Council Directives 2000/60/EC, 2001/80/EC, 2004/35/EC, 2006/12/EC, 2008/1/ EC and Regulation (EC) No 1013/2006. European Parliament and Council, , 2009.

FAURE, G.; MENSING, T. M. **Isotopes: Principles and Applications**. 3. ed. Hoboken, USA: Wiley, 2004.

FEITZ, A. J. et al. **Looking for leakage or monitoring for public assurance?** Energy Procedia, v. 63, p. 3881–3890, 2014.

FETTER, C. W. **Contaminant hydrogeology**. [s.l: s.n.].

FIANCO, A. C. B. **CONCENTRAÇÕES DE RADÔNIO NAS ÁGUAS SUBTERRÂNEAS, ROCHAS E SOLOS DE PORTO ALEGRE-RS**. Master's degree Thesis—Porto Alegre, RS: UNIVERSIDADE FEDERAL DO RIO GRANDE DO SUL, 2011.

FOULQUIER, A. et al. **Thermal influence of urban groundwater recharge from stormwater infiltration basins**. Hydrological Processes, v. 23, n. 12, p. 1701–1713, 15 jun. 2009.

FOULQUIER, A. et al. **Vertical change in dissolved organic carbon and oxygen at the water table region of an aquifer recharged with stormwater: Biological uptake or mixing?** Biogeochemistry, v. 99, n. 1, p. 31–47, 2010.

FRAGOSO CESAR, A. R. S. et al. **O Batólito Pelotas (Proterozóico Superior/Eo-Paleozóico) no Escudo do Rio Grande do Sul**. 34o Congresso Brasileiro de Geologia. Anais...Goiânia (GO), Brazil: SBG, 1986.

FRIEDMAN, I.; O'NEIL, J.; CEBULA, G. **Two New Carbonate Stable-Isotope Standards**. Geostandards and Geoanalytical Research, v. 6, n. 1, p. 11–12, abr. 1982.

FRITZ, S. J. **Survey of CBE on Piblished Analyis of Potable Ground and Surface Waters**. Groundwater, v. 32, n. 4, p. 539–546, 1994.

GAILLARDET, J. et al. **Global silicate weathering and CO2 consumption rates deduced from the chemistry of large rivers**. Chemical Geology, v. 159, n. 1–4, p. 3–30, jul. 1999.

GALE, J. **Geological storage of CO2: What do we know, where are the gaps and what more needs to be done?** Energy, v. 29, n. 9–10, p. 1329–1338, 2004.

GAL, F. et al. **Inducing a CO2 leak into a shallow aquifer (CO 2fieldlab eurogia+ project): Monitoring the CO2 plume in groundwaters**. Energy Procedia, v. 37, n. 0, p. 3583–3593, 2013.

GAL, F. et al. **CO2 leakage in a shallow aquifer - Observed changes in case of small release**. Energy Procedia, v. 63, n. 0, p. 4112–4122, 2014.

GCCSI. **Global Status of CCS 2022**. [s.l: s.n.].

GCCSI. **Global Status of CCS 2023: Scaling up through 2030**. Australia: [s.n.].

GLOBAL CCS INSTITUTE. **The Global Status of CCS 2018**. [s.l: s.n.].

GLOBAL CCS INSTITUTE. **The Global Status of CCS 2020**. Global CCS Institute. [s.l: s.n.].

GLOBAL CCS INSTITUTE. **Global Status of CCS 2021: CCS Accelerating to Net ZeroGlobal** Status of CCS 2021. [s.l: s.n.].

GOLDBERG, S. et al. **Mechanism of Molybdenum Adsorption on Soils and Soil Minerals Evaluated Using Vibrational Spectroscopy and Surface Complexation Modeling**. Developments in Earth and Environmental Sciences, v. 7, n. 07, p. 235–266, 2007.

GOLDBERG, S.; LESCH, S. M.; SUAREZ, D. L. **Predicting Boron Adsorption by Soils Using Soil Chemical Parameters in the Constant Capacitance Model**. Soil Sci. Soc. Am. J., n. 64, p. 1356–1363, 2000.

GOLDICH, S. S. **A Study in Rock-Weathering**. The Journal of Geology, v. 46, n. 1, jan. 1938.

GOMBERT, P. et al. **Selection, instrumentation and characterization of a pilot site for CO2 leakage experimentation in a superficial aquifer**. Energy Procedia, v. 63, n. 0, p. 3172–3181, 2014.

GRIMM, A. M. et al. **The combined effect of climate oscillations in producing extremes: the 2020 drought in southern Brazil**. RBRH, v. 25, 2020.

GUPTA, P. K.; YADAV, B. **Leakage of CO2 from geological storage and its impacts on fresh soil–water systems: a review**. Environmental Science and Pollution Research, v. 27, n. 12, p. 12995–13018, 2020.

HA-DUONG, M.; LOISEL, R. **Zero is the only acceptable leakage rate for geologically stored CO2: An editorial comment**. Climatic Change, v. 93, n. 3–4, p. 311–317, 2009.

HA, J. H. et al. **Changes in geochemical and carbon isotopic compositions during reactions of CO2-saturated groundwater with aquifer materials**. International Journal of Greenhouse Gas Control, v. 95, n. May 2019, p. 102961, 2020.

HANNAH, L. **The Climate System and Climate Change**. Em: Climate Change Biology. [s.l.] Elsevier, 2011. p. 13–52.

HARVEY, O. R. et al. **Geochemical implications of gas leakage associated with geologic CO 2 storage - A qualitative review**. Environmental Science and Technology, v. 47, n. 1, p. 23–36, 2013.

HEM, J. D. **Study and Interpreatation of the Chemical Characteristics of Natural Water**. [s.l.] U.S. Geological Survey, 1985.

HEPPLE, R. P.; BENSON, S. M. **Geologic storage of carbon dioxide as a climate change mitigation strategy: Performance requirements and the implications of surface seepage**. Environmental Geology, v. 47, n. 4, p. 576–585, 2005.

HOEFS, J. **Stable Isotope Geochemistry**. Cham: Springer International Publishing, 2021.

HUMEZ, P. et al. **Assessing the potential consequences of CO2 leakage to freshwater resources: A batch-reaction experiment towards an isotopic tracing tool**. Applied Geochemistry, v. 30, n. July 2012, p. 178–190, 2013.

HUMEZ, P. et al. **CO2-water-mineral reactions during CO2 leakage: Geochemical and isotopic monitoring of a CO2 injection field test**. Chemical Geology, v. 368, p. 11–30, 2014.

HVORSLEV, M. J. **Time Lag and Soil Permeability in Ground-Water Observations**. Bull. No. 36, Waterways Exper. Sta. Corps of Engrs, U.S. Army, p. 1–50, 1951.

IEA. **Energy Technology Perspectives 2020**. Energy Technology Perspectives 2020, 2020.

IEA. **Legal and Regulatory Frameworks for CCUS: An IEA CCUS Handbook**. [s.l: s.n.]. Disponível em: <www.iea.org/t&c/>.

IGLESIAS, C. et al. **Shewhart-type control charts and functional data analysis for water quality analysis based on a global indicator**. Desalination and Water Treatment, v. 57, n. 6, p. 2669–2684, 7 fev. 2016.

IGLESIAS, R. S. et al. **Modeling CO2 flow in support of a shallow subsurface controlled leakage field test**. Greenhouse Gases: Science and Technology, v. 9, n. 5, p. 1027–1042, 1 out. 2019.

IPCC. **Special report on carbon dioxide capture and storage**. New York, NY, USA: [s.n.]. Disponível em: <https://www.ipcc.ch/report/carbon-dioxide-capture-and-storage/>. Acesso em: 17 set. 2022a.

IPCC. **Climate Change 2022 - Mitigation of Climate Change** - Summary for Policymakers (SPM). [s.l: s.n.].

IPCC, 2005. **CARBON DIOXIDE CAPTURE AND STORAGE**. [s.l.] Cambridge University Press, 2005b.

IRANMANESH, A.; LOCKE, R. A.; WIMMER, B. T. **Multivariate statistical evaluation of groundwater compliance data from the Illinois Basin - Decatur Project**. Energy Procedia. Anais...Elsevier Ltd, 2014.

JENKINS, C.; CHADWICK, A.; HOVORKA, S. D. **The state of the art in monitoring and verification—Ten years on**. International Journal of Greenhouse Gas Control, v. 40, p. 312–349, 2015.

JEONG, J. et al. **Changes in geochemical composition of groundwater due to CO2 leakage in various geological media**. Water (Switzerland), v. 12, n. 9, p. 9–11, 2020.

JEONG, S.; LEE, H. A.; YOON, H. O. **Analytical methods for geochemical monitoring of CO2 capture and storage sites**. Geosciences Journal, v. 21, n. 4, p. 631–643, 2017.

JOLLIFFE, I. T. **Principal Component Analysis**. New York, NY: Springer New York, 1986.

JONES, D. G. et al. **Developments since 2005 in understanding potential environmental impacts of CO2 leakage from geological storage**. International Journal of Greenhouse Gas Control, v. 40, p. 350–377, 2015.

JONES, N. **How the World Passed a Carbon Threshold and Why It Matters**. Disponível em: <https://e360.yale.edu/features/how-the-world-passed-a-carbon-threshold-400ppm-and-why-it-matters>. Acesso em: 23 jul. 2022.

JUN, S. C. et al. **Controlled Release Test Facility to Develop Environmental Monitoring Techniques for Geologically Stored CO2 in Korea**. Energy Procedia. Anais...Elsevier Ltd, 2017.

JU, Y. J. et al. **Application of natural and artificial tracers to constrain CO2 leakage and degassing in the K-COSEM site, South Korea**. International Journal of Greenhouse Gas Control, v. 86, n. May, p. 211–225, 2019.

KANAGARAJ, G.; ELANGO, L. **Chromium and fluoride contamination in groundwater around leather tanning industries in southern India: Implications from stable isotopic ratio δ53Cr/δ52Cr, geochemical and geostatistical modelling**. Chemosphere, v. 220, p. 943–953, abr. 2019.

KEATING, E. et al. **Insights into interconnections between the shallow and deep systems from a natural CO2 reservoir near Springerville, Arizona**. International Journal of Greenhouse Gas Control, v. 25, p. 162–172, 2014.

KEATING, E. H. et al. **The impact of CO2 on shallow groundwater chemistry: observations at a natural analog site and implications for carbon sequestration**. Environmental Earth Sciences, v. 60, n. 3, p. 521–536, 2010.

KETZER, J. M.; IGLESIAS, R. S.; EINLOFT, S. **Reducing Greenhouse Gas Emissions with CO2 Capture and Geological Storage**. Em: CHEN, W.-Y. et al. (Eds.). Handbook of Climate Change Mitigation. New York, NY: Springer US, 2012. p. 1405–1440.

KETZER, J. M. M. et al. **Brazilian Atlas of CO2 Capture and Geological Storage**. Porto Alegre: EdiPUCRS, 2016.

KHARAKA, Y. K. et al. **Changes in the chemistry of shallow groundwater related to the 2008 injection of CO2 at the ZERT field site, Bozeman, Montana**. Environmental Earth Sciences, v. 60, n. 2, p. 273–284, 2010.

KHARAKA, Y. K. et al. **Changes in the chemistry of groundwater reacted with CO2: Comparison of results from laboratory experiments and the ZERT field site, Bozeman, Montana, USA**. Applied Geochemistry, v. 98, n. July, p. 75–81, 2018.

KLAPPSTEIN, G.; ROSTRON, B. **Shallow hydrogeological and hydrochemical characterization of the Aquistore CO2 sequestration site in Estevan, Saskatchewan, Canada**. Energy Procedia. Anais...Elsevier Ltd, 2014.

KORETSKY, C. **The significance of surface complexation reactions in hydrologic systems: A geochemist's perspective**. Journal of Hydrology, v. 230, n. 3–4, p. 127–171, 2000.

LAMERT, H. et al. **Feasibility of geoelectrical monitoring and multiphase modeling for process understanding of gaseous CO 2 injection into a shallow aquifer**. Environmental Earth Sciences, v. 67, n. 2, p. 447–462, set. 2012.

LASAGA, A. C. **Chemical Kinetics of Water-Rock**. Journal of Geophysical Research, v. 89, n. B6, p. 4009–4025, 1984.

LAWTER, A. et al. **Evaluating impacts of CO2 intrusion into an unconsolidated aquifer: I. Experimental data**. International Journal of Greenhouse Gas Control, v. 44, p. 323–333, jan. 2016.

LEE, K. K. et al. **Shallow groundwater system monitoring on controlled CO2 release sites: a review on field experimental methods and efforts for CO2 leakage detection**. Geosciences Journal, v. 20, n. 4, p. 569–583, 2016.

LEE, S. S. et al. **Design and and Construction of Groundwater Monitoring Network at Shallow-depth CO2 Injection and Leak Test Site, Korea**. Energy Procedia, v. 114, n. November 2016, p. 3060–3069, 2017.

LEMIEUX, J. M. Review: **The potential impact of underground geological storage of carbon dioxide in deep saline aquifers on shallow groundwater resources**. Hydrogeology Journal, v. 19, n. 4, p. 757–778, 2011.

LE QUÉRÉ, C. et al. **Temporary reduction in daily global CO2 emissions during the COVID-19 forced confinement**. Nature Climate Change, v. 10, n. 7, p. 647–653, 2020.

LE ROUX, O. et al. **The CO2-Vadose project: Time-lapse geoelectrical monitoring during CO2 diffusion in the carbonate vadose zone**. International Journal of Greenhouse Gas Control, v. 16, p. 156–166, 2013.

LEWICKI, J. L.; BIRKHOLZER, J.; TSANG, C.-F. **Natural and industrial analogues for leakage of CO2 from storage reservoirs: identification of features, events, and processes and lessons learned**. Environmental Geology, v. 52, n. 3, p. 457, 2006.

LINDSEY, R. **Climate Change: Atmospheric Carbon Dioxide**. Disponível em: <https://www.climate.gov/news-features/understanding-climate/climate-change-atmospheric-carbon-dioxide>. Acesso em: 12 abr. 2021.

LIONS, J. et al. **Potential impacts of leakage from CO2 geological storage on geochemical processes controlling fresh groundwater quality: A review**. International Journal of Greenhouse Gas Control, v. 22, p. 165–175, 2014.

LIU, Z. et al. **Near-real-time data captured record decline in global CO2 emissions due to COVID-19**. arXiv, p. 1–45, 2020.

LU, J. et al. **Potential risks to freshwater resources as a result of leakage from CO2 geological storage: A batch-reaction experiment**. Environmental Earth Sciences, v. 60, n. 2, p. 335–348, 2010.

MA, J. et al. **Advances in Geochemical Monitoring Technologies for CO2 Geological Storage**. Sustainability, v. 16, n. 16, p. 6784, 7 ago. 2024.

MARTIN-ROBERTS, E. et al. **Carbon capture and storage at the end of a lost decade**. One Earth, v. 4, n. 11, p. 1569–1584, 2021.

MAYER, B. et al. **Assessing the usefulness of the isotopic composition of CO2 for leakage monitoring at CO2 storage sites: A review**. International Journal of Greenhouse Gas Control, v. 37, p. 46–60, 2015.

MELO, C. L. et al. **CO2MOVE Project: The New Brazilian Field Lab Fully Dedicated to CO2 MMV Experiments**. Energy Procedia. Anais...Elsevier Ltd, 2017.

MERKEL, B. J.; PLANER-FRIEDRICH, B. **Groundwater Geochemistry: A Practical Guide to Modeling of Natural and Contaminated Aquatic Systems**. Berlin, Heidelberg: Springer Berlin Heidelberg, 2008.

MICKLER, P. J. et al. **Potential impacts of CO2 leakage on groundwater chemistry from laboratory batch experiments and field push-pull tests**. Environmental Science and Technology, v. 47, n. 18, p. 10694–10702, 2013.

MIGLIAVACCA, D. et al. **Atmospheric precipitation and chemical composition of an urban site, Guaíba hydrographic basin, Brazil**. Atmospheric Environment, v. 39, n. 10, p. 1829–1844, mar. 2005.

MILLER, J. B.; TANS, P. P. C**alculating isotopic fractionation from atmospheric measurements at various scales**. Tellus B, v. 55, n. 2, p. 207–214, abr. 2003.

MORSE, J. W.; ARVIDSON, R. S. **The dissolution kinetics of major sedimentary carbonate minerals**. Earth-Science Reviews, v. 58, n. 1–2, p. 51–84, 2002.

MTHEMBU, P. P. et al. **Hydrogeochemical Processes and Trace Metal Contamination in Groundwater: Impact on Human Health in the Maputaland Coastal Aquifer, South Africa**. Exposure and Health, v. 12, n. 3, p. 403–426, 10 set. 2020.

MYERS, M. et al. **CSIRO In-Situ Lab: A multi-pronged approach to surface gas and groundwater monitoring at geological CO2 storage sites**. Chemical Geology, v. 545, n. April, p. 119642, 2020.

NÉGREL, P. et al. **Heterogeneities and interconnections in groundwaters: Coupled B, Li and stable-isotope variations in a large aquifer system (Eocene Sand aquifer, Southwestern France)**. Chemical Geology, v. 296–297, p. 83–95, 2012.

NELSON, C. R. et al. **Factors affecting the potential for CO2 leakage from geologic sinks**. USA: [s.n.].

NETHONONDA, V. G.; ELUMALAI, V.; RAJMOHAN, N. **Irrigation return flow induced mineral weathering and ion exchange reactions in the aquifer, Luvuvhu catchment, South Africa**. Journal of African Earth Sciences, v. 149, p. 517–528, jan. 2019.

NEWELL, D. L. et al. **Tracing CO2 leakage into groundwater using carbon and strontium isotopes during a controlled CO2 release field test**. International Journal of Greenhouse Gas Control, v. 29, p. 200–208, 1 out. 2014.

NUGENT, C. **Carbon Dioxide Concentration in the Earth's Atmosphere Has Hit Levels Unseen for 3 Million Years**. Disponível em: <https://time.com/5588794/carbon-dioxide-earth-climate-change/>. Acesso em: 23 jul. 2022.

OELKERS, E. H.; COLE, D. R. C**arbon Dioxide Sequestration A Solution to a Global Problem**. Elements, v. 4, n. 5, p. 305–310, 1 out. 2008.

OLIVA, A. et al. G**eoelectrical Remote System for Monitoring Shallow Subsurface CO2 Migration**. [s.l: s.n.].

OLIVAA, A. et al. **A comparison of three methods for monitoring CO2 migration in soil and shallow subsurface in the Ressacada Pilot site, Southern Brazil**. Energy Procedia. Anais...Elsevier Ltd, 2014.

PARKHURST, D. L.; APPELO, C. A. J. **Description of input and examples for PHREEQC version 3—A computer program for speciation, batch-reaction, one-dimensional transport, and inverse geochemical calculations**.

PASTÉN-ZAPATA, E. et al. **Assessment of sources and fate of nitrate in shallow groundwater of an agricultural area by using a multi-tracer approach**. Science of The Total Environment, v. 470–471, p. 855–864, fev. 2014.

PEIRIS, N.; GOURDJI, S.; PANDEY, A. **Persistent La Niña Conditions Aggravate Drought-Associated Crop Losses in Southern Brazil in 2021–22**.

PÈPE, G. et al. **Atomic modelling of crystal/complex fluid/crystal contacts—Part II. Simulating AFM tests via the GenMol code for investigating the impact of CO2 storage on kaolinite/brine/kaolinite adhesion**. Journal of Crystal Growth, v. 312, n. 22, p. 3308–3315, 2010.

PETER, A. et al. **Investigation of the geochemical impact of CO2 on shallow groundwater: Design and implementation of a CO2 injection test in Northeast Germany**. Environmental Earth Sciences, v. 67, n. 2, p. 335–349, 2012.

PETER, A.; HORNBRUCH, G.; DAHMKE, A. **CO2 leakage test in a shallow aquifer for investigating the geochemical impact of CO2 on groundwater and for developing monitoring methods and concepts**. Energy Procedia, v. 4, p. 4148–4153, 2011.

PETIT, A. et al. **Aquifer-CO2 leak project: Physicochemical characterization of the CO2 leakage impact on a carbonate shallow freshwater aquifer**. International Journal of Greenhouse Gas Control, v. 106, n. May 2020, 2021.

PEZARD, P. A. et al. **Time-lapse downhole electrical resistivity monitoring of subsurface CO2 storage at the Maguelone shallow experimental site (Languedoc, France)**. International Journal of Greenhouse Gas Control, v. 48, p. 142–154, 2016.

PHILIPP, R. P. **A evolução geológica e tectônica do Batólito de Pelotas no Rio Grande do Sul**. Doctoral Degree Thesis—São Paulo: Universidade de São Paulo, 1988.

PHILLIP, R. P. et al. **O MAGMATISMO GRANÍTICO NEOPROTEROZÓICO DO BATÓLITO PELOTAS NO SUL DO BRASIL: NOVOS DADOS E REVISÃO DA GEOCRONOLOGIA REGIONAL**. Revista Brasileira de Geociências, v. 32, n. 2, p. 277–290, 1 jun. 2002.

PHILLIP, R. P.; DE CAMPOS, R. S. **Geologia, Petrografia e Litogeoquímica dos Gnaisses Porto Alegre, RS, Brasil: Implicações Geotectônicas**. Pesquisas em Geociências, v. 31, n. 2, p. 79, 31 dez. 2004.

POROWSKI; POROWSKA; HALAS. **Identification of Sulfate Sources and Biogeochemical Processes in an Aquifer Affected by Peatland: Insights from Monitoring the Isotopic Composition of Groundwater Sulfate in Kampinos National Park, Poland**. Water, v. 11, n. 7, p. 1388, 5 jul. 2019.

QAFOKU, N. P. et al. **Review of the impacts of leaking CO2 gas and brine on groundwater quality**. Earth-Science Reviews, v. 169, p. 69–84, jun. 2017.

RAMAGE, L. **HIDROGEOQUÍMICA DO SISTEMA AQÜÍFERO GRANULAR CENOZÓICO DO MUNICÍPIO DE PORTO ALEGRE, RS**. Master's degree Thesis—Porto Alegre, RS - Brazil: UNIVERSIDADE FEDERAL DO RIO GRANDE DO SUL, 2005.

REFAT NASHER, N. M.; HUMAYAN AHMED, MD. **Groundwater geochemistry and hydrogeochemical processes in the Lower Ganges-Brahmaputra-Meghna River Basin areas, Bangladesh**. Journal of Asian Earth Sciences: X, v. 6, p. 100062, dez. 2021.

RENAUD, A. et al. **Influence of vegetation-induced water table seasonality on groundwater chloride concentration dynamics in a riparian fen peatland**. Hydrological Processes, v. 37, n. 12, 1 dez. 2023.

RIEDEL, T. **Temperature-associated changes in groundwater quality**. Journal of Hydrology, v. 572, p. 206–212, maio 2019.

RILLARD, J. et al. **Geochemical assessment of CO2 perturbation in a shallow aquifer evaluated by a push-pull field experiment**. International Journal of Greenhouse Gas Control, v. 21, p. 23–32, 2014.

RITCHIE, HANNAH; ROSER, MAX AND ROSADO, P. **CO_2 and Greenhouse Gas Emissions**. Disponível em: <https://ourworldindata.org/co2-and-other-greenhouse-gas-emissions>. Acesso em: 23 jul. 2022.

ROBERTS, J. J. et al. **What Have We Learnt About CO2 Leakage in the Context of Commercial-Scale CCS?** SSRN Electronic Journal, n. October, p. 1–17, 2018.

ROBERTS, J. J.; STALKER, L. **What have we learnt about CO2 leakage from CO2 release field experiments, and what are the gaps for the future?** Earth-Science Reviews, v. 209, n. July 2018, p. 102939, 2020.

ROISENBERG, C.; VIERO, A. P.; ROISENBERG, A. **Caracterização Geoquímica e Gênese dos Principais Íons das Águas Subterrâneas de Porto Alegre, RS**. RBRH – Revista Brasileira de Recursos Hídricos, v. 8, p. 137–147, 2003.

ROSE, S.; LONG, A. **Monitoring Dissolved Oxygen in Ground Water: Some Basic Considerations**. Groundwater Monitoring and Remediation, v. 8, n. 1, p. 93–97, mar. 1988.

SCHULZ, A. et al. **Monitoring of a simulated CO2 leakage in a shallow aquifer using stable carbon isotopes**. Environmental Science and Technology, v. 46, n. 20, p. 11243–11250, 2012.

SENADO FEDERAL. **Projeto de Lei n° 1425 de 2022**.

SENTHILKUMAR, M.; ELANGO, L. **Geochemical processes controlling the groundwater quality in lower Palar river basin, southern India**. Journal of Earth System Science, v. 122, n. 2, p. 419–432, 26 abr. 2013.

SHAO, H. et al. **Coupled Geochemical Impacts of Leaking CO2 and Contaminants from Subsurface Storage Reservoirs on Groundwater Quality**. Environmental Science and Technology, v. 49, n. 13, p. 8202–8209, 2015.

SHAPIRO, S. S.; WILK, M. B. **An analysis of variance test for normality (complete samples).** Biometrika, v. 52, n. 3–4, p. 591–611, 1 dez. 1965.

SHARP, Z. **Principles of Stable Isotope Geochemistry**. 2nd. ed. Hoboken, NJ: Prentice Hall, 2017. v. 1

SHIN, W. J. et al. **Monitoring the movement of artificially injected CO2 at a shallow experimental site in Korea using carbon isotopes**. Journal of Environmental Management, v. 258, n. June 2019, p. 110030, 2020.

SNÆBJÖRNSDÓTTIR, S. et al. **Carbon dioxide storage through mineral carbonation**. Nature Reviews Earth and EnvironmentSpringer Nature, , 1 fev. 2020.

SOILMOISTURE. **Guelph Permeameter K-sat Calculator**.

SPANGLER, L. H. et al. **A shallow subsurface controlled release facility in Bozeman, Montana, USA, for testing near surface CO2 detection techniques and transport models**. Environmental Earth Sciences, v. 60, n. 2, p. 227–239, 2010.

STALLARD, R. F.; EDMOND, J. M. **Geochemistry of the Amazon: 2. The influence of geology and weathering environment on the dissolved load**. Journal of Geophysical Research: Oceans, v. 88, n. C14, p. 9671–9688, 20 nov. 1983.

STAMATAKIS, M.; TZIRITIS, E.; EVELPIDOU, N. **The geochemistry of Boron-rich groundwater of the Karlovassi Basin, Samos Island, Greece**. Central European Journal of Geosciences, v. 1, n. 2, p. 207–218, 2009.

STATISTA. A**verage carbon dioxide (CO_2) levels in the atmosphere worldwide from 1959 to 2023**. Disponível em: <https://www.statista.com/statistics/1091926/atmospheric-concentration-of-co2-historic/>. Acesso em: 12 ago. 2024.

STRAZISAR, B. R. et al. **Near-surface monitoring for the ZERT shallow CO2 injection project**. International Journal of Greenhouse Gas Control, v. 3, n. 6, p. 736–744, 2009.

STUMM, W.; MORGAN, J. J. **Aquatic Chemistry, Chemical Equilibria and Rates in Natural Waters**. 3rd. ed. New York: John Wiley & Sons, Inc., 1996.

SWAMIDASS, P. M. **Shewhart control charts**. Em: Encyclopedia of Production and Manufacturing Management. Boston, MA: Springer US, 2000. p. 685–686.

TAKENO, N. **Atlas of Eh-pH diagrams Intercomparison of thermodynamic databases**. National Institute of Advanced Industrial Science and Technology Tokyo, n. 419, p. 285, 2005.

TAMBARIA, T. N.; SUGAI, Y.; NGUELE, R. **Adsorption Factors in Enhanced Coal Bed Methane Recovery: A Review**. Gases, v. 2, n. 1, p. 1–21, 14 jan. 2022.

TIWARI, P. K. et al. **Monitoring, Measurement and Verification MMV: A Critical Component in Making the CO2 Sequestration Success**. Day 8 Tue, March 30, 2021. Anais...IPTC, 16 mar. 2021.

TORRES-MARTÍNEZ, J. A. et al. **Tracking nitrate and sulfate sources in groundwater of an urbanized valley using a multi-tracer approach combined with a Bayesian isotope mixing model**. Water Research, v. 182, p. 115962, set. 2020.

TRAUTZ, R. C. et al. **Effect of dissolved CO2 on a shallow groundwater system: A controlled release field experiment**. Environmental Science and Technology, v. 47, n. 1, p. 298–305, 2013.

UN. **The Climate Crisis – A Race We Can Win**. Disponível em: <https://www.un.org/en/un75/climate-crisis-race-we-can-win>. Acesso em: 23 jul. 2022.

US EPA. **Class VI Wells Used for Geologic Sequestration of CO2**.

UTLEY, R. E. et al. **Multi-Isotope Geochemical Baseline Study of the Carbon Management Canada Research Institutes CCS Field Research Station (Alberta, Canada), Prior to CO2 Injection**. Earth Science, Systems and Society, v. 3, 16 jan. 2023.

VARADHARAJAN, C. et al. **A laboratory study of the initial effects of dissolved carbon dioxide (CO2) on metal release from shallow sediments**. International Journal of Greenhouse Gas Control, v. 19, p. 183–211, 2013.

VIETH, A.; WILKES, H. **Stable Isotopes in Understanding Origin and Degradation Processes of Petroleum**. Em: Handbook of Hydrocarbon and Lipid Microbiology. Berlin, Heidelberg: Springer Berlin Heidelberg, 2010. p. 97–111.

WANG, G. et al. **Geochemical impacts of leaking CO2 from subsurface storage reservoirs to an unconfined oxidizing carbonate aquifer**. International Journal of Greenhouse Gas Control, v. 44, p. 310–322, 2016.

WANG, J. et al. **A geochemically informed leak detection (GILD) model for CO2 injection sites**. Applied Geochemistry, v. 155, p. 105691, ago. 2023.

WEIR, I. **Spearman's Correlation**. Disponível em: <http://www.statstutor.ac.uk/resources/uploaded/spearmans.pdf>. Acesso em: 19 nov. 2024.

WHO. **Guidelines for Drinking-Water Quality**. 4th ed. ed. Geneva, Switzerland: World Health Organization, 2017.

WINOGRAD, I.; ROBERTSON, F. **Deep Oxygenated Ground Water: Anomaly or Common Occurence?** Science, v. 216, p. 1227–1229, 1982.

XIAO, T. et al. **Arsenic mobilization in shallow aquifers due to CO2 and brine intrusion from storage reservoirs**. Scientific Reports, v. 7, n. 1, p. 2763, 5 jun. 2017.

XIE, W.-Q.; GONG, Y.-X.; YU, K.-X. **Simple and accurate method for determining dissolved inorganic carbon in environmental water by reaction headspace gas chromatography**. Journal of Separation Science, v. 41, n. 5, p. 1091–1095, mar. 2018.

YALE ENVIRONMENT 360. **Extreme Weather Events Have Increased Significantly in the Last 20 Years**. Disponível em: <https://e360.yale.edu/digest/extreme-weather-events-have-increased-significantly-in-the-last-20-

years#:~:text=Climate%2Drelated%20disasters%20jumped%2083,droughts%2C%20wildfires%2C%20and%20heatwaves.>. Acesso em: 17 set. 2022.

YAN, B. et al. **Association of groundwater constituents with topography and distance to unconventional gas wells in NE Pennsylvania**. Science of The Total Environment, v. 577, p. 195–201, jan. 2017.

YANG, C. et al. **Single-well push-pull test for assessing potential impacts of CO2 leakage on groundwater quality in a shallow Gulf Coast aquifer in Cranfield, Mississippi**. International Journal of Greenhouse Gas Control, v. 18, p. 375–387, 2013.

YANG, C. et al. **Field demonstration of CO2 leakage detection in potable aquifers with a pulselike CO2-release test**. Environmental Science and Technology, v. 48, n. 23, p. 14031–14040, 2014.

YANG, J. et al. **Visualization of Aqueous Geochemical Data Using Python and WQChartPy**. Groundwater, v. 60, n. 4, p. 555–564, 1 jul. 2022.

YANG, X. et al. **Monitoring CO2 migration in a shallow sand aquifer using 3D crosshole electrical resistivity tomography**. International Journal of Greenhouse Gas Control, v. 42, p. 534–544, 1 nov. 2015.

ZHENG, L. et al. **Geochemical modeling of changes in shallow groundwater chemistry observed during the MSU-ZERT CO2 injection experiment**. International Journal of Greenhouse Gas Control, v. 7, p. 202–217, 2012.

ZHENG, L. et al. **Impacts of elevated dissolved CO2 on a shallow groundwater system: Reactive transport modeling of a controlled-release field test**. Chemical Geology, v. 447, p. 117–132, 2016.

ZHENG, L. et al. **Potential impacts of CO2 leakage on groundwater quality of overlying aquifer at geological carbon sequestration sites: A review and a proposed assessment procedure**. Greenhouse Gases: Science and TechnologyJohn Wiley and Sons Inc, , 1 out. 2021.

ZHU, C.; SCHWARTZ, F. W. H**ydrogeochemical processes and controls on water quality and water management**. Elements, v. 7, n. 3, p. 169–174, 2011.

ZHU, Q. et al. **Impacts of CO2 leakage into shallow formations on groundwater chemistry**. Fuel Processing Technology, v. 135, p. 162–167, 2015.

ZIELINSKI, J. P. T. et al. **CO_2-shallow groundwater interaction and related hydrogeochemical mechanisms: A review on reduced-scale CO2 release field experiments**. Greenhouse Gases: Science and TechnologyJohn Wiley and Sons Inc, , 2023.

ZIELINSKI, J. P. T. et al. **Hydrogeological assessment and seasonal hydrogeochemical monitoring of the TECNOPUC-Viamão CO_2 controlled-release experimental site, Rio Grande do Sul state, Southern Brazil**. Environmental Earth Sciences, v. 83, n. 16, p. 459, 2 ago. 2024.

ANEXO A

Material complementar do Capítulo 5.

Supplementary Information

Hydrogeological assessment and seasonal hydrogeochemical monitoring of the TECNOPUC-Viamão CO_2 controlled-release experimental site, Rio Grande do Sul state, Southern Brazil

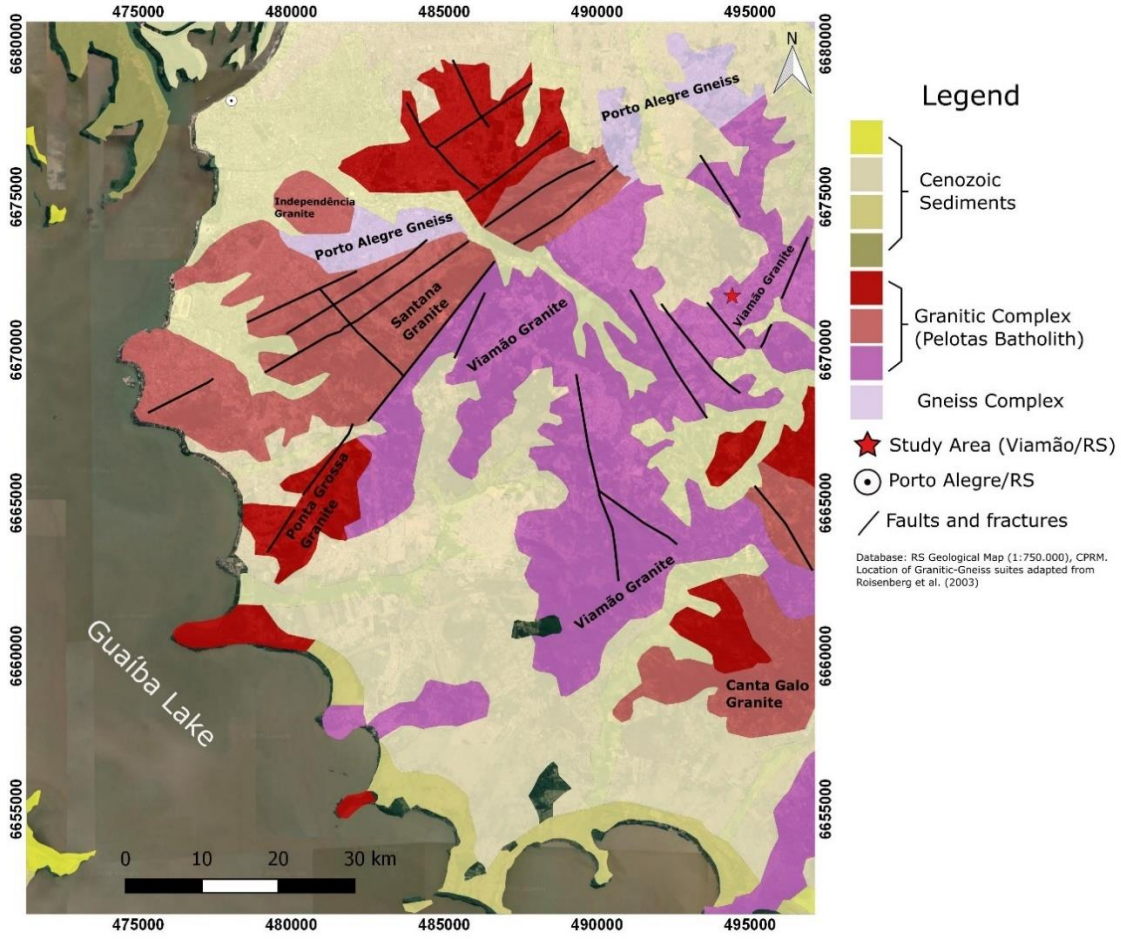

Figure S1. *Simplified geological map of the study area and related granitic-gneissic basement suites.*

***Table S1**. Location of geological boreholes and wells in the study area, along with their respective depths and intended purposes.*

WELL	UTM COORDINATES (m)			DEPTH (m)	PURPOSE
	X	Y	Z		
M1A	494323.53	6671949.49	106.95	1	SAMPLING
M1B	494322.95	6671950.01	106.96	2,5	SAMPLING
M1C	494323.81	6671950.11	106.95	3,5	SAMPLING
M2A	494323.74	6671943.91	107.07	1	SAMPLING
M2B	494323.21	6671943.24	107.10	2,5	SAMPLING
M2C	494323.93	6671943.12	107.07	3,5	SAMPLING
M3A	494309.48	6671945.27	107.80	1	SAMPLING
M3B	494308.75	6671945.85	107.85	2,5	SAMPLING
M3C	494308.54	6671944.86	107.91	3,5	SAMPLING
M4A	494339.99	6671944.18	106.71	1	SAMPLING
M4B	494340.64	6671944.62	106.73	2,5	SAMPLING
M4C	494340.38	6671943.80	106.75	3,5	SAMPLING
DPT06	494327.80	6671963.74	106.75	8,5	WATER LEVEL
DPT08	494328.48	6671928.22	107.34	9,6	WATER LEVEL
DPT09	494305.40	6671962.69	107.89	3,5	WATER LEVEL
DPT11	494334.40	6671953.00	-	2,9	WATER LEVEL
DPT12	494354.50	6671954.80	106.40	2,9	WATER LEVEL
DPT13	494341.50	6671934.47	106.93	2,9	WATER LEVEL

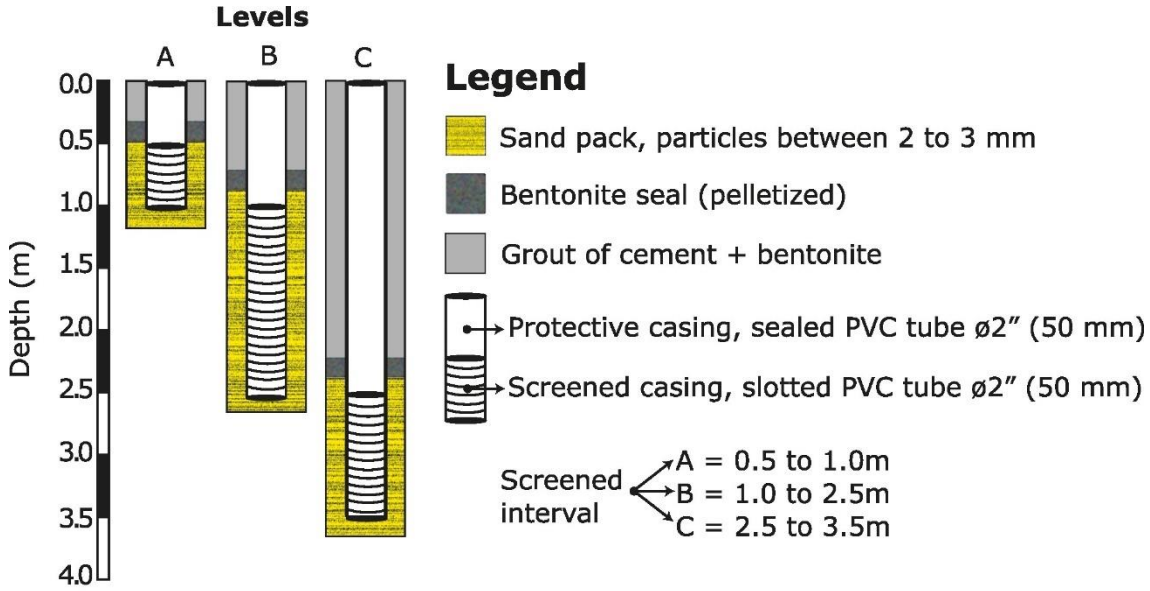

Figure S2. *Constructive features of the multi-level monitoring wells used for groundwater sampling.*

Figure S3. *Spatial distribution of the locations where in-situ permeability tests using the Guelph Permeameter were conducted.*

Calculation steps to consider isotope fractionation and mass balance

To calculate the theoretical enrichment factor (ε), the following equations were employed, considering the temperatures (T) in ºC measured at the time of sample collection:

$$\varepsilon^{13}C_{H_2CO_3-CO_{2(g)}} = -0.000014T^2 + 0.0049T - 1.18 \quad (1)$$

$$\varepsilon^{13}C_{HCO_3-CO_{2(g)}} = 0.00032T^2 - 0.124T + 10.87 \quad (2)$$

Furthermore, considering the presence of both H2CO3 and HCO3- species in the samples, isotopic mass balance calculations were performed to proportionally account for the contribution of each species to the isotopic fractionation of the CO2 source to the DIC response (Clark, 2015). Initially, the relative fraction of H2CO3 and HCO3- concerning the total DIC was calculated:

$$f_{H_2CO_3} = \left[H_2CO_3\ (\tfrac{mg}{L})\right] \Big/ \left[DIC\ (\tfrac{mg}{L})\right] \quad (3)$$

$$f_{HCO_3^-} = \left[HCO_3^-\ (\tfrac{mg}{L})\right] \Big/ \left[DIC\ (\tfrac{mg}{L})\right] \quad (4)$$

Since both species are theoretically in equilibrium with the soil CO2, the fractionation of each species can be represented by the following equations:

$$\delta^{13}C_{H_2CO_3} = \delta^{13}C_{CO_2} + \varepsilon^{13}C_{H_2CO_3-CO_{2(g)}} \quad (5)$$

$$\delta^{13}C_{HCO3^-} = \delta^{13}C_{CO_2} + \varepsilon^{13}C_{HCO_3-CO_{2(g)}} \quad (6)$$

Finally, the isotopic mass balance equations used to determine δ¹³C-DIC are a combination of the above equations to estimate the relative contribution fraction of each component:

$$\delta^{13}C_{-DIC} = (f_{H_2CO_3}\ x\ \delta^{13}C_{H_2CO_3}) + (f_{HCO_3^-}\ x\ \delta^{13}C_{HCO3^-}) \quad (7)$$

The laboratory analysis effectively provided the δ¹³C-DIC values, enabling the subsequent theoretical δ¹³C-DIC calculation. This calculation respected the observed proportionality of H2CO3 and HCO3- to model the response of the carbon source

isotopic ratio ($\delta^{13}C\text{-}CO_2$). This estimation allowed us to infer the magnitude and identify the carbon reservoir contributing to the carbon present in the DIC.

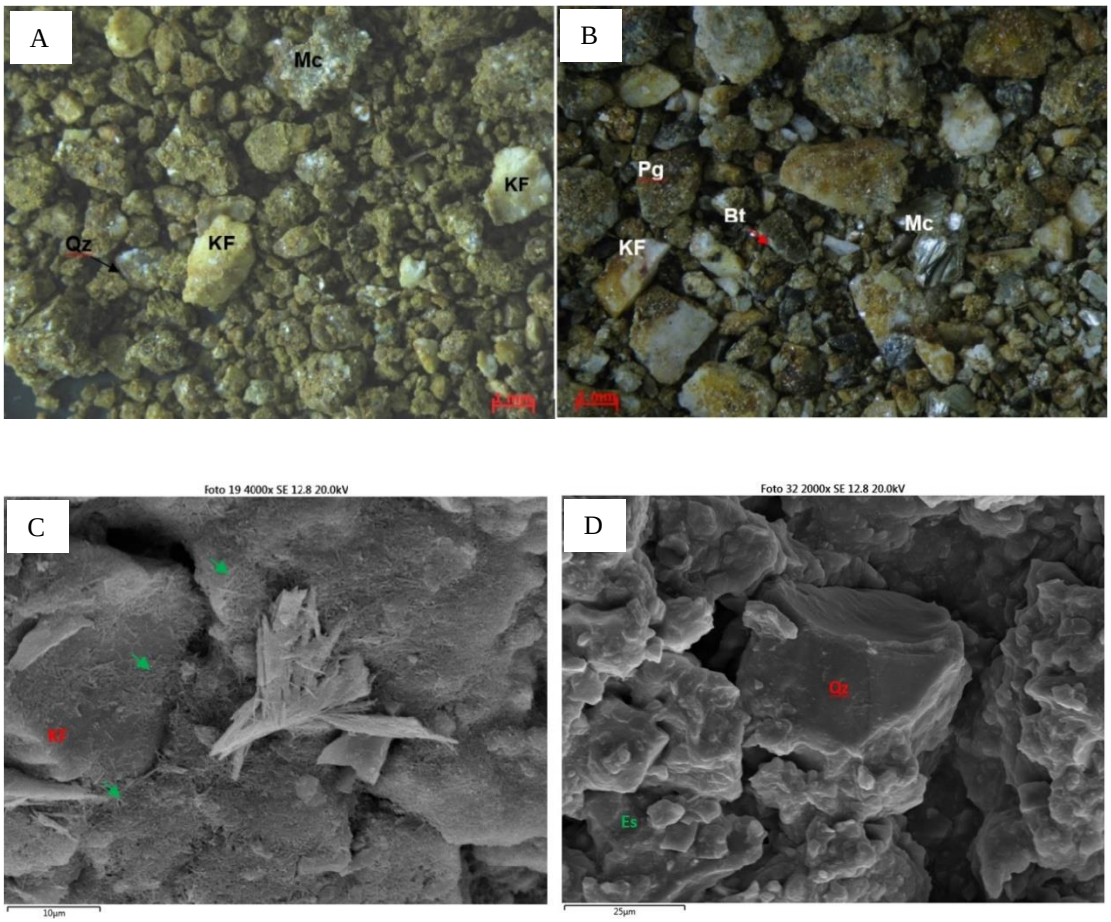

Figure S4*. Representative binocular microscope images of two samples: A) DPT 05 (3.00-4.15m), composed predominantly of Quartz (Qz), Potassium Feldspar (KF), and Muscovite (Mc); and B) DPT 05 (6.00-7.15m), with Potassium Feldspar (KF), Plagioclase (Pg), Biotite (Bt), and Muscovite (Mc). SEM images of samples from boreholes DPT 10 and DPT 06: C) Potassium Feldspar (KF) with iron oxide needles (green arrows), sample DPT 10 (4.5-5.65m); and D) Quartz (Qz) surrounded by Smectite (Es) crystals, sample DPT-06 (0-1.15m).*

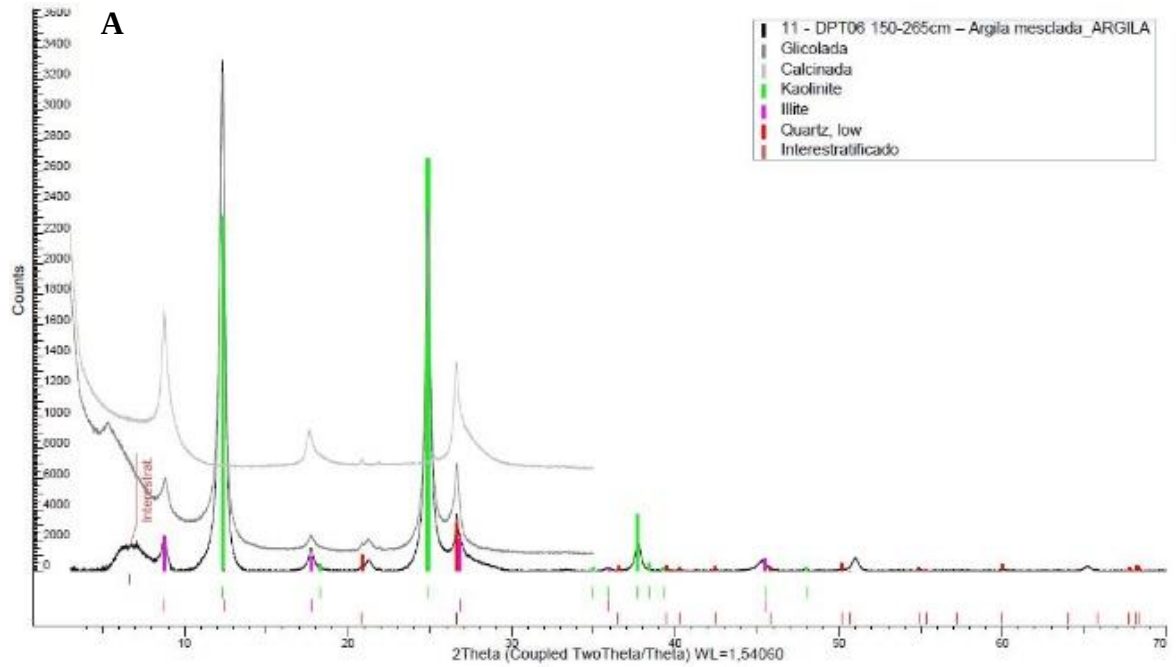
A
11 - DPT06 150-265cm – Argila mesclada_ARGILA
Glicolada
Calcinada
Kaolinite
Illite
Quartz, low
Interestratificado
Counts
2Theta (Coupled TwoTheta/Theta) WL=1,54060

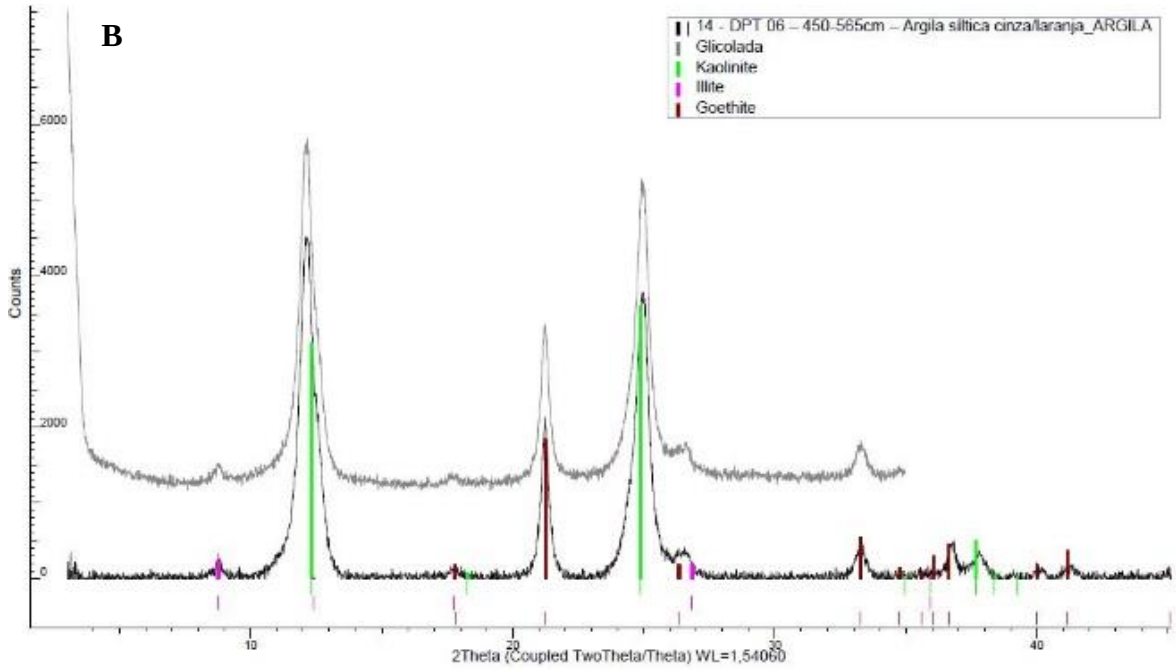
B
14 - DPT 06 – 450-565cm – Argila siltica cinza/laranja_ARGILA
Glicolada
Kaolinite
Illite
Goethite
Counts
2Theta (Coupled TwoTheta/Theta) WL=1,54060

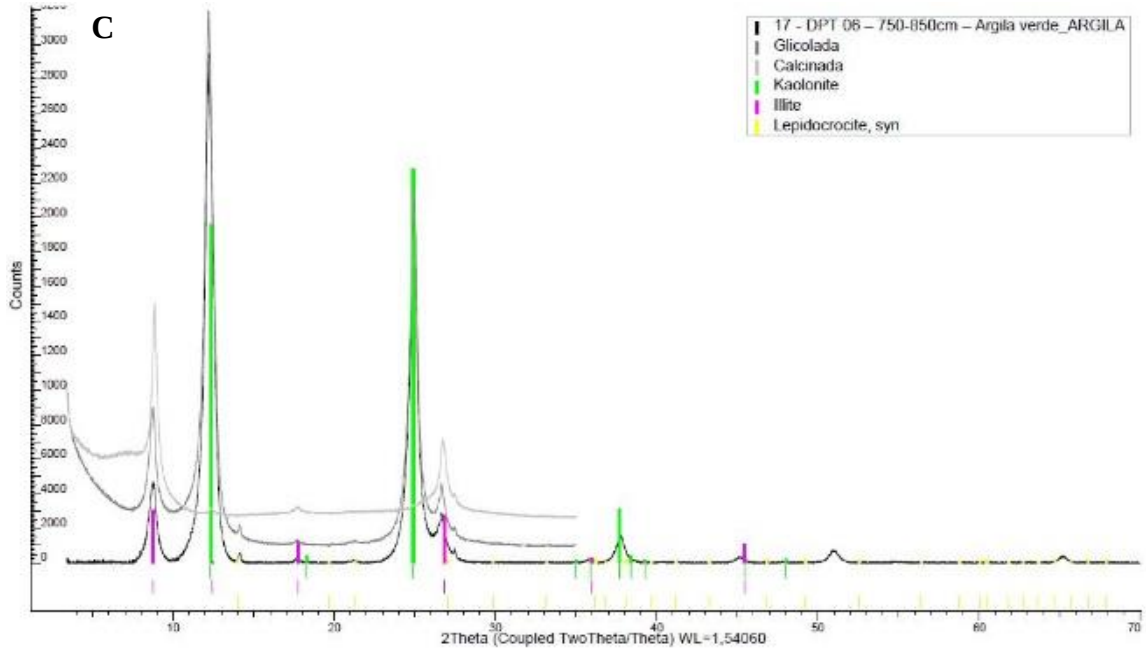

***Figure S5**. XRD diffractograms of some clay fraction samples analyzed: A) sample DPT06 (1.50-2.65m); B) sample DPT06 (4.5-5.65m); and C) sample DPT06 (7.5-8.50m).*

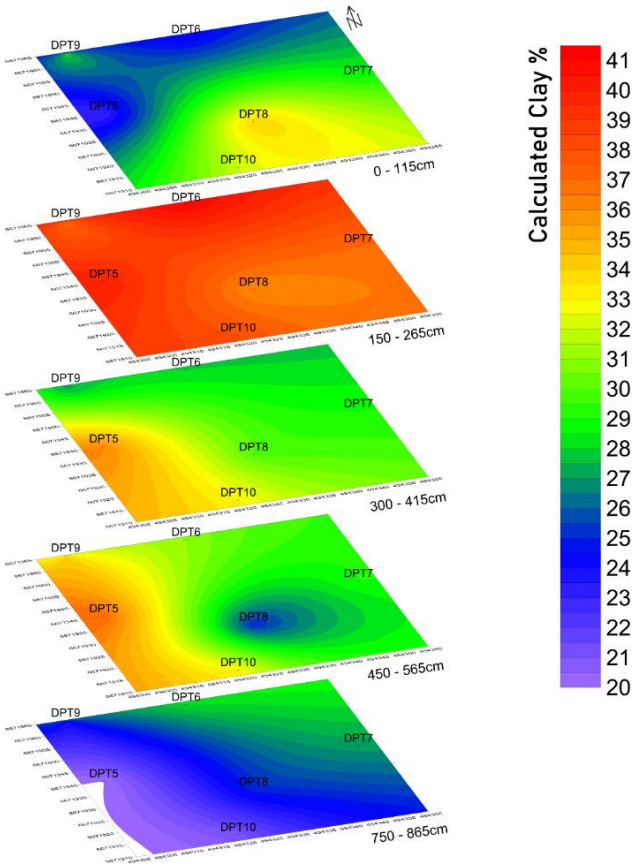

***Figure S6.** Map of clay percentage with depth, developed based on the granulometric analyses conducted on the sampled sections.*

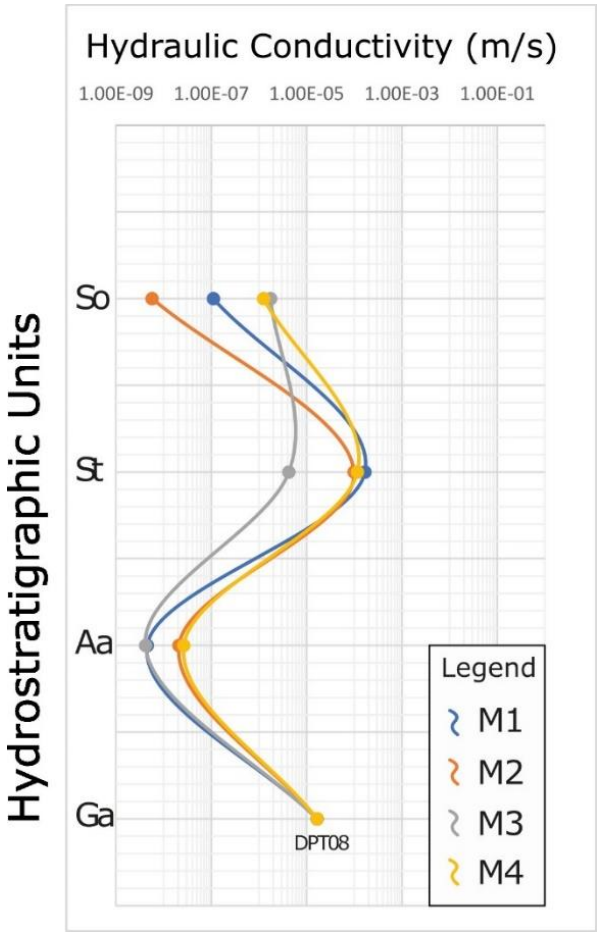

Figure S7. *Average hydraulic conductivity values obtained from various wells, each corresponding to its respective hydrostratigraphic unit representation.*

ANEXO B

Material complementar do Capítulo 6.

Supplementary Information

Hydrogeochemical changes in a silicate-dominated aquifer during a controlled CO_2 release: insights for monitoring unintended CO_2 leakage at CCS sites

***Table S2**. Sample identifications, corresponding wells, hydrostratigraphic units, sampling campaigns, and physicochemical parameters of evaluated samples.*

Sample ID	Well	HU	Phase	Date (dd/mm/yyyy)	Time (24-hour format)	Temp. (°C)	EC (µS/cm)	DO (mg/L)	pH (units)	ORP (mV)
M1A SB3	M1A	St	BG	12/01/2024	11:19	26.1	288.0	2.4	5.8	-164
M1A SI6	M1A	St	Injection	19/01/2024	11:12	26.9	428.0	2.4	5.9	-130
M1A SI7	M1A	St	Injection	22/01/2024	11:00	26.2	319.3	1.7	6.0	-105
M1A SI9	M1A	St	Injection	26/01/2024	11:00	25.8	276.3	1.9	6.0	-119
M1A SI10*	M1A	St	Injection	29/01/2024	10:10	25.5	285.3	1.1	6.0	-102
M1A SI11	M1A	St	Injection	31/01/2024	11:15	25.6	291.0	1.2	6.0	-135
M1A SI12*	M1A	St	Injection	05/02/2024	10:34	26.9	333.0	1.2	5.9	-146
M1A SI13	M1A	St	Injection	07/02/2024	11:01	26.7	355.7	1.3	5.8	-117
M1A SI15	M1A	St	Injection	14/02/2024	10:53	26.9	507.0	1.4	5.7	-49
M1A SI16	M1A	St	Injection	16/02/2024	09:32	25.7	557.3	1.4	5.8	-75
M1A SI17	M1A	St	Injection	20/02/2024	11:07	26.5	613.0	1.0	5.5	-72
M1A SI18	M1A	St	Injection	23/02/2024	11:40	26.9	570.3	1.1	5.6	-67
M1A SI19	M1A	St	Injection	28/02/2024	10:46	26.7	481.0	1.1	5.9	-77
M1A SI20	M1A	St	Injection	01/03/2024	11:10	26.7	455.3	1.1	5.7	-55
M1A SP21	M1A	St	PI	05/03/2024	11:12	26.0	443.3	1.3	5.7	-35
M1A SP22	M1A	St	PI	08/03/2024	10:20	25.3	430.7	1.4	5.8	12
M1A SP23	M1A	St	PI	12/03/2024	11:49	26.3	431.3	1.9	5.9	10
M1A SP24	M1A	St	PI	15/03/2024	11:03	26.1	392.3	1.3	5.8	7
M1A SP25	M1A	St	PI	17/07/2024	11:40	16.0	270.7	1.3	6.2	79
M1B SB1	M1B	St	BG	08/01/2024	13:10	26.1	319.0	1.6	6.4	66
M1B SB2	M1B	St	BG	10/01/2024	10:40	25.8	314.0	2.1	6.3	-63
M1B SB3	M1B	St	BG	12/01/2024	10:33	24.6	301.7	2.2	5.8	-79
M1B SI4	M1B	St	Injection	15/01/2024	11:58	25.4	294.3	2.0	5.8	-99
M1B SI5	M1B	St	Injection	18/01/2024	15:23	25.7	296.0	1.9	5.8	-97
M1B SI6	M1B	St	Injection	19/01/2024	10:24	26.0	281.0	2.0	6.1	-112
M1B SI7	M1B	St	Injection	22/01/2024	09:52	25.2	276.3	1.7	6.1	-124
M1B SI8	M1B	St	Injection	24/01/2024	10:02	25.1	273.0	2.0	6.1	-113
M1B SI9	M1B	St	Injection	26/01/2024	10:00	24.7	266.3	2.1	6.1	-93
M1B SI10	M1B	St	Injection	29/01/2024	09:42	24.8	264.3	1.2	6.1	-77
M1B SI11	M1B	St	Injection	31/01/2024	10:20	24.8	265.0	1.2	6.0	-78

M1B SI12	M1B	St	Injection	05/02/2024	10:03	25.3	300.3	1.2	5.9	-60
M1B SI13	M1B	St	Injection	07/02/2024	10:10	25.6	331.0	1.1	5.9	-55
M1B SI14	M1B	St	Injection	09/02/2024	10:05	25.7	368.0	1.5	5.9	-37
M1B SI15	M1B	St	Injection	14/02/2024	11:40	25.3	435.0	1.3	5.8	-23
M1B SI16	M1B	St	Injection	16/02/2024	10:17	24.9	483.3	1.9	5.9	-36
M1B SI17	M1B	St	Injection	20/02/2024	10:15	25.7	512.0	1.3	5.6	-17
M1B SI18	M1B	St	Injection	23/02/2024	10:46	26.1	515.3	1.5	5.6	4
M1B SI19	M1B	St	Injection	28/02/2024	10:05	25.9	490.7	1.3	5.8	-8
M1B SI20	M1B	St	Injection	01/03/2024	10:25	26.0	470.0	1.5	5.6	1
M1B SP21	M1B	St	PI	05/03/2024	10:20	25.2	455.3	1.4	5.7	67
M1B SP22	M1B	St	PI	08/03/2024	09:36	24.7	426.3	1.9	5.7	62
M1B SP23	M1B	St	PI	12/03/2024	11:10	25.7	439.3	1.5	5.8	66
M1B SP24	M1B	St	PI	15/03/2024	10:06	25.2	386.7	1.3	5.7	65
M1B SP25	M1B	St	PI	17/07/2024	10:55	18.1	272.0	1.4	6.2	101
M2A SI13	M2A	St	Injection	07/02/2024	14:13	26.9	307.3	1.1	5.8	-22
M2A SI14	M2A	St	Injection	09/02/2024	11:10	27.5	315.0	1.4	6.0	-31
M2B SB1	M2B	St	BG	08/01/2024	14:40	25.8	271.7	2.3	6.3	NM
M2B SB2	M2B	St	BG	10/01/2024	12:00	26.3	270.0	2.1	6.3	-89
M2B SB3	M2B	St	BG	12/01/2024	13:43	24.9	257.3	2.1	5.6	-104
M2B SI4	M2B	St	Injection	15/01/2024	14:09	25.5	253.0	2.2	5.6	-109
M2B SI5	M2B	St	Injection	18/01/2024	16:15	25.6	254.0	1.8	5.8	-121
M2B SI6	M2B	St	Injection	19/01/2024	13:45	25.8	245.0	1.9	6.0	-123
M2B SI7	M2B	St	Injection	22/01/2024	14:17	25.3	239.3	1.9	5.9	-115
M2B SI8	M2B	St	Injection	24/01/2024	11:07	24.7	241.7	2.1	6.0	-123
M2B SI9	M2B	St	Injection	26/01/2024	13:53	25.1	236.7	1.9	6.0	-102
M2B SI10	M2B	St	Injection	29/01/2024	11:08	24.9	231.7	1.2	6.0	-104
M2B SI11	M2B	St	Injection	31/01/2024	14:02	25.1	225.0	1.2	5.9	-83
M2B SI12	M2B	St	Injection	05/02/2024	11:30	25.6	220.0	1.4	6.0	-112
M2B SI13	M2B	St	Injection	07/02/2024	15:00	25.8	223.0	1.6	5.9	-80
M2B SI14	M2B	St	Injection	09/02/2024	13:23	26.6	223.3	1.4	6.0	-67
M2B SI15	M2B	St	Injection	14/02/2024	13:53	25.7	256.3	1.9	5.9	-60
M2B SI16	M2B	St	Injection	16/02/2024	11:25	24.5	269.3	1.5	6.0	-63
M2B SI17	M2B	St	Injection	20/02/2024	13:05	25.8	286.7	1.2	5.7	-50
M2B SI18	M2B	St	Injection	23/02/2024	14:00	26.3	287.3	1.5	5.8	-41
M2B SI19	M2B	St	Injection	28/02/2024	11:40	26.0	278.7	1.3	6.0	-55
M2B SI20	M2B	St	Injection	01/03/2024	13:27	25.9	266.0	1.3	5.8	-26
M2B SP21	M2B	St	PI	05/03/2024	13:42	25.3	274.7	1.4	5.8	-22
M2B SP22	M2B	St	PI	08/03/2024	11:16	24.8	272.0	1.2	5.9	62
M2B SP23	M2B	St	PI	12/03/2024	14:10	26.1	282.3	1.3	5.9	13
M2B SP24	M2B	St	PI	15/03/2024	11:55	25.5	259.7	1.4	5.9	17
M2B SP25	M2B	St	PI	17/07/2024	13:33	18.7	209.3	1.7	6.1	71
M2C SI13	M2C	Aa	Injection	07/02/2024	11:28 [NS]	30.0	629.7	3.6	5.8	161
M3B SB1	M3B	Aa	BG	08/01/2024	17:12	25.0	203.7	1.7	6.0	127

M3B SB2	M3B	Aa	BG	10/01/2024	09:43	24.5	199.3	2.8	5.9	151
M3B SB3	M3B	Aa	BG	12/01/2024	09:35	24.1	190.3	4.0	5.4	202
M3B SI4	M3B	Aa	Injection	15/01/2024	11:01	24.6	183.7	4.2	5.4	207
M3B SI5	M3B	Aa	Injection	18/01/2024	14:32	25.6	233.0	6.0	5.7	195
M3B SI6	M3B	Aa	Injection	19/01/2024	09:35	25.3	229.7	5.0	6.0	203
M3B SI7	M3B	Aa	Injection	22/01/2024	09:05	24.3	238.7	4.4	6.0	215
M3B SI8	M3B	Aa	Injection	24/01/2024	09:13	24.5	226.3	3.8	5.9	245
M3B SI9	M3B	Aa	Injection	26/01/2024	09:10	24.3	218.3	3.5	5.9	228
M3B SI10	M3B	Aa	Injection	29/01/2024	08:53	23.9	141.6	2.2	5.8	242
M3B SI11	M3B	Aa	Injection	31/01/2024	09:30	24.3	195.3	1.9	5.8	196
M3B SI12	M3B	Aa	Injection	05/02/2024	09:12	24.4	184.7	1.8	5.6	199
M3B SI13	M3B	Aa	Injection	07/02/2024	09:03	24.5	181.3	1.6	5.6	199
M3B SI14	M3B	Aa	Injection	09/02/2024	09:13	24.7	181.0	1.9	5.8	166
M3B SI15	M3B	Aa	Injection	14/02/2024	09:57	24.1	187.7	2.3	5.7	187
M3B SI16	M3B	Aa	Injection	16/02/2024	13:48	23.7	196.3	1.8	5.7	209
M3B SI17	M3B	Aa	Injection	20/02/2024	09:13	24.7	199.3	2.0	5.5	212
M3B SI18	M3B	Aa	Injection	23/02/2024	09:57	25.0	193.7	2.0	5.5	217
M3B SI19	M3B	Aa	Injection	28/02/2024	09:18	25.1	185.3	1.6	5.7	202
M3B SI20	M3B	Aa	Injection	01/03/2024	09:36	25.1	176.7	1.9	5.5	203
M3B SP21	M3B	Aa	PI	05/03/2024	09:30	24.6	177.3	1.9	5.6	195
M3B SP22	M3B	Aa	PI	08/03/2024	13:39	23.9	178.0	1.6	5.6	128
M3B SP23	M3B	Aa	PI	12/03/2024	10:10	24.7	185.7	2.7	5.7	184
M3B SP24	M3B	Aa	PI	15/03/2024	09:15	24.6	170.7	2.5	5.6	190
M3B SP25	M3B	Aa	PI	17/07/2024	10:05	18.7	197.0	2.4	5.8	169
M4B SB2	M4B	St	BG	10/01/2024	14:55	24.3	493.3	2.5	6.5	-187
M4B SB3	M4B	St	BG	12/01/2024	14:47	23.9	492.3	2.2	6.1	-190
M4B SI4	M4B	St	Injection	15/01/2024	15:03	24.7	443.7	1.8	6.0	-181
M4B SI5	M4B	St	Injection	18/01/2024	17:03	24.7	451.3	1.8	6.0	-182
M4B SI6	M4B	St	Injection	19/01/2024	14:30	25.3	437.0	1.7	6.3	-191
M4B SI7	M4B	St	Injection	22/01/2024	15:10	24.6	416.7	1.6	6.2	-186
M4B SI8	M4B	St	Injection	24/01/2024	13:58	22.7	407.7	1.8	6.3	-168
M4B SI9	M4B	St	Injection	26/01/2024	14:03	23.8	393.7	1.6	6.2	-160
M4B SI10	M4B	St	Injection	29/01/2024	13:30	23.2	390.3	1.0	6.2	-144
M4B SI11	M4B	St	Injection	31/01/2024	14:53	23.8	394.3	1.0	6.2	-166
M4B SI12	M4B	St	Injection	05/02/2024	14:10	24.3	402.3	1.0	6.2	-154
M4B SI14	M4B	St	Injection	09/02/2024	14:18	25.1	417.3	1.2	6.4	-147
M4B SI15	M4B	St	Injection	14/02/2024	14:59	24.1	434.0	1.7	6.2	-112
M4B SI17	M4B	St	Injection	20/02/2024	13:51	24.3	461.3	1.0	6.1	-91
M4B SI18	M4B	St	Injection	23/02/2024	14:48	25.2	475.7	1.2	6.1	-83
M4B SI19	M4B	St	Injection	28/02/2024	13:49	24.7	460.0	1.3	6.3	-83
M4B SI20	M4B	St	Injection	01/03/2024	14:17	24.7	455.0	1.2	6.2	-81
M4B SP21	M4B	St	PI	05/03/2024	14:32	24.3	478.3	1.2	6.2	-68
M4B SP22	M4B	St	PI	08/03/2024	12:16	23.4	506.7	1.1	6.3	-6

M4B SP23	M4B	St	PI	12/03/2024	15:05	25.0	467.7	1.1	6.3	-3
M4B SP24	M4B	St	PI	15/03/2024	12:51	24.3	418.0	1.2	6.2	5
M4B SP25	M4B	St	PI	17/07/2024	14:33	18.1	375.0	2.1	6.3	81

Notes:

Sample ID = Well Number + Sampling Campaign (SB = Sampling Background / SI = Sampling Injection / SP = Sampling Post-Injection);

HU = Hydrostratigraphic Unit (as in Zielinski et al., 2024);

BG = Background; PI = Post-Injection;

NM = Variable Not Measured;

**Indicates samples not collected, but with physicochemical parameters monitored in the field.*

***Table S3**. Chemical analysis of major cations, minor metals, and trace elements assessed in the study.*

Sample ID	Total Alk. (mg/L $CaCO_3$)	pCO2* (atm)	CBE* (%)	Ca (mg/l)	Mg (mg/l)	K (mg/l)	Na (mg/l)	Fe (mg/l)	Si (mg/l)	Ba (mg/l)	Sr (mg/l)	Mn (mg/l)	Al (mg/l)
M1A SB3	135.2	0.26	-3.8	37.78	6.33	18.48	1.60	1.74	5.97	0.11	0.18	<0.05	<0.03
M1A SI6	187.5	0.29	-2.5	59.98	9.76	12.71	1.96	0.65	9.43	0.14	0.31	<0.05	<0.03
M1A SI7	146.5	0.18	-4.8	45.14	6.90	11.60	1.42	0.32	10.13	0.05	0.22	<0.05	<0.03
M1A SI9	129.2	0.16	-1.2	44.10	6.24	10.62	1.29	0.33	9.93	0.05	0.20	<0.05	<0.03
M1A SI11	145.9	0.18	2.6	50.57	6.88	13.73	1.43	0.59	9.90	0.05	0.22	<0.05	<0.03
M1A SI13	145.5	0.28	10.8	57.90	8.95	13.25	2.12	1.33	9.31	0.12	0.27	<0.05	<0.03
M1A SI15	249.5	0.60	1.6	83.73	11.90	15.09	2.55	1.17	11.02	0.17	0.36	<0.05	<0.03
M1A SI16	262.5	0.49	2.0	86.55	12.31	15.35	2.55	1.73	10.00	0.19	0.37	<0.05	<0.03
M1A SI17	289.2	1.10	-2.2	87.26	12.69	15.19	2.65	1.78	9.60	0.39	0.40	0.14	<0.03
M1A SI18	259.6	0.79	0.7	80.56	12.58	16.46	2.65	2.93	8.76	0.24	0.38	0.10	<0.03
M1A SI19	209.2	0.32	3.2	68.20	10.87	16.21	2.70	3.27	7.77	0.20	0.33	<0.05	<0.03
M1A SI20	221.7	0.54	1.7	69.24	11.19	16.23	2.73	3.38	7.59	0.19	0.33	<0.05	<0.03
M1A SP21	215.8	0.52	-2.9	65.52	8.05	16.04	2.03	2.09	5.50	0.20	0.32	<0.05	<0.03
M1A SP22	211.7	0.40	-0.9	62.75	10.17	15.75	2.65	2.81	7.64	0.19	0.31	<0.05	<0.03
M1A SP23	195.4	0.30	-2.8	60.78	9.46	15.08	2.57	1.33	6.98	0.19	0.30	<0.05	<0.03
M1A SP24	193.4	0.38	-0.4	60.31	9.37	14.95	2.49	1.79	6.78	0.19	0.29	<0.05	<0.03
M1A SP25	136.6	0.09	-0.5	44.30	7.10	7.40	1.30	0.82	5.67	0.09	NM	<0.05	<0.03
M1B SB1	100.6	0.05	7.5	37.41	6.46	13.09	1.69	0.28	6.35	0.05	0.05	<0.05	<0.03
M1B SB2	111.4	0.07	3.4	37.13	6.43	13.62	1.66	0.35	6.32	0.11	0.19	<0.05	<0.03
M1B SB3	135.2	0.26	-3.9	38.11	6.65	13.48	1.78	0.38	6.27	0.12	0.21	<0.05	<0.03
M1B SI4	132.6	0.26	-3.8	38.03	6.45	13.57	1.71	0.37	6.31	0.12	0.21	<0.05	<0.03
M1B SI5	129.7	0.25	-5.9	36.75	6.15	13.41	1.34	0.93	6.64	0.05	0.15	0.12	<0.03
M1B SI6	120.9	0.12	-2.5	37.15	6.04	13.64	1.35	0.36	6.54	0.12	0.21	<0.05	<0.03
M1B SI7	122.1	0.12	-6.5	35.86	5.71	11.74	1.30	0.37	6.59	0.12	0.20	<0.05	<0.03
M1B SI8	123.3	0.12	-13.5	27.03	5.96	17.59	1.24	0.38	6.65	0.11	0.20	<0.05	<0.03
M1B SI9	119.0	0.11	-5.9	34.88	5.81	12.44	1.25	0.39	6.53	0.11	0.20	<0.05	<0.03

M1B SI10	119.0	0.12	-5.1	35.67	5.80	11.71	1.29	0.39	6.47	0.11	0.20	<0.05	<0.03
M1B SI11	121.6	0.15	-5.5	35.62	5.95	12.03	1.29	0.41	6.45	0.11	0.19	<0.05	<0.03
M1B SI12	145.5	0.22	-12.0	33.55	7.27	10.67	1.90	0.56	7.71	0.13	0.23	<0.05	<0.03
M1B SI13	163.2	0.25	1.0	52.10	8.01	15.84	1.95	0.63	7.56	0.15	0.26	<0.05	<0.03
M1B SI14	187.2	0.29	1.4	57.45	8.90	17.27	2.09	0.70	7.98	0.17	0.29	<0.05	<0.03
M1B SI15	207.2	0.39	0.4	65.90	9.69	17.06	2.35	0.92	8.72	0.20	0.33	<0.05	<0.03
M1B SI16	227.2	0.34	-5.9	61.98	9.98	15.58	2.18	0.88	8.19	0.18	0.30	<0.05	<0.03
M1B SI17	234.4	0.71	0.7	74.17	10.99	17.87	2.52	1.17	9.37	0.23	0.38	0.11	<0.03
M1B SI18	229.9	0.70	4.0	75.10	11.20	17.67	2.56	1.25	9.60	0.23	0.38	0.11	<0.03
M1B SI19	216.7	0.41	2.7	72.99	10.89	17.84	2.59	1.28	9.39	0.22	0.38	0.11	<0.03
M1B SI20	228.7	0.69	0.9	72.41	10.70	17.29	2.59	1.27	9.32	0.21	0.37	0.11	<0.03
M1B SP21	226.2	0.54	-0.4	69.50	10.22	17.51	2.63	1.24	9.32	0.21	0.35	0.11	<0.03
M1B SP22	206.6	0.49	0.1	64.10	10.00	16.57	2.46	1.14	9.05	0.19	0.33	0.10	<0.03
M1B SP23	205.8	0.39	-1.4	61.11	10.09	16.19	2.44	0.99	8.34	0.20	0.33	0.10	<0.03
M1B SP24	193.0	0.46	7.6	71.38	9.79	18.65	2.35	1.04	8.21	0.19	0.31	<0.05	<0.03
M1B SP25	124.0	0.09	4.3	45.40	6.40	10.00	1.30	0.31	6.00	0.10	NM	0.07	<0.03
M2A SI13	144.4	0.28	1.5	47.75	7.59	8.24	1.85	2.27	8.36	0.10	0.24	<0.05	<0.03
M2A SI14	142.4	0.18	4.2	47.88	7.68	9.05	1.87	2.48	8.01	0.10	0.24	<0.05	<0.03
M2B SB1	79.9	0.05	11.5	31.81	6.33	9.20	1.53	0.05	7.45	0.05	0.05	<0.05	<0.03
M2B SB2	111.4	0.07	0.6	33.07	6.31	12.76	1.55	0.73	7.50	0.11	0.17	<0.05	<0.03
M2B SB3	116.9	0.36	-4.0	32.25	6.42	9.78	1.60	0.79	7.44	0.05	0.05	<0.05	<0.03
M2B SI4	113.7	0.35	-3.4	31.77	6.13	10.75	1.47	0.65	7.81	0.11	0.17	<0.05	<0.03
M2B SI5	109.3	0.21	-5.0	32.11	5.87	7.72	1.26	0.46	6.74	0.11	0.17	<0.05	<0.03
M2B SI6	103.0	0.13	-2.8	31.72	5.85	8.22	1.24	0.48	6.86	0.11	0.17	<0.05	<0.03
M2B SI7	104.0	0.16	-13.8	23.69	5.78	8.45	1.24	0.47	6.54	0.11	0.17	<0.05	<0.03
M2B SI8	108.4	0.13	-6.6	31.22	5.88	8.24	1.23	0.49	6.60	0.11	0.17	<0.05	<0.03
M2B SI9	110.6	0.14	0.5	33.77	5.88	8.45	1.25	0.54	7.08	0.05	0.17	<0.05	<0.03
M2B SI10	106.3	0.13	-4.8	31.03	5.68	7.71	1.24	0.56	7.23	0.10	0.16	<0.05	<0.03
M2B SI11	104.7	0.16	5.3	40.24	5.58	7.75	1.23	0.57	7.49	0.10	0.16	<0.05	<0.03
M2B SI12	102.9	0.13	20.2	56.93	5.83	8.17	1.76	0.68	8.46	0.10	0.16	<0.05	<0.03
M2B SI13	103.2	0.16	4.9	37.78	5.92	8.33	1.72	0.73	8.05	0.11	0.16	<0.05	<0.03
M2B SI14	108.6	0.14	-0.4	34.62	6.01	8.70	1.77	0.77	8.00	0.11	0.15	<0.05	<0.03
M2B SI15	113.3	0.18	0.5	35.70	6.55	9.30	1.98	1.34	7.87	0.12	0.17	<0.05	<0.03
M2B SI16	104.2	0.13	3.5	35.35	6.64	9.33	2.01	0.88	7.99	0.12	0.17	<0.05	<0.03
M2B SI17	122.8	0.30	1.3	38.65	7.10	13.69	2.06	0.90	8.10	0.13	NM	0.11	<0.03
M2B SI18	117.4	0.23	5.3	39.40	7.25	15.90	2.11	0.84	8.03	0.13	0.19	<0.05	<0.03
M2B SI19	114.5	0.14	3.6	37.51	7.07	12.97	2.19	0.88	7.78	0.13	0.18	<0.05	<0.03
M2B SI20	119.3	0.23	1.4	38.63	7.01	9.86	2.22	0.89	7.75	0.13	0.18	<0.05	<0.03
M2B SP21	123.6	0.24	1.1	38.03	7.21	12.43	2.35	0.94	7.72	0.13	0.18	<0.05	<0.03
M2B SP22	122.5	0.19	2.3	38.66	7.35	12.14	2.40	0.92	7.93	0.13	0.18	<0.05	<0.03
M2B SP23	121.5	0.19	0.2	37.54	7.05	9.67	2.29	0.89	7.36	0.13	0.24	<0.05	<0.03
M2B SP24	122.0	0.19	-1.5	36.33	7.06	9.72	2.25	0.94	7.43	0.13	0.18	<0.05	<0.03
M2B SP25	101.2	0.09	1.2	33.50	5.90	6.00	1.20	0.25	7.09	0.08	NM	<0.05	<0.03

M3B SB1	28.0	0.03	9.9	11.67	3.80	23.88	1.37	0.80	2.27	0.12	0.16	<0.05	<0.03
M3B SB2	44.7	0.07	-3.2	11.62	3.76	24.46	1.38	0.05	2.26	0.05	0.05	<0.05	<0.03
M3B SB3	47.1	0.23	-5.6	11.06	3.66	24.53	1.38	0.05	2.23	0.05	0.05	<0.05	<0.03
M3B SI4	44.9	0.22	-4.9	11.01	3.59	25.16	1.44	0.05	2.22	0.05	0.05	<0.05	<0.03
M3B SI5	93.4	0.23	-8.7	22.77	5.25	21.81	1.37	0.05	5.63	0.12	0.13	<0.05	<0.03
M3B SI6	96.5	0.12	-6.8	24.60	5.37	21.43	1.34	0.05	5.92	0.12	0.15	<0.05	<0.03
M3B SI7	94.2	0.11	-10.2	24.72	4.65	18.18	1.11	0.05	4.53	0.11	0.13	<0.05	<0.03
M3B SI8	90.4	0.14	-4.3	24.50	5.12	20.83	1.31	0.16	4.31	0.11	0.13	<0.05	<0.03
M3B SI9	83.8	0.13	-7.2	20.85	4.96	20.21	1.30	0.05	3.88	0.11	0.12	<0.05	<0.03
M3B SI10	68.4	0.13	2.6	21.63	4.37	26.98	1.38	0.05	3.13	0.11	0.10	<0.05	<0.03
M3B SI11	62.6	0.12	-4.3	15.22	4.22	26.48	1.40	0.05	2.83	0.10	0.05	<0.05	<0.03
M3B SI12	53.9	0.17	-3.1	13.87	4.08	23.98	1.84	0.05	2.94	0.05	0.05	<0.05	<0.03
M3B SI13	50.3	0.16	-2.8	12.85	3.94	24.42	1.80	0.05	2.72	0.05	0.05	<0.05	<0.03
M3B SI14	49.9	0.10	-5.4	12.64	3.87	24.94	1.76	0.05	2.51	0.05	0.05	<0.05	<0.03
M3B SI15	46.7	0.11	-2.9	12.13	3.77	23.38	1.80	0.05	2.95	0.05	0.05	<0.05	<0.03
M3B SI16	47.5	0.12	-4.4	11.31	3.65	23.52	1.75	0.05	2.49	0.05	0.05	<0.05	<0.03
M3B SI17	45.0	0.18	-0.6	12.49	3.75	24.93	1.79	0.05	2.49	0.05	0.05	<0.05	<0.03
M3B SI18	43.1	0.17	-4.9	11.46	3.79	23.59	1.76	0.05	2.47	0.05	0.05	<0.05	<0.03
M3B SI19	39.6	0.10	-0.9	11.01	3.62	23.78	1.81	0.05	2.42	0.05	0.05	<0.05	<0.03
M3B SI20	40.4	0.16	-3.5	10.66	3.53	24.17	1.80	0.05	2.43	0.05	0.05	<0.05	<0.03
M3B SP21	41.0	0.13	-5.6	10.24	3.47	24.09	1.82	0.05	2.39	0.05	0.05	<0.05	<0.03
M3B SP22	43.2	0.13	-4.5	10.94	3.60	23.62	1.82	0.05	2.59	0.05	0.05	<0.05	<0.03
M3B SP23	44.1	0.11	-2.4	11.42	3.72	24.07	1.84	0.05	2.54	0.05	0.05	<0.05	<0.03
M3B SP24	43.9	0.14	-5.8	11.05	3.56	24.00	1.77	0.05	2.32	0.05	0.05	<0.05	<0.03
M3B SP25	61.9	0.11	-4.0	16.90	5.60	16.10	1.70	0.06	2.14	0.09	NM	<0.002	<0.03
M4B SB2	218.8	0.08	-2.6	57.60	14.03	8.77	6.00	1.64	7.62	0.25	0.29	0.31	<0.03
M4B SB3	249.5	0.23	-5.1	62.79	14.82	8.80	6.16	1.57	9.21	0.05	0.25	0.80	<0.03
M4B SI4	223.6	0.27	-3.9	57.36	13.84	8.59	5.93	1.61	7.49	0.20	0.23	0.71	<0.03
M4B SI5	227.9	0.27	-5.4	55.73	14.26	8.55	6.00	1.65	6.65	0.27	0.28	0.29	<0.03
M4B SI6	218.8	0.13	-1.3	60.19	13.96	8.29	6.10	1.72	6.70	0.27	0.30	0.29	<0.03
M4B SI7	216.5	0.16	-7.5	50.17	13.10	8.37	5.71	1.59	6.44	0.27	0.28	0.25	<0.03
M4B SI8	216.5	0.12	0.1	62.88	13.47	8.27	5.68	1.77	6.85	0.26	0.28	0.05	<0.03
M4B SI9	205.9	0.15	-5.5	50.43	12.82	8.30	5.48	1.88	6.93	0.21	0.51	0.28	<0.03
M4B SI10	205.8	0.15	-0.7	66.64	12.94	7.80	5.45	1.99	6.89	0.23	0.27	0.29	<0.03
M4B SI11	206.6	0.15	-3.3	54.91	12.85	7.24	5.46	1.90	7.05	0.23	0.26	0.30	<0.03
M4B SI12	212.5	0.16	-0.9	60.64	13.35	7.47	5.89	2.27	8.27	0.24	0.28	0.32	<0.03
M4B SI14	211.1	0.10	0.4	62.11	13.37	7.89	5.88	2.24	8.21	0.32	0.28	0.45	<0.03
M4B SI15	216.5	0.16	-6.8	54.24	12.20	7.20	5.40	1.78	7.28	0.39	0.26	0.47	<0.03
M4B SI17	221.8	0.21	-1.3	62.72	13.62	9.25	6.23	2.35	8.64	0.25	0.30	0.34	<0.03
M4B SI18	222.0	0.21	0.3	64.45	13.84	9.68	6.27	2.30	8.67	0.25	0.31	0.34	<0.03
M4B SI19	221.5	0.13	-0.4	63.08	14.11	9.22	6.26	2.05	8.30	0.26	0.30	0.29	<0.03
M4B SI20	228.5	0.17	-0.4	64.92	14.32	8.55	6.28	1.98	8.28	0.26	0.31	0.29	<0.03
M4B SP21	242.0	0.18	-0.5	69.35	14.71	8.81	6.38	1.95	9.41	0.27	0.32	0.30	<0.03

M4B SP22	262.8	0.15	-1.7	73.97	15.19	8.23	6.42	2.08	11.14	0.27	0.34	0.34	<0.03
M4B SP23	228.4	0.14	-2.4	62.59	13.65	8.18	6.24	2.00	7.85	0.26	0.30	0.29	<0.03
M4B SP24	228.5	0.17	-1.5	62.98	14.39	8.25	6.30	2.06	7.82	0.27	0.31	0.28	0.16
M4B SP25	202.5	0.11	2.2	61.20	13.6	6.0	5.1	1.08	7.99	0.18	NM	0.21	<0.03

Notes:

NM = Variable Not Measured;

CBE = Charge Balance Error;

**Indicates parameters and index calculated by PHREEQC;*

Table S4. *Chemical analysis of anions assessed in the study.*

Sample ID	HCO_3^- (mg/l)	SO_4^{2-} (mg/l)	Cl^- (mg/l)	NO_3^- (mg/l)	PO_4^{3-} (mg/l)
M1A SB3	164.9	18.04	2.56	1.43	0.00
M1A SI6	228.8	25.19	5.36	0.46	1.02
M1A SI7	178.7	22.61	4.12	0.00	1.69
M1A SI9	157.6	22.50	2.96	0.00	1.69
M1A SI11	178.0	17.42	2.76	0.00	1.94
M1A SI13	177.5	16.02	3.16	0.05	0.44
M1A SI15	304.4	16.40	3.37	1.60	0.36
M1A SI16	320.3	15.80	3.64	0.12	0.00
M1A SI17	352.8	15.98	4.58	0.05	0.00
M1A SI18	316.7	14.91	4.77	0.05	0.00
M1A SI19	255.3	14.96	6.20	0.00	0.00
M1A SI20	270.5	14.45	5.36	0.05	0.00
M1A SP21	263.2	15.07	5.43	0.00	0.00
M1A SP22	258.3	14.26	5.52	0.00	0.00
M1A SP23	238.4	16.87	4.84	3.10	0.00
M1A SP24	236.0	16.52	4.95	0.45	0.00
M1A SP25	166.6	16.67	0.83	0.05	0.59
M1B SB1	122.8	16.87	2.72	0.00	1.52
M1B SB2	135.9	16.27	2.77	0.00	1.57
M1B SB3	165.0	15.64	3.35	0.00	1.46
M1B SI4	161.8	16.55	3.63	0.00	1.57
M1B SI5	158.2	23.28	1.60	0.00	1.64
M1B SI6	147.5	22.47	1.38	0.00	1.63
M1B SI7	149.0	24.50	1.68	0.00	1.75
M1B SI8	150.4	27.44	1.67	0.00	1.71
M1B SI9	145.2	23.80	2.08	0.00	1.66
M1B SI10	145.2	23.39	1.69	0.00	1.96

M1B SI11	148.3	23.05	1.58	0.00	1.85
M1B SI12	177.5	19.12	2.03	0.00	1.55
M1B SI13	199.1	18.41	2.45	0.00	1.47
M1B SI14	228.3	11.94	2.29	0.05	1.12
M1B SI15	252.8	16.69	3.88	0.05	1.27
M1B SI16	277.2	16.16	4.01	0.05	1.26
M1B SI17	286.0	16.30	5.01	0.00	1.24
M1B SI18	280.4	8.11	4.68	0.00	1.16
M1B SI19	264.4	15.27	9.08	0.00	1.03
M1B SI20	279.0	15.09	4.95	0.00	1.10
M1B SP21	275.9	14.62	5.05	0.00	1.14
M1B SP22	252.1	15.24	5.18	0.05	1.08
M1B SP23	251.1	15.73	4.83	0.00	1.12
M1B SP24	235.4	15.19	4.73	0.00	1.07
M1B SP25	151.3	17.66	0.90	0.00	1.91
M2A SI13	176.2	14.78	3.56	0.00	1.47
M2A SI14	173.8	11.32	2.94	0.00	1.38
M2B SB1	97.4	12.73	2.36	0.00	2.99
M2B SB2	135.9	12.73	2.59	0.00	3.10
M2B SB3	142.6	12.93	3.15	0.00	3.12
M2B SI4	138.7	13.82	2.38	0.00	3.21
M2B SI5	133.4	17.84	1.74	0.00	2.71
M2B SI6	125.6	18.17	1.77	0.00	2.70
M2B SI7	126.9	20.86	1.75	0.00	2.75
M2B SI8	132.3	20.82	1.77	0.00	2.70
M2B SI9	134.9	7.62	2.59	0.00	2.76
M2B SI10	129.7	15.35	2.62	0.00	3.61
M2B SI11	127.7	14.55	2.77	0.00	3.74
M2B SI12	125.6	14.49	2.81	0.05	3.21
M2B SI13	125.9	14.46	2.92	0.05	3.13
M2B SI14	132.5	14.66	3.53	0.00	3.32
M2B SI15	138.2	14.00	4.05	0.05	2.91
M2B SI16	127.1	13.91	4.47	0.05	3.08
M2B SI17	149.8	14.10	5.90	0.00	2.81
M2B SI18	143.2	13.38	5.98	0.00	3.00
M2B SI19	139.6	13.39	5.44	0.00	3.09
M2B SI20	145.5	13.63	5.05	0.05	2.90
M2B SP21	150.8	13.76	4.67	0.00	2.77
M2B SP22	149.4	13.43	4.73	0.00	2.93
M2B SP23	148.3	13.25	4.55	0.00	2.79
M2B SP24	148.9	14.45	4.55	0.00	2.79
M2B SP25	123.5	12.25	1.34	0.05	2.18
M3B SB1	34.2	34.79	1.48	0.00	0.00

M3B SB2	54.5	35.81	1.74	0.00	0.00
M3B SB3	57.4	35.27	1.84	0.05	0.17
M3B SI4	54.8	36.31	1.96	0.13	0.12
M3B SI5	113.9	27.13	1.42	1.85	0.53
M3B SI6	117.7	27.52	1.22	1.04	0.51
M3B SI7	115.0	26.83	1.41	1.87	0.60
M3B SI8	110.2	28.26	1.09	0.30	0.29
M3B SI9	102.2	29.24	1.31	0.28	0.24
M3B SI10	83.5	31.71	1.11	0.46	0.29
M3B SI11	76.3	33.71	1.13	0.46	0.29
M3B SI12	65.8	33.46	1.49	0.30	0.00
M3B SI13	61.4	33.19	1.55	0.45	0.00
M3B SI14	60.9	35.79	2.89	0.49	0.00
M3B SI15	57.0	33.05	1.55	0.43	0.00
M3B SI16	58.0	32.40	1.55	0.35	0.17
M3B SI17	54.9	33.21	2.61	0.18	0.00
M3B SI18	52.6	38.89	1.63	0.22	0.00
M3B SI19	48.3	35.19	1.60	0.05	0.10
M3B SI20	49.3	37.05	1.97	0.05	0.00
M3B SP21	50.0	38.27	1.82	0.12	0.00
M3B SP22	52.6	36.96	1.64	0.00	0.00
M3B SP23	53.8	34.74	1.52	0.15	0.00
M3B SP24	53.6	38.25	1.50	0.19	0.00
M3B SP25	75.6	29.59	1.01	0.86	0.26
M4B SB2	266.9	11.2	8.2	0.0	0.0
M4B SB3	304.4	11.4	8.4	0.0	0.0
M4B SI4	272.8	11.5	8.0	0.05	0.0
M4B SI5	278.0	11.1	8.2	0.0	0.0
M4B SI6	266.9	11.2	8.1	0.0	0.0
M4B SI7	264.1	12.3	6.7	0.0	0.0
M4B SI8	264.1	12.7	6.4	0.0	0.0
M4B SI9	251.2	13.5	6.8	0.0	0.0
M4B SI10	251.0	33.4	6.3	0.0	0.0
M4B SI11	252.0	13.8	6.5	0.0	0.0
M4B SI12	259.2	14.6	7.5	0.05	0.0
M4B SI14	257.6	13.9	7.9	0.0	0.0
M4B SI15	264.1	13.9	7.4	0.0	0.0
M4B SI17	270.6	14.2	9.2	0.0	0.0
M4B SI18	270.8	12.9	8.8	0.0	0.0
M4B SI19	270.2	12.6	9.4	0.0	0.0
M4B SI20	278.8	11.1	8.9	0.0	0.0
M4B SP21	295.3	12.1	8.3	0.0	0.0
M4B SP22	320.6	11.8	7.7	0.0	0.0

M4B SP23	278.6	11.9	8.5	0.0	0.0
M4B SP24	278.8	12.3	8.4	0.0	0.0
M4B SP25	247.1	11.03	4.4	0.05	0.05

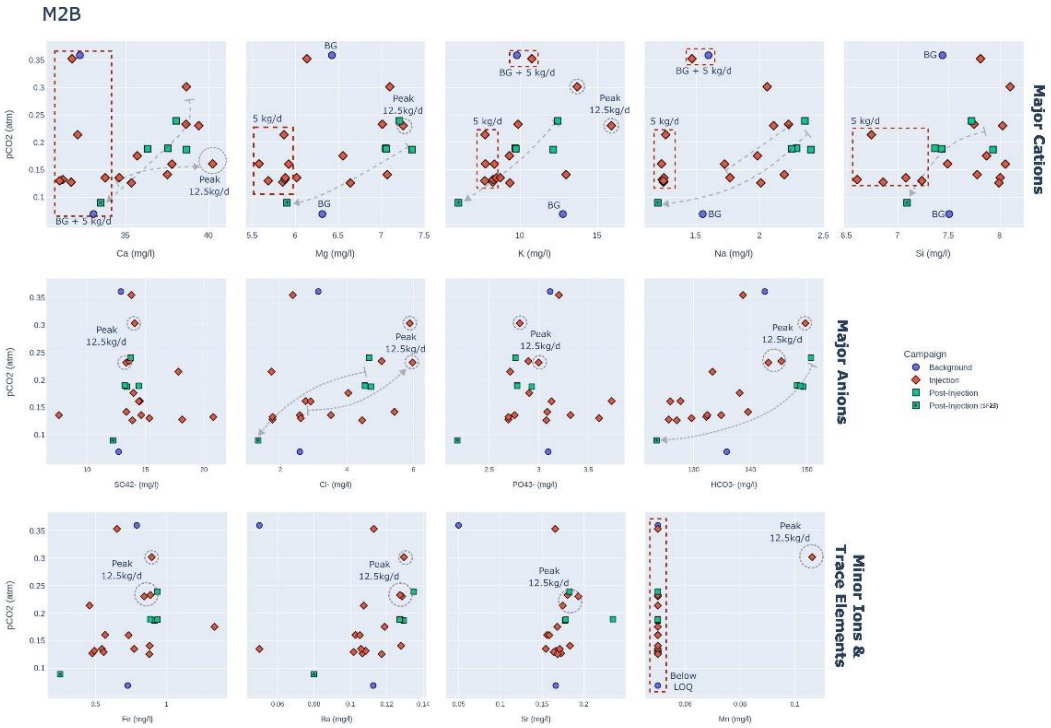

***Figure S1**. Evolutionary pathway of ion and trace element concentrations for M2B during background conditions, low CO_2 injection rates, increasing injection rates, peak levels, and subsequent return to background levels during both immediate and long-term post-injection phases.*

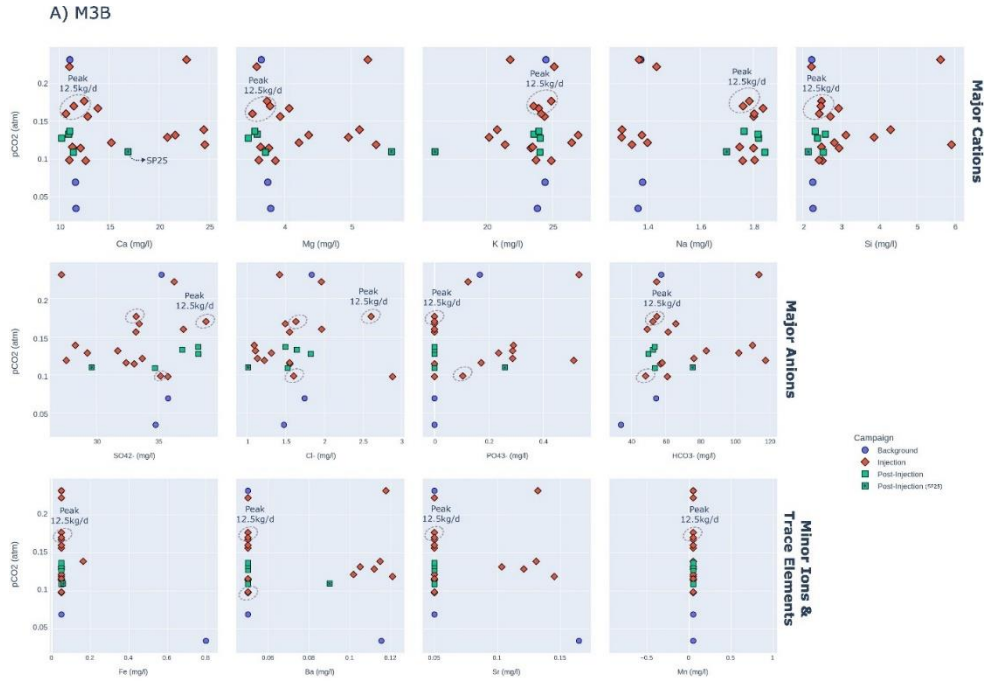

Figure S2. *Evolutionary pathway of ion and trace element concentrations for M3B during background conditions, low CO_2 injection rates, increasing injection rates, peak levels, and subsequent return to background levels during both immediate and long-term post-injection phases.*

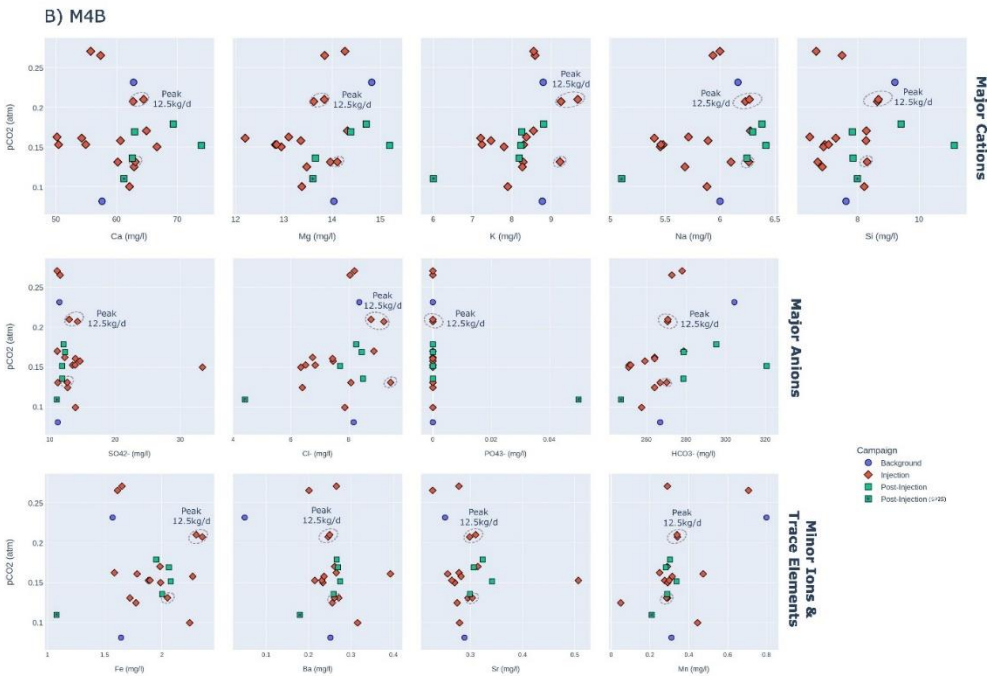

Figure S3*. Evolutionary pathway of ion and trace element concentrations for M4B during background conditions, low CO_2 injection rates, increasing injection rates, peak levels, and subsequent return to background levels during both immediate and long-term post-injection phases.*